CSDL-R-2088

CONTROL OF FLEXIBLE STRUCTURES-II (COFS-II) FLIGHT CONTROL, STRUCTURE, AND GIMBAL SYSTEM INTERACTION STUDY

by

Stanley Fay, Stephen Gates, Timothy Henderson, Lester Sackett, Kim Kirchwey, Isaac Stoddard, Joel Storch

September 1988

The Charles Stark Draper Laboratory, Inc.
555 Technology Square
Cambridge, Massachusetts 02139

R-2088

CONTROL OF FLEXIBLE STRUCTURES-II (COFS-II) FLIGHT CONTROL, STRUCTURE, AND GIMBAL SYSTEM INTERACTION STUDY

By

Stanley Fay, Stephen Gates, Tim Henderson, Christopher Kirchwey,
Lester Sackett, Isaac Stoddard, Joel Storch

September 1988

Approved: Stanley Fay
Stanley Fay
Program Manager

Approved: N. Sears
Norm Sears
Space Programs
Director

Approved: ----------
Eli Gai
Control & Decision
Systems, Director

The Charles Stark Draper Laboratory, Inc.
Cambridge, Massachusetts 02139

ACKNOWLEDGEMENT

The report was prepared by the Charles Stark Draper Laboratory, Inc., for the Langley Research Center of the National Aeronautics and Space Administration under contract No. NAS9-17560. The contract monitor at LaRC was Mr. Claude Keckler and the project manager at CSDL was Mr. Stanley Fay.

The authors wish to thank Claude Keckler, Jon Pyle, Victor Cooley and others at LaRC for their help and direction in meeting the contract objectives.

The principal authors of the report were as follows:

Section 1: - All
Section 2: - Christopher Kirchwey, Lester Sackett
Section 3: - Lester Sackett
Section 4: - Tim Henderson
Section 5: - Christopher Kirchwey
Section 6: - Steve Gates, Joel Storch
Section 7: - Isaac Stoddard
Section 8: - Christopher Kirchwey
Section 9: - Lester Sackett
Section 10: - Stanley Fay
Section 11: - All

The publication of this report does not imply approval by the sponsor of the content and conclusions contained herein.

Table of Contents

Figures

Tables

SECTION 1
INTRODUCTION

This report documents the work done at CSDL on NASA contract NASA9-17560 for the Langley Research Center for the task of COFS-II Flight Experiment Definition Support and specifically for Task 2, Dynamic Interaction of COFS-II Experiment and Shuttle Orbiter. Task 1, Computer Requirements Definition, was reported elsewhere.

The COFS-II flight experiment was expected to be the second Control of Flexible Structures (COFS) flight experiment. The first was to have included only the COFS mast plus a compact tip mass. The second experiment and the subject of this study includes the COFS-I mast and the Langley 15-meter hoop/column antenna attached to the tip of the mast by means of an adapter structure and a two degree-of-freedom gimbal. The gimbal to be used is based on the Sperry Advanced Gimbal System with 110 degrees deflection plus and minus in elevation and lateral angles. The maximum gimbal slew rate is 4 deg/s with 33.9 N-m (25 ft-lb) maximum torque. The mast will be mounted in the Space Shuttle Orbiter payload bay. A set of proof-mass dampers will be placed on the mast for experimental damping of flexure. The dampers may be inactive or may provide approximately the equivalent of 5% structural damping in the first several flexure modes. An illustration of the Shuttle/COFS-II configuration is shown in Figure 1-1.

The Shuttle Orbiter Flight Control System (FCS) controls the firings of reaction control system (RCS) jets for attitude control and also translational maneuvering. The attitude control system may be active with the COFS-II mast and antenna deployed. It was assumed that only the low thrust vernier RCS (VRCS) would be used. The VRCS can be used for automatic attitude hold and for manual or automatic attitude maneuvering. Because the COFS-II system is flexible, there exists a concern about possible dynamic interaction between the flexible structure and the flight control system. Probably the Orbiter would be in free drift during experimental periods and during antenna slewing. There is also a concern about the loads on the COFS-II caused by RCS firings.

The goals of the dynamic interaction study included the following.

To determine the Orbiter pointing requirements. This task involves Shuttle operational procedures and affects the free drift time that would be allowed for COFS-II experiments.

To determine the interaction between the FCS and the flexible COFS-II with and without active mast dampers. The interaction includes the stability of the FCS given the flexible structure, other interactions during attitude holds or maneuvers, loads produced by RCS firings on the base of the mast, tip of the mast, and base of the antenna, and the effect of adding the mast dampers on stability and damping.

To study the interaction of the gimbal servos and the flexible structure assuming the FCS is inactive.

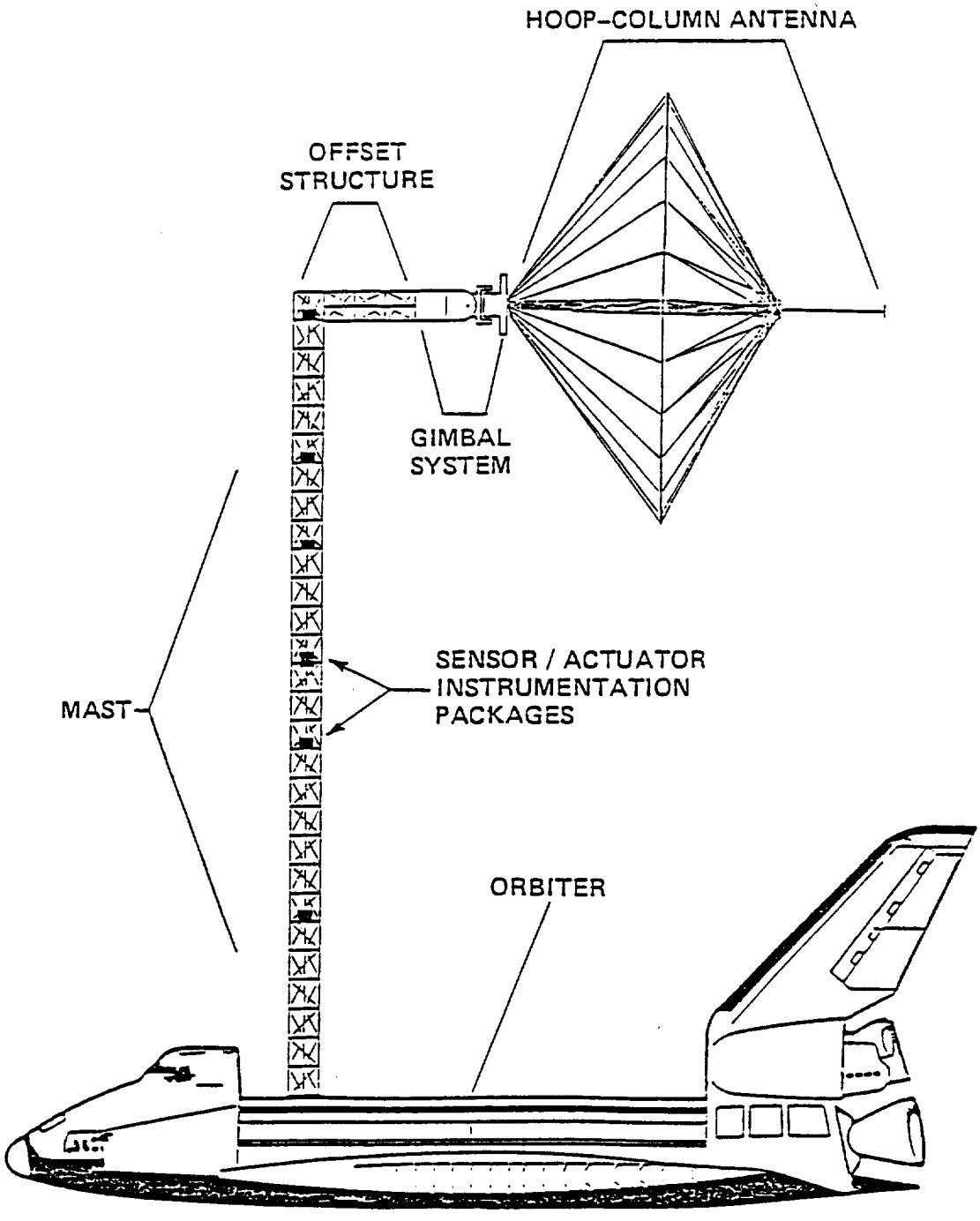

Figure 1-1. Orbiter/COFS-II flight configuration.

The study was limited to 100% mast deployment length. Two model sets were created, one with a high fidelity structure in fixed configurations and one with a lower fidelity structure with a steerable antenna. Three fixed configurations were assessed. In the nominal configuration the antenna is facing aft with its column perpendicular to the COFS mast (as depicted in Figure 1-1). In the second configuration, the antenna is pointing up from the payload bay. In the third configuration, the antenna is pointed 45 degrees from the nominal configuration in both elevation and lateral gimbals. The effect of antenna slewing in which the initial orientation was one of the three, but the pointing of the antenna changed, was also investigated. Slewing in only one axis at a time was considered. Because of the limited capability of the gimbal motors, the servo was assumed to be saturated with the maximum 33.9 N-m torque during gimbal slew. The maximum 4 deg/s slew rate can almost never be reached given the gimbal angular range and the mass properties of the antenna.

Locations in the Space Shuttle Orbiter and Orbiter mass properties are commonly given with respect to the Fabrication coordinate frame. The origin of the Fabrication coordinate system is in the Orbiter plane of symmetry, 10.16 m (400 in.) below the centerline. Positive sense is from the nose toward the tail of the Orbiter. The Z-axis is in the Orbiter plane of symmetry perpendicular to the X-axis. Positive sense is upward in the Orbiter landing configuration. The Y-axis is out the right wing, completing a rotating, right-handed Cartesian coordinate system.

FCS quantities are usually given in the Vehicle coordinate frame. The origin of the Vehicle body coordinate system, like that of the Fabrication frame, is fixed relative to the vehicle. It is located near the tail of the Orbiter with coordinates relative to the Fabrication from of (38.1, 0, 10.16) m or (1500, 0, 400) inches. In the Vehicle frame, the X-axis points toward the nose, Y is out the right wing, and Z is down. It is a right-handed, rotating Cartesian coordinate frame.

Other coordinate frames are introduced in this report as needed.

The following topics are addressed in the remaining sections of this report. For better understanding of the sections which follow, the FCS is described in Section 2. Section 3 discusses Shuttle Orbiter pointing requirements. Much of the information is taken from NASA documentation on Shuttle requirements and capabilities, from flight experience, and from limited analysis. In order to assess the dynamic interaction of the COFS-II and the FCS, structural models of the Orbiter/COFS-II were necessary. The fixed configuration models using finite element methods are described in Section 4. The dynamic interaction was investigated primarily by simulation. The simulator and FCS software used for investigation of the fixed configurations are discussed in Section 5. For antenna slewing studies, a model of the articulated system was necessary. The development of the articulated system model is described in the Section 6. That model was input to the industry-known flexible body dynamics program, DISCOS, and combined with an FCS software library, as described in Section 7. Results of the extensive simulation studies are then given, first for the fixed configurations in Section 8 and

then for the articulated system in Section 9. In Section 10, the modeling, analysis, and simulation of the gimbal servo with the flexible structure and the results are discussed. Finally there are a concluding section and appendices.

SECTION 2
THE FLIGHT CONTROL SYSTEM

The Orbiter Flight Control System controls the firing of RCS jets for attitude and translational control. There are thirty-eight 3871.5 N (870 pound) thrust primary jets and six 111.25 N (25-pound) vernier jets. For this study only the VRCS jets were assumed to be used.

Figure 2-1 shows the FCS functional block diagram and its relationship to the vehicle control loop. The FCS elements included for this study are (from sensor to effectors) an inertial measurement unit (IMU), an attitude state estimator, selectable closed-loop manual and automatic maneuver logic, a phase plane switching controller, vernier jet selection logic, and the VRCS jets.

The IMU is an attitude sensor with gimbal kinematics followed by an analog-to-digital converter. There is a hardware plus software transport time lag between an attitude reading and the resulting application of force by the VRCS. The state estimator generates body-axis vector estimates of Orbiter attitude, angular rate and disturbance angular acceleration from the IMU gimbal and angle data, and from jet firing information supplied by the jet selection logic which helps compensate for the transport lag.

The closed loop manual mode generates an angular rate command for each body rotation axis (roll, pitch, and yaw) in response to corresponding deflections of the rotational hand controller (RHC). The command has the value -MR, +MR, or 0 for negative, positive, or zero RHC deflection, where MR is the crew-selected maneuver rate. In each axis, the desired attitude is obtained by integration of the desired rate, and is reset equal to the current attitude whenever the RHC is moved out of or into the zero (center detent) position (which initiates or halts a maneuver about that axis). Because of the attitude integration, this logic implements a "rate hold" (accurate long-term average rate maintenance) during maneuvers and an attitude hold at other times.

The closed loop automatic maneuver logic issues rate and attitude commands to perform a rotation to any target attitude about a single rotation axis (SRA), which ideally is fixed in both the inertial reference axes and the Orbiter body axes. The SRA is cyclically recomputed to allow for non-ideal response to the commands. The vector magnitude of the rate command is equal to the crew-specified maneuver rate (MR). When the vector magnitude (AM) of the difference between the current and target attitudes becomes less than the size of the per-axis attitude deadband being used in the phase plane (see below), the logic switches to the attitude hold mode, commanding zero rate and the target attitude. During attitude hold, if disturbances cause AM to exceed twice the phase plane deadband, the logic returns to the maneuver mode.

In the remaining sections of the FCS, attitude and angular rate errors are formed by comparing the desired values with the corresponding estimated values, and the phase plane switcher in turn compares the errors with permissible error limits, referred to as a deadband and a rate limit. Depending on the outcome of these comparisons and on the value of the estimated disturbance acceleration, the phase plane may command a jet firing to reduce errors in one or more of the body control axes. If the errors in a particular axis do not warrant a firing, the phase plane indicates a "preferred" value of residual acceleration for that axis in case a firing is

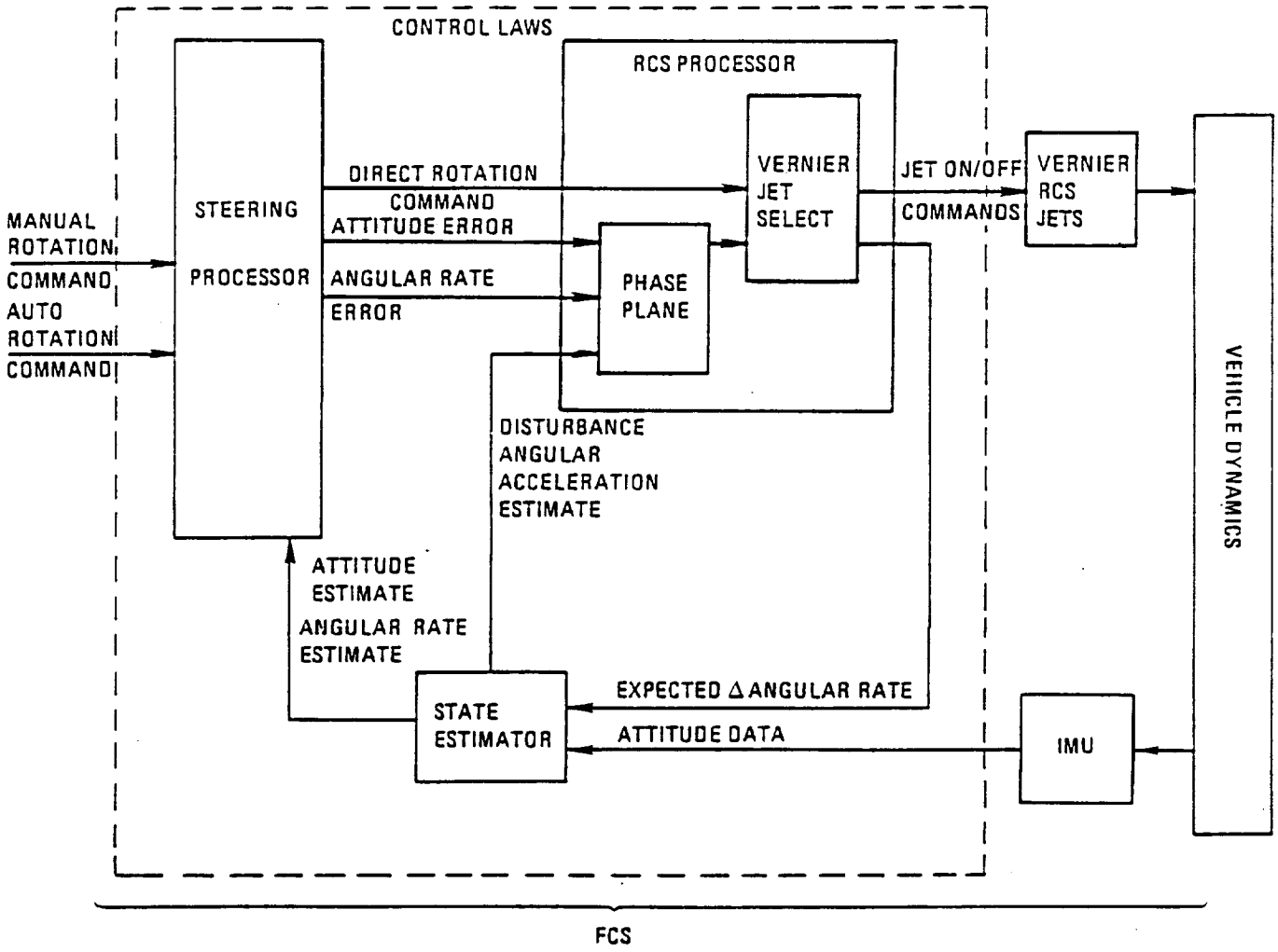

Figure 2-1. FCS functional block diagram.

commanded in any other axis. See Figure 2-2 for a diagram of the phase plane and the switching lines. The jet selection logic then chooses up to three VRCS jets whose acceleration vector(s) provide a reasonable match with the command vector from the phase plane. The VRCS jets generate constant steady state forces with uniform buildup and tailoff profiles caused by electrical valve open/close delays and jet ignition characteristics. They can be modeled with little loss of fidelity as constant forces and torques applied for integer multiples of the 80-ms FCS computational cycle, with either time or thrust magnitude adjustments made to the first and last 80-ms portions. References 2-1, 2-2, and 2-3 provide a more detailed description of the on-orbit FCS.

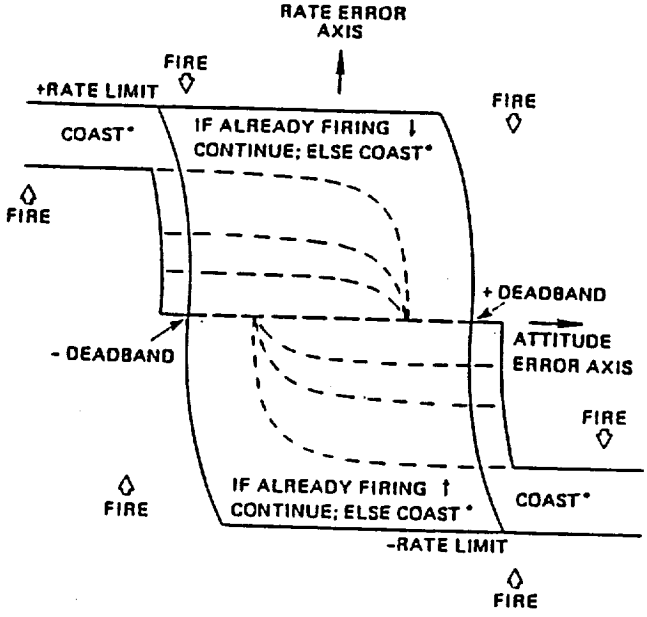

Figure 2-2. Phase plane controller.

REFERENCES

2-1 L. L. Sackett and C. B. Kirchwey, "Dynamic Interaction of the Shuttle On-Orbit Flight Control System with Deployed Flexible Payloads". AIAA Paper 82-1535, August 1982.

2-2 Shuttle On-Orbit Flight Control Characterization (Simplified Digital Autopilot), prepared by The Charles Stark Draper Laboratory, Inc., NASA JSC-18511, August 1982.

2-3 Space Shuttle Orbiter Operational Level C Functional Subsystem Software Requirements, Guidance, Navigation, and Control, Part C, Flight Control Orbit DAP, Rockwell International, STS 83-0009B, June 30, 1987.

SECTION 3
ORBITER POINTING REQUIREMENTS

3.1 The Problem

Part of the task was to determine the Shuttle Orbiter pointing requirements when the COFS-II experiment is deployed and to estimate the maximum testing period during which the Orbiter may be maintained in a free drift mode. The experimenters would like to have a long period in which there are no firings so that the ability of the structure, the gimbal servos, and the mass dampers to dampen vibrations can be investigated.

3.2 Thermal Constraints

According to Ref. 3-1, there exist limitations on the duration of an arbitrary attitude due to thermal constraints. Portions of the Shuttle may get either too cold or too hot. In general, thermal constraints may limit the Orbiter to 6 hours in an arbitrary attitude. Under many conditions, the length of free drift time could be longer.

3.3 Communication Constraints

The Orbiter uses several S-band antennas for general communication with the earth. There are no attitude constraints or pointing requirements for use of the S-band antennas (Ref. 3-1). The Ku-band antenna is located in the payload bay. It may be used for communication with the TDRS. If so, the Orbiter or the deployed payload must not shadow the antenna or electrically interfere with it. Normally the Orbiter will not have a requirement for communication with the TDRS, although the payload may. Thus there are no general Orbiter communication constraints on the length of free drift time.

3.4 IMU Alignment

According to Ref. 3-2, IMU alignments occur every 10-14 hours. In general, an attitude maneuver precedes the alignment.

3.5 Orbiter Attitude

If it is desired to maintain an inertial attitude, then the FCS must be active. If the Orbiter is in free drift it will tend to align itself in a "stable" gravity gradient/aero torque balance state (tail generally toward the earth). If the Orbiter is initialized in such a state, it will tend to oscillate about an equilibrium due to the varying forcing of the aero forces. According to flight experiments reported in Refs. 3-2 and 3-3, the roll attitude will diverge but remain within 2 deg of its initial state for about 15 minutes. After 6 hours the oscillations will typically have an amplitude of 10 deg but could be as much as 20 deg or more. The pitch and yaw attitudes will remain within about 2 deg of nominal.

If the FCS is used to maintain an attitude when the disturbance torques are negligible, a two-sided limit cycle will ensue. Typically, minimum impulse firings will occur. A simple analysis which assumes that there is a two sided limit cycle with minimum impulses at either attitude error deadband limit in three axes predicts a firing approximately every 10 minutes for a deadband of 1 deg. The period of the firings is proportional to the deadband. Thus for a 2 deg deadband the firings would be about every 20 minutes. However, the firings would be

more frequent if occasionally a firing was longer than one minimum impulse. Also, generally there will be some disturbance acceleration due to small gravity gradient torques, the varying aero torques, ventings, crew motion, and payload flexure. These may cause more frequent firings than would occur for the minimum impulse two-sided limit cycle. See Figure 3-1 for an illustration of the attitude error/rate error phase plane during the 2-sided limit cycle. (Ref. 3-4)

If it is desired to maintain the Orbiter in an arbitrary attitude, then the gravity gradient torques could be large and cause more frequent jet firings to maintain the attitude and rate errors within a given rate limit and deadband. For the Orbiter with deployed COFS-II, maximum gravity gradient accelerations are about 0.00008, 0.00005, 0.00010 deg/s/s in the roll, pitch, and yaw axes, respectively. If the altitude of the orbit is over 150 miles, the aero torques will be small compared to the gravity gradient torques. If there is a disturbance acceleration in a control axis, then typically a one-sided limit cycle results (see Figure 3-2 for an illustration). For example, if the gravity gradient torque is at a maximum in the yaw axis, and if the deadband is 1 deg and the rate error deadband (rate limit) is 0.02 deg/s or greater, then a simple analysis predicts that there will be jet firings (equal to several minimum impulses) about every 6 minutes. The frequency will vary depending on the deadband, rate limit, the exact values of the disturbances in each axis, etc. Payload flexibility will tend to cause more frequent firings also. Generally, firings every 2-5 minutes may be expected for typical deadbands or rate limits.

3.6 Ventings

Ventings are another source of disturbances which can cause jet firings if control is active, or can disturb the payload even if the FCS is in free drift. However, according to information in Ref. 3-1, at least 6 hours can pass between scheduled ventings, often much longer. In any case, the torques are quite small. There are some contingency or failure ventings which produce large torques, but these need not be considered for nominal operations.

3.7 Crew Motion

Crew motion can cause significant disturbances according to Ref. 3-2 and 3-3. These disturbances can influence the frequency of jet firings if the FCS is active, or can disturb the payload even if the Orbiter is in free drift. During critical experiment periods, it may be desirable to minimize crew motion.

3.8 Free Drift Time

Based on the factors discussed above, from an Orbiter requirements point of view, the Orbiter may be in free drift for at least 6 hours.

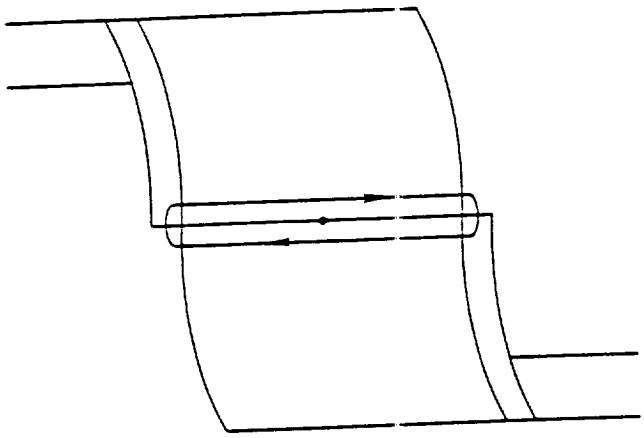

Figure 3-1. Example of two-sided limit cycle phase plane trajectory.

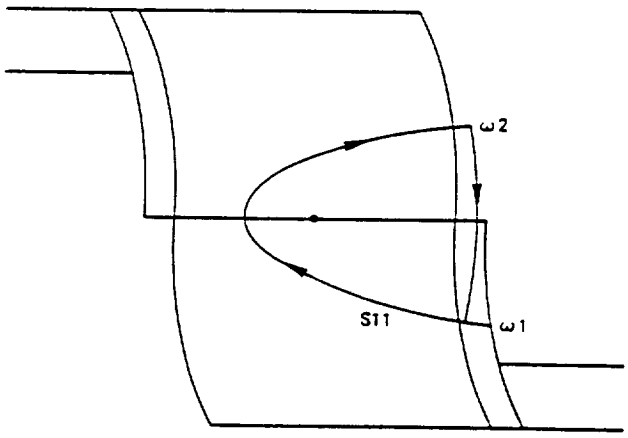

Figure 3-2. Example of one-sided limit cycle phase plane trajectory, small disturbance.

REFERENCES

3-1 Shuttle Operational Data Book, Vol. 1, NASA JSC. JSC-08934(Vol. 1) Rev. D, October 1984, with revisions to April 1987.

3-2 R. Schlundt, et. al., SDI Space Shuttle Based Experiments for Acquisition, Tracking, and Pointing: Definition of Space Shuttle Operational Environment, C. S. Draper Lab., CSDL-R-1868, 15 April 1986.

3-3 J. Miller, "Shuttle Pointing Error Reduction", C.S. Draper Lab., Memo no. CSDL-ATP-16, 18 December 1985.

3-4 L. L. Sackett and C. B. Kirchwey, "Dynamic Interaction of the Shuttle On-Orbit Flight System with Deployed Flexible Payloads", AIAA Paper 82-155, August 1982 (also CSDL-P-1581).

SECTION 4
FIXED CONFIGURATION COFS-II MODELS

4.1 Introduction

This chapter contains a description of the finite element models used in the fixed configuration COFS-II simulations. In these models, the orbiter is represented as a rigid body with the appropriate mass and inertia properties. The mast and antenna are represented with flexible finite element models. These three structures were combined to form three different finite element models corresponding to the three COFS-II configurations. The three configurations are:

Configuration #1: zero gimbal angles - antenna pointing aft

Configuration #2: elevation gimbal angle = 90 - antenna pointing up

Configuration #3 elevation gimbal and lateral gimbal angles = 45

In all cases the gimbal are assumed to be locked.

Each model was analyzed using the MSC/NASTRAN finite element program to compute the undamped natural frequencies and mode shapes of the system. The modal data was expanded to include the internal forces in the mast structure at selected locations. The model has been modified to allow recovery of the total internal load at the top and bottom of the mast and at the base of the antenna. Since the mast and antenna base were modeled by equivalent beam elements, these loads are the total forces on the structural sections, not the forces in individual members. Included in this section are descriptions of the COFS-II finite element models, mass properties of the COFS-II, orbiter, and the combined system and the natural frequencies and mode shapes of all three configurations.

4.2 Model Description

The finite element model of the COFS-II system was assembled using the data in References 4-1, 4-2, & 4-3 and the configuration described in Section 6. The COFS-II system consists of five major components: the mast, offset structure, two axis gimbal, the 15 meter antenna, and the orbiter. The model of each component will be described in the following paragraphs.

The mast was modeled by 27 equivalent beam elements with additional lumped masses added at the sensor/actuator instrumentation package locations. Each beam element represents two bays of the deployed truss. The mass and stiffness characteristics of the beams, as defined in Reference 4-3, are:

Mass/Length	= 4.641 kg/m
EA	= 124.5×10^6 n
GA	= 2.11×10^6 n
EI_x	= 28.63×10^6 n-m^2
EI_y	= 32.29×10^6 n-m^2
GK	= 0.40×10^6 n-m^2

where EI_x and EI_y refere to bending about the fabrication frame x and y axes, EA is the axial stiffness, GA is the transverse shear stiffness, and GK is the portional stiffness. The mass properties of the instrumentation packages are given in Table 4-1 by reference to the bay number in the mast and the node number in the finite element model. In this table I_{zz} is the mass moment of inertia about the axis of the mast.

Table 4-1. COFS-II Mast Instrumentation package mass properties.

Bay #	Node #	Mass (kg)	I_{zz} (kg-m^2)
12	5006	50.1	2.8
24	5012	14.4	2.8
30	5015	50.1	2.8
38	5019	14.4	2.8
44	5022	50.1	2.8
54	5027	147.1	21.6

The offset from the mast to the gimbal system, the gimbal system, and the payload platform were modeled as a series of rigid bodies connected y rigid elements. These elements are known in Figure 4-1 and the mass properties of these components are given in Table 4-2.

The finite element model of the 15 meter Harris-Hoop-Column antenna was provided by NASA/Langley. The mesh antenna surface was not included in this model since it does not contribute significantly to the response of the antenna in the frequency range of interest and would greatly increase the size and complexity of the finite element model. The finite element model of the antenna is shown in Figure 4-2, and Figure 4-3. The model of the antenna includes the stiffening effects of the pretensioned cables attached to the rim. The orbiter was modeled as a rigid body with its mass and inertia properties lumped at node point 4900 located at the orbiter center of mass. The location of the base of the COFS-II mast, node 5000, in the fabrication frame is:

x = 22.634 meters
y = 0.00 meters
z = 9.007 meters

Node 4900, the orbiter center of mass, is rigidly attached to node 5000. The mass properties of the empty orbiter are given in Figure 4-7.

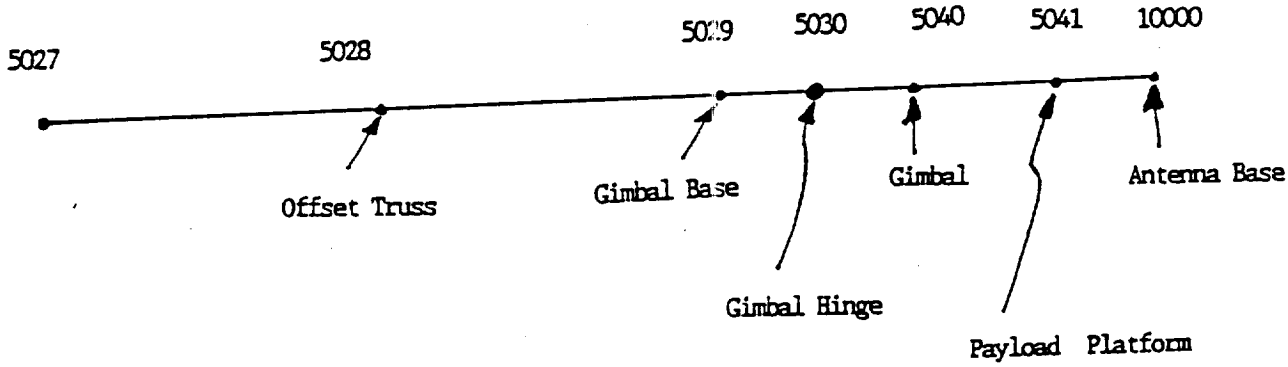

Figure 4-1. Offset structure and gimbal elements.

Table 4-2. Offset structure and gimbal mass properties.

Offset Truss:	Node 5028
	Mass = 11.788 kg
	I_{xx} = 4.826 kg-m^2
	I_{yy} = 25.35 kg-m^2
	I_{zz} = 25.35 kg-m^2
Gimbal Base:	Node 5029
	Mass = 90.621 kg
	I_{xx} = 1.436 kg-m^2
	I_{yy} = 5.395 kg-m^2
	I_{zz} = 5.395 kg-m^2
Gimbal:	Node 5040
	Mass = 58.900 kg
	I_{xx} = 0.475 kg-m^2
	I_{yy} = 3.087 kg-m^2
	I_{zz} = 3.087 kg-m^2
Payload Platform:	Node 5041
	Mass = 113.28 kg
	I_{xx} = 11.84 kg-m^2
	I_{yy} = 6.072 kg-m^2
	I_{zz} = 6.072 kg-m^2

MSC/NASTRAN finite elements models of the three COFS-II/orbiter configurations were constructed using the data provided and are shown in Figure 4-4, Figure 4-5, and Figure 4-6.

The mass properties of the three COFS-II payload configurations are given in Figure 4-8, Figure 4-10, and Figure 4-12, and the mass properties of the combined COFS-II/orbiter system are given in Figure 4-9, Figure 4-11, and Figure 4-13. The inertias are given with respect to the center of mass and the products of inertia are given as positive integrals. The principal mass moments of inertia and the transformation matrix from the fabrication frame to the principal axes are also given.

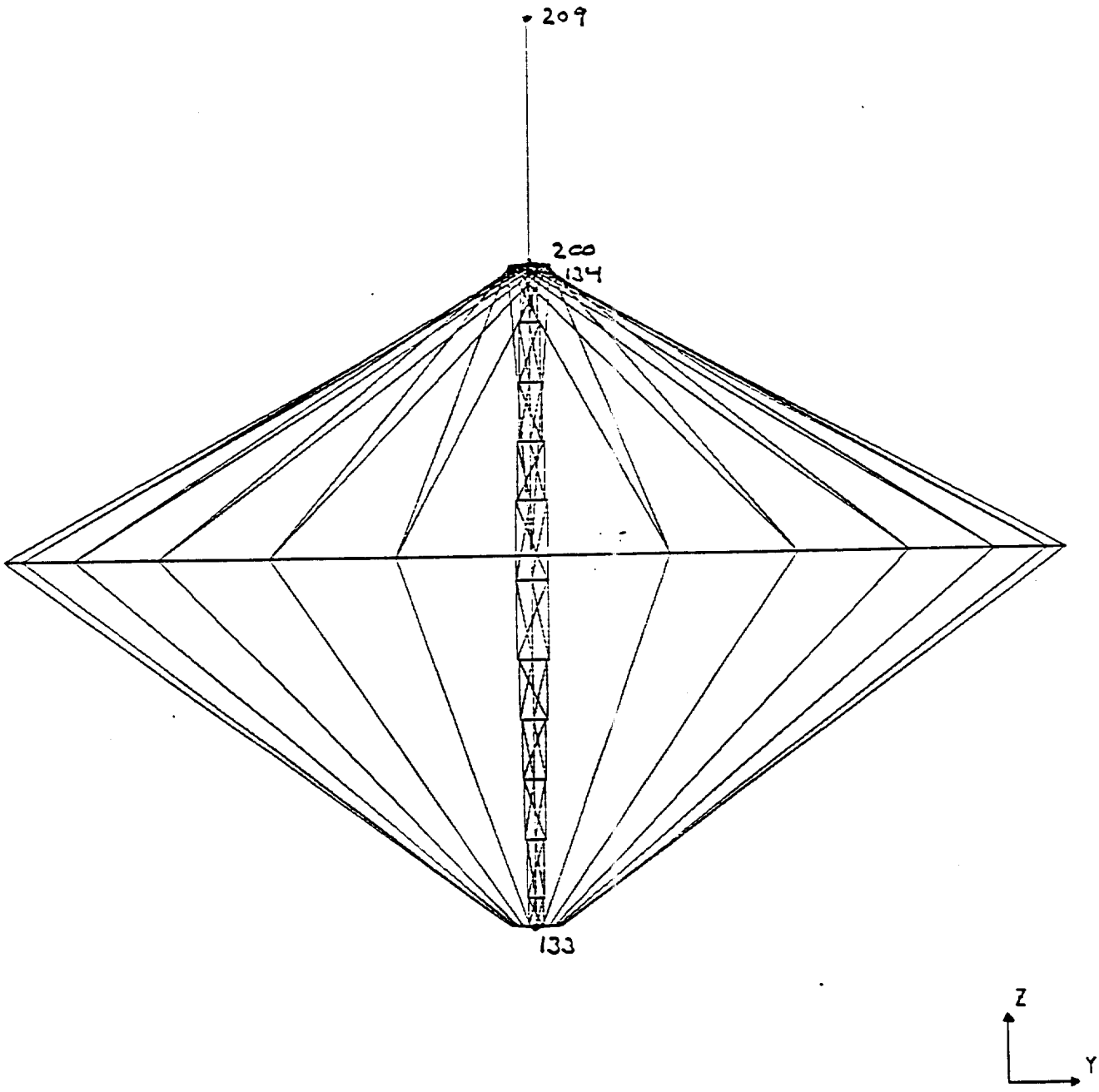

Figure 4-2. Harris hoop/column finite element model.

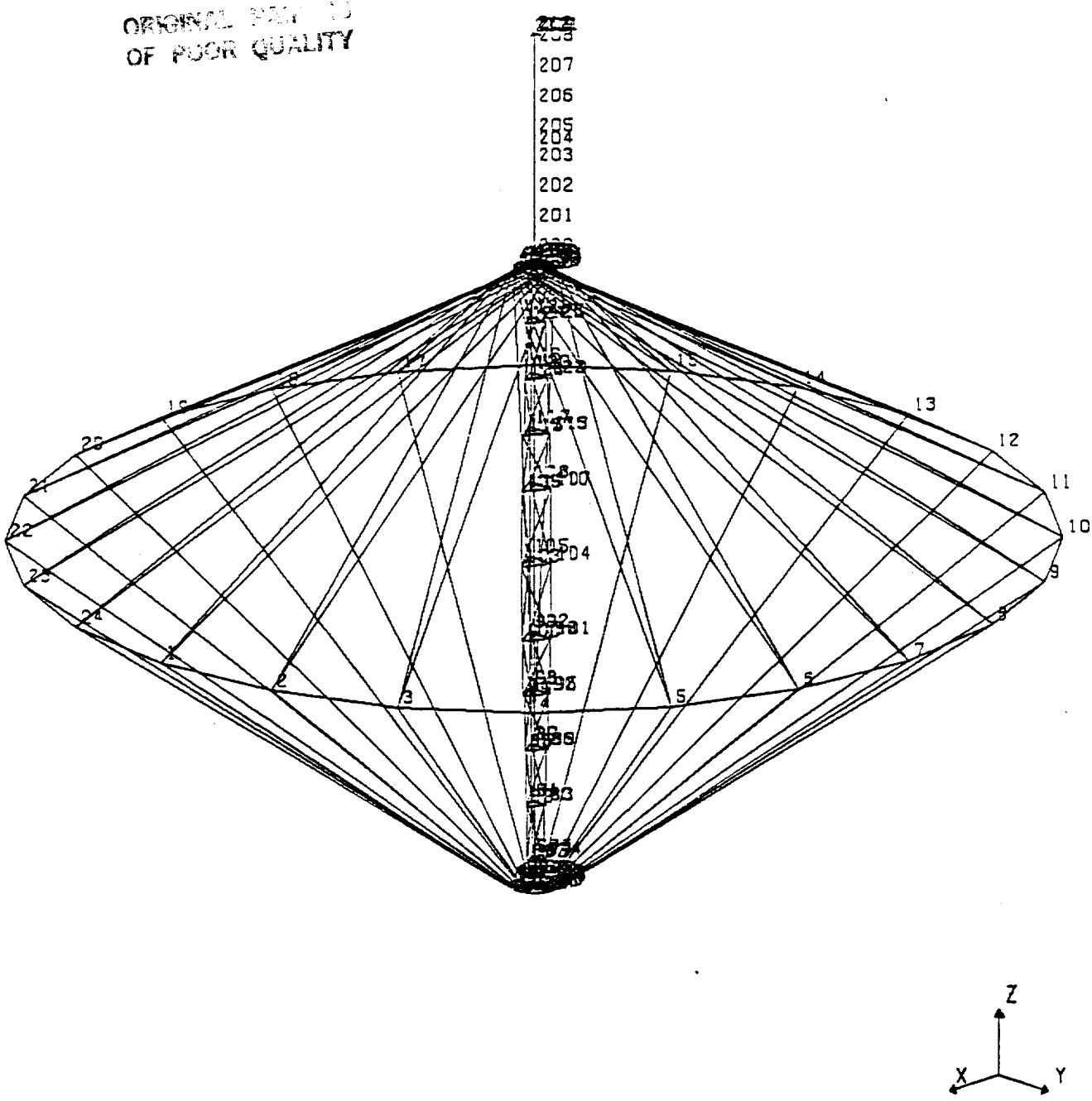

Figure 4-3. Harris hoop/column finite element model.

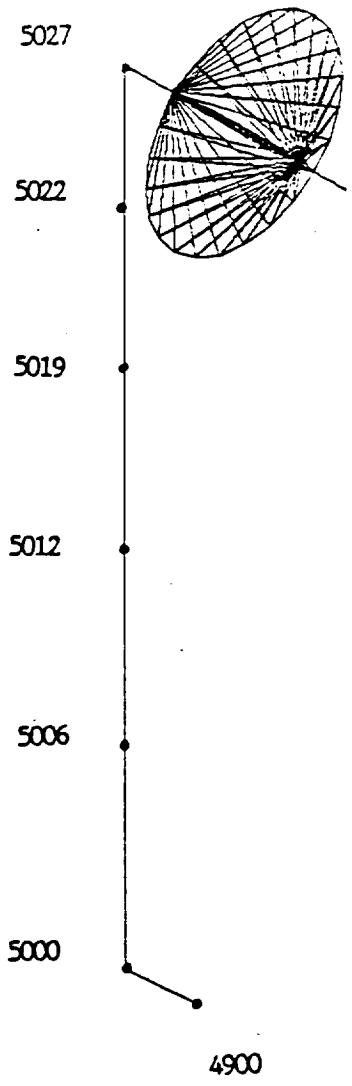

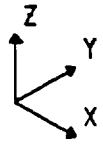

Figure 4-4. COFS-II finite element model: Configuration #1.

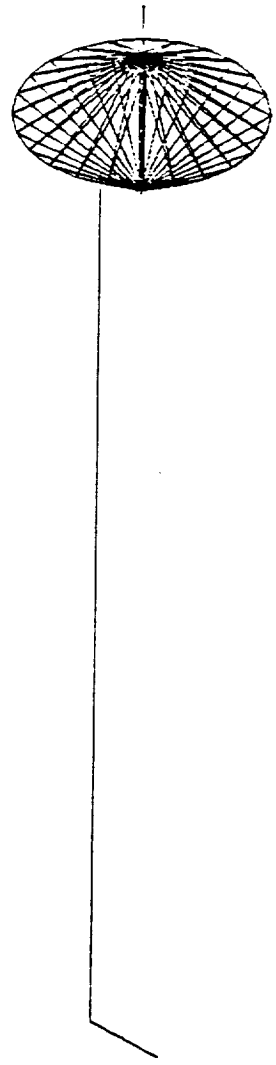

Figure 4-5. COFS-II finite element model: Configuration #2.

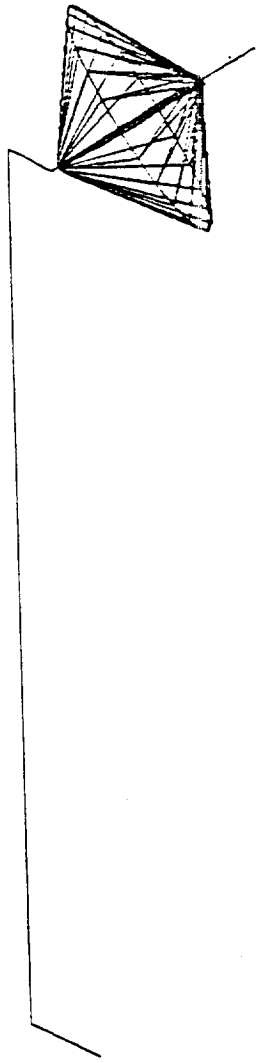

Figure 4-6. COFS-II finite element model: Configuration #3.

Orbiter

Mass: 84831.40 kg

Center of Mass: (28.020, 0.019, 9.211) m

Inertia:

$I_{xx} = 1.2533 \times 10^6$ kg-m^2
$I_{yy} = 8.9134 \times 10^6$ kg-m^2
$I_{zz} = 9.4325 \times 10^6$ kg-m^2
$P_{xy} = 1.2307 \times 10^4$ kg-m^2
$P_{xz} = 3.2695 \times 10^5$ kg-m^2
$P_{yz} = 3.9910 \times 10^3$ kg-m^2

Principal Inertia:

$IP_{xx} = 8.9134 \times 10^6$ kg-m^2
$IP_{yy} = 9.4449 \times 10^6$ kg-m^2
$IP_{zz} = 1.2410 \times 10^6$ kg-m^2

Principal Axes:

Rotation Matrix From Fabrication Frame to Principal Axes

$$R = \begin{bmatrix} 0.0019 & -.9999 & -.0065 \\ 0.0386 & 0.0066 & -.9992 \\ 0.9993 & 0.0017 & 0.0386 \end{bmatrix}$$

Figure 4-7. Orbiter mass properties.

COFS-II

Mass: 1246.90 kg

Center of Mass: (26.63, 0.00, 58.81) m

Inertia:

$I_{xx} = 3.8026 \times 10^5$ kg-m^2
$I_{yy} = 4.1276 \times 10^5$ kg-m^2
$I_{zz} = 3.9353 \times 10^4$ kg-m^2
$P_{xy} = 5.934 \times 10^{-4}$ kg-m^2
$P_{xz} = 5.4290 \times 10^4$ kg-m^2
$P_{yz} = 1.108 \times 10^{-5}$ kg-m^2

Principal Inertia:

$IP_{xx} = 3.8870 \times 10^5$ kg-m^2
$IP_{yy} = 4.1276 \times 10^5$ kg-m^2
$IP_{zz} = 3.0915 \times 10^4$ kg-m^2

Principal Axes:

Rotation Matrix From Fabrication Frame to Principal Axes

$$R = \begin{bmatrix} 0.98814 & 0.0 & 0.15356 \\ 0.0 & 1.0000 & 0.0 \\ -1.5356 & 0.0 & 1.0000 \end{bmatrix}$$

Figure 4-8. COFS-II mass properties: Configuration #1 zero gimbal angles.

ORBITER & COFS-II

Mass: 86078.21 kg

Center of Mass: (28.00, 0.02 9.93) m

Inertia:

$I_{xx} = 4.6568 \times 10^6$ kg-m^2
$I_{yy} = 1.2352 \times 10^7$ kg-m^2
$I_{zz} = 9.4743 \times 10^6$ kg-m^2
$P_{xy} = 1.2339 \times 10^4$ kg-m^2
$P_{xz} = 2.8679 \times 10^5$ kg-m^2
$P_{yz} = 2.8143 \times 10^3$ kg-m^2

Principal Inertia:

$IP_{xx} = 9.4912 \times 10^6$ kg-m^2
$IP_{yy} = 1.2352 \times 10^7$ kg-m^2
$IP_{zz} = 4.6397 \times 10^6$ kg-m^2

Principal Axes:

Rotation Matrix From Fabrication Frame to Principal Axes

$$R = \begin{bmatrix} 0.0592 & -.0016 & 0.9982 \\ -.0007 & 0.9999 & 0.0017 \\ -.9982 & -.0008 & 0.0592 \end{bmatrix}$$

Figure 4-9. Orbiter and COFS-II combined mass properties: Configuration #1.

COFS-II

Mass: 1246.90 kg

Center of Mass: (24.29, 0.00, 61.16) m

Inertia:

$I_{xx} = 4.6328 \times 10^5$ kg-m^2
$I_{yy} = 4.6659 \times 10^5$ kg-m^2
$I_{zz} = 1.0173 \times 10^4$ kg-m^2
$P_{xy} = 1.025 \times 10^{-3}$ kg-m^2
$P_{xz} = 2.7368 \times 10^4$ kg-m^2
$P_{yz} = 1{,}666 \times 10^{-3}$ kg-m^2

Principal Inertia:

$IP_{xx} = 4.6493 \times 10^5$ kg-m^2
$IP_{yy} = 4.6659 \times 10^5$ kg-m^2
$IP_{zz} = 8.5256 \times 10^3$ kg-m^2

Principal Axes:

Rotation Matrix From Fabrication Frame to Principal Axes

$$R = \begin{bmatrix} 0.99819 & 0.0 & 0.06007 \\ 0.0 & 1.0000 & 0.0 \\ -.06007 & 0.0 & 0.99819 \end{bmatrix}$$

Figure 4-10. COFS-II mass properties: Configuration #2.

Orbiter & COFS-II

Mass: 86078.21 kg

Center of Mass: (27.97, 0.02, 9.96) m

Inertia:

$I_{xx} = 5.0321 \times 10^6$ kg-m^2
$I_{yy} = 1.2713 \times 10^7$ kg-m^2
$I_{zz} = 9.4598 \times 10^6$ kg-m^2
$P_{xy} = 1.2396 \times 10^4$ kg-m^2
$P_{xz} = 1.0630 \times 10^5$ kg-m^2
$P_{yz} = 2.7588 \times 10^3$ kg-m^2

Principal Inertia:

$IP_{xx} = 9.4624 \times 10^6$ kg-m^2
$IP_{yy} = 1.2713 \times 10^7$ kg-m^2
$IP_{zz} = 5.0295 \times 10^6$ kg-m^2

Principal Axes:

Rotation Matrix From Fabrication Frame to Principal Axes

$$R = \begin{bmatrix} 0.0240 & -.0017 & 0.9997 \\ -.0007 & 0.99990 & 0.0012 \\ -.9997 & -.0008 & 0.0240 \end{bmatrix}$$

Figure 4-11. Orbiter and COFS-II combined mass properties: Configuration #2.

COFS-II

Mass: 1246.90 kg

Center of Mass: (27.97, 0.02, 9.96) m

Inertia:

$I_{xx} = 4.2663 \times 10^5$ kg-m^2
$I_{yy} = 4.2996 \times 10^5$ kg-m^2
$I_{zz} = 2.9613 \times 10^4$ kg-m^2
$P_{xy} = 1.0315 \times 10^4$ kg-m^2
$P_{xz} = 4.5676 \times 10^4$ kg-m^2
$P_{yz} = 2.9357 \times 10^4$ kg-m^2

Principal Inertia:

$IP_{xx} = 4.3895 \times 10^5$ kg-m^2
$IP_{yy} = 4.2511 \times 10^5$ kg-m^2
$IP_{zz} = 2.2170 \times 10^4$ kg-m^2

Principal Axes:

Rotation Matrix From Fabrication Frame to Principal Axes

$$R = \begin{bmatrix} 0.69828 & 0.70673 & 0.11373 \\ -.71534 & 0.69482 & 0.00743 \\ -.02649 & -.01333 & 0.99073 \end{bmatrix}$$

Figure 4-12. COFS-II mass properties: Configuration #3.

Orbiter & COFS-II

Mass: 86078.21 kg

Center of Mass: (27.98, 0.04, 9.95) m

Inertia:

$I_{xx} = 4.8509 \times 10^6$ kg-m^2
$I_{yy} = 1.2519 \times 10^7$ kg-m^2
$I_{zz} = 9.4735 \times 10^6$ kg-m^2
$P_{xy} = 1.7473 \times 10^4$ kg-m^2
$P_{xz} = 2.0306 \times 10^5$ kg-m^2
$P_{yz} = 1.3554 \times 10^5$ kg-m^2

Principal Inertia:

$IP_{xx} = 4.8420 \times 10^6$ kg-m^2
$IP_{yy} = 1.2526 \times 10^7$ kg-m^2
$IP_{zz} = 9.4764 \times 10^6$ kg-m^2

Principal Axes:

Rotation Matrix From Fabrication Frame to Principal Axes

$$R = \begin{bmatrix} -.99903 & -.00105 & 0.04398 \\ -.00300 & 0.99902 & -.04420 \\ -.04389 & -.04429 & -.99805 \end{bmatrix}$$

Figure 4-13. Orbiter and COFS-II combined mass properties: Configuration #3.

4.3 Analysis Results

The natural frequencies and mode shapes of the combined COFS-II/orbiter system were computed using the MSC/NASTRAN finite element program. The natural frequencies for the three configurations are listed in Table 4-3, Table 4-4, and Table 4-5.

Table 4-3. Natural frequencies: orbiter attached COFS-II: Configuration #1.

Mode #	Frequency (hz)
1-6	0.0
7	0.069
8	0.080
9	0.127
10	0.226
11	0.240
12	0.941
13	1.237
14	1.394
15	1.749
16	2.037
17	3.382
18	3.793
19	4.059
20	5.048
21	5.304
22	5.572
23	5.921
24	5.996
25	6.420
26	6.832
27	6.832
28	7.061
29	7.061
30	7.174
31	7.808

Table 4-4. Natural frequencies: orbiter attached COFS-II: Configuration #2.

Mode #	Frequency (hz)
1-6	0.0
7	0.072
8	0.117
9	0.117
10	0.162
11	0.314
12	0.427
13	1.225
14	1.380
15	1.787
16	1.789
17	3.137
18	3.792
19	4.071
20	4.872
21	5.304
22	5.572
23	5.749
24	5.752
25	6.438
26	6.832
27	6.832
28	7.017
29	7.061
30	7.061
31	7.808

Table 4-5. Natural frequencies: orbiter attached COFS-II: Configuration #3.

Mode #	Frequency (hz)
1-6	0.0
7	0.070
8	0.086
9	0.136
10	0.215
11	0.268
12	0.862
13	1.247
14	1.391
15	1.760
16	1.932
17	3.359
18	3.793
19	4.062
20	5.021
21	5.302
22	5.571
23	5.839
24	5.895
25	6.430
26	6.832
27	6.832
28	7.061
29	7.061
30	7.099
31	7.808

Plots of the first five flexible modes for each configuration are given in Figure 4-15, Figure 4-16 and Figure 4-17. Only the lowest twenty modes are valid because of possible interaction of the higher modes with the flexible modes of the orbiter. The node points are described in Table 4-6.

Table 4-6. Node point descriptions.

Node #	Description
4900	Orbiter Center of Mass
1-24	Hoop
25-48	Top Stay Attachment Ring
49-72	Bottom Stay Attachment Ring
73-132	Column
133	Bottom of Column
134	Top of Column
200	Bottom of Feed Mast
201-208	Feed Mast
209	Top of Feed Mast
210-212	Feed Horn
401-425	Not Used
673-675	Extra Mast Points
1000-1002	Not used
5000	Bottom of Mast
5001-5026	Mast
5027	Top of Mast
5028	Rigid Offset Center of Mass
5029	Gimbal Base Center of Mass
5030	Gimbal
5040	Upper Gimbal Center of Mass
5041	Gimbal Platform Center of Mass
10000	Platform/Antenna Interface
25000	Forces on Base of mast (node 5000)
25027	Forces o Top of Mast (node 5027)
30000	Forces on Base of Antenna (node 10000)

The first 213 points represent structural nodes and the last 3 points are additional non-structural points which are used to include the nodal forces at the lower and upper ends of the mast and at the base of the antenna. All grid points have six degrees of freedom. For the structural node points they correspond to three translations (Δx, Δy,Δz), and three rotations (Θx, Θy, Θz) in the orbiter fabrication frame. In the case of the extra force node points, the six degrees of freedom correspond to the internal forces in the following manner:

Degree of Freedom #1 === F_x Force in Local X-Direction
Degree of Freedom #2 === F_y Force in Local Y-Direction
Degree of Freedom #3 === F_z Force in Local Z-Direction
Degree of Freedom #4 === M_x Moment About Local X-Axis
Degree of Freedom #5 === M_y Moment About Local Y-Axis
Degree of Freedom #6 === M_z Moment About Local Z-Axis

The local axes are parallel to the fabrication frame axes and are centered at the three node points as is shown in Figure 4-14.

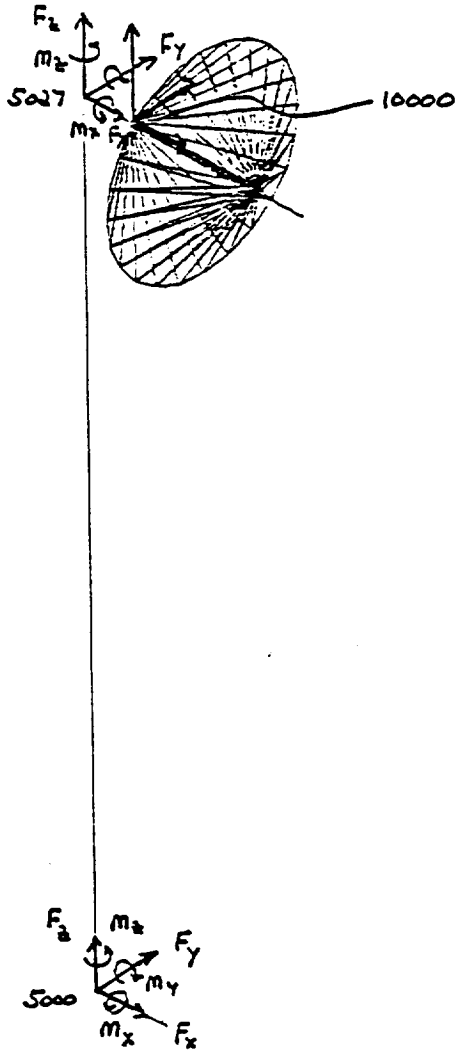

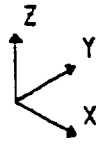

Figure 4-14. Internal force sign conventions.

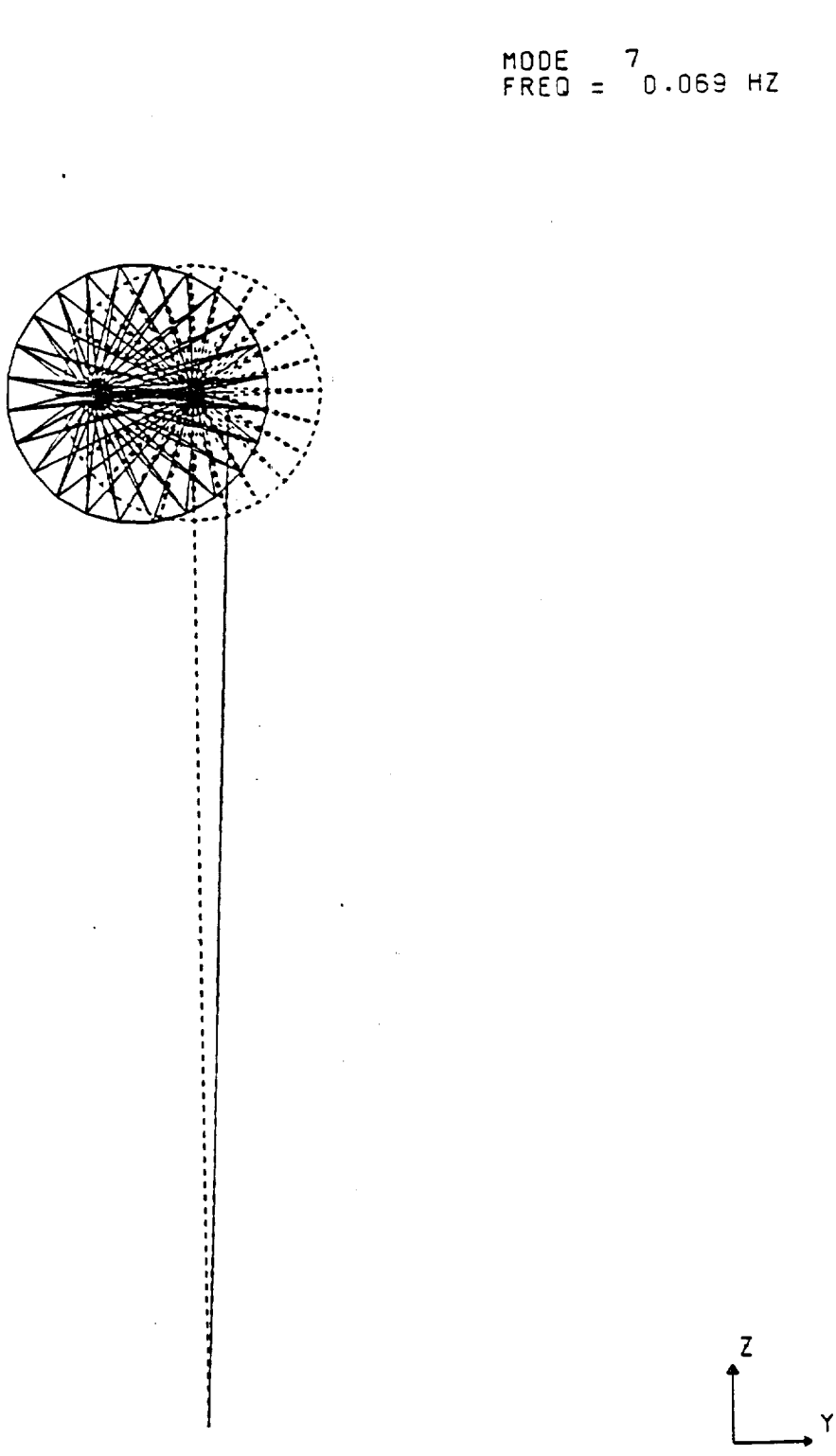

Figure 4-15. COFS-II Configuration #1: Mode 7. (Part 1 of 5)

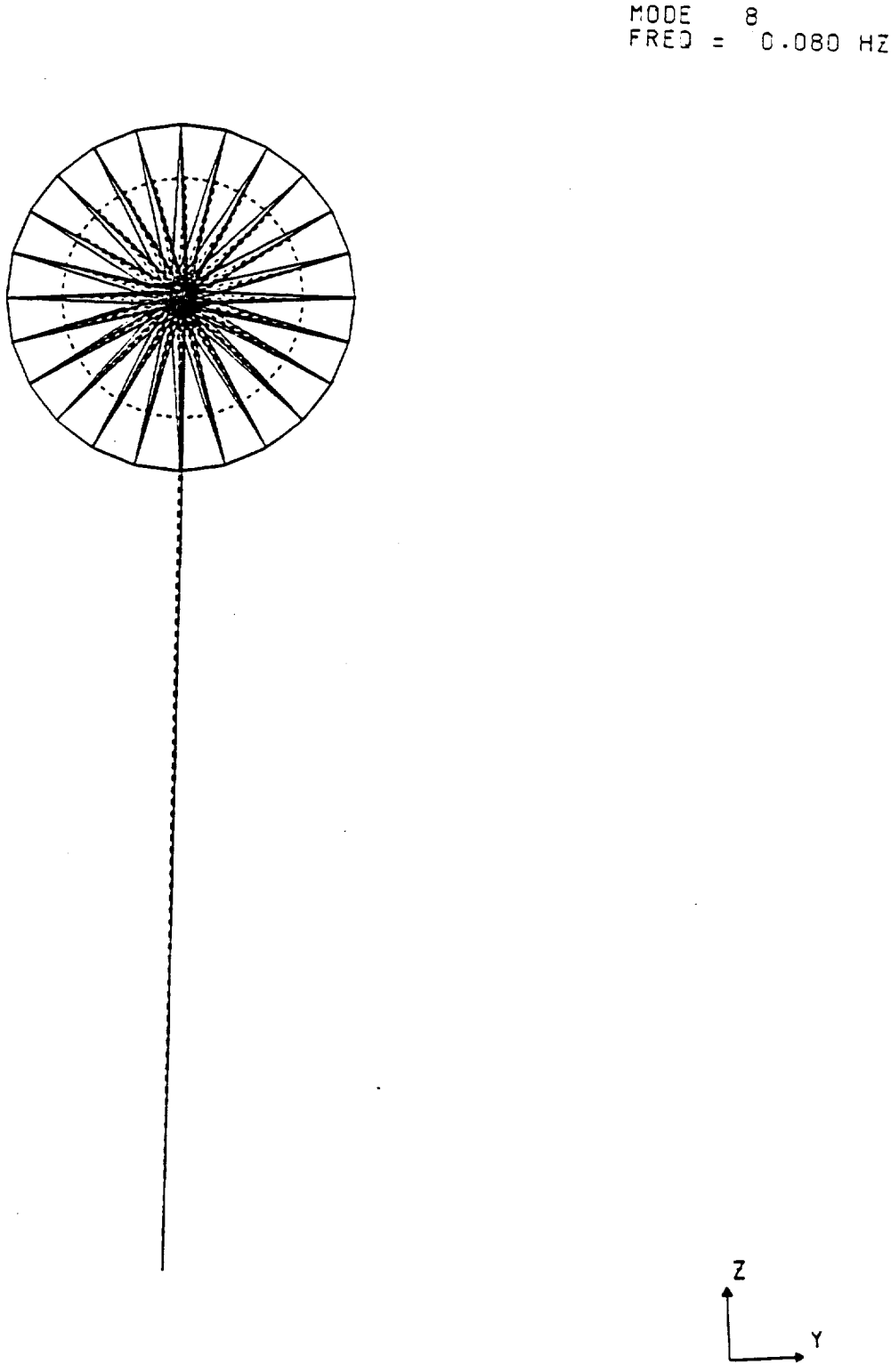

Figure 4-15. COFS-II Configuration #1: Mode 8. (Part 2 of 5)

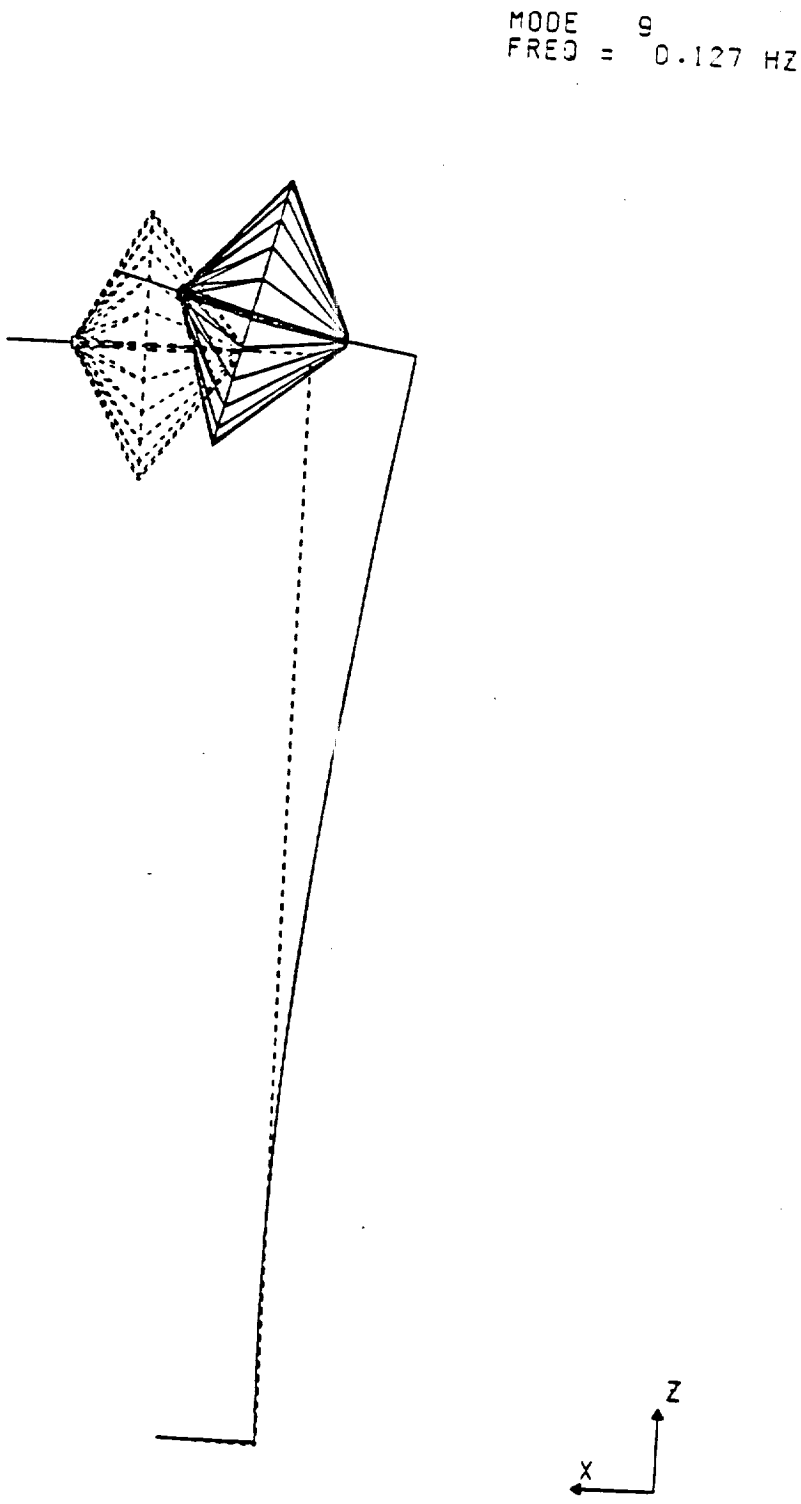

Figure 4-15. COFS-II Configuration #1: Mode 9. (Part 3 of 5)

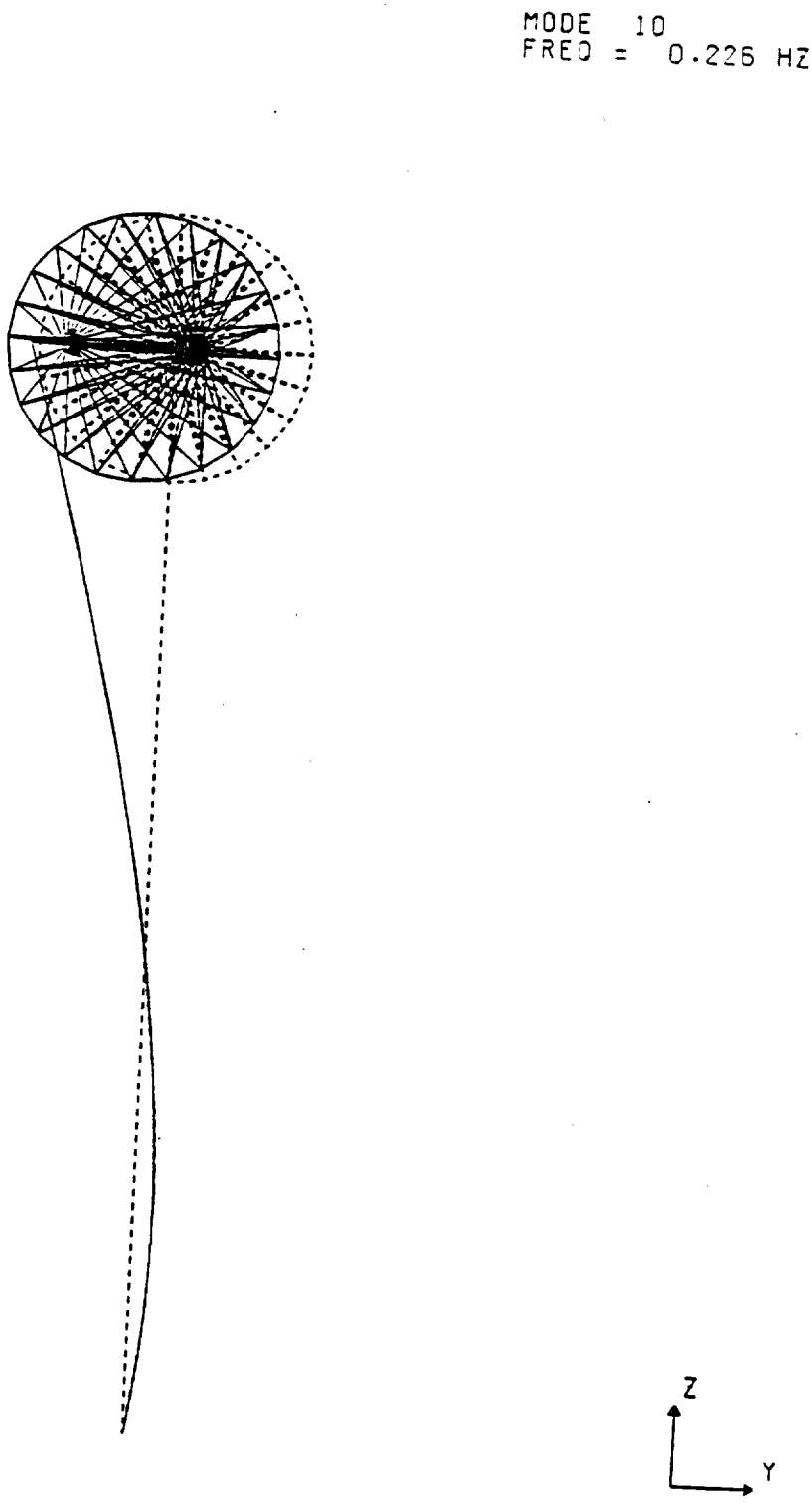

Figure 4-15. COFS-II Configuration #1: Mode 10. (Part 4 of 5)

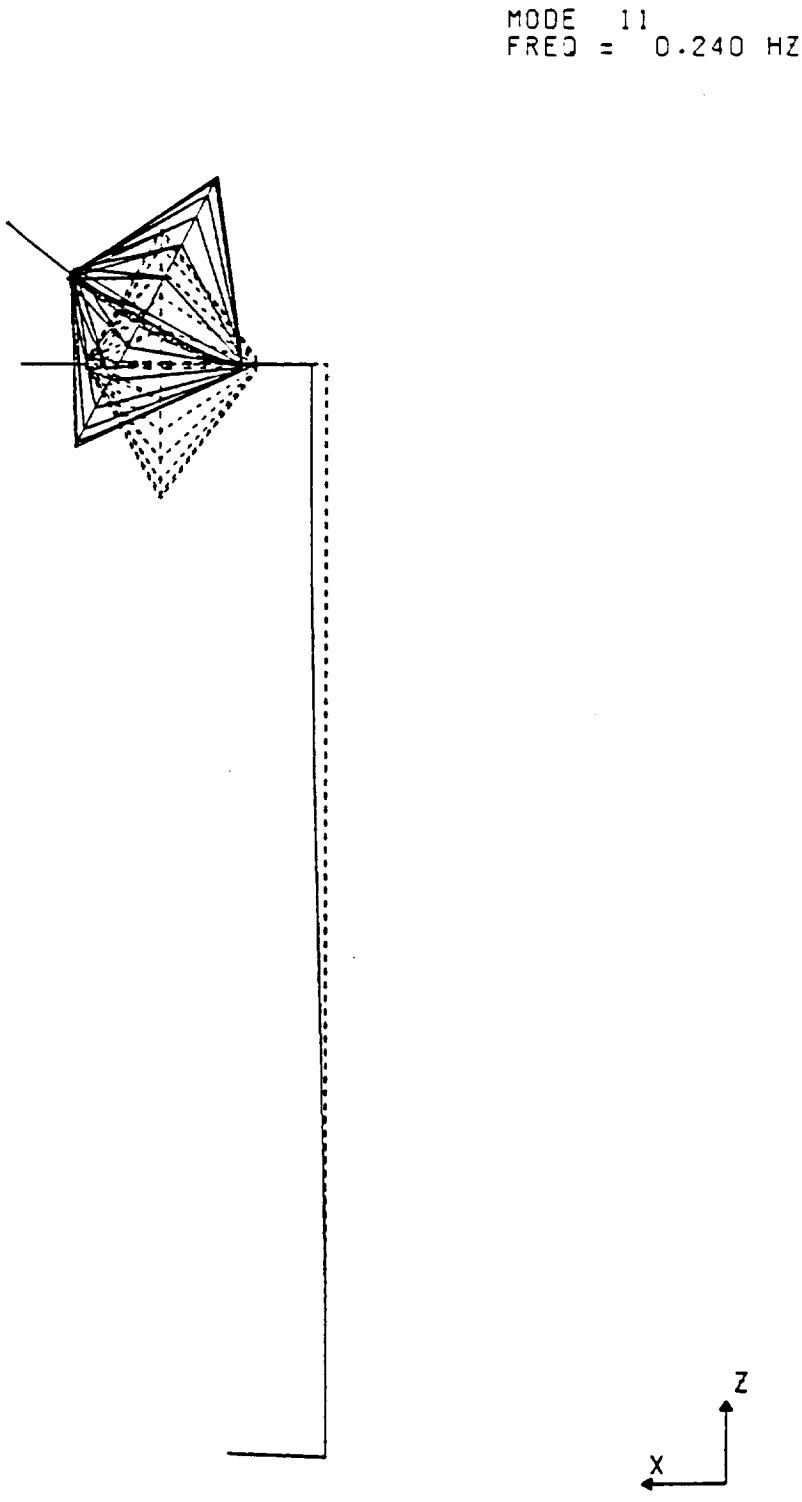

Figure 4-15. COFS-II Configuration #1: Mode 11. (Part 5 of 5)

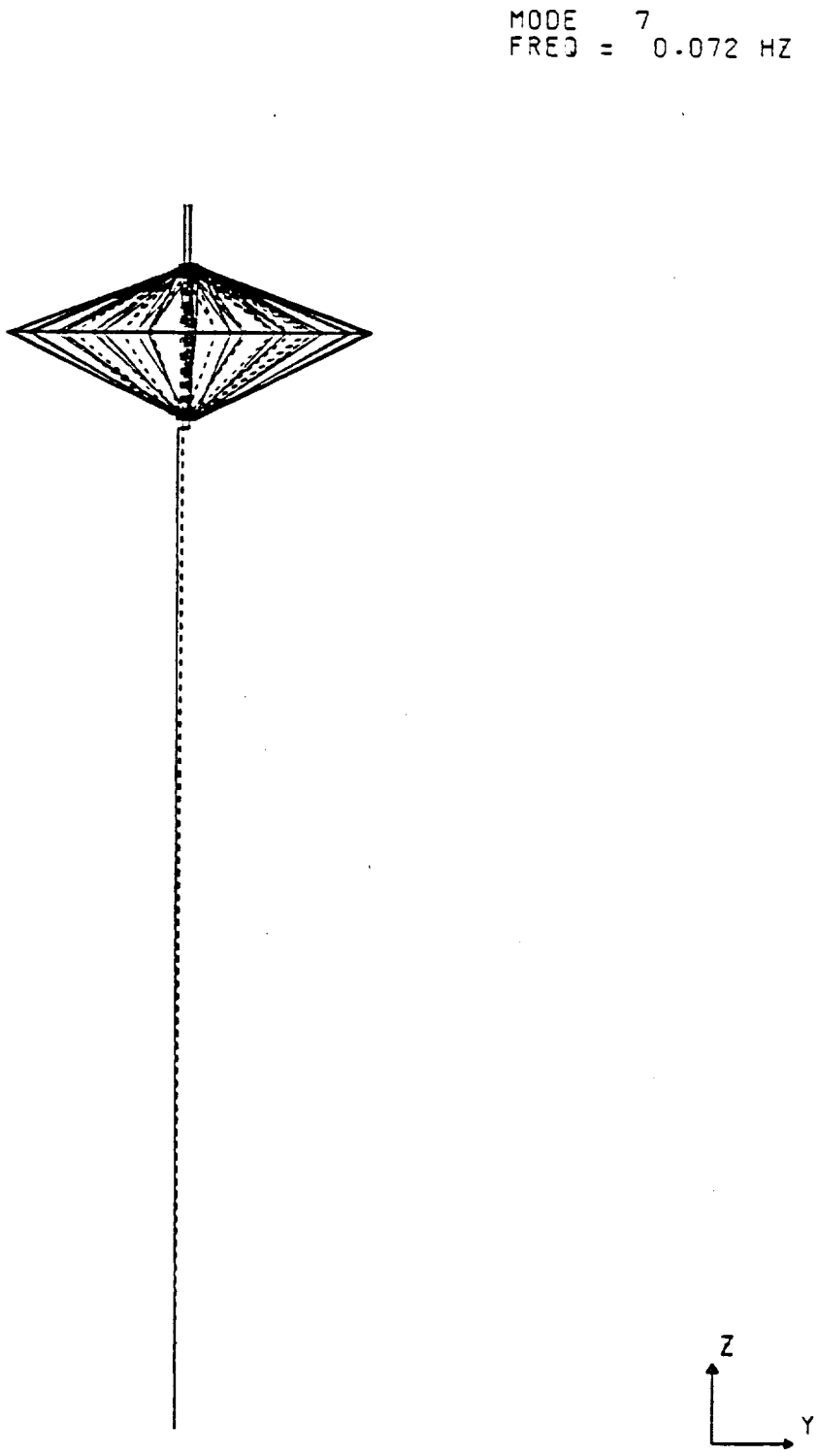

Figure 4-16. COFS-II Configuration #2: Mode 7. (Part 1 of 5)

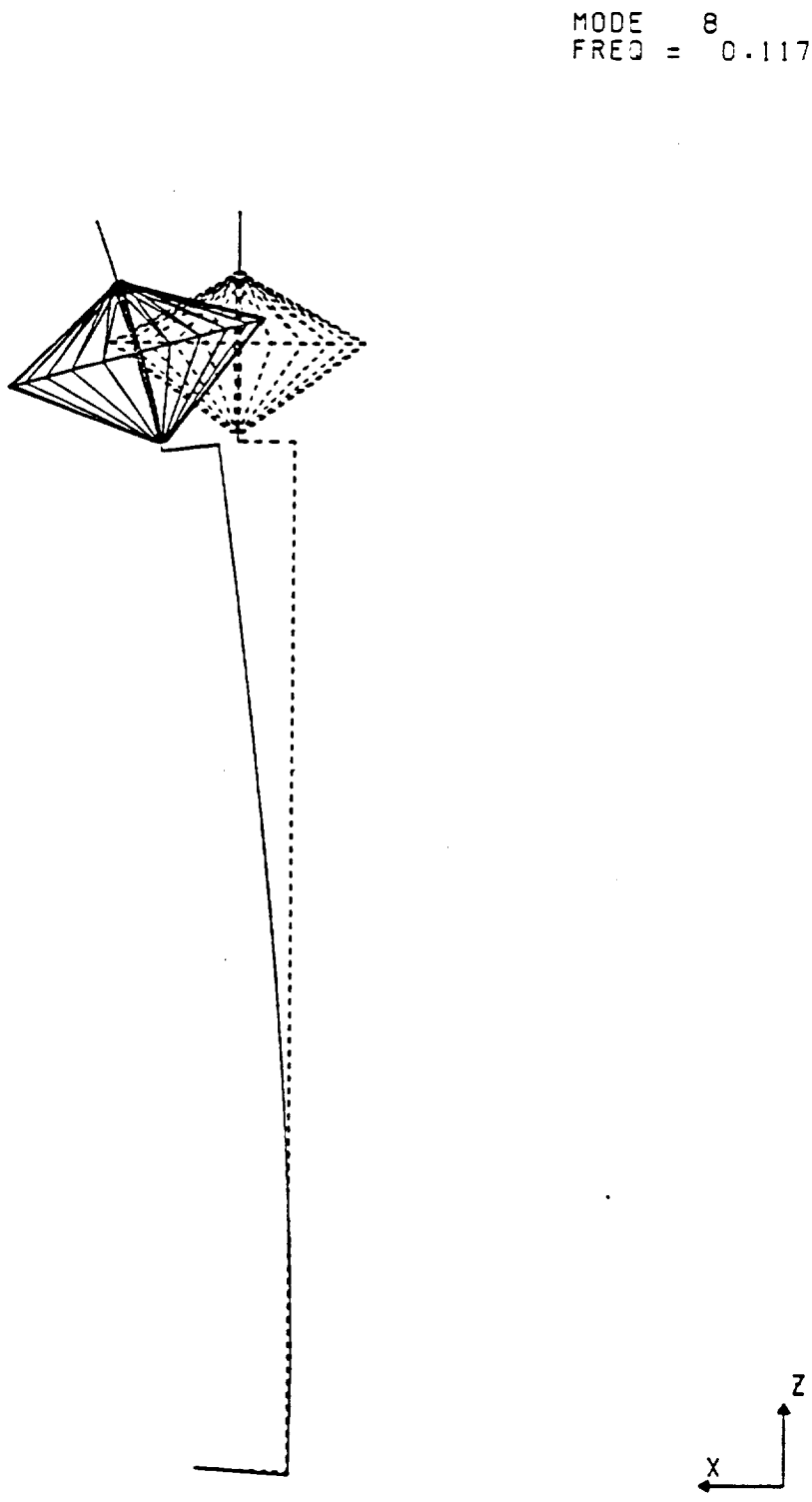

Figure 4-16. COFS-II Configuration #2: Mode 8. (Part 2 of 5)

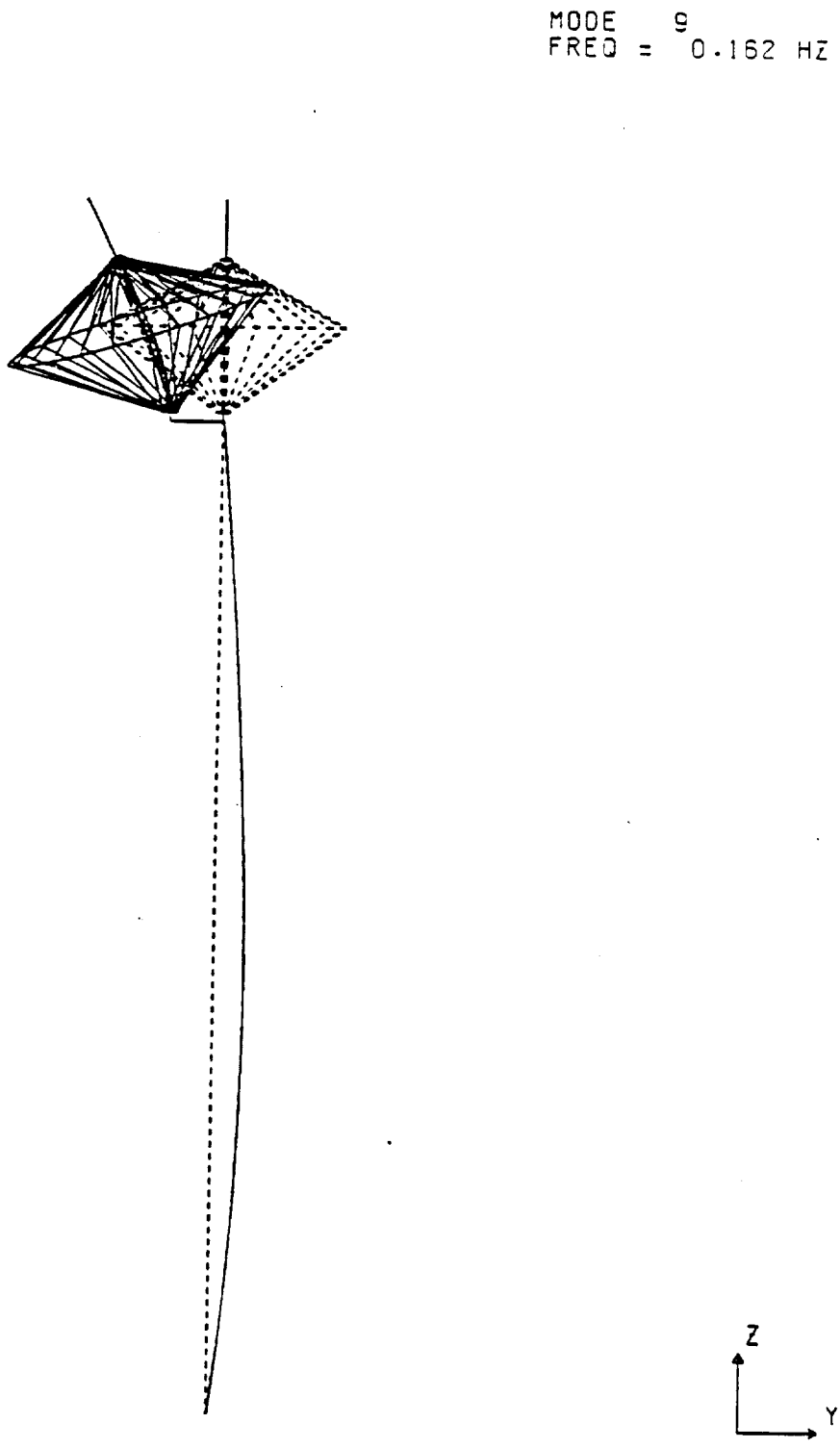

Figure 4-16. COFS-II Configuration #2: Mode 9. (Part 3 of 5)

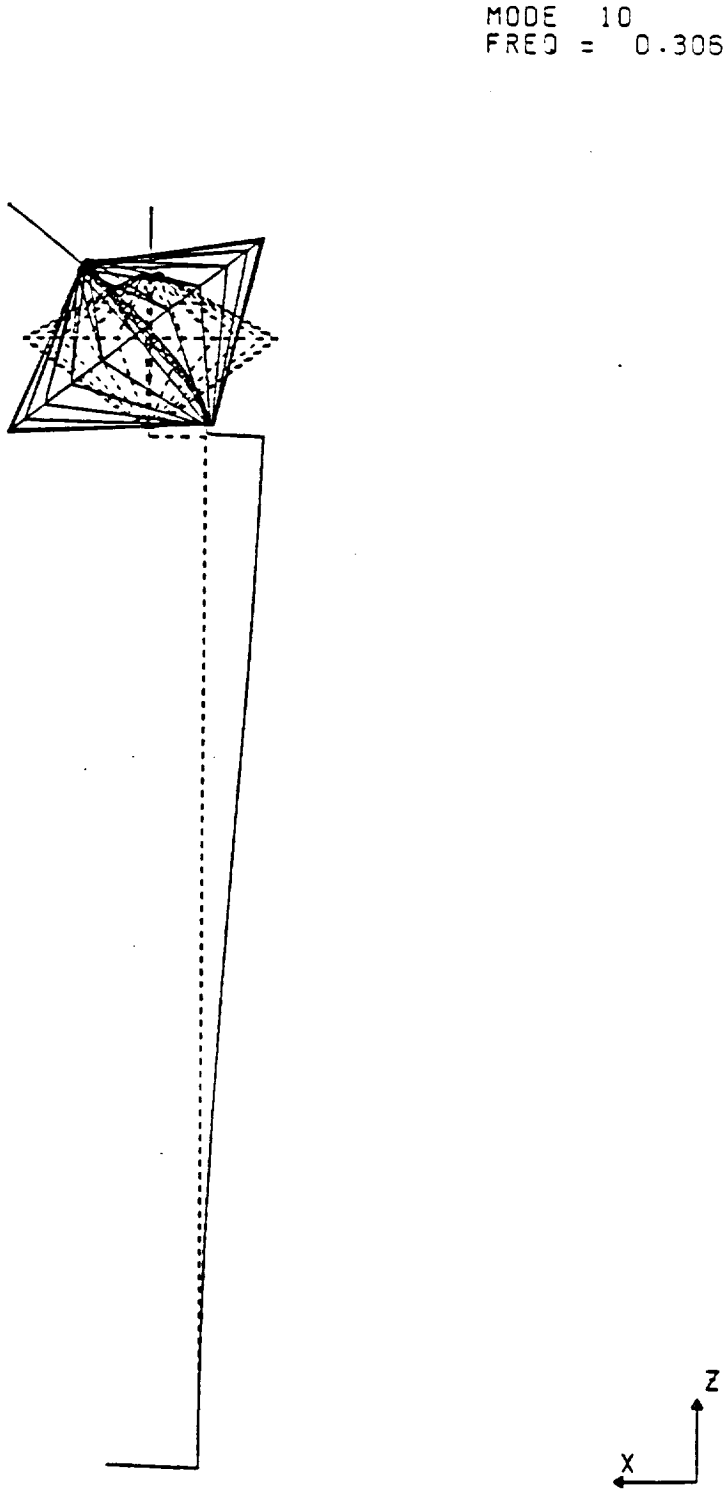

Figure 4-16. COFS-II Configuration #2: Mode 10. (Part 4 of 5)

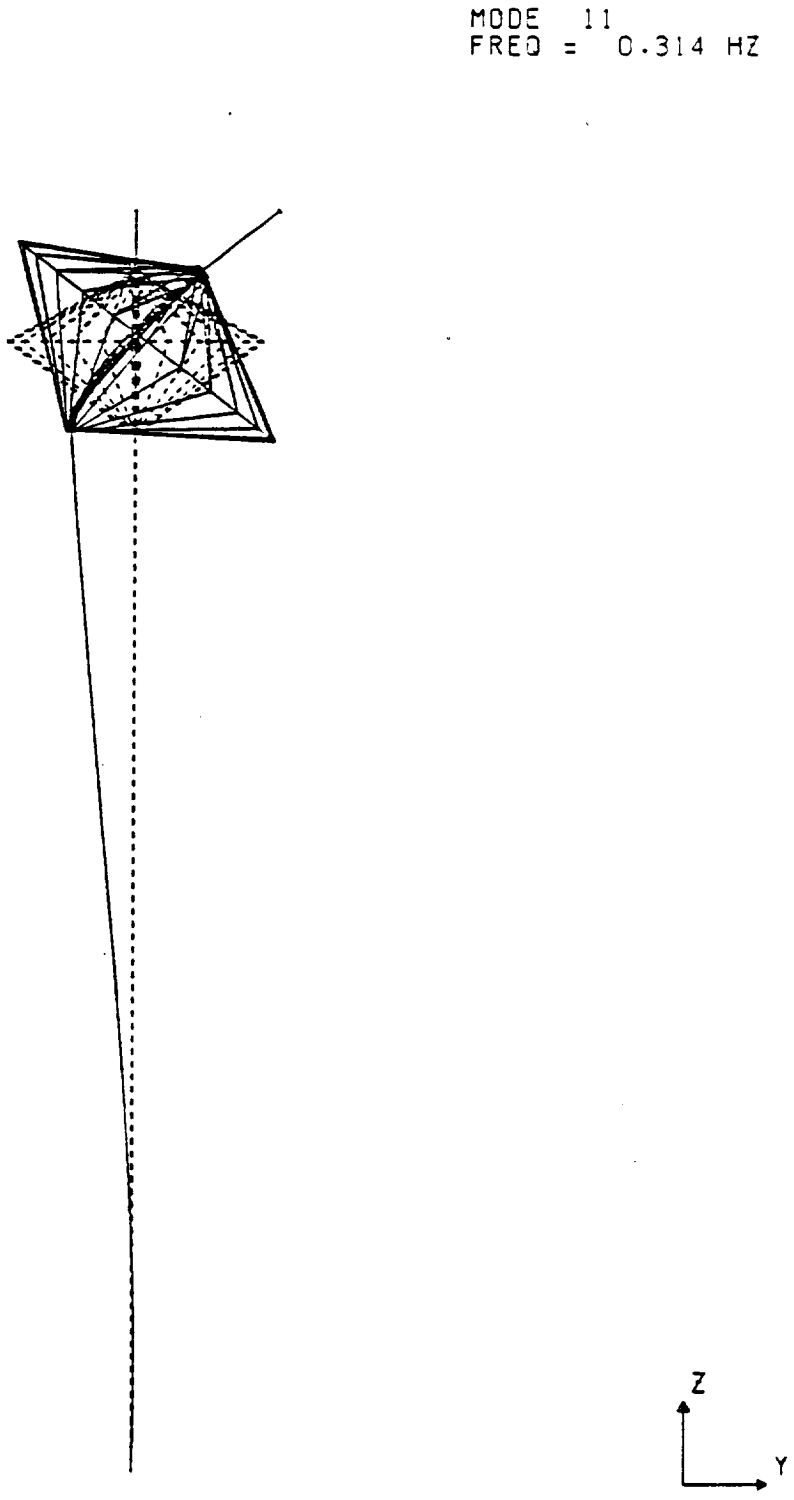

Figure 4-16. COFS-II Configuration #2. Mode 11. (Part 5 of 5)

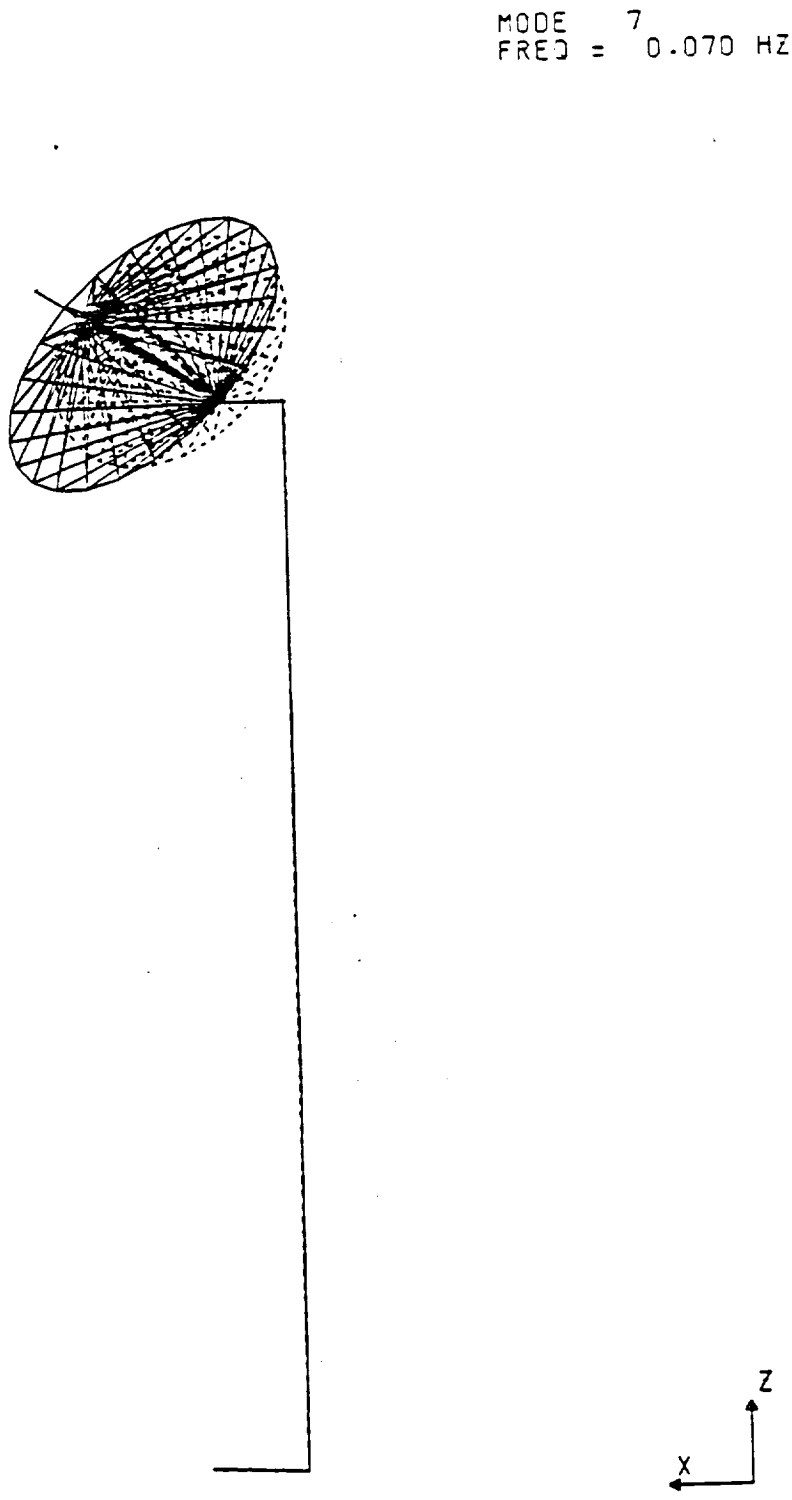

Figure 4-17. COFS-II Configuration #3: Mode 7. (Part 1 of 5)

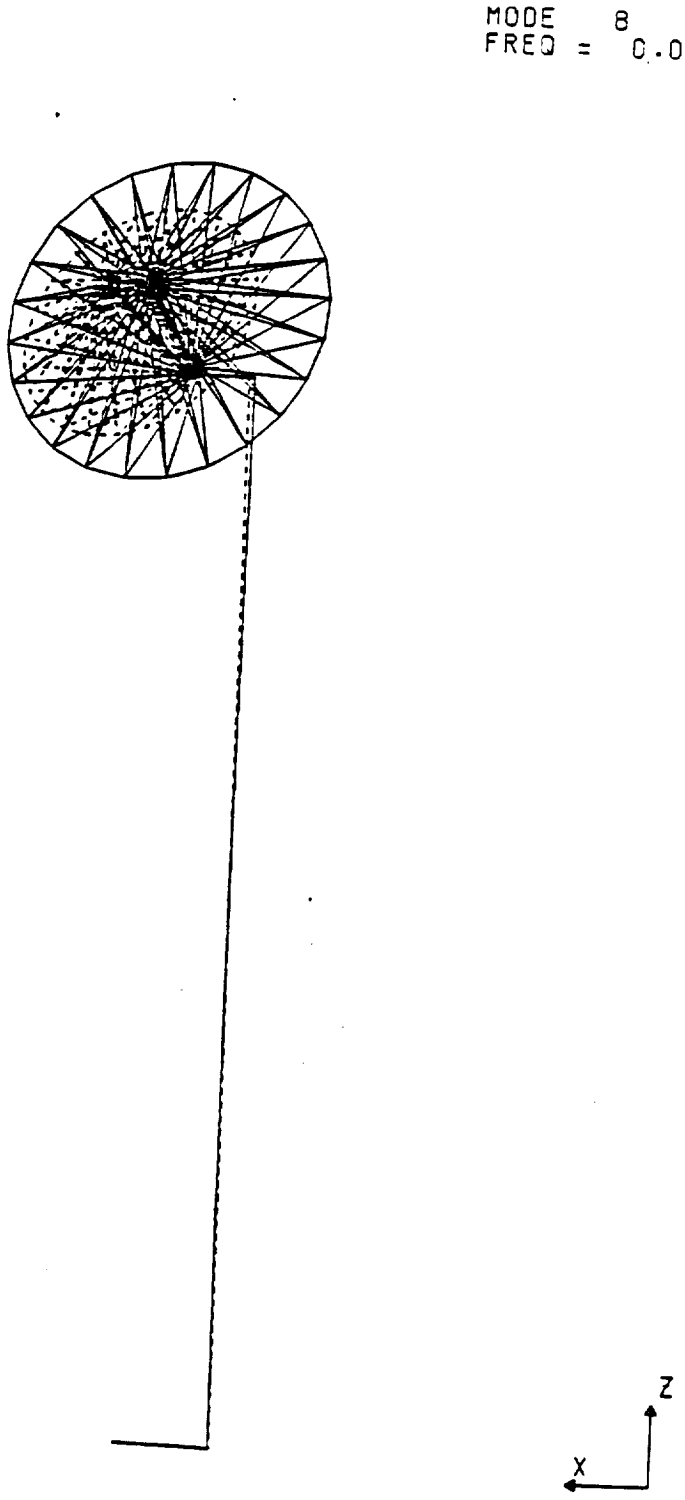

Figure 4-17. COFS-II Configuration #3: Mode 8. (Part 2 of 5)

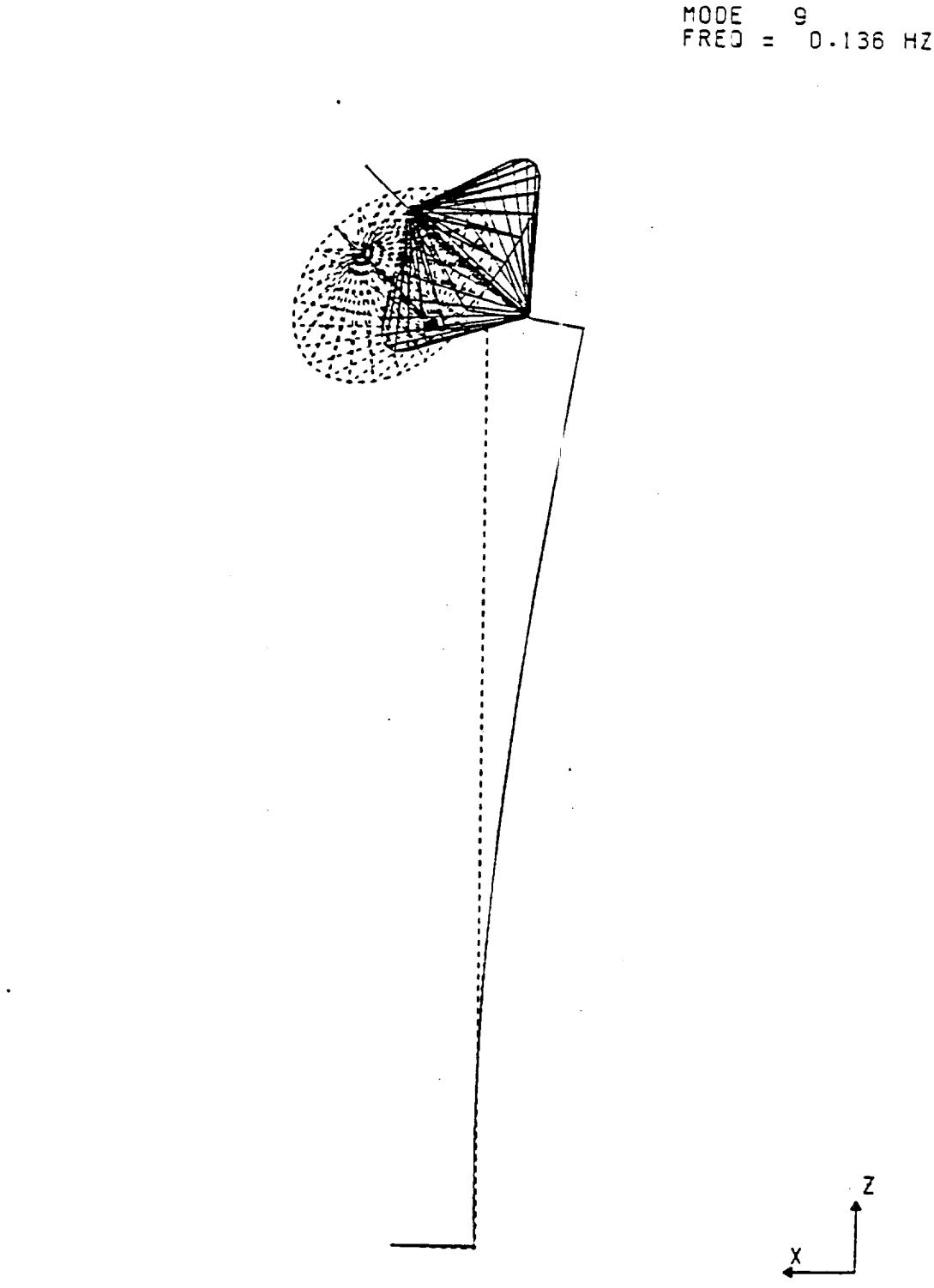

Figure 4-17. COFS-II Configuration #3: Mode 9. (Part 3 of 5)

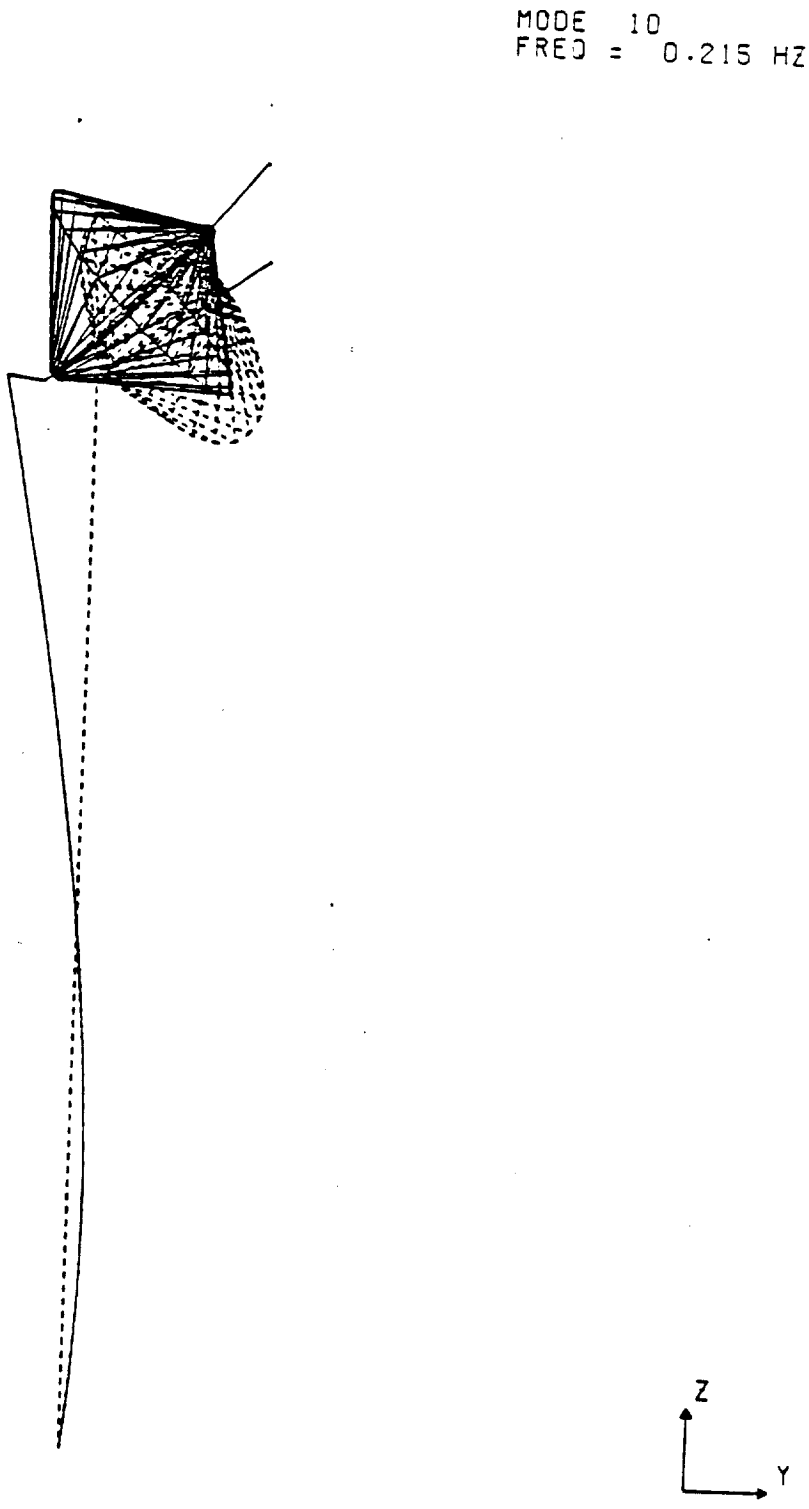

Figure 4-17. COFS-II Configuration #3: Mode 10. (Part 4 of 5)

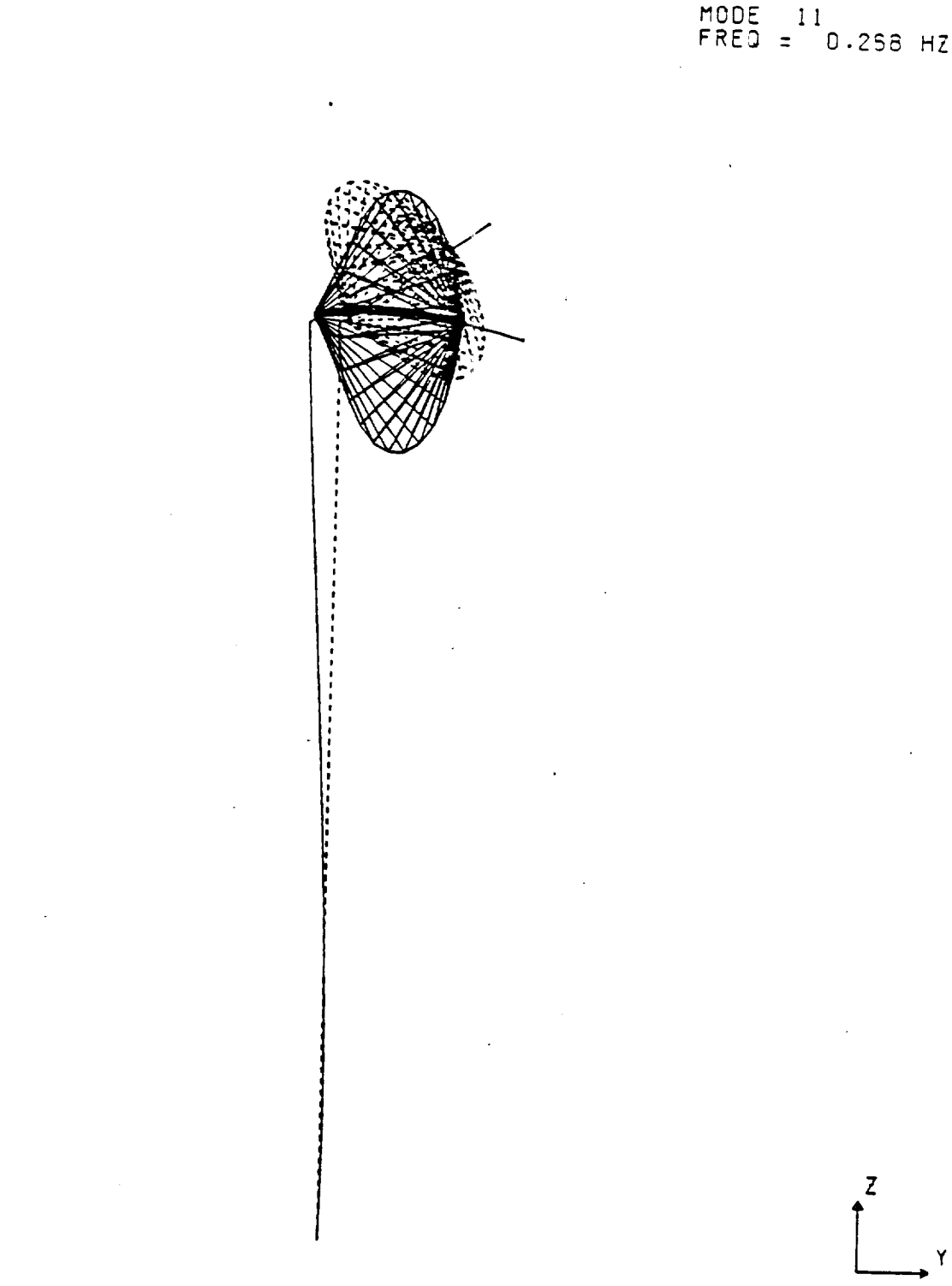

Figure 4-17. COFS-II Configuration #3: Mode 11. (Part 5 of 5)

REFERENCES

4-1 Pyle, J.S., Montgomery, R., "COFS-II 3-D Dynamics and Controls Technology", NASA CP-2447, pp. 327-345, Presented at First NASA/DOD CSI Technology Conference, Nov. 18-21, 1986, Norfolk, Virginia.

4-2 Belvin, WK., Edighoffer, H.H., "15-Meter Hoop-Column Antenna Dynamics: Test and Analysis", NASA CP-2447, pp. 167-185, Presented at First NASA/DOD CSDL Technology Conference, Nov. 18-21, 1986, Norfolk, Virginia.

4-3 Lenzi, D.C., Shipley, J.W., "Mast Flight System Beam Structure and Beam Structure Performance", NASA CO-2447, pp. 265-279, Presented at First NASA/DOD CSI Technology Conference, Nov. 18-21, 1986, Norfolk, Virginia.

SECTION 5
SIMULATOR FOR THE FIXED CONFIGURATIONS

5.1 Introduction

Part of the study of flight control system (FCS) interaction with the Orbiter/COFS-II system was carried out using the three fixed configuration finite element models described in Section 4, in conjunction with the orbital control functional simulator (OCFS), a high fidelity engineering simulation which includes attitude and structural dynamics and a model of the FCS. The OCFS accepts structural models with up to 50 flexible modes included. There is extensive, easily modified output capability. The OCFS or its precursors have been used in dynamic interaction studies for such systems as the Waves in Space Plasma experiment (WISP, Ref. 5-1, a long, Orbiter-attached dipole antenna), and the Stabilized Payload Deployment System (SPDS, Ref. 5-2). The remainder of this section describes the OCFS in more detail.

5.2 Simulation Overview

The simulation consists of essential elements of the Shuttle on-orbit FCS used for attitude control coupled to a dynamics model. An input interface enables specification of the test conditions, and outputs consist of time plots of key variables and printouts of initial and terminal conditions.

5.2.1 Flight Control System

The FCS elements simulated are described in Section 2. The IMU is modeled as an error-free attitude sensor. A higher fidelity modeling option, which was used in the maneuver and attitude hold simulations reported in Section 8, includes IMU gimbal kinematics, analog-to-digital converter quantization, and FCS software to convert the quantized gimbal angles to Orbiter body axis attitude data. The digital autopilot is constructed per the Section 2 description. The VRCS jets are modeled as constant forces and torques applied for integer multiples of the 80 ms FCS computational cycle, with added time lags representing the thrust buildup/tailoff profiles. The overall lag between reading of the IMU and application of jet forces due to the resulting commands can be adjusted to equal the actual total (hardware plus software) lag.

5.2.2 Dynamics Model

The dynamics model receives jet forces and torques from the FCS, and separately computes the rigid-body and bending responses of the Orbiter/COFS-II system. The Orbiter attitude change due to bending is added to the rigid-body attitude to obtain total Orbiter attitude, which is fed back to the IMU model in the FCS for attitude estimation and closed-loop control if desired.

The rigid-body attitude equations include effects of jet torques, nonlinear Euler rotation coupling and a user-specified constant external torque. Total system moments and products of inertia are necessary inputs to these computations.

The bending equations are driven by jet forces and torques only. Thus static centrifugal deflection, differential Euler coupling and differential gravity gradient torques are among the inertial effects that are neglected. In the rigid Orbiter/flexible appendage formulation, equivalent forces and torques at the Orbiter center of mass are first computed. The resulting 6-D vector is shaped by multiplication by a constant influence coefficient matrix to yield a vector of forcing functions, one per flexible mode. For each mode, application of the forcing function and integration of the bending equations yields a modal displacement, or generalized coordinate.

Various constant matrices multiply the vector of generalized coordinates to provide physical displacements of the Orbiter and of various nodes of the COFS-II structure, and loads at selected points. The constant matrices are the output of the finite element modeling process described in Section 4. These matrices, together with the modal frequencies and damping ratios, comprise the flexibility data input to the simulation.

5.2.3 **Inputs and Initialization**

In setting up the simulation for a particular run, the user specifies the initial body-axis angular rate of the Orbiter/COFS-II system and the external disturbance torque. The state estimator can optionally be initialized such that its outputs and internal variables "agree" with these disturbances. For special studies requiring initial modal excitation, the first derivative of selected generalized coordinates can be specified.

Other inputs specify run conditions and FCS mode and control parameters. The simulated-time duration, system configuration, node point indexes, and inclusion or exclusion of flex modeling comprise a typical run-condition specification. The FCS mode is selected from auto, manual or open-loop. FCS parameters include the maneuver rate, phase plane deadband and rate limit, expected available per-axis control acceleration, expected VRCS jet accelerations, and maneuver commands. The user may input the mass property-dependent FCS parameters (i.e., expected per-axis and jet accelerations) directly, or may request that "ideal" values be computed from total system mass properties and actual jet forces, locations and autopilot-generated jet commands. Angular rate commands (in manual mode) or a new target attitude (in auto mode) can be input at any time in the run.

5.2.4 **Output plotting and Printing**

The plotted outputs indicate behavior of the Orbiter/COFS-II system and of the FCS. System performance indicators in the plotted data are the angular acceleration, rate and attitude of both the Orbiter and the composite system, and deflections and loads at selected points of the COFS-II structure. It should be noted that the deflections given in Section 8 are always with respect to the composite body, not the Orbiter.

Indications of FCS behavior are provided by plots of attitude error, rate error, estimated disturbance acceleration, phase plane output commands, individual VRCS jet activity, and cumulative fuel consumption. The first six generalized coordinates are also plotted to provide insight into which modes are contributing significantly to loads and deflections.

The printed output consists of input echoes (for verification of successful read-in of desired conditions and flex data), derived initial conditions, and terminal conditions. The derived initial conditions are mass property-dependent FCS parameters and disturbance dependent state estimator outputs. Useful terminal condition data are inertial attitude (all simulation runs start with the composite body axes aligned with the inertial reference axes) and VRCS usage statistics (per-jet and total firings and fuel consumption).

REFERENCES

5-1 Kirchwey, C., Sackett, L., and Satter, C., "Wisp Antenna Dynamics and Orbiter Control System Interaction", Charles Stark Draper Report CSDL-R-1763, March, 1985.

5-2 Sackett, L., and Kirchwey, K., "SPDS Dynamic Interaction Study", Charles Stark Draper Laboratory Memorandum DI 87-5, April 9, 1987.

SECTION 6
VARIABLE CONFIGURATION MODEL

This section describes the dynamics model employed to simulate the motion of the COFS-II system during large angle maneuvers of the antenna relative to the Shuttle Orbiter. This model when combined with the algorithmic descriptions of the gimbal servo-motors and the Shuttle attitude control system formed the integrated simulation used for studies involving Shuttle-antenna reconfiguration.

To simulate the COFS-II system undergoing these maneuvers, an articulated multibody dynamics model was used. The system was modelled as an assembly of rigid and flexible bodies with carefully defined interconnections. The general purpose multibody dynamics and control simulation program, DISCOS[6-1] was used to numerically synthesize and integrate the equations of motion and provide the interbody forces and torques.

A detailed description of the idealized mechanical model and the values of the parameters implemented in DISCOS follow. Further information on the integrated simulation is provided in Section 7. Results from simulation case studies are presented in Sections 9 and 10.

6.1 General System Description

Figure 6-1 illustrates a planar view of the COFS-II system in the reference configuration. Cantilevered to the Orbiter cargo bay is a large deployable truss structure, considered to be identical to the COFS-I mast described in Reference 6-2. An offset structure, having the same truss design as the mast, is fixed to the mast tip. A two-axis gimbal system controls antenna pointing in elevation and lateral degrees of freedom. Mounted to the offset structure, this system is based on the Sperry Advanced Gimbal System, described in Reference 6-3. The NASA Langley/Harris 15m Hoop Column antenna is attached to the gimbal system payload platform. This large lightweight axisymmetric structure is described in References 6-4 and 6-5. A finite element model of the antenna was provided to CSDL by NASA/LaRC.

6.2 Mechanical Idealization

6.2.1 Antenna

Figure 6-2 shows a cross-sectional view of the Hoop Column antenna, indicating various elements of the structure. The column is considered to be cantilevered to the base which represents its mounting to the gimbal system payload platform.

According to Reference 6-4, 97% of the antenna mass is contained in its three major components: the hoop (33%), the column (34%), and the feed mast and horn (30%). These components are each complex structures with intricate interconnections. After examination of the free vibration characteristics of the antenna obtained from the LaRC finite element model, the first five mode shapes of which are shown in Figure 6-3, we chose to idealize the antenna as the simple rigid body assembly shown in Figure 6-4. The three primary components are portrayed as separate rigid bodies interconnected by discrete massless torsional springs and

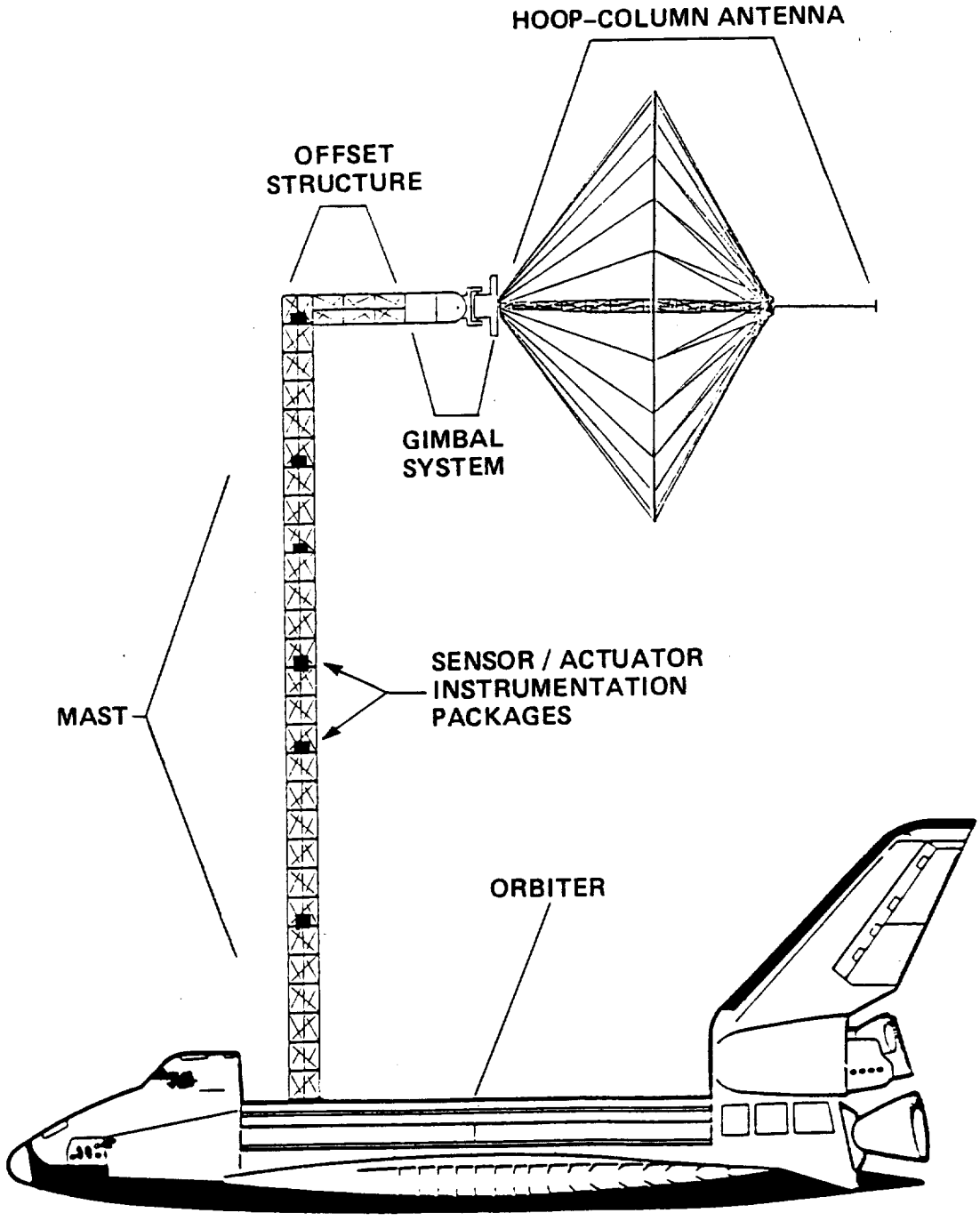

Figure 6-1. Flight configuration of shuttle/COFS II system planar view.

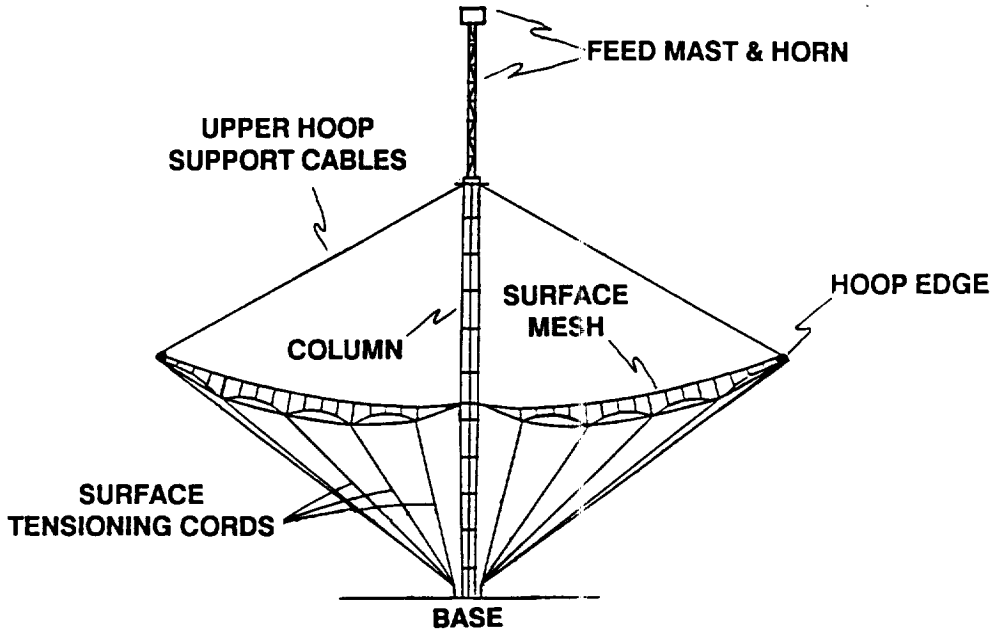

Figure 6-2. Diametrical cross section view of hoop — column antenna.

dashpots. While this representation ignores the inertial effects of the surface mesh, tensioning cords, and the hoop support cables, it does capture their essential stiffening influence. The dashpots, arranged in parallel with the torsional springs, model the intrinsic damping of the structure.

For the idealized antenna of Figure 6-4, the column is connected to the base through a hinge which permits rotation about two mutually orthogonal axes oriented perpendicular to the column's nominal longitudinal axis. These two rotational degrees of freedom are resisted by identical pairs of springs and dashpots. The hoop is constrained to lie in a plane perpendicular to the column's longitudinal axis at a fixed distance above the base. During deformation the hoop follows the column such that the only relative displacement between them is a simple rotation of the hoop in its plane about the column axis. This relative angular motion is resisted by spring and dashpot pair. The feed mast and horn combination is connected to the column top through a hinge. The hinge permits rotation of the feed body relative to the column about two mutually orthogonal axes perpendicular to the column's longitudinal axis. These two degrees of freedom are resisted by identical pairs of springs and dashpots.

The idealized antenna model has five degrees of freedom. These degrees of freedom are discrete representations of selected structural deflections, and as such are meaningful only when they are small in an engineering sense.

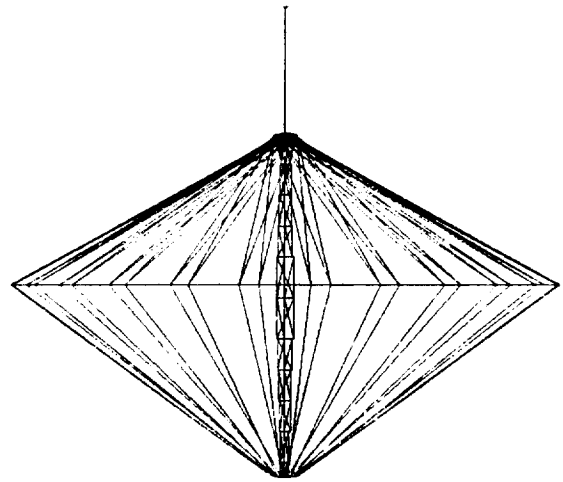

MODE 1
HOOP TORSION
ω_1 = 0.08 Hz

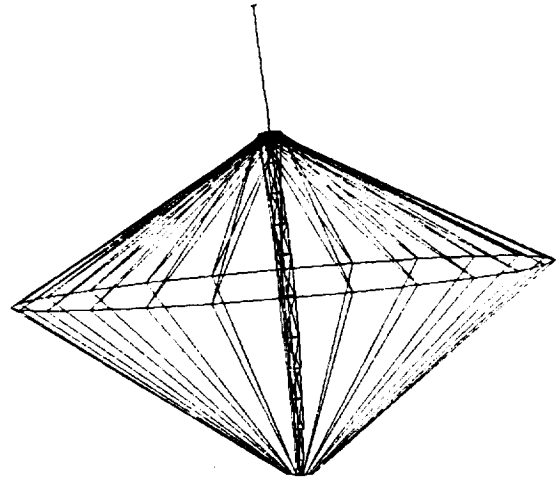

MODES 2 & 3
1st PLANAR BENDING
$\omega_2 = \omega_3$ = 0.24 Hz

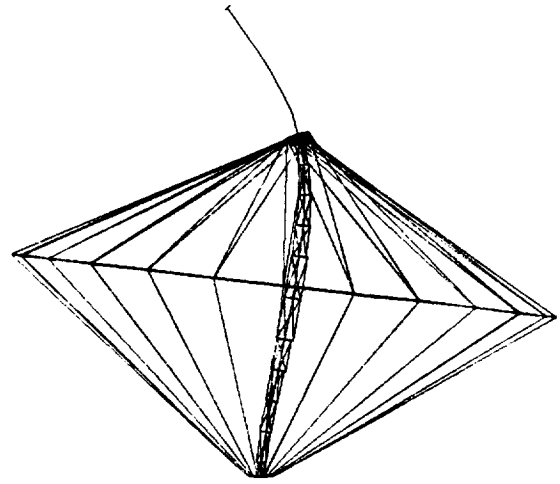

MODES 4 & 5
2nd PLANAR BENDING
$\omega_4 = \omega_5$ = 1.74 Hz

Figure 6-3. Finite element model cantilevered mode shapes.

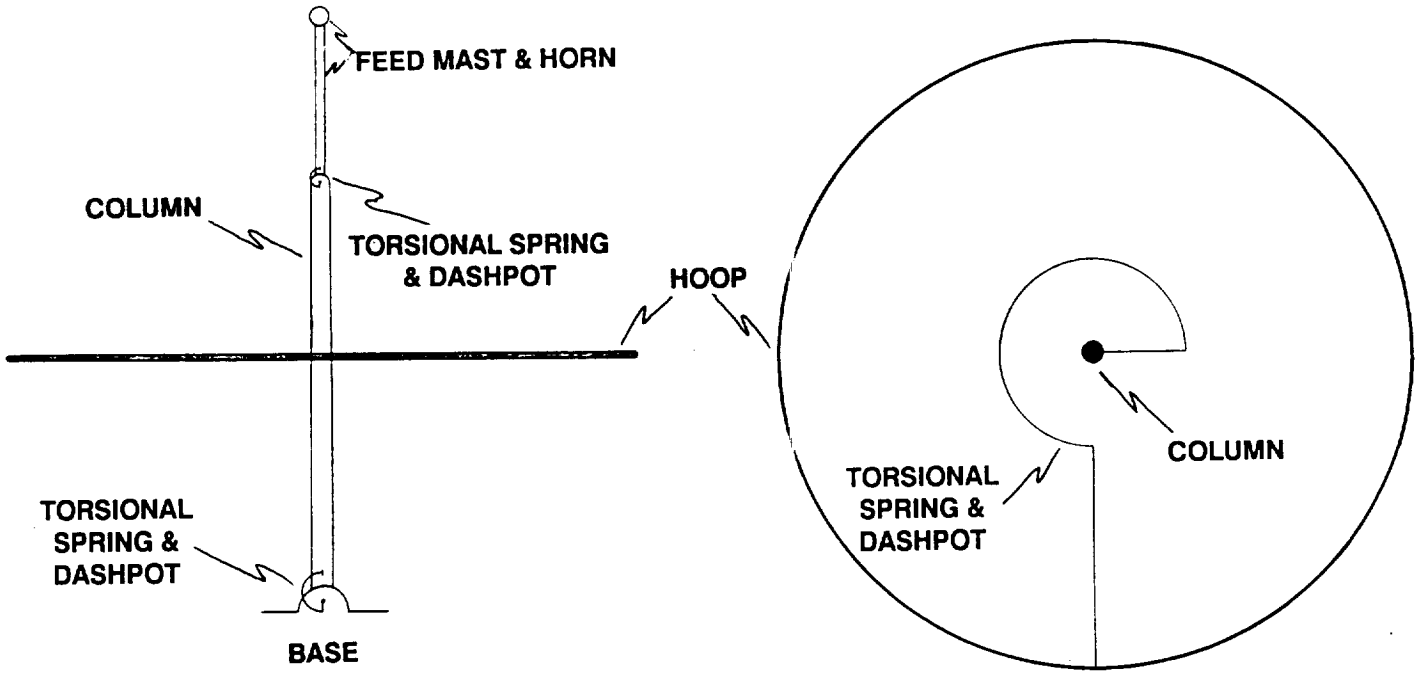

Figure 6-4. Three rigid-body antenna idealization, side and top views.

The method used to select numerical values for the antenna s spring constants is presented in Appendix A. Those values appear together with all other parameter values later in this section.

The undamped mode shapes and natural frequencies for the three-rigid-body model of the antenna are portrayed in Figure 6-5. Those characteristics show good agreement with the corresponding modes and frequencies of the LaRC finite element model (shown in Figure 6-3).

For each of the parallel spring-dashpot pairs, the dashpot coefficients were chosen to be directly proportional to the corresponding spring constants. This simple approach permitted the introduction of damping into each of the vibration modes. For the dashpot coefficients selected, (see Table 6-3) the modal damping was: $\zeta_1 = \zeta_2 = \zeta_3 = 0.005$, $\zeta_4 = \zeta_5 = 0.036$ (where the i^{th} modal coordinate, η_i, for damped free vibration satisfies: $\ddot{\eta}_i + 2\zeta_i \omega_i \dot{\eta}_i + \omega_i^2 \eta_i = 0$, with ω_i being the modal frequency).

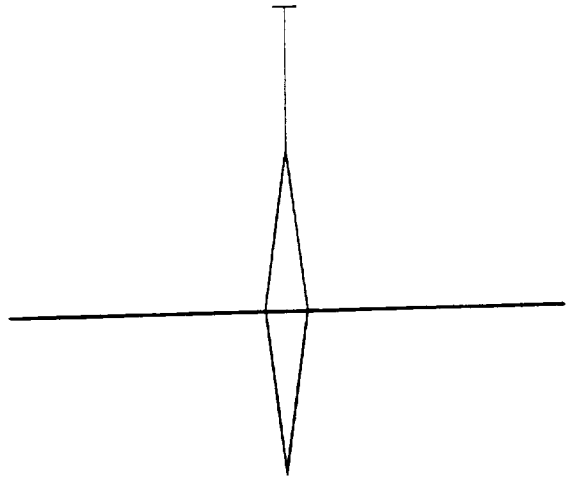

HOOP TORSION

ω_1 = 0.08 Hz

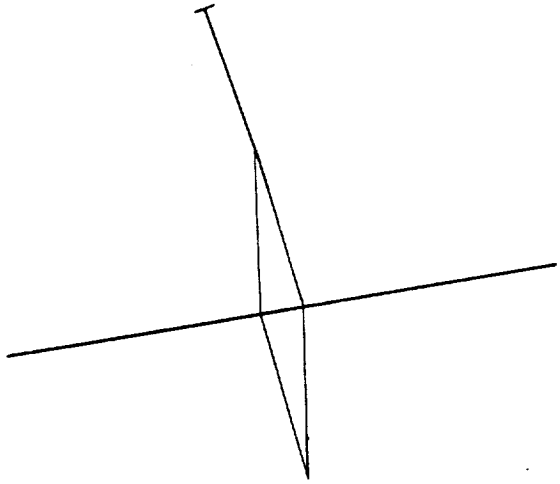

1st PLANAR BENDING

$\omega_2 = \omega_3$ = 0.24 Hz

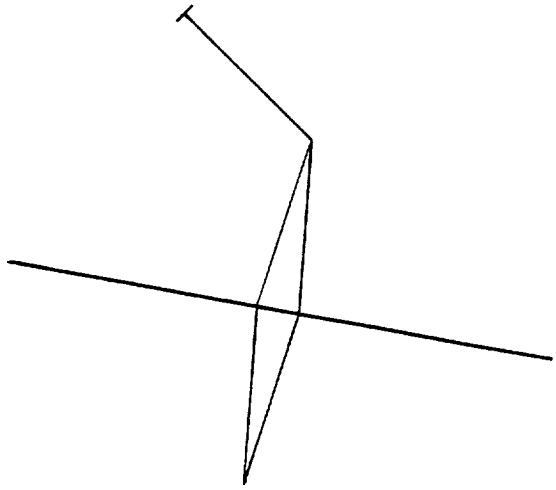

2nd PLANAR BENDING

$\omega_4 = \omega_5$ = 1.74 Hz

Figure 6-5. Three rigid-body antenna model cantilevered mode shapes.

6.2.2 Gimbal System and Offset Structure

The gimbal system is considered to consist of three primary sections: the base, joint assembly, and payload platform (Figure 6-6). The payload platform is represented as a distinct rigid body. The two axis gimbal assembly is idealized as a two degree of freedom pivot point joining the payload platform to the gimbal base. The respective gimbals are capable of large angular displacements in response to motor torques, or, their motions can be specified by rheonomic constraints. The gimbal base and offset structure are considered to be a single composite rigid body, rigidly attached to the mast tip.

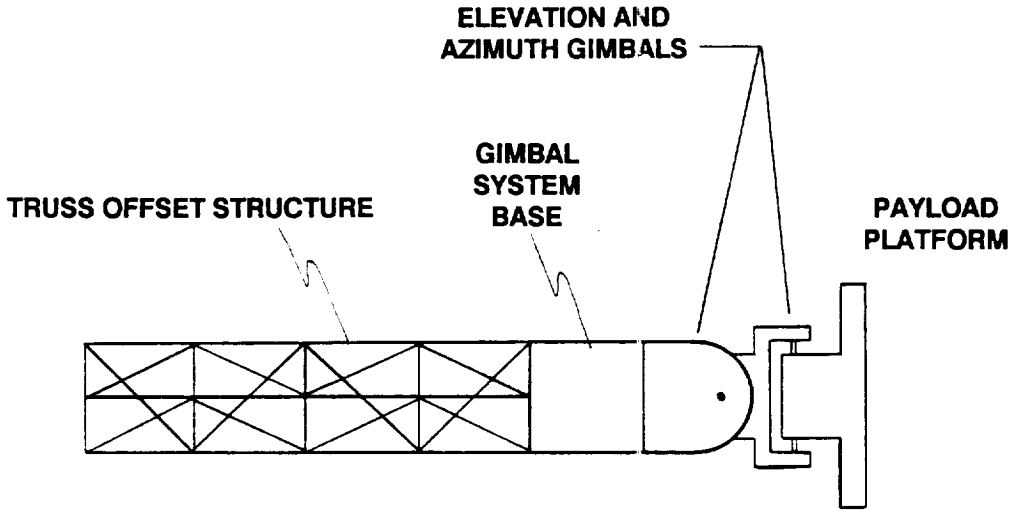

Figure 6-6. Offset structure and gimbal system.

6.2.3 Mast

The mast structure with the sensor and actuator instrumentation packages is idealized as a uniform cantilevered beam carrying a set of compact rigid bodies fixed along its length. The beam is considered to be inextensible and is permitted small transverse bending deflections in two orthogonal planes as well as torsional deflections about its longitudinal axis. Appendix B presents a free vibration analysis of this structure.

In the DISCOS program the beam with point bodies was modelled as a single flexible body described by its first five mode shapes and natural frequencies.[1] These mode shapes, which were generated from a lumped mass finite element model, included the first and second bending modes for each of the two orthogonal planes and one torsion mode.

---

1 While it is recognized that there are inaccuracies associated with such portrayals under certain circumstances [6-6], the conditions for the studies reported here reduce their impact.

To portray both the intrinsic damping of the structure, as well as the enhanced damping provided by the action of the mast damping control system, simple modal damping was employed. The natural damping was assumed to provide a uniform modal damping factor for each mode of $\zeta = 0.005$. The modal damping factor was assumed to increase for each mode to $\zeta = 0.05$ when the vibration control system was active.

6.2.4 Orbiter

The Shuttle Orbiter is treated as a rigid body and is provided six unrestricted degrees of freedom. External forces and torques act on the Orbiter as a result of the action of the vehicle's attitude control thrusters. A more detailed description of the flight control system appears in Sections 2 and 7.

6.3 DISCOS Model

An exploded-view of the idealized COFS-II system appears in Figure 6-7, with the DISCOS model hinges and references frames identified.

Many other possible choices exist for idealizing the system, each of which entails trade-offs between different aspects of the simulation. As an example, the Orbiter, mast, and offset structure-gimbal base could have been treated as a single composite flexible body. While this model would produce a faster simulation, the DISCOS program would no longer compute the forces and torques acting between the Orbiter and mast and between the mast and offset, which were desired quantities. Alternate idealizations such as this, do however, provide a means for corroborating implementations of complicated models.

The DISCOS model was subjected to a hierarchy of validation tests, beginning with simple situations for which the correct response was known a priori, and progressing through comparisons between distinct simulations for increasingly complicated conditions. The simulation comparisons were made between the seven-body DISCOS model and:

1) Finite element based models, for fixed configuration cases. These models and associated simulations are described elsewhere in this report. Good agreement was obtained for attitude motions and structural loads and deflections.

2) A two-body DISCOS model, for variable configuration cases. This model treated the Orbiter + mast + offset structure as one flexible body and the payload platform + antenna as another. Excellent agreement was obtained for attitude motions and antenna pointing motions.

This chapter concludes with the specification of the geometric, mass, and stiffness parameters implemented in the DISCOS model. The data is given in Figures 6-8 through 6-15, and Tables 6-1 through 6-3. The information was derived primarily from References 6-2 through 6-5, and the antenna finite element model provided by NASA LaRC. Note that in the following, the respective body fixed frames are parallel, in the reference configuration, to the Orbiter fabrication frame.

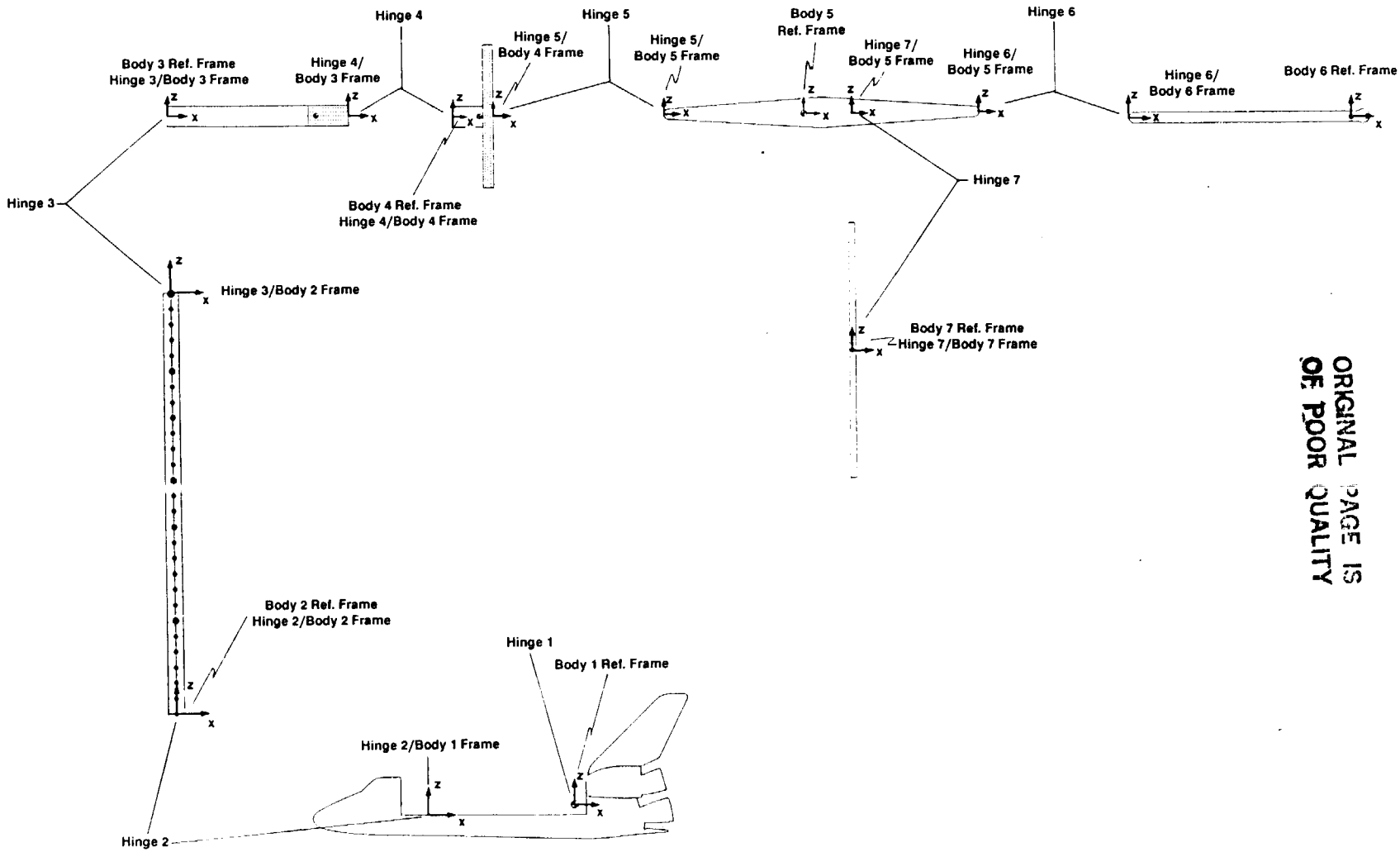

Figure 6-7. System topology and DISCOS model reference frames for nominal configuration.

ORBITER

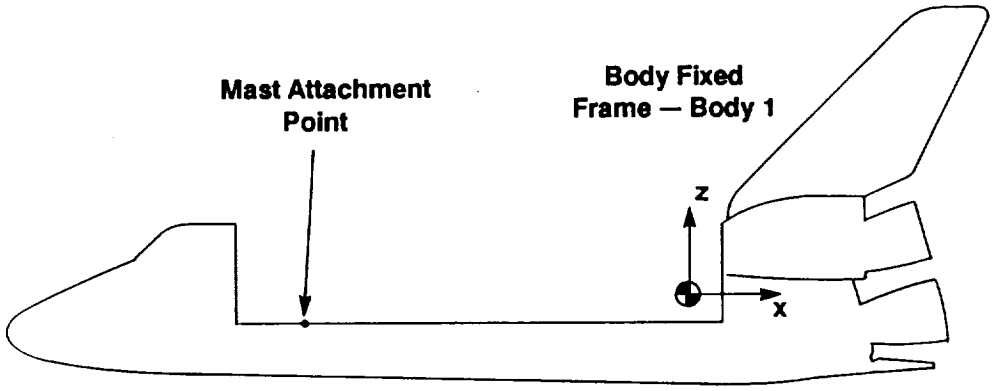

Mass = 84831.4 kg

Inertia matrix with respect to the orbiter mass center and the body fixed frame axes:

$$[I_1] = \begin{bmatrix} 1253282.0 & -12307.0 & -326951.0 \\ & 8913427.0 & -3991.0 \\ \text{sym} & & 9432545.0 \end{bmatrix} \text{kg} - \text{m}^2$$

Position of mast attachment point relative to the orbiter body fixed reference frame:

(—5.386, 0.0, -0.205) m

Figure 6-8. Orbiter geometric and mass properties.

MAST

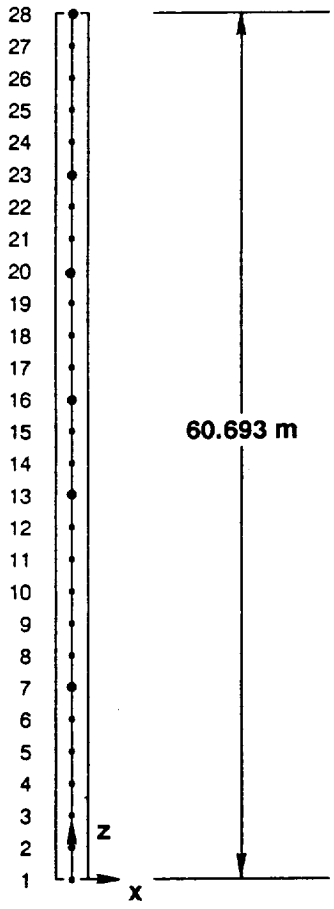

BODY FIXED
FRAME — BODY 2

28 node, lumped mass, finite element model.

27 beam elements of equal length.

Cantilevered @ node 1, free @ node 28.

Transverse bending deflections permitted in x—z, and y—z planes.

Torsional deflection about z—axis permitted.

Rotary inertia in bending neglected.

Uniform geometric and material properties:

Bending stiffness y—z plane
$EI_x = 28.63 \bullet 10^6\ N - m^2$

Bending stiffness x—z plane
$EI_y = 32.39 \bullet 10^6\ N - m^2$

Torsional stiffness
$GK = 0.5 \bullet 10^6\ N - m^2$

Mass/length = 4.641 kg/m

Moment of inertia about z-axis/length
$= 1.9\ kg - m^2/m$

Instrumentation packages located at nodes:
#7, 13, 16, 20, 23, and 28

Figure 6-9. Mast geometric, mass, and material properties.

NODAL MASSES AND TORSIONAL MOMENTS OF INERTIA

Node Number	Mass (kg)	Moment of Inertia about z—axis ($kg—m^2$)
1	5.2162	2.1355
2—6, 8—12, 14, 15 17—19, 21, 22, 24—27	10.4325	4.2710
7, 16, 23	60.5325	7.071
13, 20	24.8325	5.271
28	152.3162	23.7355

Table 6-1.

VIBRATION CHARACTERISTICS OF CANTILEVERED MAST

Mode	Description	Natural Frequency (Hz)
1	1^{st} bending mode y—z plane	0.194
2	1^{st} bending mode x—z plane	0.206
3	2^{nd} bending mode y—z plane	1.359
4	2^{nd} bending mode x—z plane	1.436
5	1^{st} torsion mode about z	1.727

Table 6-2.

OFFSET STRUCTURE & GIMBAL BASE

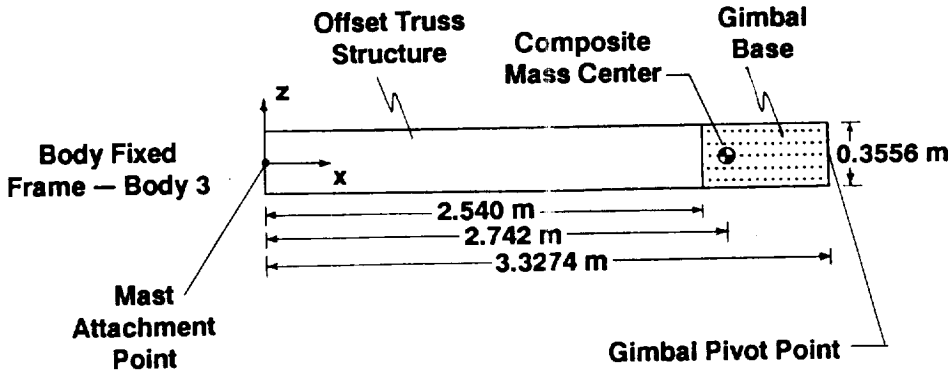

Total mass = 102.409 kg

Inertia matrix with respect to the body fixed frame origin and axes:

$$[I_3] = \begin{bmatrix} 6.262 & 0.0 & 0.0 \\ & 810.683 & 0.0 \\ \text{sym} & & 810.683 \end{bmatrix} \text{kg} - \text{m}^2$$

Figure 6-10. Offset structure and gimbal base composite body geometric and mass properties.

GIMBAL PAYLOAD PLATFORM

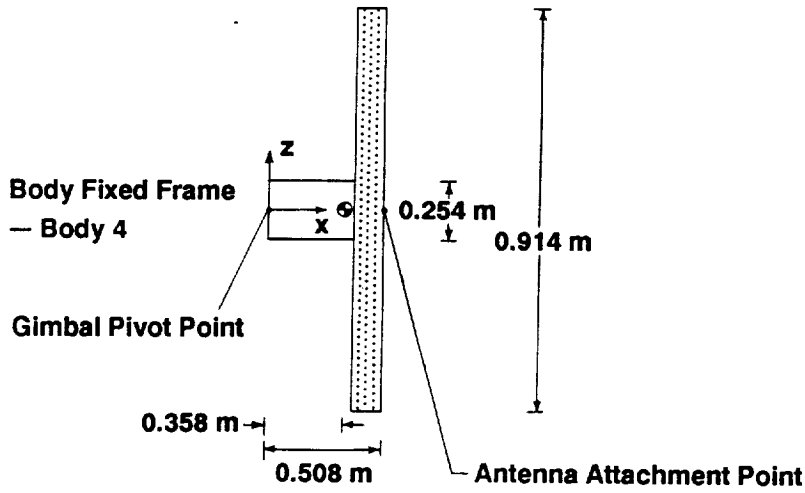

Total mass = 172.176 kg

Inertia matrix with respect to body fixed frame origin and axes:

$$[I_4] = \begin{bmatrix} 12.315 & 0.0 & 0.0 \\ & 31.54 & 0.0 \\ \text{sym} & & 31.54 \end{bmatrix} \text{kg} - \text{m}^2$$

Figure 6-11. Gimbal payload platform geometric and mass properties.

ANTENNA COLUMN

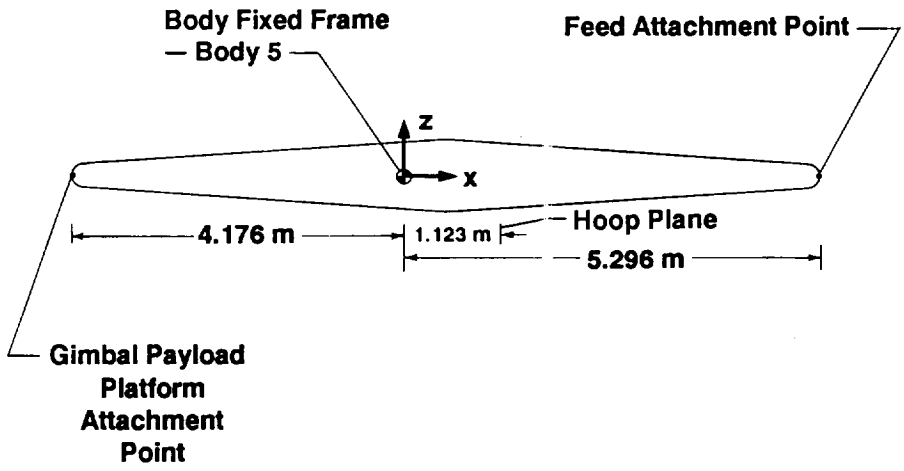

Mass = 126.951 kg

Inertia matrix with respect to the mass center and the body fixed frame axes:

$$[I_5] = \begin{bmatrix} 11.264 & 0.0 & 0.0 \\ & 1743.736 & 0.0 \\ \text{sym} & & 1743.736 \end{bmatrix} \text{kg} - \text{m}^2$$

Figure 6-12. Antenna column geometric and mass properties.

FEED MAST & HORN

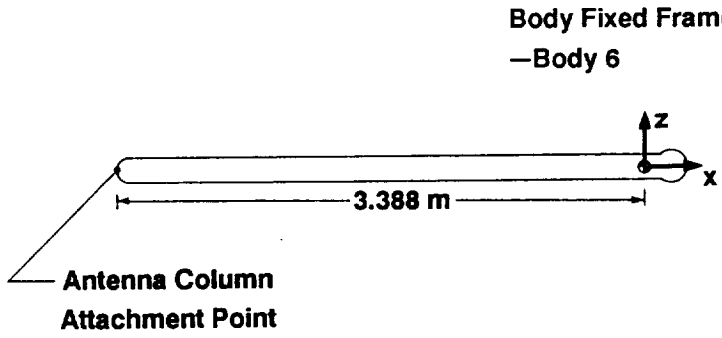

Mass = 117.234 kg

Inertia matrix with respect to mass center and body fixed frame axes:

$$[I_6] = \begin{bmatrix} 0.853 & 0.0 & 0.0 \\ & 34.861 & 0.0 \\ \text{sym} & & 34.861 \end{bmatrix} \text{kg} - \text{m}^2$$

Figure 6-13. Feed mast and horn geometric and mass properties.

ANTENNA HOOP

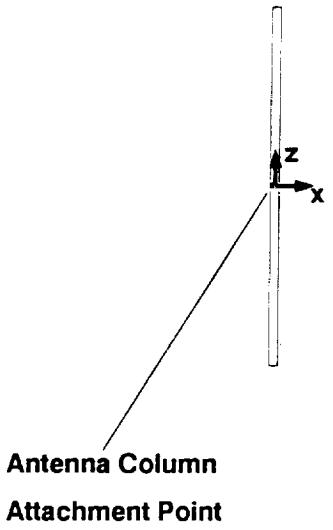

Mass = 118.337 kg

Inertia matrix with respect to mass center and body fixed frame axes:

$$[I_7] = \begin{bmatrix} 6631.537 & 0.0 & 0.0 \\ & 3315.772 & 0.0 \\ \text{sym} & & 3315.772 \end{bmatrix} \text{kg} - \text{m}^2$$

Figure 6-14 Antenna hoop and mass properties.

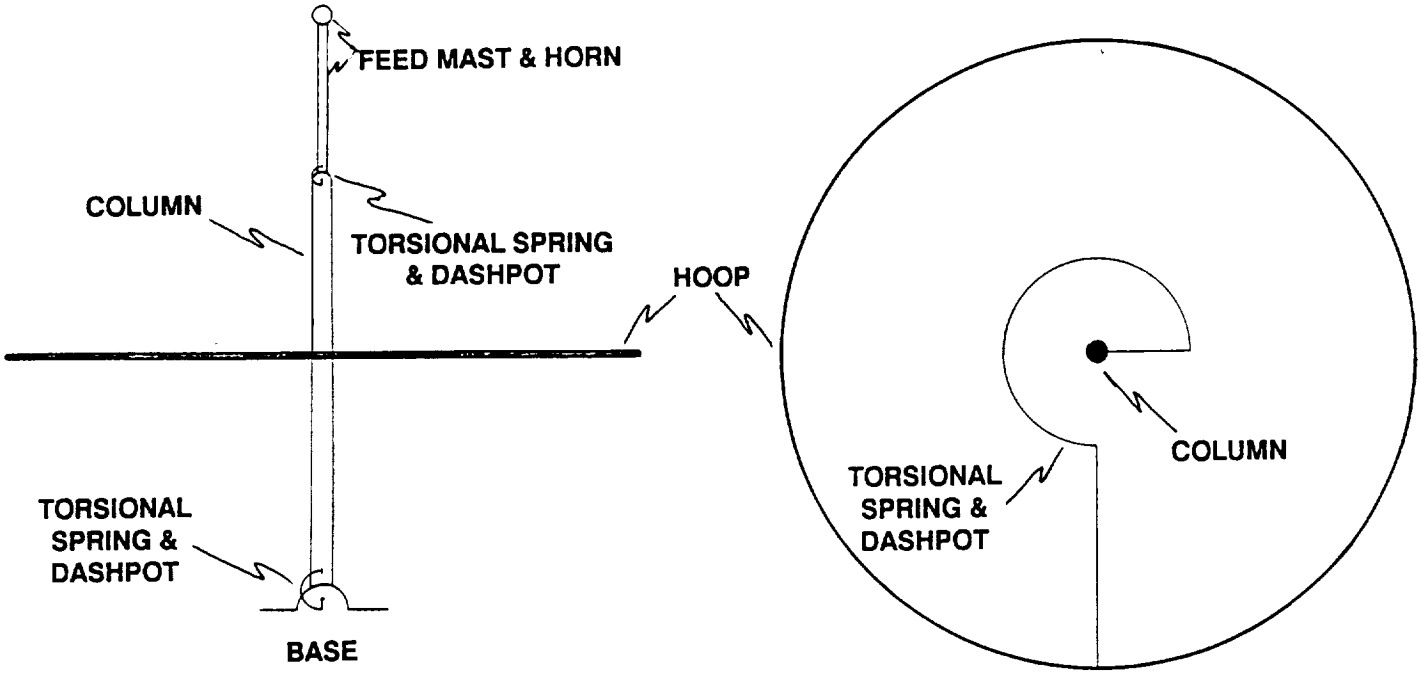

Figure 6-15 Antenna Spring and Dashpot Coefficients.

Table 6-3. Antenna spring and dashpot coefficients.

Spring-Dashpot Connection	Spring Stiffness (N-m/rad)	Dashpot Coefficient (N-m-s/rad)
Column-Base	71422.17	471.518
Feed-Column	57829.16	381.738
Hoop-Column	1698.141	33.556

REFERENCES

6-1 Bodley, C.S., Dever, A.D., Park, A.C., and Frisch, H.P., "A Digital Computer Program for the Dynamic Interaction Simulation of Controls and Structure (DISCOS)," Vols. I and II, NASA Technical Paper 1219, May 1978.

6-2 Lenzi, D.C., and Shipley, J.W., "Mast Flight System Beam Structure and Beam Structure Performance," NASA CP-2447, pp. 265-279, Presented at the First NASA/DoD CSI Technology Conference, November 18-21, 1986, Norfolk, Viginia.

6-3 "AGS Control System Design and Pointing Performance Report," Books 1 and 2, Sperry Flight Systems, Phoenix, Arizona, December 1982.

6-4 Belvin, W.K., and Edighoffer, H.H., "15-Meter Hoop-Column Antenna Dynamics: Test and Analysis," NASA CP-2447, pp. 167-185, Presented at the First NASA/DoD CSI Technology Conference, November 18-21, 1986, Norfolk, Virginia.

6-5 "Development of the 15-Meter Diameter Hoop-Column Antenna," NASA Contractor Report 4038, December 1986.

6-6 Ryan, R.R., "Flexibility Modelling Methods in Multibody Dynamics," AAS Paper 87-431, Presented at the AAS/AIAA Astrodynamics Specialist Conference, Kalispell, Montana, August 1987.

SECTION 7
SIMULATOR FOR THE VARIABLE CONFIGURATION SYSTEM

7.1 Introduction

This section describes the integrated Space Shuttle Orbiter and COFS-II payload dynamics and control simulation. It was installed on the CSDL IBM 3090 MVS computer system, and was written in IBM FORTRAN 77.

This simulation was built to study the mutual interactions between the Orbiter's attitude control functions and the COFS-II payload. Results obtained using the simulation are presented in Sections 9 and 10.

The simulation was based on version 2 of the DISCOS multibody dynamics and control analysis program (Ref. 7-1). As described in Section 6 of this report, the COFS-II system is modelled as a collection of interconnected rigid and flexible bodies. At their interconnections, they are excited by internal forces and torques, and they are disturbed by external forces and torques. This implementation represents Orbiter jet firings as external disturbance forces and torques, and antenna control torques as internal torques. The system is controlled by a combination of simplified DAP (SDAP) and antenna gimbal control laws. The algorithms defining these controllers are interfaced to DISCOS through user-supplied subroutines.

The SDAP emulates the portion of the Space Shuttle flight control system which is active during on-orbit operations, when the payload is unlatched from its ascent position, but may still be connected to the Orbiter. SDAP, because of its simplification, permits only rotational control. SDAP receives its input from the IMU model as an attitude matrix, and constructs rotation rates from its history. Given the switch settings and gains configuring the SDAP, its output is then a series of jet firing commands to the Reaction Control System (RCS) model.

In preparing an experiment, data inputs are classed as for SDAP configuration, Orbiter motion commands, gimbal control torque parameters, payload motion commands, and simulation execution control.

In all experiments, a comprehensive set of plots is produced for each simulation run, so that the behavior of either the Orbiter or the payload may be reviewed more easily. Printout simulation time interval and amount listed can be varied to suit the experiment.

7.2 Simulation System Description

The integrated simulation system consists of the program DISCOS, its associated user-supplied subroutines, and the model of the Space Shuttle on-orbit digital autopilot SDAP.

DISCOS is a multibody dynamics and controls analysis package, developed for NASA, and distributed by COSMIC. It permits a user to model the dynamics of a system of articulated rigid and/or flexible bodies, subject to user-defined constraints, controls, and external actions. A dynamics problem is formulated as a topological tree of flexible bodies, then routines are added to represent the action of model actuators and sensors. The problem is constructed by first creating a data file, which describes the topology of body interconnection and orientation

and specifies the interbody hinge degrees of freedom, body mass and geometric parameters, and then writing FORTRAN subroutines to define disturbance and control forces and torques based on user-selected conditions.

The program DISCOS, as used here, numerically synthesizes and integrates the equations of motion governing the mechanical system which the user has defined.

The user-supplied subroutines specify forces and torques acting between adjacent bodies, and those disturbances exerted by the environment on the bodies. For this simulation, the external forces and torques acting on the Orbiter include those due to the firing of the attitude control thrusters. The choice of which thrusters to fire and how long to fire them is determined by the model of SDAP.

The subroutine for internal force and torque models is used to define the effects of torsional springs and dashpots acting between the antenna components, as well as the control torques from the gimbal motors. It also computes the potential energy. Nominally, any device which develops forces or torques *between adjacent bodies* must be defined in this subroutine.

The autopilot subroutine performs as a nonlinear state-space controller, and may be set to a variety of different configurations, such as holding attitude, performing a maneuver automatically, or performing a manual maneuver, as described in Section 2 of this report. The autopilot receives attitude dynamics, samples the control panel settings for the input data if necessary, determines the allowable motion from the controller phase plane limits and availability of jets, and returns a set of appropriate jet firing commands.

7.3 System Dynamics and Control Functions

As mentioned in earlier sections, the SDAP may be viewed as a feedback controller in a typical plant-sensor-collector-actuator feedback control system. The SDAP is driven by inputs from both sensors and users (i.e., simulated crew). While the attitude sensor inputs vary continuously, the user inputs generally do not. The SDAP outputs are binary commands to turn jets either on or off. Each jet acts as a force actuator, with accompanying torque due to the jet's position on the vehicle. The vehicle model reacts, changing its attitude, the sensors detect the attitude change, and the cycle continues.

7.3.1 SDAP Inputs: Configuration from Simulated Cockpit

Performance of the SDAP may be altered by simulated crew inputs, depending on the requirements of the task. There are several categories of inputs which may be changed either at the keyboard or by switches: configuration constants, maneuver variables, and mode switches.

Most constants are used in the state space controller section. They may be varied from mission to mission. For further information, see Reference 7-2, Table 1.

Maneuver variables can be specific to a particular maneuver. They provide commanded attitude and rate, controller rate limit and attitude deadband, and allowable coupling from commanded motion to other axes. For further information, see Reference 7-2, Table 3.

Mode switches provide automatic or manual performance selection, jet group exclusion, mass property set choice, and position of the Rotational Hand Controller (RHC). For further information, see Reference 7-2, Table 4.

Translational control is not included in the SDAP model. Only rotational motion is sensed, commanded, and controlled. Jet-ON failures may be simulated, but this function was not exercised outside the benchmark runs.

Motion is commanded either automatically or manually. Manual control is triggered by operation of the RHC. Automatic control is engaged by setting control panel switches and entering keyboard inputs to the guidance computer.

Additional details on inputs are also available in Reference 7-3.

7.3.2 SDAP Inputs: Sensed Attitude

The SDAP requires attitude inputs to be in the Body reference frame, but the attitude rates available from DISCOS were in the inertial frame at the body c.g., parallel to the Fabrication frame axes, so there were some rotations required at the interface.

All frames are shown in Figure 7-1.

The Fabrication frame is a prime reference for much Orbiter-related kinematics and dynamics. It is centered a distance ahead of the Orbiter nose, with the X-axis along the longitudinal direction from nose to tail, the Y-axis pointing from the X-axis out the starboard wing, and the Z-axis pointing from belly pan to cargo bay.

The Vehicle frame is defined at station (38.1,0,10.16) meters or (1500,0,400) inches in the Fabrication frame, shown as $r\ ^{F}_{F/V}$ in Figure 7-1, near the mass center of the empty Orbiter. Its X-axis points from tail to nose, Y-axis out the starboard wing as that of the Fabrication frame, and Z-axis from inside the vehicle out through the belly pan.

The Body reference frame has its origin at the Orbiter mass center. Its axes are parallel to those of the Vehicle frame.

7.3.3 Simulation Inputs: Execution Control

Controlling the simulation is a matter of choosing the start and finish times, initial body attitude, position, and rates, and integration interval.

The integration interval, or integrator step time, must be an integer divisor of the 80 ms SDAP clock period in this simulation. This has an impact on the jet model construction, described later in this section. The choice for experimental runs was 20 ms, or a quarter period.

7.3.4 Payload Inputs: Gimbal Control Torques

The only payload actuators are elevation and lateral gimbals. They can be controlled one at a time in this simulation. Varying the antenna gimbal control law parameters can change the characteristic response of the antenna to a steering command.

Simple servo control laws, discussed more fully in Section 10 of this document, were implemented to model the antenna gimbal torque motors. Identical and independent control loops were assumed for both gimbal axes.

The control law outputs torque as a function of commanded angle, gimbal angle error, and error rate. The maximum torque available is 33.894 N-m (25 foot-pounds), so the output saturates easily. The assessment in Section 10 assumed operation in the linear range of output. For large angle slews, the torque would saturate almost immediately.

Slews were simulated by applying a constant torque for a given period and then reversing the polarity of the torque for an equal period. Due to the limit on the torque available from the motor as modelled, the speed of "fast" slewing was relatively slow. A test slew of several tens of seconds was usually required to sweep a 45 to 90 degree angle.

7.4 Sensor Model: IMU

The IMU was modelled as a simple noiseless process. It serves to transform attitude data from the DISCOS inertial reference frame, at the Orbiter body mass center but parallel to the Fabrication frame, to the SDAP Body frame.

7.5 Actuator Model: Jets

One major design problem for the simulation was to resolve how best to model jet performance to fit the coarseness of the dynamic model, yet retain compatibility with respect to the more complicated model in the CSDL Statement-Level Simulator (SLS; Ref. 7-4) model used as performance benchmark. The jet model design goals required conservation of impulse as well as frequency content of the jet's output. The problem may be outlined as follows.

The Orbiter flight control system operates with an 80 ms cycle time. The SLS models actual start-up and tail-off delays. The PRCS on-delay is 34 ms, and off-delay is 22 ms; the VRCS has 15 ms and 10 ms times. The simulation time step was constrained to be an integral divisor of 80 ms for practical purposes.

The pulse output shape and phasing for jet firings was affected by the integration time step size. Alternative situations could be handled in the simulation.

The simulation allows the inclusion of turn-on and turn-off delays which are integer multiples of the integrator period. For the 20 ms integrator interval, the delays were 40 ms and 20 ms, respectively for PRCS jets, and both 20 ms for VRCS jets.

A 2 ms clock was tried, but had an unusually large CPU/simulation clock time ratio, even on the CSDL IBM 3090 model 200, hence was deemed impractical for the serious experiments in this study.

The SLS and DISCOS simulated impulses are compared in Figure 7-2. The SLS impulse is shown as a solid line, that of DISCOS as dashes. The epochs A through F are described in Table 7-1.

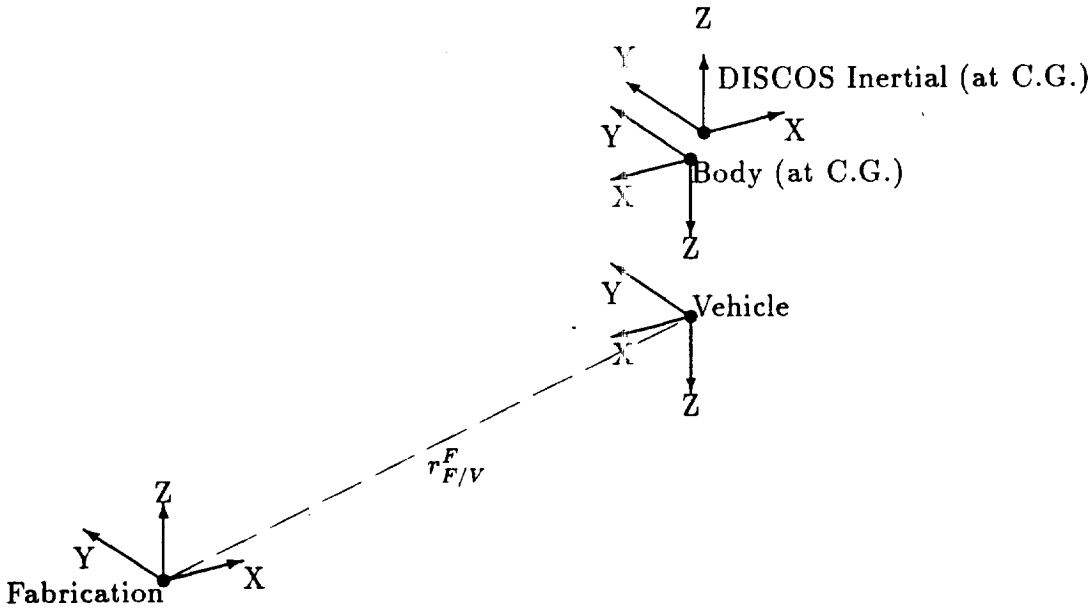

Figure 7-1. Reference frames for simulation.

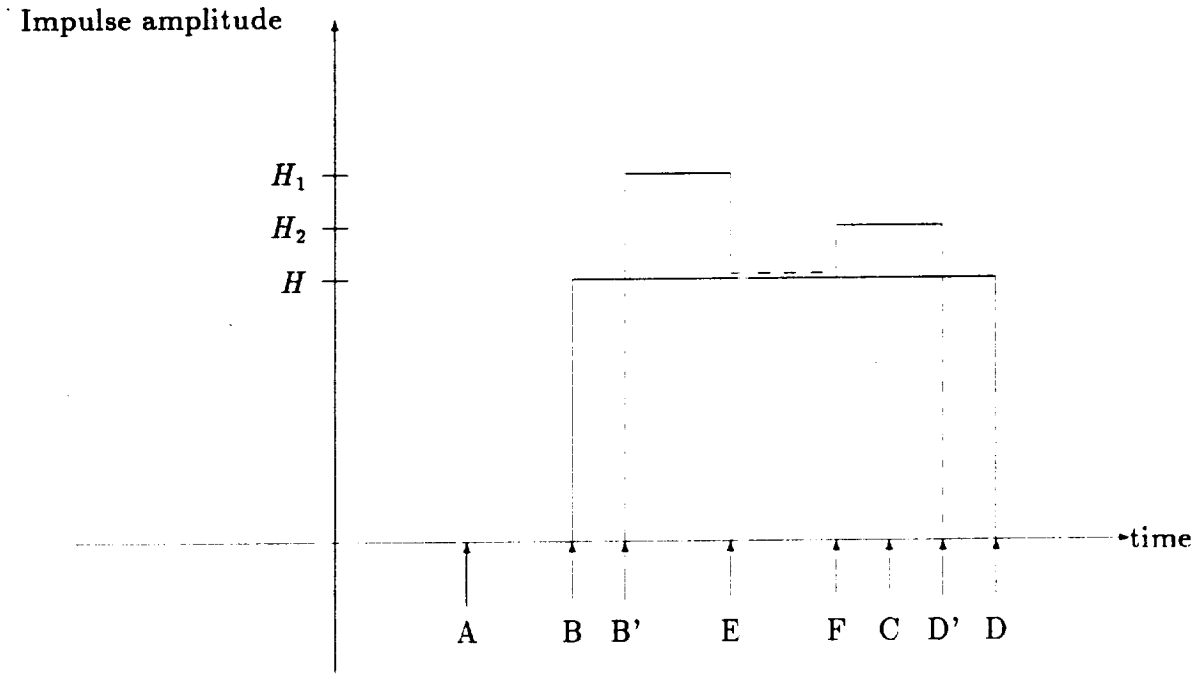

Figure 7-2. Impulse profile.

Epoch	Event
A	Ignition command issued
B	Jet ignition (SLS)
B'	Jet ignition (DISCOS)
C	Turn-off command issued
D	Turn-off response (SLS)
D'	Turn-off response (DISCOS)
E,F	.SDAP cycle clock event on non-minimum impulse burns
H	level of nominal thrust
H_1	level of first simulated DISCOS impulse
H_2	level of last simulated DISCOS impulse

Table 7-1. Impulse profile epochs and events.

In designing the jet emulation, it was considered most important to match epochs B with B' and D with D'. The reason for attempting to match epochs to the same millisecond, is that the closer the SLS and DISCOS simulations' event sequences are to each other, the closer the results will be (all other things being equal), and the more confidence will support the results. This is where the simulation clock pulse duration came into play. Ideally, all simulations and the real thing would fire the jets and turn them off at exactly the same time. Since that was impractical in these circumstances, the impulse off-nominal amplitude was chosen to provide equivalent total impulse in the case of a minimum impulse firing. The details may be noted with reference to the figure.

7.6 Simulation System Checkout

To provide benchmarks of performance and accuracy for the COFS-II simulation, the software system was tested first with a rigid-body Orbiter without payload. Resultant system performance of a given maneuver was compared against the same maneuver on the SLS.

For all test runs, the Orbiter was configured at simulation start in a nominal attitude of payload bay open to earth, nose along orbital path, and rotating once per orbit with respect to earth reference. Nominal orbital parameters were given in any run where appropriate.

Gravity gradient torques were neglected in all but one test run. In order to match one SLS benchmark, they were emulated by an external torque, which was applied as a constant independent of attitude and altitude.

Aerodynamic torques and solar pressure torques were neglected.

REFERENCES

7-1 Carl S. Bodley, A. Darrell Devers, A. Colton Park and Harold P. Frisch. A digital computer program for the Dynamic Interaction Simulation of Controls and Structure (DISCOS). Technical Paper 1219, NASA, May 1978. Volumes I, II, III, IV.

7-2 P. Hattis, C. Kirchwey, H. Malchow, D. Sargent, and S. Tavan. Simplified Model of the Space Shuttle On-Orbit Flight Control System. Report CSDL-R-1562, The Charles Stark Draper Laboratory, Inc., July 1982.

7-3 Isaac A. Stoddard. Manual for COFS-II Payload Interaction Simulation. Report unpublished, The Charles Stark Draper Laboratory, Inc., January 1988.

7-4 Leonard W. Silver (ed.) ESIM Model for the C.S. Draper Laboratory Statement Level Simulator. Report CSDL-R-776, revision 5, The Charles Stark Draper Laboratory, Inc., April 1981.

SECTION 8
RESULTS FOR THE FIXED CONFIGURATIONS

8.1 Introduction

The three rigid Orbiter/flexible COFS-II fixed configuration models described in Section 4 were subjected to analysis and simulation to determine the effects of interaction with the FCS. Of concern were the effects both on the COFS-II structure and on FCS performance. The remainder of this section provides an overview of the interaction problem (both its mechanism and its potential ill effects) followed by results of the analytical and simulation studies.

8.2 Interaction Overview

The FCS constitutes a source of flexural excitation to the combined Orbiter/COFS-II system, raising the possibility of undesired structural deflections and loads. When the FCS is operating as a closed loop controller, there is the additional possibility of flexural rotation of the rigid Orbiter being fed back through the IMU into the autopilot, and the effect on FCS performance can range from negligible to catastrophic.

A nonnegligible but noncatastrophic effect would be inefficient attitude maneuvering, as evidenced by a few excess jet firings and greater fuel consumption compared to rigid body performance, perhaps accompanied by degraded maneuver path control accuracy. A more severe effect would be a high-energy phase plane limit cycle, augmented from the expected rigid body cycle by flexure, which could result in a large excess of jet firings and fuel use, especially during a long-term attitude hold. Many excess firings can shorten the lifespan of the jets, and unexpectedly high fuel consumption could force early mission termination.

If the FCS/structure closed loop gain and phase characteristics at some structural frequency permit, the high-energy cycle could "run away," with jet firings driven by phase plane commands of alternating polarity becoming locked to or near that frequency, and structural deflections and loads increasing either to failure or to limits determined by damping.

CSDL has developed a set of analytical tools (Refs. 8-1, 8-1, 8-3) for predicting the possibility of such runaway behavior and recommending autopilot parameters and mission timelines that will prevent it. Accordingly, before beginning the simulation effort, analysis of the FCS/Orbiter/COFS-II system was performed to suggest initial values of autopilot parameters and the degree of jet-induced excitation needed to demonstrate instability, and to propose alternate parameter sets and stratagems for its avoidance.

8.3 Analytic Techniques

The analytical tools enable prediction of the possibility of unstable feedback interaction for a given set of phase plane control parameters DB (deadband) and RL (rate limit) and for a given RCS jet option (in this case limited to the VRCS jets). The "possibility" is output in the form of two indicators.

The first indicator is the location of each system flexible mode on a parameter plane containing a boundary defining "stable" and "unstable" areas. The axes of the plane are the natural frequency of the mode and a parameter β that characterizes the flexural rotation response of the Orbiter, at that mode, to excitation by the selected jet option. The stable/unstable boundary is specific to a particular combination of DB, RL, and a parameter γ defining the rigid body acceleration of the chosen jet option.

For each flexible mode, attitude control axis and jet option, β and γ are assessed using the rigid body mass properties, the Orbiter flexural response data that is an output of the finite element modelling process, and the jet forces and torques. The corresponding point on the β-frequency plane is then marked, and the stable/unstable boundary for γ and the desired DB and RL is overlaid. Many of these boundaries have been generated, assuming a degree of structural excitation just sufficient to exceed either the selected DB or RL by a factor of two, and a damping coefficient ζ of 0.005. The result of this process is a go/no-go indication of whether bipolar flexural feedback-driven jet firings, once started, will drive the structure to larger-amplitude vibrations (unstable), or allow the vibrations to decrease (stable).

The second indicator gives insight into the likelihood of achieving sufficient excitation, on the premise that the only credible source of excitation is the jets themselves. The inputs to this process are β, γ, natural frequency, ζ, and either DB or RL. The result is the number N of successive worst case jet firings needed to generate sufficient flexural Orbiter rotation to just exceed either DB or RL in a bipolar fashion. We define a worst case firing sequence as a train of contiguous, alternating polarity jet force pulses, each pulse having a duration of one-half the modal period. Note that, neglecting losses due to damping, any odd-integer multiple of this duration is also worst case. Usually, N-values less than 10 are considered to deserve special attention, since some manual maneuvering scenarios can require repeated application of pulses, and closed loop attitude maintenance in the presence of a steady state torque disturbance can generate cyclic firings. Very low values of N indicate that sufficient excitation may be achieved in the course of normal maneuvers, if the commanded maneuver rate MR is large enough to require start and stop firings of sufficient duration to approximate the worst case pulse definition.

It should be pointed out that instability can only be considered improbable when both DB and RL are selected appropriately. Unstable interaction is quite possible with a combination of wide DB and too-narrow RL or vice versa. Another caveat is that the analysis considers one mode at a time, and does not allow for the effect of additive mode responses. Also, as will be shown in subsection 8.5, there exists a region of the phase plane control logic in which the effective rate limit is much smaller than the value of RL and thus sensitivity to flexure is much greater than elsewhere in the phase plane. Operation in this region can be avoided through FCS parameter selection.

8.4 Analytic Results

The results of the preceding assessments predicted instability and relatively great sensitivity to excitation for a number of modes in each configuration when the deadband was relatively narrow (0.1 deg) or when the rate limit was the smallest allowed for VRCS (0.01 deg/sec), and ζ was assumed equal to 0.005, as shown in Table 8-1. The situations (i.e., combinations of mode, control axis and DB or RL) in this table for which N is less than 30 are unstable. (This is not a general rule, but happens to be true for the FCS and structural configurations under study). Increasing the deadband to 1 deg made it very difficult to excite deadband oscillations, and stabilized the subsequent closed loop response. Increasing the rate limit to 0.02 deg/sec reduced but did not eliminate the unstable rate limit modes, and made excitation more difficult. The 0.01 and 0.02 deg/sec RL values are generally preferred to larger values which can cause sloppy maneuver and attitude hold performance by allowing large unwanted rates, and by generating large rate-change commands when operation is temporarily outside the deadband.

The damping coefficient ζ of the modes associated with mast bending was then set to 0.05 to emulate the expected damping present when the experiment proof mass actuators are active. As Table 8-2 shows, the total number of easily excited modes for DB = 0.1 deg or RL = 0.01 deg/sec declined to three, so the assessment was repeated for DB = 0.05 deg, which brought the excitable mode count to seven. Stable/unstable boundaries have not been generated for $\zeta = 0.05$, but the three or four smallest numbers in Table 8-2 strongly suggest possible instability.

Both roll and pitch unstable modes exist. Roll modes are generally more easily excited, which can be attributed to the Orbiter's much smaller roll moment of inertia. The analysis showed negligible yaw rotation of the Orbiter due to flexure.

8.5 Simulation Results

Using the findings of the foregoing analysis, simulations were run using the OCFS (Section 5) to investigate three main areas of FCS/payload interaction, which are reported in the following three subsections. First, excitability and stability were studied using relatively stressed conditions -- either deliberate excitation, or the normal closed loop response to an initial condition of high angular rate. Next, various attitude maneuvers were studied to evaluate the effect of flexibility on performance, and to assess typical loads associated with maneuvering. Finally, several long term attitude holds were simulated to determine the likelihood of achieving sufficient excitation for instability under unstressed conditions. A goal common to the three areas of study was to obtain a set of FCS parameters which provided acceptable performance and adequate immunity to unstable behavior.

Table 8-1. RHC excitation analysis summary (ζ = 0.005).

Config	Mode	Axis	Number of half-period pulses required to excite given DB or RL			
			DB=0.1	DB=1.0	RL=0.01	RL=0.02
1	1	r	2.4	30.	1.7	3.5
1	3	p	9.7	-	12.	27.
1	4	r	7.1	-	16.	38.
2	1*	r	74.	-	46.	-
2	2	p	7.3	-	8.3	18.
2	3	r	3.7	52.	5.7	12.
3	1	r	7.1	-	5.1	11.
3	2*	r	14.	-	12.	26.
3	3	r	14.	-	19.	47.
3	4	r	9.8	-	22.	56.
3	5*	r	150.	-	-	-

* = mode is not considered a "mast" (i.e., 5% dampable) mode.

Table 8-2. RHC excitation analysis summary (ζ = 0.05).

Config	Mode	Axis	Number of half-period pulses required to excite given DB or RL			
			DB=0.05	DB=0.1	RL=0.01	RL=0.02
1	1	r	1.3	3.0	2.0	4.9
1	3	p	7.9	-	-	-
1	4	r	4.8	-	-	-
2	2	p	4.9	-	-	-
2	3	r	2.1	5.2	13.	-
3	1	r	4.8	-	9.3	-
3	4	r	8.0	-	-	-

8.5.1 Excitation/Stability Results

The immediate aim of the excitation/stability simulations was to corroborate the findings of analysis; i.e., to demonstrate that unstable interaction in any of the three configurations was not only possible but also easily excited if the FCS attitude control parameters DB and RL were sufficiently tight. Another desire was to determine the degree of stabilization provided by the active proof mass actuators with their assumed ζ of 0.05.

Table 8-3 summarizes the results of the excitation/stability simulations for all three configurations. Case numbers in the first column are for reference in this subsection. The second column in the table gives the configuration number (1 = antenna facing aft; 2 = antenna facing up; 3 = antenna rotated up 45 deg and to the right side of the Orbiter 45 deg from the aft facing position). Configuration 1 was selected for the majority of the test cases, because it became available for use earliest and because the analysis indicated that one of its modes was the most susceptible to excitation.

The next two columns in Table 8-3 describe the excitation applied to the system; i.e., which mode was excited, and the method used to obtain the excitation. "Modal" excitation makes use of the capability of the OCFS to initialize the first derivative of any selected mode(s) to a specified level. While use of this feature provides no information on ease of excitation, it does give a quick indication of stable or unstable response once sufficient excitation is achieved. The modal excitation cases used the minimum value for the first derivative needed to produce Orbiter flexural rotation about the roll control axis sufficient to exceed either DB or RL by a factor of two.

"RHC" (rotational hand controller) excitation simulates the insertion of manual rotation commands by the crew. In these simulations, we assumed worst case crew inputs producing rotation commands that resonate the desired mode, each command being one half modal period in duration. The control axis the commands were issued in (r = roll, p = pitch) and the number of manual commands input are also cited in the method column.

Several simulations investigated a region of the phase plane (Figure 2-2) known to be potentially sensitive to rate error oscillations. The out-of-deadband coast "corridor" is intended to maintain the rate error at a value that will drive the phase point back inside the deadband without exceeding RL. When the phase point is above or below the corridor, the logic produces firing commands to drive it back inside the corridor. Within the corridor, the firings are cut off. The corridor has only 0.2 times as large a rate deadzone as the in-deadband region (i.e., 0.4 RL vs. 2 RL), hence the greater sensitivity.

When attitude hold is commanded, the attitude current at the time of the command is "snapshot" as the desired attitude, and the attitude error seen by the phase plane is the deviation from this reference. If the angular rate at the time of the attitude hold command is large and DB is small, the attitude error can go beyond the deadband by the time the rate is nulled, and the phase point will be driven into the corridor. The time spent in the corridor depends on the

Case	Cfg.	-Excitation- mode	method[1]	DB, deg	RL, d/s	Closed-loop axes	Mast-mode damping	Results[2]
1	1	1	modal/r	0.1	0.01	r,p,y	0.005	divergent
2	1	1	modal/r	0.2	0.02	r,p,y	0.005	divergent
3	1	1	RHC/r1	0.1	0.01	r,p,y	0.005	divergent
4	1	1	RHC/r2	1.0	0.01	r,p,y	0.005	insuf. exc.
5	1	1	RHC/r2	1.0	0.01	r only	0.005	divergent
6	1	1	RHC/r4	1.0	0.01	r,p,y	0.005	divergent
7	1	1	RHC/r4	1.0	0.02	r,p,y	0.005	insuf. exc.
8	1	1	RHC/r4	1.0	0.02	r only	0.005	divergent
9	1	1	RHC/r4	0.1	0.01	r,p,y	0.05	sustained
10	1	1	RHC/r4	1.0	0.01	r,p,y	0.05	sustained
11	1	4	modal/r	0.1	0.01	r,p,y	0.005	divergent
12	1	4	modal/r	0.1	0.01	r,p,y	0.05	damped
13	1	4	RHC/r11	0.1	0.01	r,p,y	0.005	divergent
14	1	4	RHC/r11	0.1	0.01	r,p,y	0.05	insuf. exc.
15	1	4	RHC/r16	0.2	0.02	r,p,y	0.005	sustained
16	1	4	RHC/r23	0.2	0.02	r,p,y	0.005	divergent
17	1	-	ωr_o=0.03	0.1	0.01	r,p,y	0.005	damped
18	1	-	ωr_o=0.04	0.1	0.01	r,p,y	0.005	damped
19	1	-	ωr_o=0.05	0.1	0.01	r,p,y	0.005	damped
20	1	-	ωr_o=0.06	0.1	0.01	r,p,y	0.005	damped
21	1	-	ωr_o=0.07	0.1	0.01	r,p,y	0.005	divergent
22	1	-	ωr_o=0.08	0.1	0.01	r,p,y	0.005	divergent
23	1	-	ωr_o=0.09	0.1	0.01	r,p,y	0.005	damped
24	1	-	ωr_o=0.10	0.1	0.01	r,p,y	0.005	divergent
25	2	2	RHC/p4	0.1	0.01	r,p,y	0.005	sustained
26	2	2	RHC/p6	0.1	0.01	r,p,y	0.005	divergent
27	2	3	modal/r	0.1	0.01	r,p,y	0.005	divergent
28	2	3	RHC/r2	0.1	0.01	r,p,y	0.005	insuf. exc.
29	2	3	RHC/r2	0.1	0.01	r only	0.005	divergent
30	2	3	RHC/r6	0.1	0.01	r only	0.05	divergent
31	2	3	RHC/r6	0.1	0.01	r,p,y	0.005	divergent
32	2	3	RHC/r6	1.0	0.01	r,p,y	0.005	insuf. exc.
33	2	3	RHC/r6	1.0	0.01	r only	0.005	divergent
34	3	1	RHC/r4	0.1	0.01	r,p,y	0.005	insuf. exc.
35	3	1	RHC/r6	0.1	0.01	r only	0.005	sustained
36	3	4	modal/r	0.1	0.01	r,p,y	0.005	divergent

Notes: 1. **(Excitation method) "modal" = mode first derivative set such that Orbiter flex rotation about the indicated axis is the minimum needed to exceed either DB or RL by a factor of 2; "RHC" = manual rotation +/- command sequence at modal frequency, with axis and number of commands as indicated; "ωr_o" = initial rigid body roll rate as indicated (in deg/sec).**

2. **(Results) "divergent" = closed loop firings appreciably increase flex amplitude; "sustained" = firings maintain amplitude approx. same as caused by excitation; "damped" = firings occur but allow appreciable decrease of amplitude (and firings may stop); "insuf. exc." = excitation does not provoke significant closed loop firings.**

Table 8-3. Excitation/stability simulation results summary.

attitude error excess beyond the deadband and the average rate inside the corridor. Some excitation/stability cases used initial roll rates with DB = 0.1 deg in the hope of provoking unstable behavior in the corridor. These are identified in the excitation method column with "ωr_o" and the initial composite body angular rate in deg/sec.

Remaining columns in Table 8-3 give values for DB and RL, mention which FCS control axes were active (r = roll, p = pitch, y = yaw), specify the damping coefficient ζ for the mast modes, and summarize the results of the closed loop interaction. Although three-axis attitude control (the normal configuration in an actual mission) was generally used, it was occasionally necessary in RHC roll excitation cases to close only the roll axis in order to achieve sufficient excitation for feedback interaction when using the predicted number of pulses. The reason is that flexure and coupling from the roll jets into other axes create uncommanded rates causing the three-axis control system to issue additional commands in pitch or yaw. These commands are realized as either added or removed jets that reduce the effectiveness of the roll excitation. Analytical prediction of the number N of firings needed assumes maximum effectiveness; i.e., that only a single-axis command is present. The FCS allows such axis-by-axis mode selection when in manual control.

The results column shows that many unstable or divergent cases exist when either DB = 0.1 deg or RL = 0.01 deg/sec. Mode 1 of configuration 1 is particularly sensitive. Case 3 in Table 8-3 shows this clearly (only one RHC command needed for divergence) and also illustrates two effects not accounted for in the analysis (which predicted 1.7 or 2.4 pulses were needed). Although only one rate command was input via the RHC, the closed loop manual mode behavior described in Section 2 caused a second, opposed firing to partially null the rate as soon as the RHC returned to center position. This increased the structural excitation to the equivalent of about 1.6 worst case pulses, which the analysis predicted was nearly, but not quite, enough to start a closed loop feedback cycle. However, another FCS response to the removal of the RHC command is the resetting of the desired attitude to the current attitude, thus setting the attitude error to zero. The timing of the worst case command pulse is such that absolute flexural displacement is a maximum when the pulse terminates and the desired attitude is reset. Thus if the vibrational cycle continues freely, the attitude error oscillates between the extremes of zero and twice the flexural amplitude (neglecting damping).

Since the analysis assumes attitude error oscillations that are symmetrical about zero, the pulse number N it predicts as necessary to exceed a given DB is an overestimate for this situation. The result is that the deadband can be exceeded at least once with fewer than N pulses, causing at least one additional pulse that increases the excitation. If these additional pulses can increase the excitation to the equivalent of N pulses by the time they have driven the rigid body attitude error to zero, a bipolar deadband firing cycle will occur. This additional-pulse mechanism has a greater relative effect when N is small. Thus in case 3, a single command pulse caused one additional pulse due to normal manual mode behavior, and another pulse due to a combination of normal behavior and flexure, and the result was sufficient excitation to start a feedback cycle.

The initial rate/coast corridor simulations (cases 17 through 24) provide an illustration both of the sensitivity of this region as previously described, and of the apparently chaotic nature of the excitation obtained from the closed-loop, nonlinear FCS in the pre-divergence phase. Cases 21, 22 and 24 (ωr_o = 0.07, 0.08 and 0.10 deg/sec) were unstable, while the remaining five cases (including one "bracketed" by the unstable cases) were stable.

All of these cases started with a firing to damp the roll rate. These firings varied from 14 to 32 seconds in duration and produced excitations of modes 1 and 4 that ranged from negligible to nearly the equivalent of a worst case single pulse. The unstable cases resulted from near-worst case equivalent mode 1 excitations which initiated a low duty factor bipolar firing cycle.

Figure 8-1 illustrates the evolution of the divergent bipolar firing cycle for a typical case, that with ωr_o = 0.10 deg/sec. Shown are plots of the phase plane trajectory, roll firing commands, generalized coordinates for flexible modes 1 and 4, and the resulting roll moment at the base of the mast. (The numerical values of the generalized coordinates do not represent physical quantities). The firing command in any axis is primarily a function of the rate error, and shows the effect of both rigid body and flexural rates. Its value can range from -1.0 to 1.0, but it only generates a jet firing when it or the command from another axis has an absolute value of 1.0.

The initial rate damping command lasted 32 seconds, and its termination provided some reinforcement to the oscillations started by its initiation, for both modes 1 and 4. During the next 50 seconds of travel along the coast corridor, uniformly spaced command pulses of alternating polarity occurred at an average rate of one pulse per 6.45 seconds. (The closely spaced positive pulse pair at about 45 seconds is considered a single pulse.) This rate corresponds to a frequency of 0.0775 Hz, which is 12% higher than mode 1, but whose third multiple is only 3% higher than mode 4. Thus while initially driven primarily by the mode 1 component of the rate error, the firings nearly resonated mode 4, which can be seen to increase in amplitude as mode 1 decreases in the 30-80 second range.

Although analysis predicted that mode 4 would require the equivalent of three worst case excitation pulses to start a bipolar cycle in the corridor, while mode 1 would require less than one worst case equivalent pulse, the emerging dominance of mode 4 can be explained by the durations of the VRCS pulses during this time in addition to their repetition rate. The average pulse duration was about 1 second, as compared to the worst case pulse lengths of 7.2 seconds for mode 1 and 2.2 seconds for mode 4. Thus each pulse was a substantial fraction of the worst case duration for mode 4, in addition to being in a train of pulses having a large mode 4 repetition-rate content.

The following two pulse pairs, at about 85 and 100 seconds, were closely spaced, nearly worst case doublets for mode 4, and their effect on the mode 4 generalized coordinate amplitude is visible, as is their damping effect on mode 1. Finally, at about 110 seconds, a third mode 4 doublet precipitated a full-scale instability, at which point the jet command duty factor became nearly 100%. The roll moment at the base of the mast (which is almost entirely due to mode 4) then started to increase rapidly, exceeding 9096 n-m at about 180 seconds. The phase

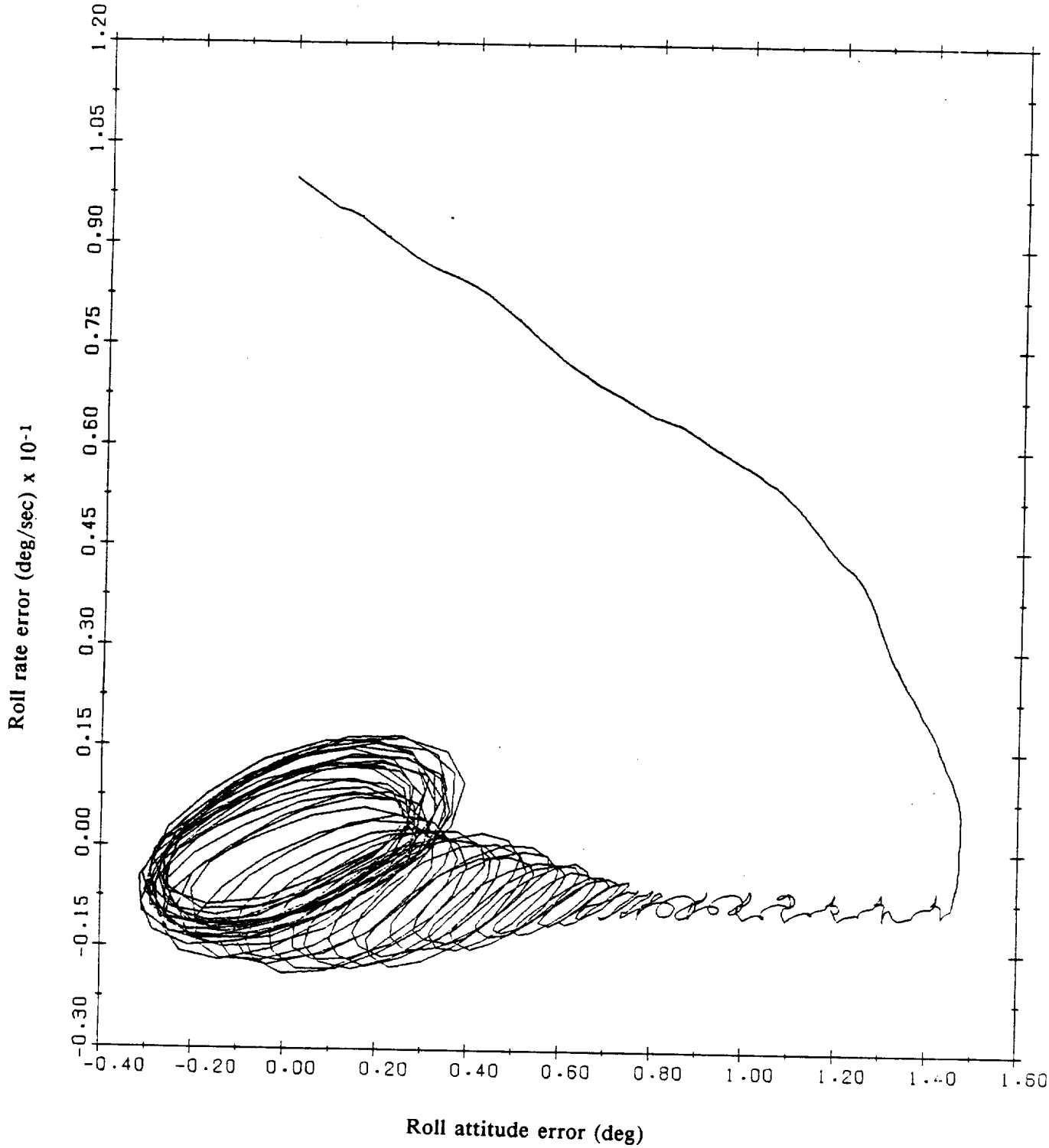

Figure 8-1a. Initial rate case, roll phase plane.

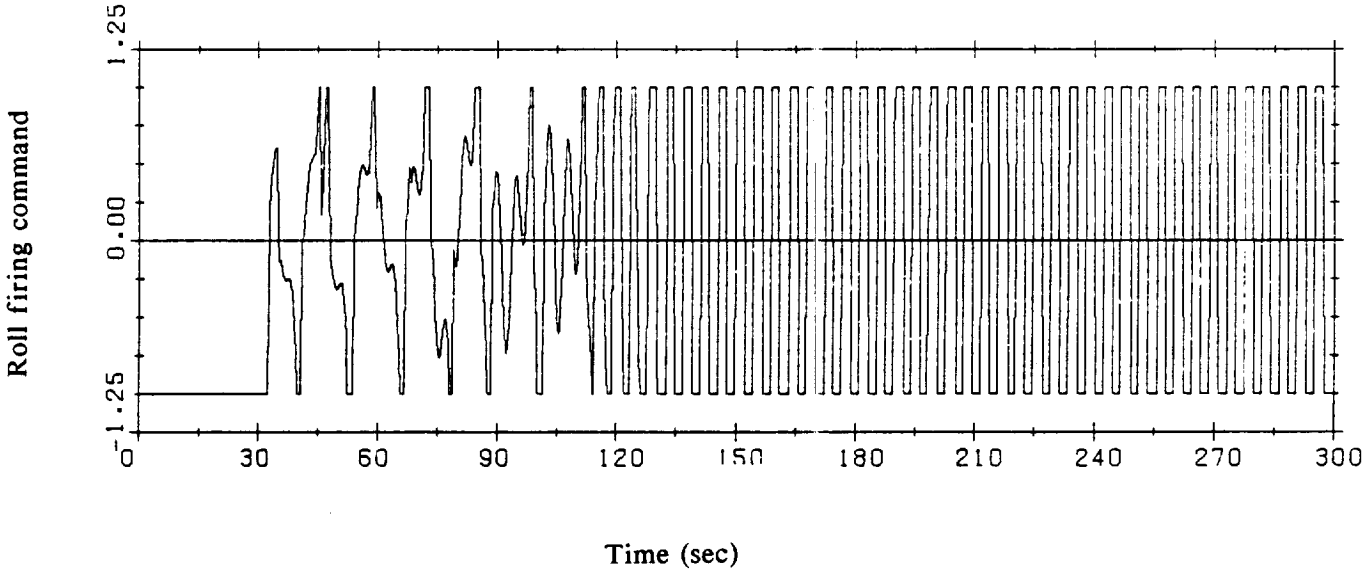

Figure 8-lb. Initial rate case, roll firing command.

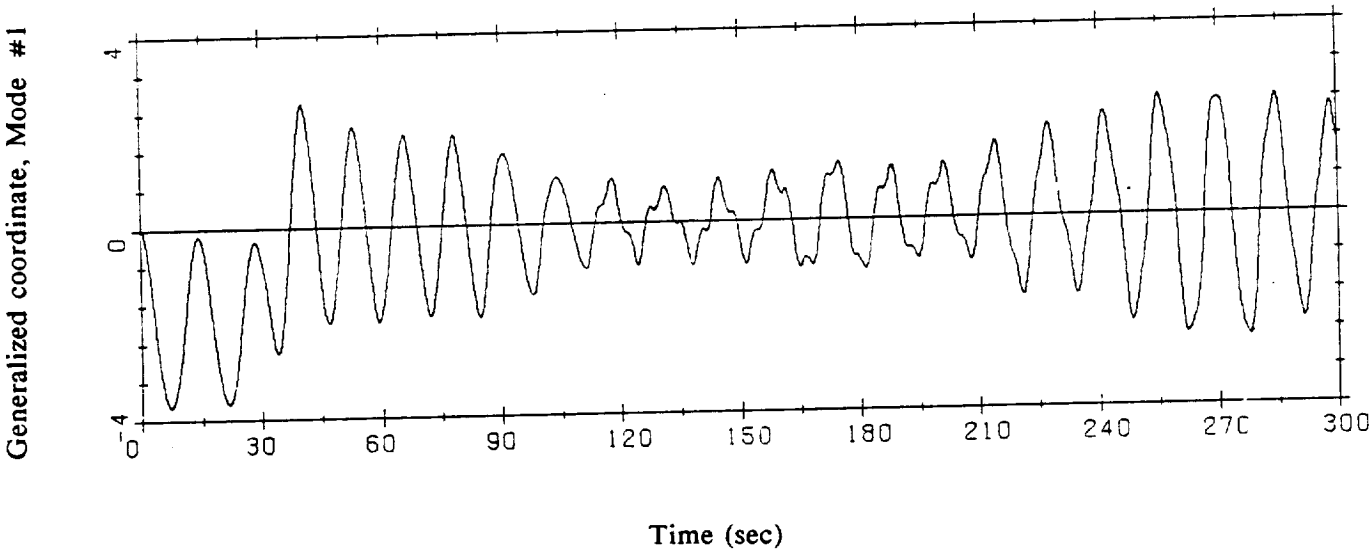

Figure 8-1c. Initial rate case, generalized coordinate, flexible mode 1.

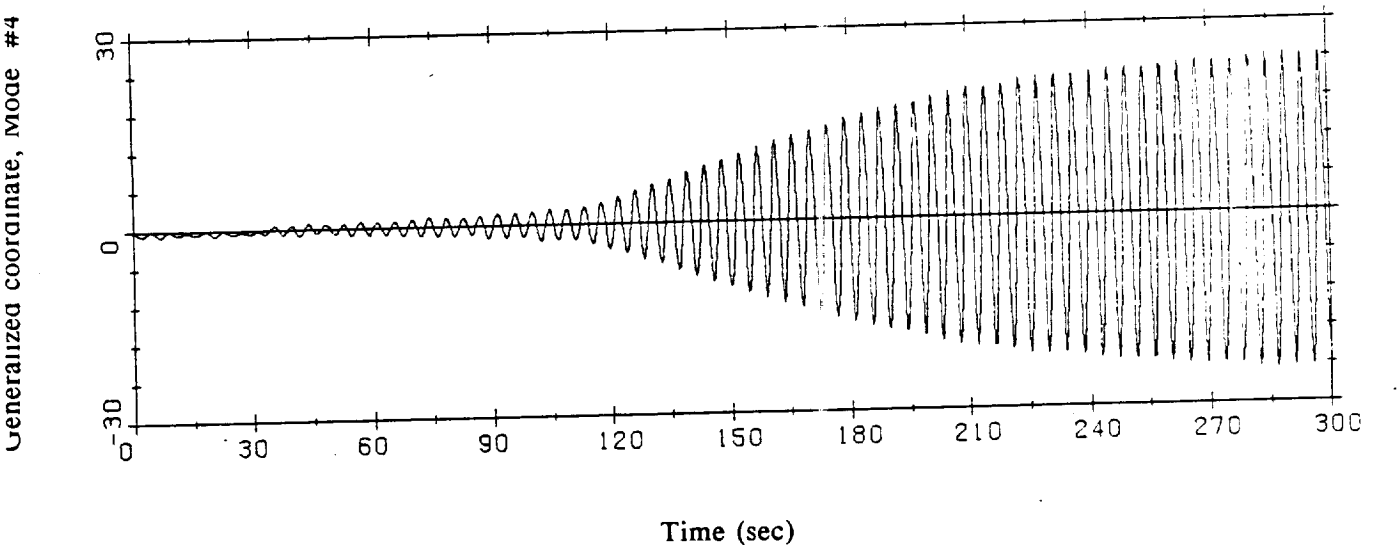

Figure 8-1d. Initial rate case, generalized coordinate, flexible mode 4.

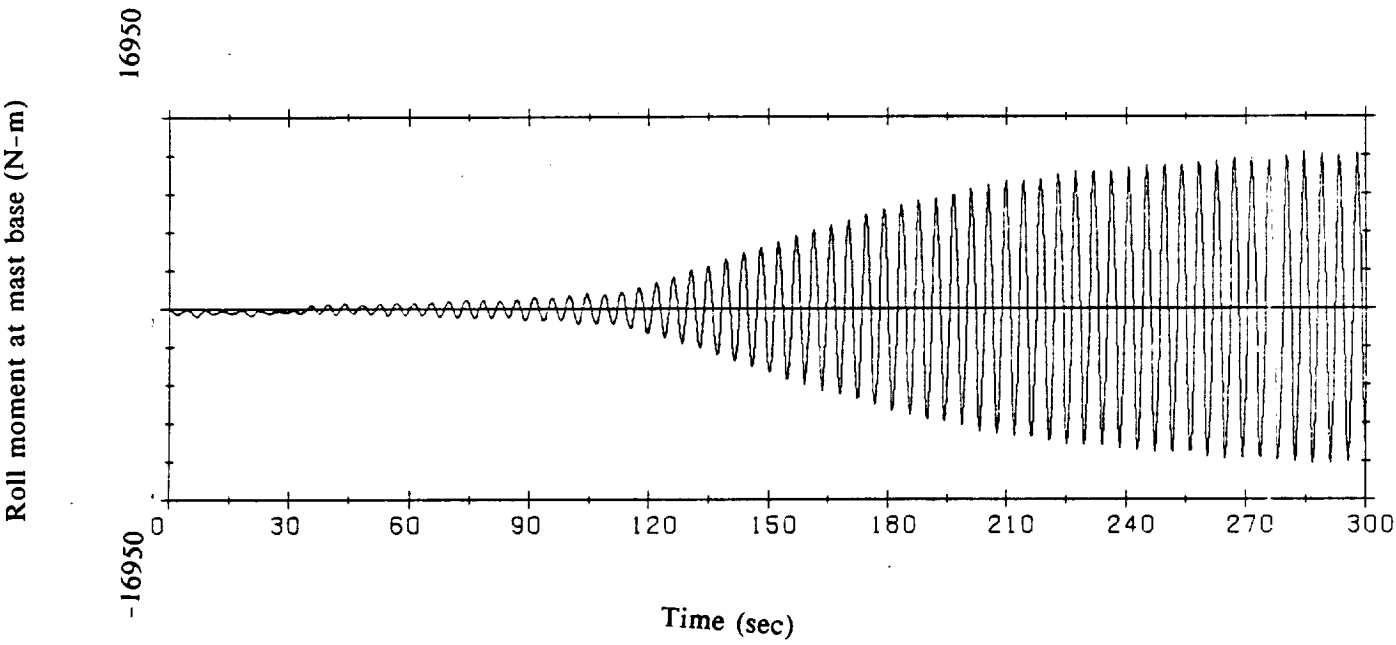

Figure 8-1e. Initial rate case, roll moment at mast base.

plane trajectory for this case shows counterclockwise rotation due to phase lag in the rate estimate from the filter in the state estimator. The usual rigid body trajectory is effectively clockwise; i.e., attitude error increasing when rate error is positive and vice versa.

The results of the simulations summarized in Table 8-3, and previously discussed considerations favoring small rate limits, led to a tentative adoption of DB = 1.0 deg, RL = 0.02 deg/sec as the "baseline" phase plane parameter set for the maneuver and attitude hold simulations to follow. Although instability did occur under conditions of deliberate excitation with DB = 1.0 deg, RL = 0.02 deg/sec, the likelihood of exciting unstable behavior with this set is acceptably low, as long as manual maneuvers are avoided and automatic maneuvers are assessed in advance of being performed. The 1.0 deg DB gives a comfortable excitation margin, as Table 8-1 showed. The 0.02 deg/sec RL, with a 3.5 worst pulse excitation level in the worst case of the three configurations tested, provides a margin that should be adequate for most automatic maneuvers and attitude holds. When this parameter set was used in case 7 in Table 8-3, four worst pulses failed to achieve sufficient excitation for instability to occur when in the three-axis (e.g., automatic) control mode. However, the approximately 3 to 45 second firing durations typical of the start and stop phases of automatic maneuvers easily span the worst case durations, and maneuvers at the high end of the tested MR range of 0.05 to 0.2 deg/sec (see subsection 8.5.2) could possibly cause operation in the out-of-deadband coast channel of the phase plane, which should be avoided. Thus a "baseline" value of MR = 0.05 deg/sec was also adopted to complete the initial FCS parameter selection.

8.5.2 Maneuver Results

Five basic maneuver types were selected as representative of the range of stresses likely to occur during normal operation. The simulations performed and results obtained are summarized in Table 8-4. The selected maneuvers consisted of a 5 deg total maneuver angle command, with the axis of rotation varied to explore the effects of jet off-axis torques, the composite body moment of inertia, and flexure. The maneuver column in Table 8-4 indicates the axis of rotation for each case. The "+r, +p, +y" cases commanded clockwise rotation about an axis that was equally displaced from the forward-pointing roll axis, the rightward-pointing pitch axis, and the downward-pointing yaw axis. Similarly, the "+r, +p, -y" cases commanded clockwise rotation about a forward-rightward-upward axis. The "+roll," "+pitch" and "+yaw" cases commanded clockwise rotation about single vehicle basis axes. If the effects of off-axis rotations are "favorable" (e.g., if +roll, +pitch and +yaw are commanded, and a combination of jets can be found to provide the desired accelerations in approximately the desired proportions), the rate changes needed to start and stop the maneuver should be accomplished with a few long firings, whereas "unfavorable" coupling should cause more, shorter firings and reversals of angular acceleration. Thus using both relative polarities of roll and yaw commands should produce results that cover a range of performance and firing signatures.

Flexure caused some of the 0.05 deg/sec multiaxis maneuvers to exhibit inefficient behavior, as evidenced by excessive roll firings and fuel consumption when compared to their rigid body equivalents. Figure 8-2 shows the roll phase plane trajectory and the roll firing command

Config	Maneuver	Results: Mnvr. qual.	RCS activity: firings	RCS activity: fuel, kg	Mast base moment, 10^3 N-m
1	+r,+p,+y	poor[1]	54	2.49	1.21
2	+r,+p,+y	poor[1]	48	2.25	1.03
3	+r,+p,+y	OK	18	1.71	0.95
1[2]	+r,+p,+y	OK	27	1.88	-
2[2]	+r,+p,+y	OK	39	2.30	-
1	+r,+p,-y	poor[1]	40	2.28	1.01
2	+r,+p,-y	poor[1]	49	2.77	1.01
3	+r,+p,-y	poor[1]	44	2.83	1.12
1[2]	+r,+p,-y	OK	25	1.53	-
2[2]	+r,+p,-y	OK	31	1.89	-
3[2]	+r,+p,-y	OK	24	1.60	-
1	+roll	OK	47	2.20	0.58
2	+roll	OK	57	2.83	0.97
3	+roll	OK	47	2.31	0.62
1	+pitch	OK	16	1.43	1.80
2	+pitch	OK	14	1.40	1.63
3	+pitch	OK	17	1.46	1.43
1	+yaw	OK	19	1.56	1.98
2	+yaw	OK	30	1.87	1.25
3	+yaw	OK	23	1.70	1.13
1[3]	+r,+p,-y	OK	62	4.15	0.93
2[3]	+r,+p,-y	OK	54	4.08	1.06
3[3]	+r,+p,-y	OK	55	4.10	1.06
1[4]	+r,+p,-y	OK	104	5.74	1.32
2[4]	+r,+p,-y	OK[5]	95	5.77	1.35
3[4]	+r,+p,-y	OK	104	6.25	1.19

Notes:
1. "Poor" quality seen as flex-caused roll command reversal of several seconds duration
2. Rigid-body model
3. Maneuver rate = 0.1 deg/sec
4. Maneuver rate = 0.2 deg/sec
5. Short pitch command reversal

Table 8-4. Maneuver simulation results summary. (All simulations used run time = 300 sec, DB = 1.0 deg, RL = 0.02 deg/s, maneuver rate = 0.05 deg/s except as noted, total maneuver angle = 5 deg, gravity gradient roll torque = 6.4 N-m [57 in-lbf], mast-mode damping = 0.005 x critical).

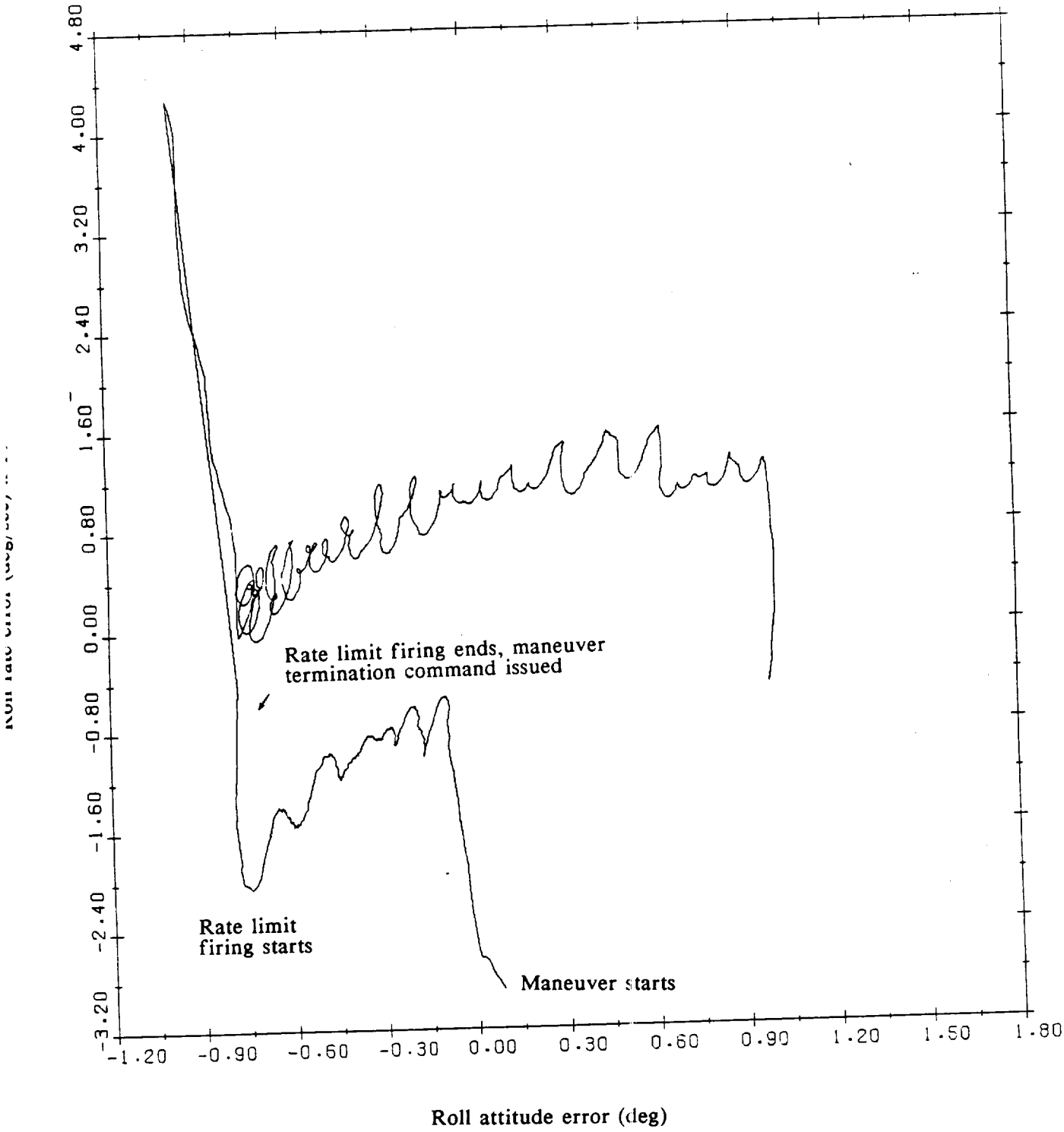

Figure 8-2a. Maneuver case, with flexure, roll phase plane.

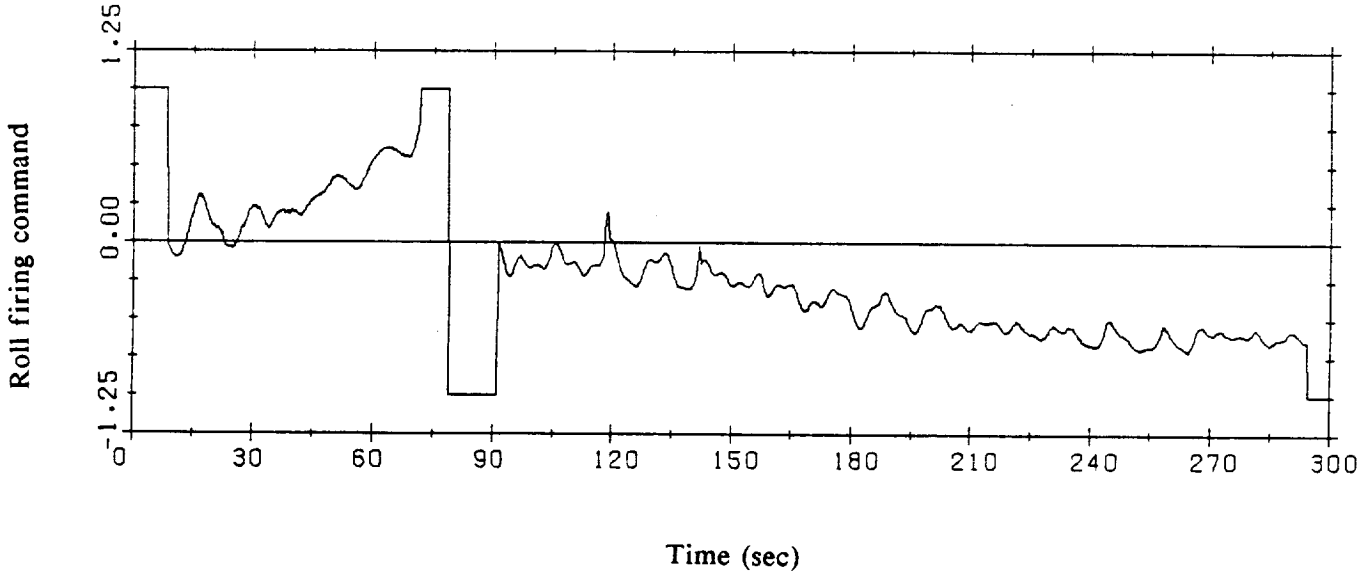

Figure 8-2b. Maneuver case, with flexure, roll firing command.

for a typical case, the +r, +p, -y maneuver using configuration 3. The maneuver started reasonably cleanly, but the combination of rigid body Euler coupling and flexure produced a rate limit firing at about 72 seconds, which was reversed about 7 seconds later by the maneuver termination command. In the rigid body equivalent shown in Figure 8-3, the pre-termination rate limit firing did not occur, due to the absence of flexure and the slightly different rates established at the start of the maneuver.

In general the single-axis maneuvers were better behaved than the three-axis maneuvers, although the effects of flexure could be seen. However, there is probably no advantage to performing maneuvers one axis at a time (i.e., in an Euler sequence) rather than as single equivalent (eigenaxis) rotations, because of the additional time and fuel expenditure required for three sequential maneuvers. Furthermore, flexure does not always degrade all aspects of multiaxis maneuvers, as shown, for instance, by the slightly reduced fuel consumption of the configuration-2 +r, +p, +y maneuver with flexure present. Other maneuvers (with different total maneuver angles, maneuver rates and eigenaxes) might be better or worse behaved than those simulated.

The effect of maneuver rate on performance and stability (especially involving the phase plane coast corridor as discussed in subsection 8.5.1) was assessed in six simulations using the +r, +p, -y maneuver at 0.1 and 0.2 deg/sec for each configuration. The larger rate commands produced longer firings at the start of the maneuvers, but load values differed insignificantly. In all maneuvers, bending moments measured at the base of the mast never exceeded 2000 N-m. The maximum torsion at that location was 130 N-m. At the tip of the mast and the base of the antenna, the maximum moments were 140 N-m.

None of the maneuvers exhibited instability (i.e., a bipolar jet firing cycle). However, for the 0.2 deg/sec maneuvers, this was fortuitous. The mass properties of the composite system, the VRCS jet forces, and the nature of the VRCS jet selection logic are such that roll acceleration, when simultaneous roll, pitch and yaw commands exist, is much smaller than the pitch and yaw accelerations. Thus during these relatively small maneuvers, the roll rate never reached more than about one half the commanded rate of 0.115 deg/sec (the single-axis component of the vector of magnitude 0.2 deg/sec). With so large a rate error seen by the phase plane during most of the maneuver, the roll phase point was never inside the coast corridor. However, the attitude error (essentially the integral of the rate error) grew quite large, going well beyond the deadband. Had the maneuver been larger, the roll rate error would eventually have been driven down, and the phase point would have entered the coast corridor, probably remaining there for the remainder of the maneuver, and providing an opportunity for instability similar to that seen in Figure 8-1.

From the results described in this subsection we can conclude that highly efficient performance of maneuvers with the COFS-II erected is a goal that is unlikely to be achieved. The fuel budget must allow for greater than normal expenditures due to flexure. The mission timeline should provide adequate time for maneuvering at low rates, preferably 0.05 deg/sec. Extensive simulations of any planned maneuvers are necessary to assure stability.

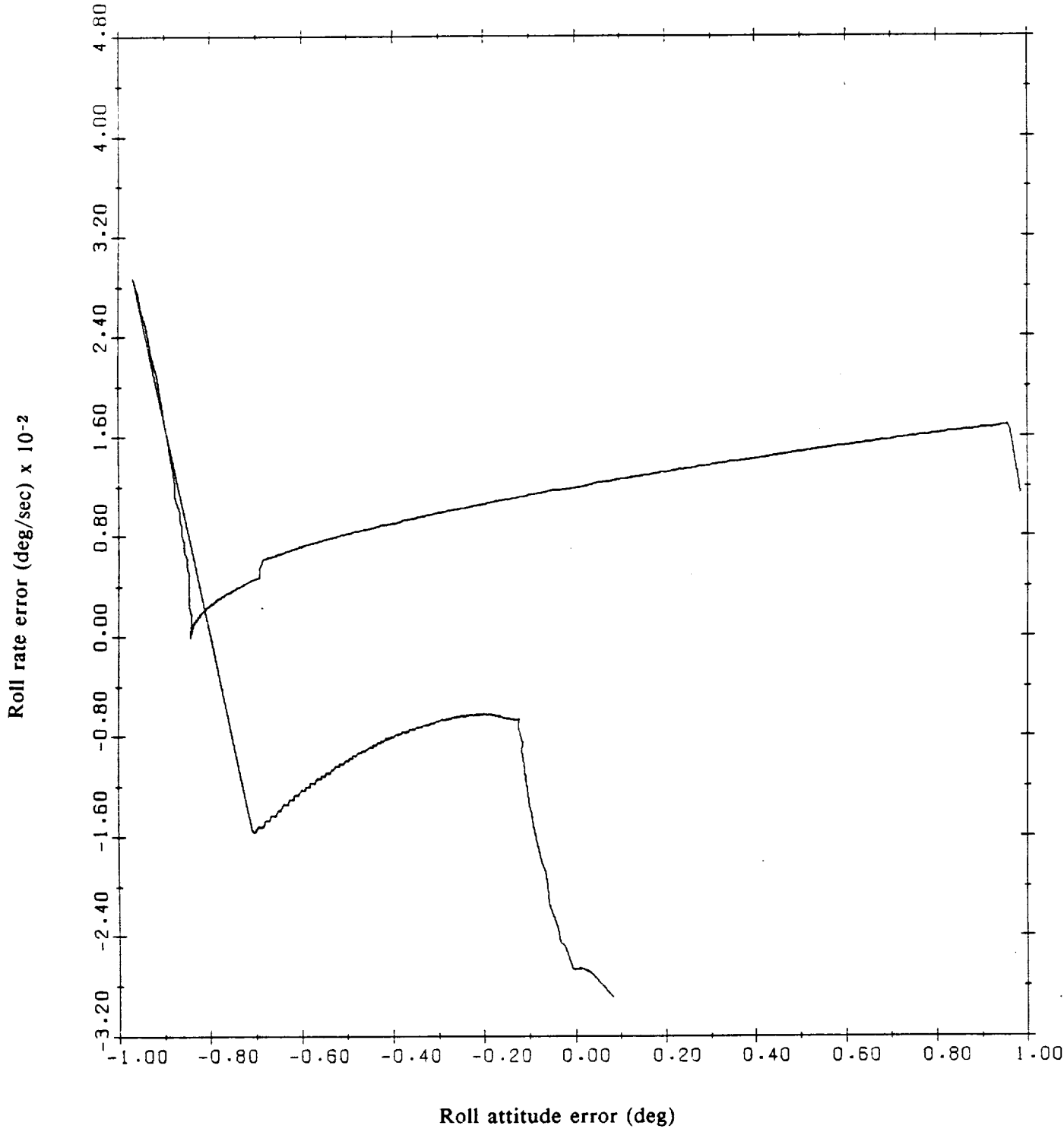

Figure 8-3a. Maneuver case, rigid body, roll phase plane.

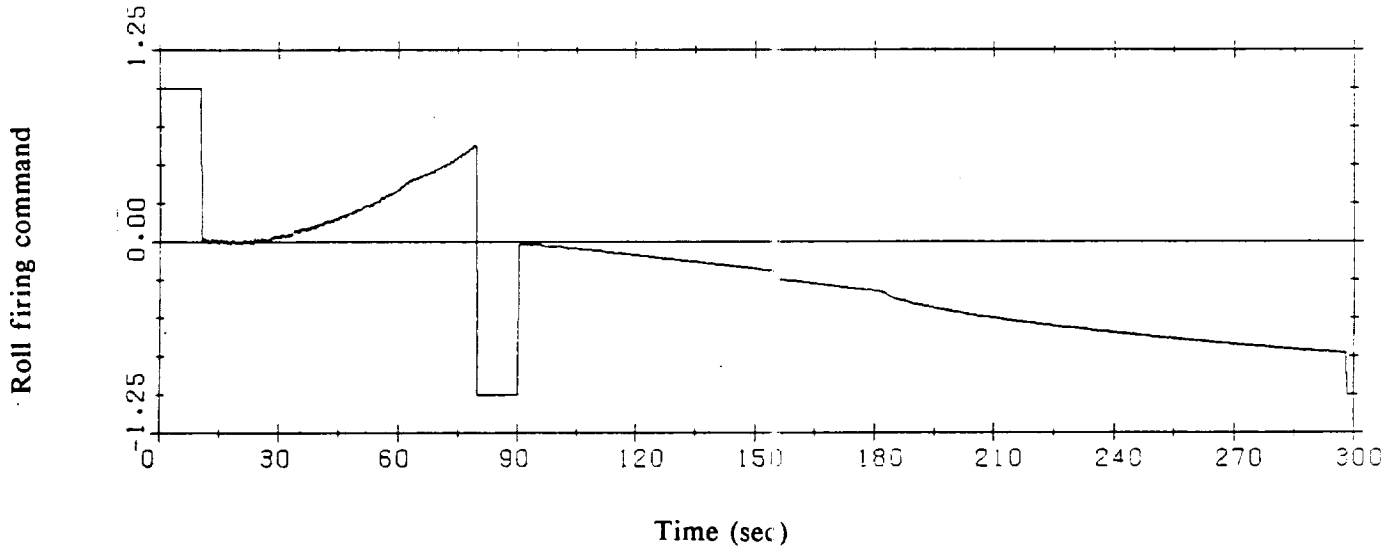

Figure 8-3b. Maneuver case, rigid body, roll firing command.

8.5.3 Attitude Hold Results

Attitude hold simulation cases were run for the tentative "baseline" phase plane parameter set of DB = 1.0 deg, RL = 0.02 deg/sec, and for a set offering tighter control, DB = 0.1 deg, RL = 0.01 deg/sec. For each parameter set, the three configurations were tested with roll-only and three-axis gravity gradient torques. These were simulated as constant torques whose values were obtained by averaging the maximum single-axis values for the three configurations. Deviations from average did not exceed ±9% for any configuration. The three-axis torques were "worse than worst case," since no earth-relative attitude can produce simultaneous maxima in two or three axes. (The roll axis values were also applied in the maneuver simulations).

Ideal single-axis phase plane attitude hold performance in the presence of a constant disturbance torque produces a "one-sided" limit cycle; i.e., generation of regularly spaced unipolar commands that oppose the disturbance. If the RL/DB ratio exceeds a minimum value (which it does in both parameter sets used in these simulations), a stable cycle is established in which the disturbance drives the phase point beyond the deadband (never the rate limit) and the resulting command drives the rate error from its current value approximately to its negative. The disturbance then acts alone to move the phase point in a parabolic trajectory until the deadband is exceeded again, completing the cycle. Multiaxis disturbance torques, off-axis torque coupling and contamination of the disturbance acceleration estimate supplied by the state estimator will cause less than ideal performance. In these simulations, flexure was expected to be an appreciable source of contamination.

The results of the attitude hold simulations are listed in Table 8-5. Performance with the tentative baseline phase plane parameter set was stable, although mode 1 of configuration 1 caused one or two reversals of the roll firing commands in both the roll-only and the three-axis torque cases. These reversals did not cause significant fuel waste or excessive firings. The roll phase plane trajectory and firing command history for the configuration 1 three-axis torque case are shown in Figure 8-4. (The jagged appearance of the phase plane plot is due to the combined effects of flexure and the sampling rate of the plotting routine, which is limited to a total of 1000 data points.) The nonideal behavior is readily apparent as gross deviations from a single trajectory, and the flexure amplitude is large. Flexure caused the phase point to reach the negative rate limit once, as shown by the largest negative spike in the phase plane plot, causing a wrong-polarity firing command. The firing commands are irregularly spaced. In contrast, Figure 8-5 shows the roll phase plane trajectory and firing command history for the configuration 2 roll-axis torque case. The phase plane trajectory comes close to the ideal model, traversing a series of cycles that closely resemble each other. The firing commands occur with regularity, and flexure amplitude is small. In spite of such variations in performance, mast base bending loads in all the baseline parameter set attitude hold cases were less than 1300 N-m.

The tight control parameter set produced divergence for configurations 1 and 2 in both the roll-only and three-axis disturbance torque cases. It is interesting to note that the configuration 1 cases resonated mode 1 but did not progress to dominance by mode 4, in contrast with the coast-corridor instability case (subsection 8.5.1) which used the same configuration and

Config	DB, deg	RL, d/s	Tgg[1] axes	Results: RCS activity firings	RCS activity fuel, kg	Mast base moment, 10^3 N-m
1	1.0	0.02	roll	226	10.1	0.84
2	1.0	0.02	roll	190	9.1	0.68
3	1.0	0.02	roll	215	9.7	0.74
1	1.0	0.02	r,p,y	216	14.5	1.25
2	1.0	0.02	r,p,y	254	14.7	1.27
3	1.0	0.02	r,p,y	251	15.8	1.19
1	0.1	0.01	roll	3622	118.	3.47[2]
2	0.1	0.01	roll	7004	260.	22.2 [3]
3	0.1	0.01	roll	643	12.1	1.19
1	0.1	0.01	r,p,y	5565	210.	3.54[2]
2	0.1	0.01	r,p,y	6569	240.	22.2 [3]
3	0.1	0.01	r,p,y	523	17.0	1.15

Notes: 1. Tgg = gravity gradient torque
= 6.4 N-m (57 in-lbf) roll
= 9.8 N-m (87 in-lbf) pitch (if used)
= 16.3 N-m (144 in-lbf) yaw (if used)
2. Divergent case; divergence largely due to mode 1; load largely due to modes 1 and 4 (mast modes)
3. Divergent case; divergence and load largely due to mode 3 (a mast mode)

Table 8-5. Attitude hold simulation results summary. (All simulations used run time = 4000 sec, mast-mode damping = 0.005 x critical).

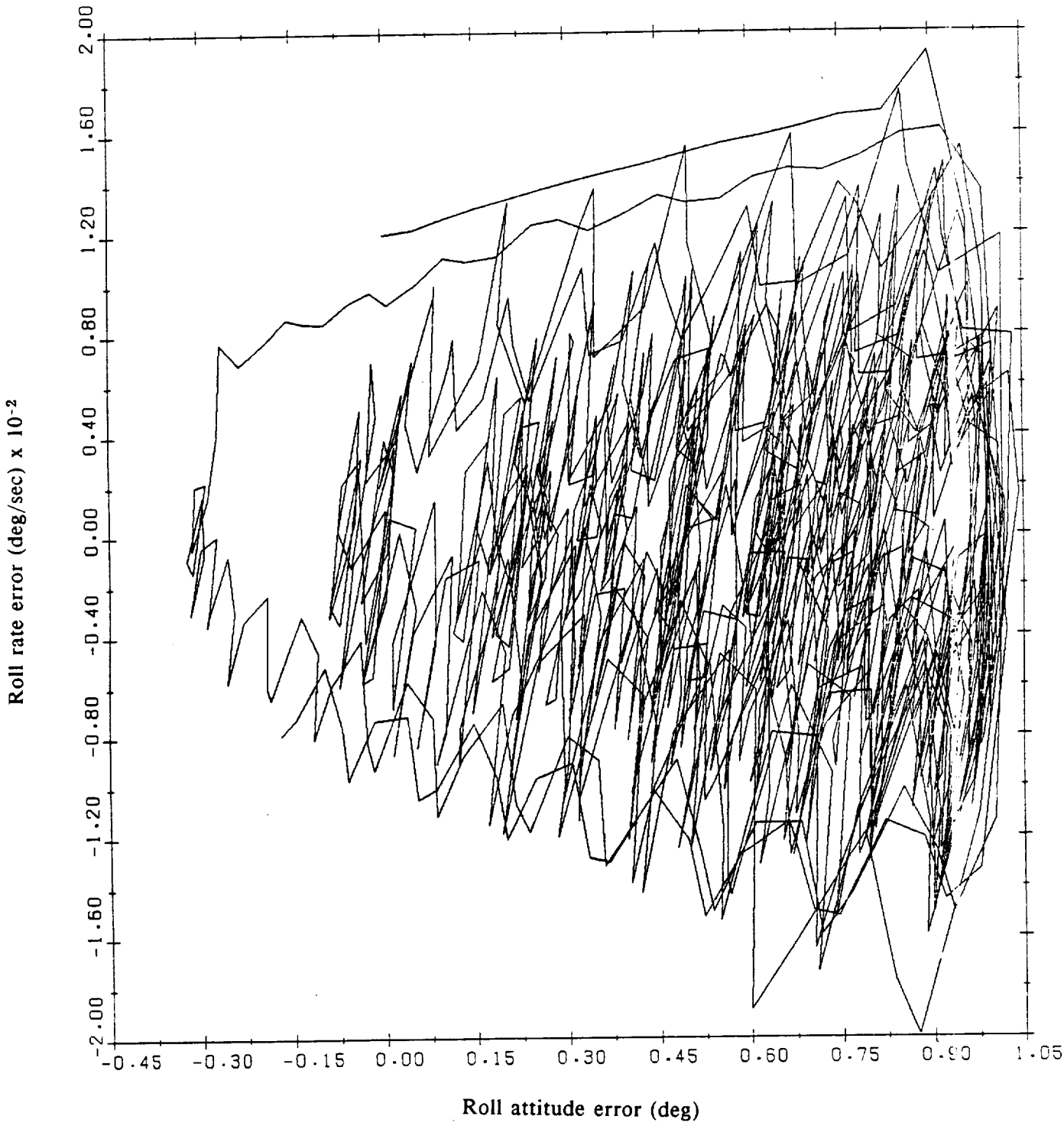

Figure 8-4a. Attitude hold, configuration 1 three-axis torque case, roll phase plane.

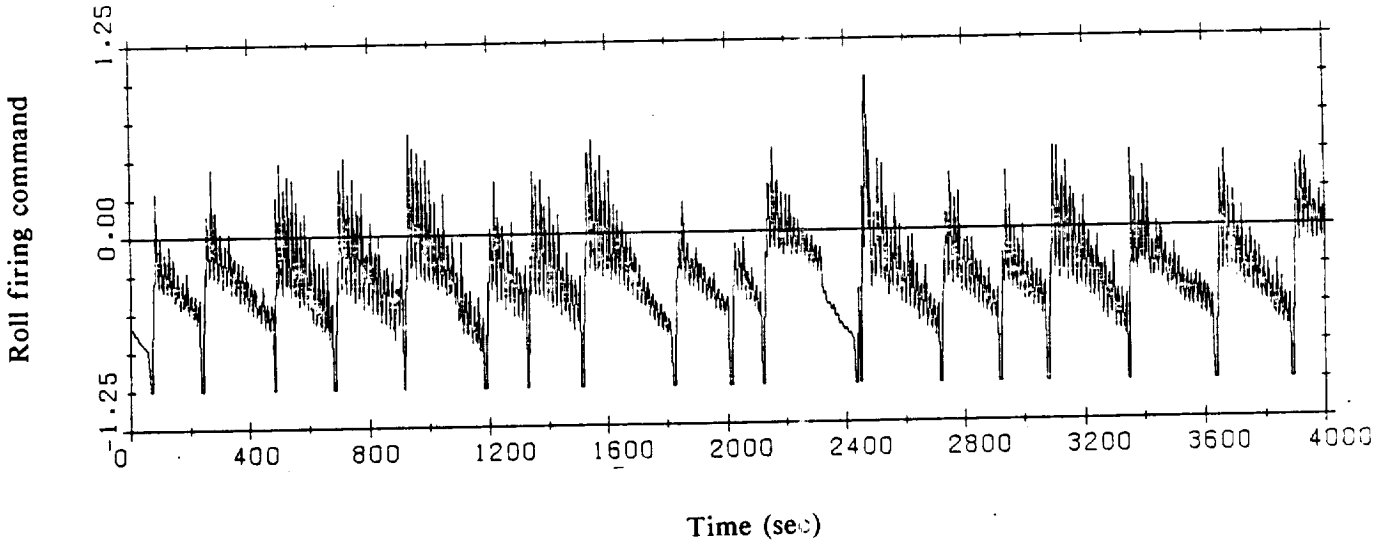

Figure 8-4b. Attitude hold, configuration 1 three-axis torque case, roll firing command.

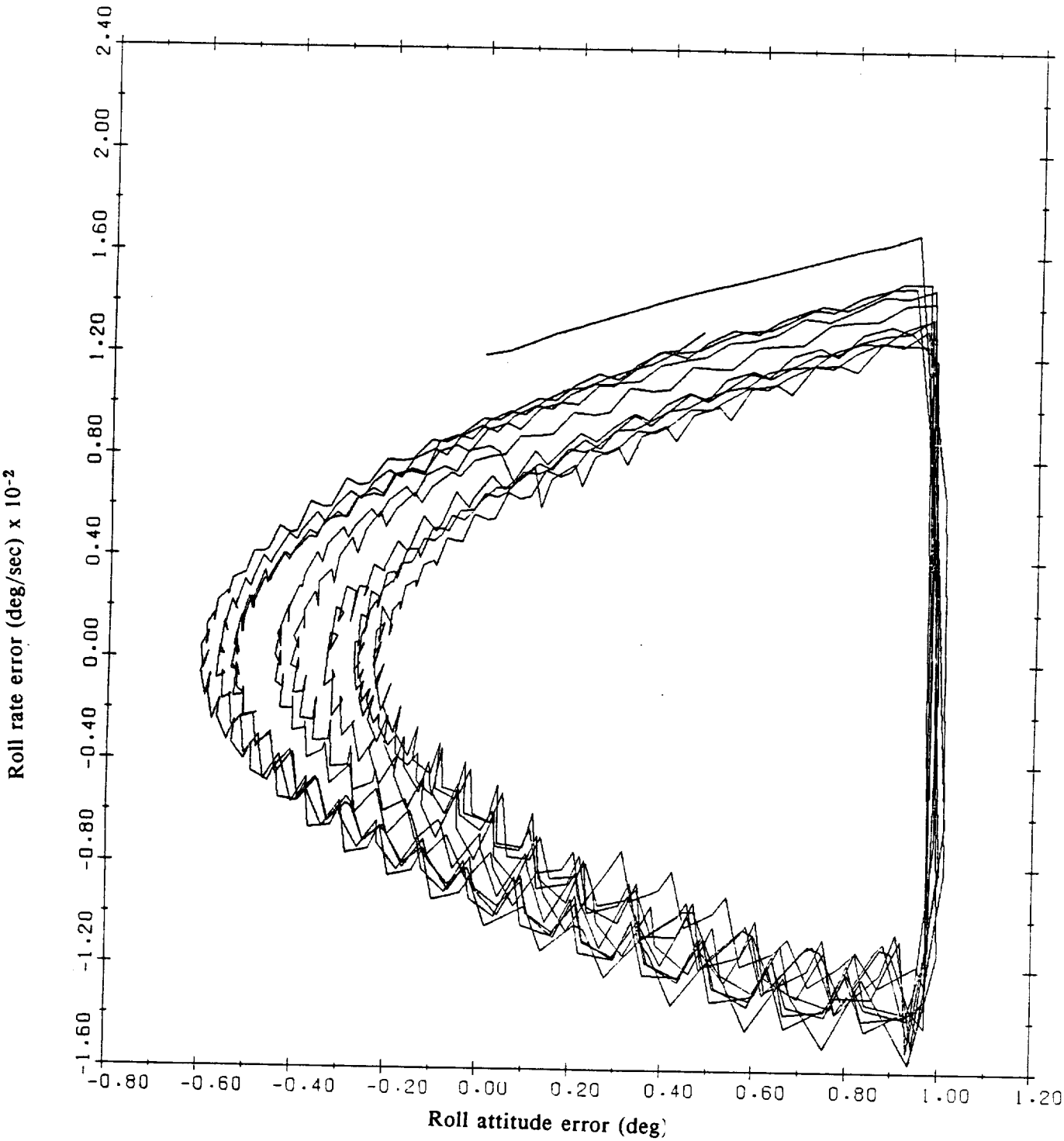

Figure 8-5a. Attitude hold, configuration 3 roll-axis torque case, roll phase plane.

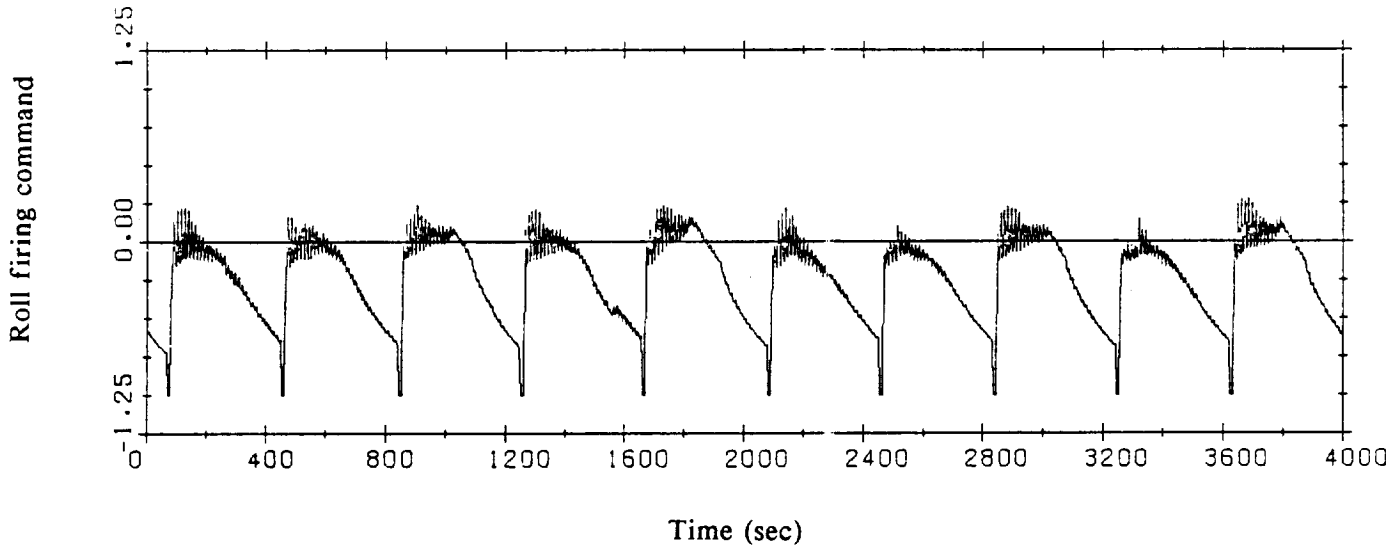

Figure 8-5b. Attitude hold, configuration 3 roll-axis torque case, roll firing command.

parameter set. As a result, the bending loads at the mast base approached about 3500 N-m as an asymptotic value, well below the assumed 9096 N-m limit. (The asymptotic load value due to mode 4 in the coast corridor instability case was about 14,000 N-m.)

The reason mode 1 retained dominance lies in the different nature of the firing commands preceding the divergence. The attitude hold firings occurred at an average rate of about once per 60 seconds, compared to once per 6.5 seconds in the coast-corridor case, whereas the durations of the firing commands were about the same (1 second) in both cases. The greatly reduced rate and similar duration of the pulses would tend to give mode 1 a relative advantage in the attitude hold case because of the greater proportional damping losses between pulses for the higher frequency mode.

The configuration 2 cases resonated mode 3 and produced asymptotic load values of about 22,000 N-m. Differences in fuel use and jet firings among the four divergent cases reflect only the different times of onset of divergence. The jet firing patterns before onset were similar in all of these cases, as were the firing patterns after onset.

The baseline parameter set provides greater immunity to excitation than the tight control set, in direct proportion to the sizes of DB and RL. The simulations showed that it also provides a much longer time span between firings (200 to 400 seconds vs. 60 to 80 seconds) allowing greater damping losses. The 0.02 deg/sec rate limit is the only source of concern in the baseline set. Although some cases showed rate limit firings caused by flexure, none of these firings drove the phase point near the opposite rate limit to create an unstable cycle. The baseline set should provide stable if not ideal performance in attitude hold situations.

REFERENCES

8-1 "Shuttle On-Orbit FCS Screening Criterion for 'Pivot' Type Deployable Payloads," NASA/JSC Avionics Systems Division Internal Note JSC-20104, prepared by Charles Stark Draper Laboratory, September 1984.

8-2 Kirchwey, C., and Sackett, L., "Stability of the Shuttle On-Orbit Flight Control System for a Class of Flexible Payloads," Charles Stark Draper Laboratory Report CSDL-P-1708, June 1983.

8-3 Kirchwey, C., "Computer Programs for 3-D Stability Gain Evaluation," Charles Stark Draper Laboratory Internal Memorandum KBK 85-1, August 6, 1985.

SECTION 9
RESULTS FOR THE VARIABLE CONFIGURATION SYSTEM

The DISCOS/SDAP simulation was used to investigate the dynamic interaction of the COFS-II system during antenna slewing with the FCS active. Although it is unlikely that the FCS will be active during antenna slewing, the results of this section consider that possibility. The simulator was not configured to include an active FCS and an active gimbal angle hold simultaneously; therefore, only slewing was considered. Because of the very low torque level at which the gimbals saturate, it was assumed that during a slew the servo would be saturated at 33.9 N-m (25 ft-lb). Slewing was limited to one axis at a time, either the elevation (EL) or lateral (LAT) gimbal. Active mast damping was included in some cases.

Slewing always began with the antenna pointing in one of the three "standard" configurations: antenna pointing aft, antenna pointing upward away from the payload bay, or antenna gimballed 45 deg in EL and LAT from the aft direction. Slewing was performed by commanding an open loop torque at the gimbal location. A maximum accelerating torque was commanded followed by the reversed polarity decelerating torque for an equal length of time. For example, a 40 s acceleration followed by a 40 s deceleration results in a slew of about 90 deg. The maximum slew rate in that example is about 2 deg/s. Given the limited gimbal range it is unlikely that the given maximum gimbal rate of 4 deg/s would ever be reached. Therefore, there would be no "coast" period, and none was included in any of the simulations.

The input to the FCS includes mission dependent parameters called I-loads. These include expected available per-axis control accelerations and expected individual VRCS jet accelerations used by the phase plane and jet select. Actual accelerations depend on the mass properties of the composite vehicle and change as the configuration changes. Some of the simulations used a set of jet acceleration values which were based on the first configuration, antenna pointing aft. Other simulations used a set of jet accelerations which were chosen by assessing actual accelerations for the three standard configurations and by picking a set expected to give reasonable performance for all three configurations.

The attitude error deadband and the attitude rate deadband (rate limit) may be changed by the crew for different mission requirements. For most of our simulations, we used typical values for VRCS operations of 1.0 deg and 0.02 deg/s, respectively. For slewing, it was assumed that the FCS would be in an automatic attitude hold mode.

Fourteen cases were simulated illustrating typical slews with FCS attitude hold. Some characteristics of the cases and selected results are summarized in Table 9-1. The FCS attitude error deadband ranged from 0.2 deg for cases 1-4, to 2.0 deg in cases 11 and 14. The rate limit was 0.02 deg/s except in cases 11 and 14. The slew acceleration was 10 s followed by a slew deceleration of 10 s in cases 1-4; acceleration and deceleration were 40 s each for other cases. A deceleration was followed by a 10 s period with free gimballing, since the software had no capability to either lock the gimbal or to perform an active servo hold following a slew. The gimbal axis about which the slew occurred is given (EL, parallel to the Orbiter pitch axis, and LAT, often parallel to the roll/yaw axes). The I-load choice is shown: 1 refers to jet accelerations based on configuration 1 mass properties, 4 refers to a selected set based on all three

Case	Deadband (deg)	Rate Limit (deg/s)	Slew Period (s)	Gimbal Axis (EL,LAT)	I-Loads	Initial Configuration	Mast Damping (%)	Maximum Torque Magnitudes(N-m)			Maximum Antenna Base Deflection (millideg)	Antenna Slew Angle (deg)	No. of jet firings	RCS Fuel Use (Kg)
								Mast Base	Mast Tip	Antenna Base				
1	0.2	0.02	20	ALT	1	1	0.5	195	328	77	58	6.0	0	0
2	0.2	0.02	20	AZ	1	1	0.5	999	83	55	21	6.3	27	1.2
3	0.2	0.02	20	ALT	1	2	0.5	757	67	75	59	6.8	0	0
4	0.2	0.02	20	AZ	1	2	0.5	752	63	68	17	6.8	33	1.3
5	1.0	0.02	80	ALT	1	2	0.5	2209	297	77	61	93.0	8	0.7
6	1.0	0.02	80	AZ	1	2	0.5	781	307	75	45	92.1	136	5.2
8	1.0	0.02	80	AZ	1	1	0.5	1817	144	89	71	84.8	70	4.1
11	2.0	0.05	80	AZ	1	1	0.5	1308	114	87	71	95.1	32	4.4
12	1.0	0.02	80	AZ	1	3	0.5	945	230	100	80	78.2	114	5.6
13	1.0	0.02	80	AZ	4	3	0.5	992	230	114	91	78.3	116	5.6
14	2.0	0.10	80	AZ	4	3	0.5	978	230	109	87	87.6	24	4.0
15	1.0	0.02	80	AZ	4	1	5.0	1278	101	82	61	84.5	76	4.2
16	1.0	0.02	80	AZ	4	3	5.0	709	230	76	61	78.5	113	5.6
17	1.0	0.02	80	ALT	1	2	5.0	1402	235	77	61	93.7	8	1.0

- Slew period includes slew acceleration followed by equal time of slew deceleration
- Gimbal axes
  - EL: elevation
  - LAT: lateral
- I-loads used by FCS phase plane, state estimator, and jet select, based on composite mass properties
  - 1: configuration 1 mass properties (antenna facing aft)
  - 4: selected for better performance in all 3 initial configurations
- Initial configurations
  (1) antenna facing aft
  (2) antenna facing upwards
  (3) antenna gimballed 45 deg in EL and LAT

Table 9-1. Antenna slew simulation results summary.

initial configurations. The initial configuration is indicated: 1 refers to the antenna facing aft, 2 to the antenna facing upwards, and 3 to the antenna gimballed +45 deg in EL and LAT (upward and toward the right wing). The mast damping is listed. Most cases assumed only the standard structural damping of 0.5% of critical. Cases 15-17 included 5% damping in the mast flex modes to approximate the effect of the active proof mass mast dampers.

The remaining columns show simulation output quantities. The maximum torque magnitudes are given for three locations of interest: the mast base, the mast tip, and the antenna base. The mast base maximum torque ranged from 195 N-m to 2209 N-m for the 14 cases. Based on data obtained on COFS-I, the maximum allowed mast base load is 9096 N-m. The mast base loads for the 14 simulations were well below that limit. The mast tip maximum torque ranged from 63 to 628 N-m, and the antenna base maximum torque ranged from 55 to 114 N-m. No load limits were provided for these locations. The maximum antenna base deflection with respect to the platform ranged from 17 to 91 mdeg. Because of the nature of the antenna model used in DISCOS, the antenna deflection is actually the model's column base deflection. The total antenna slew angle excursion is shown. The 20 s slews resulted in 6 to 6.8 deg gimballing. The 80 s slews resulted in 78.2 to 95.1 deg gimballing. It varied because the torques caused by RCS firings were added to the 33.9 N-m saturated servo torque over the period of the slew. The number of VRCS jet firings ranged from 0 to 136 and fuel use ranged from 0 to 5.6 kg.

In the short runs of cases 1 and 3, there were no RCS jet firings. For the other cases, VRCS firings occurred when the rate error estimate reached the rate deadband. There was no external torque disturbance such as gravity gradient. At the initial time, the servo torque was applied as a step function. As the antenna moved, so did the Orbiter. The Orbiter IMU detected the motion and its measurements drove the state estimator. Both rate and disturbance acceleration are estimated and input to the attitude controller. Typically, the rate limit was reached before the attitude deadband. A jet firing then followed to maintain the phase point within the rate limit. The estimate of disturbance acceleration (caused by the estimator-unmodelled antenna motion) affected the firing termination time. Both the rate estimate and the disturbance acceleration estimate lag the actual values of each due to the dynamics of the estimator. This characteristic can cause poor FCS performance when there are unmodelled disturbance accelerations such as flexibility and antenna gimballing. During the antenna slew, the FCS is trying to maintain Orbiter pointing within the attitude and rate deadbands.

The system pitch moment of inertia is much larger than the roll moment of inertia. The moments of inertia of the antenna about the EL and LAT axes are about the same. Thus slewing of the antenna in an axis parallel to the pitch axis tends to have less effect on the Orbiter. The EL axis is parallel to the pitch axis for configurations 1 and 2. If the disturbance were confined to the pitch axis, it would take a while for the phase point to reach a firing line. There would be a correcting firing and then a non-firing period again. Slewing in LAT typically caused Orbiter response in the roll and yaw axes. Because of the smaller roll moment of inertia, and the firing lines were reached more quickly. Typically this contributed to longer firings, more firings, and more fuel use.

A few cases were run with deadbands and rate limits increased over the nominal values. Because of the long firing times for any rate limit associated with LAT slews, the effect was small. Larger rate limits did tend to reduce the number of firings for pitch plane slews or small angle slews.

The first four cases were short runs with total slew periods of 20 seconds. Two initial configurations and two slew axes were included. For the EL slews of cases 1 and 3, there were no RCS firings. Orbiter motion was confined to the pitch plane, and because of the large Orbiter pitch moment of inertia, the phase point did not reach a firing line for the small slew angle. The relatively large mast tip torque in case 1 was due to the transient start-up torque of the servo step function, which may not be realistic. For the LAT slews of cases 2 and 4 the phase point did reach a firing line in the roll control axis and so there were jet firings. There was not much difference in the results due to the different initial configurations.

The initial conditions of case 5 were the same as in case 3, but the slew was 80 seconds long. There were jet firings. Figure 9-1 shows the pitch axis phase plane. The phase point remains well within the attitude error deadband of 1.0 deg. As the Orbiter rate decreases in response to the antenna slew, the phase point approaches the lower rate limit of 0.02 deg/s. When it reaches the rate limit, there is a firing which moves the phase point to the S11 cut-off line, near the positive rate limit. The location of the S11 line is affected by the disturbance acceleration. Following that firing, the antenna slew rate begins to decrease and so the Orbiter rate error estimate begins to increase. When the positive rate limit is reached there is a firing which cuts off when the S11 line is reached. Due to estimator lag, the S11 line is slowly moving downward. The phase point again drifts up to the rate limit. There is another firing, longer this time, since S11 has moved further. The undulations in the phase point are due to flexibility.

Figure 9-2 shows time histories of the estimated pitch rate and the estimated pitch disturbance acceleration for case 5. The sharp vertical slopes on the rate plot indicate jet firing times. The disturbance estimate lags the actual disturbance. The estimate is shown to change sign at about the time of the termination of the third pitch firing. Figure 9-3 shows the Orbiter pitch torque and the mast base y-axis (pitch) torque. Note that the three pulses each reinforced the base load.

The initial conditions of case 6 were the same as in case 5; however, the LAT gimbal was slewed. The Orbiter roll axis experienced quite a bit more jet firing activity than the pitch axis had in case 5. The number of jet firings and the fuel use was considerably larger. There was not the flex reinforcement that occurred in case 5, and thus the mast base load was smaller.

Cases 8 and 11 were similar except that the deadband and rate limit were increased over the nominal values for case 11. The principal effect was a change in the timing and number of the firings, causing some difference in loads and fuel use.

Cases 1-12 and 17 used I-loads based on configuration 1 mass properties. Cases 13-16 used I-loads based on inspection of the mass property effect of the three initial configurations.

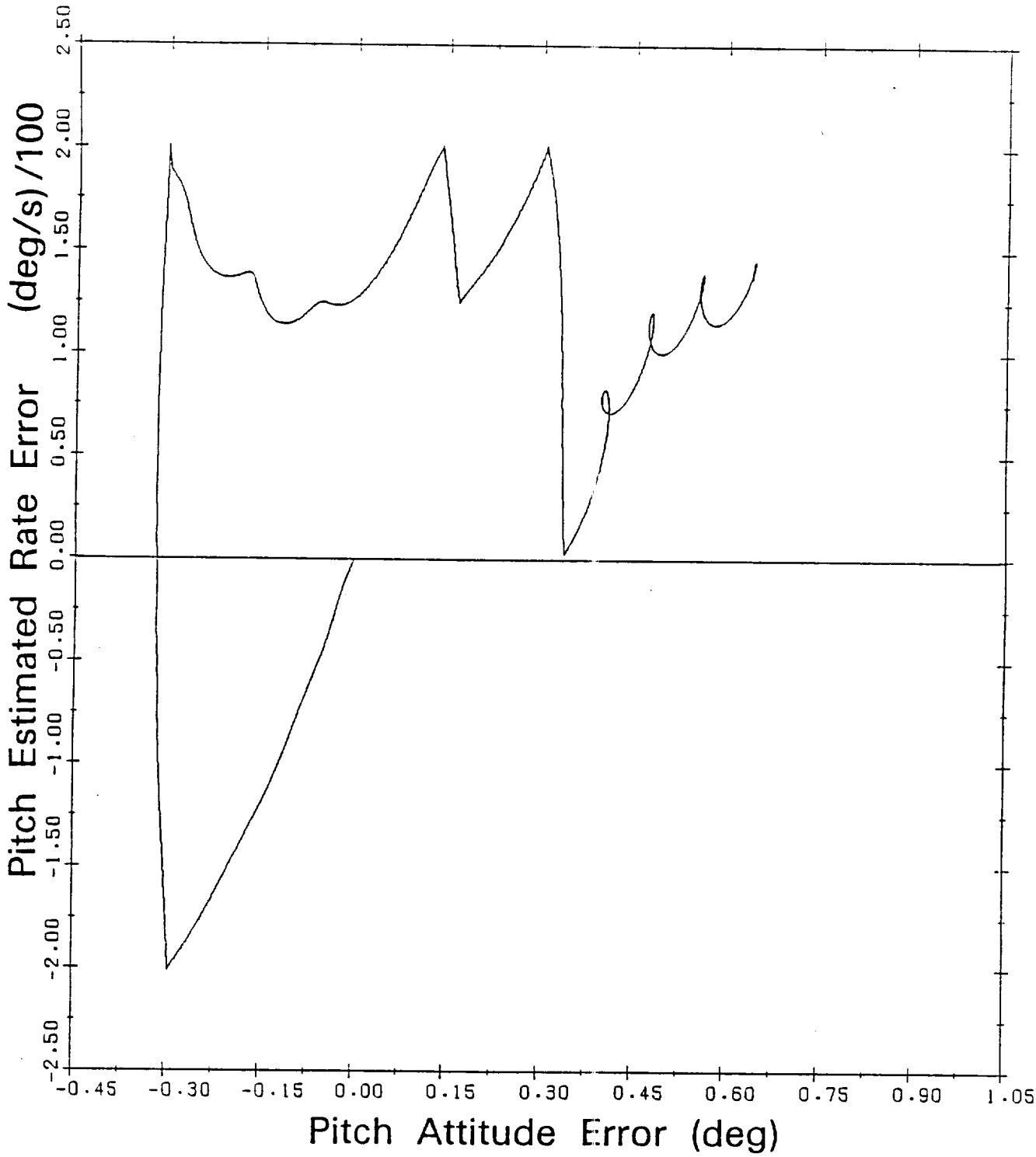

Figure 9-1. Run 5 - pitch phase plane.

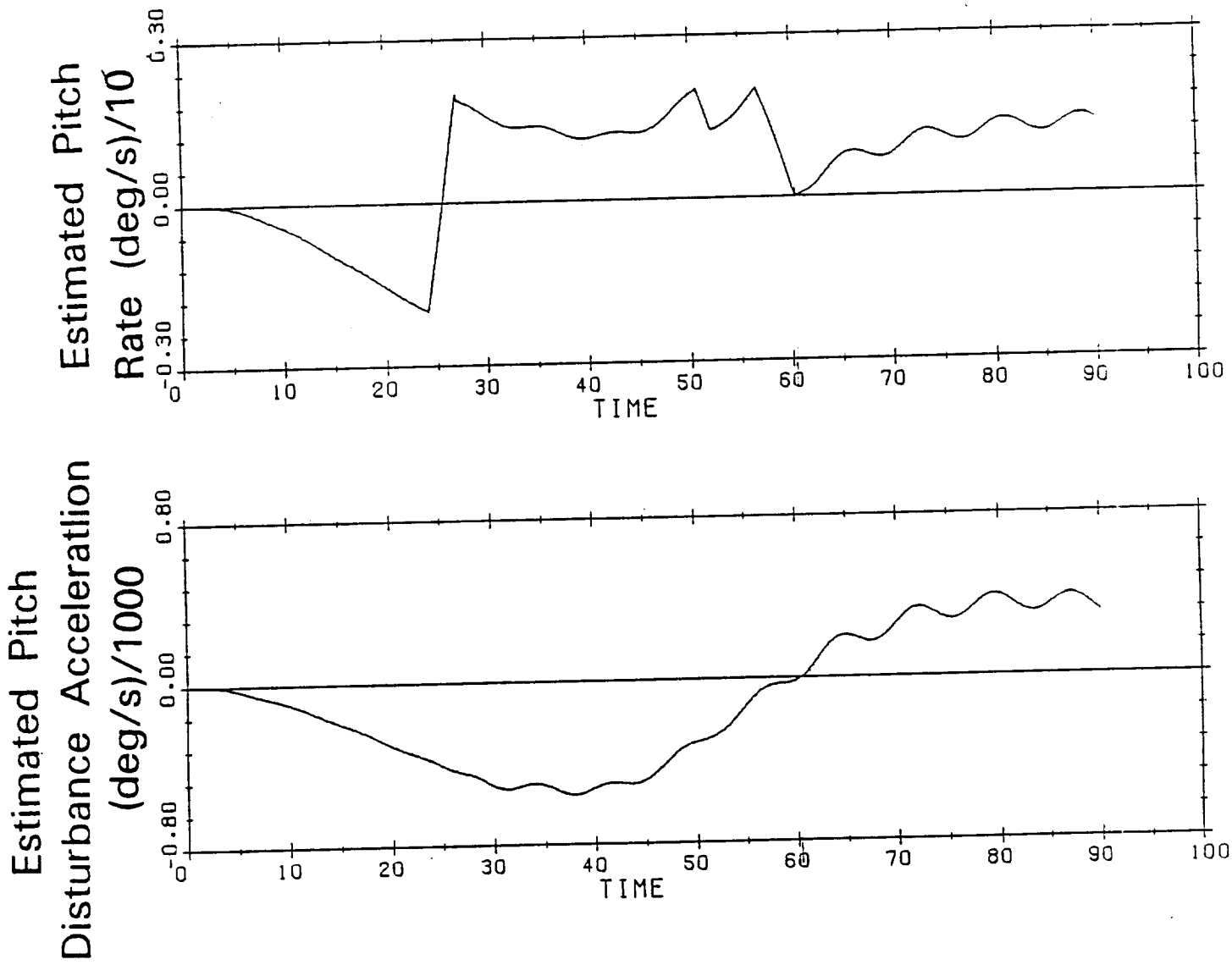

Figure 9-2. Run 5 - rate and disturbance acceleration estimates.

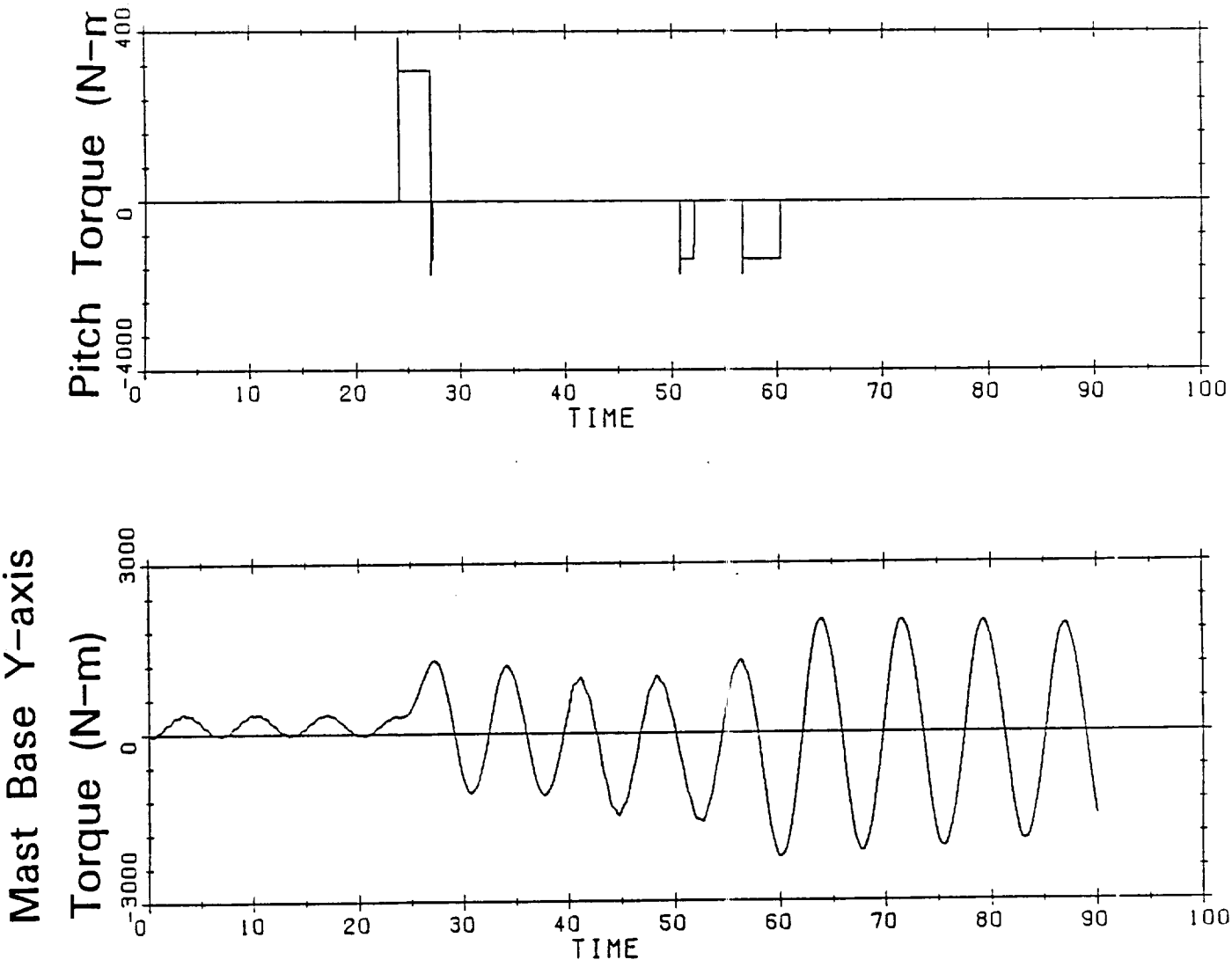

Figure 9-3. Run 5 - pitch jet torque and mast base load.

The difference between these two sets of I-loads was not great, although I-load differences based on the other configurations would be greater. Cases 12 and 13 were similar except for the use of the two sets of I-loads. There were minor differences in the results.

Case 13 illustrates one cause of poor FCS performance during an antenna slew. Figure 9-4 shows the roll phase plane for case 13. The phase point remains within the attitude error deadband, but as the Orbiter attitude changes as the antenna slews, the phase point moves toward the lower rate limit. When it reaches the rate limit, jets begin to fire. Jets continue to fire until nearly the end of the run. With the large roll moment of inertia of the COFS-II, the roll jet torque authority is relatively small. Because of the initial antenna location, antenna slewing causes attitude error build-up in all three control axes. Although a roll axis command continues, the actual jet combinations selected change as conditions and commands from the pitch and yaw axes influence the jet selection. In the roll phase plane, the phase point is driven upward by the jet firings. After crossing the zero rate line, the phase point slope is affected by the antenna slew deceleration which begins at 40 s. The firing continues until S11, which is close to the upper rate limit, is reached. By this time, however, the actual disturbance acceleration has changed sign, although the disturbance estimate lags. The S11 line starts to move downwards, but the phase point is pushed upward now, and the roll jet command changes sign. After some chattering between the rate limit and the nearby S11 line, the phase point moves above the rate limit and the roll command remains on. Axis cross-coupling causes the actual jet combinations to vary over time. Gradually, the disturbance decreases (as the slew decelerates) and the phase point can be controlled to within the rate limit. The S11 line has moved below the zero rate axis and the jet firings carry the phase point downward.

Figure 9-5 shows the estimated roll rate and the actual roll rate for case 13. The flexure is more noticeable in the roll axis because of the smaller Orbiter roll moment of inertia. The estimator's smoothing and lag characteristics cause distinct differences in the two quantities. Figure 9-6 shows the jet torques in the orbiter roll, pitch, and yaw axes as various jet combinations are selected. Figure 9-7 shows the mast base load torques in the x-axis and the y-axis. The effect of the varying jet combination firings and the flexure is indicated. The peak load occurs at about 57 seconds. Because the jets have been on almost continuously, there was high fuel use of 5.6 kg.

The deadband and rate limit were increased above nominal in case 14; otherwise case 14 is similar to case 13. There were fewer firings and less fuel used in case 14, but the loads were similar.

Cases 1-14 included nominal structural damping of 0.5% of critical. Cases 15-17 increased the damping to 5% in the mast to approximate the effect of the active proof-mass dampers. Case 15 is similar to case 8 except for the increased damping and the I-load change. There is a lower mast base load, although that is primarily due to random differences in the firing patterns. Cases 16 and 13 differ only in the damping included. The differences in the results are small.

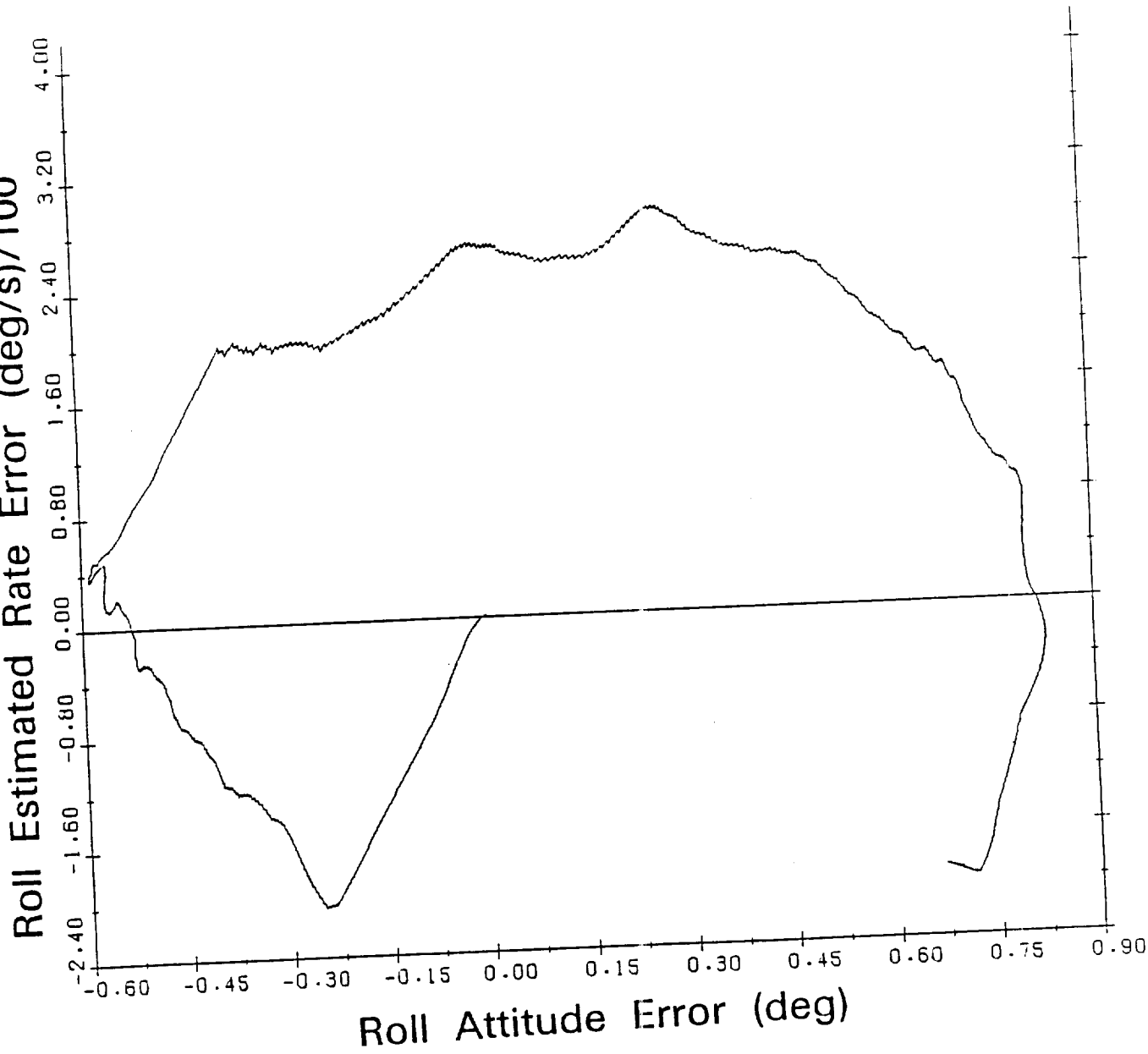

Figure 9-4. Run 13 - roll phase plane.

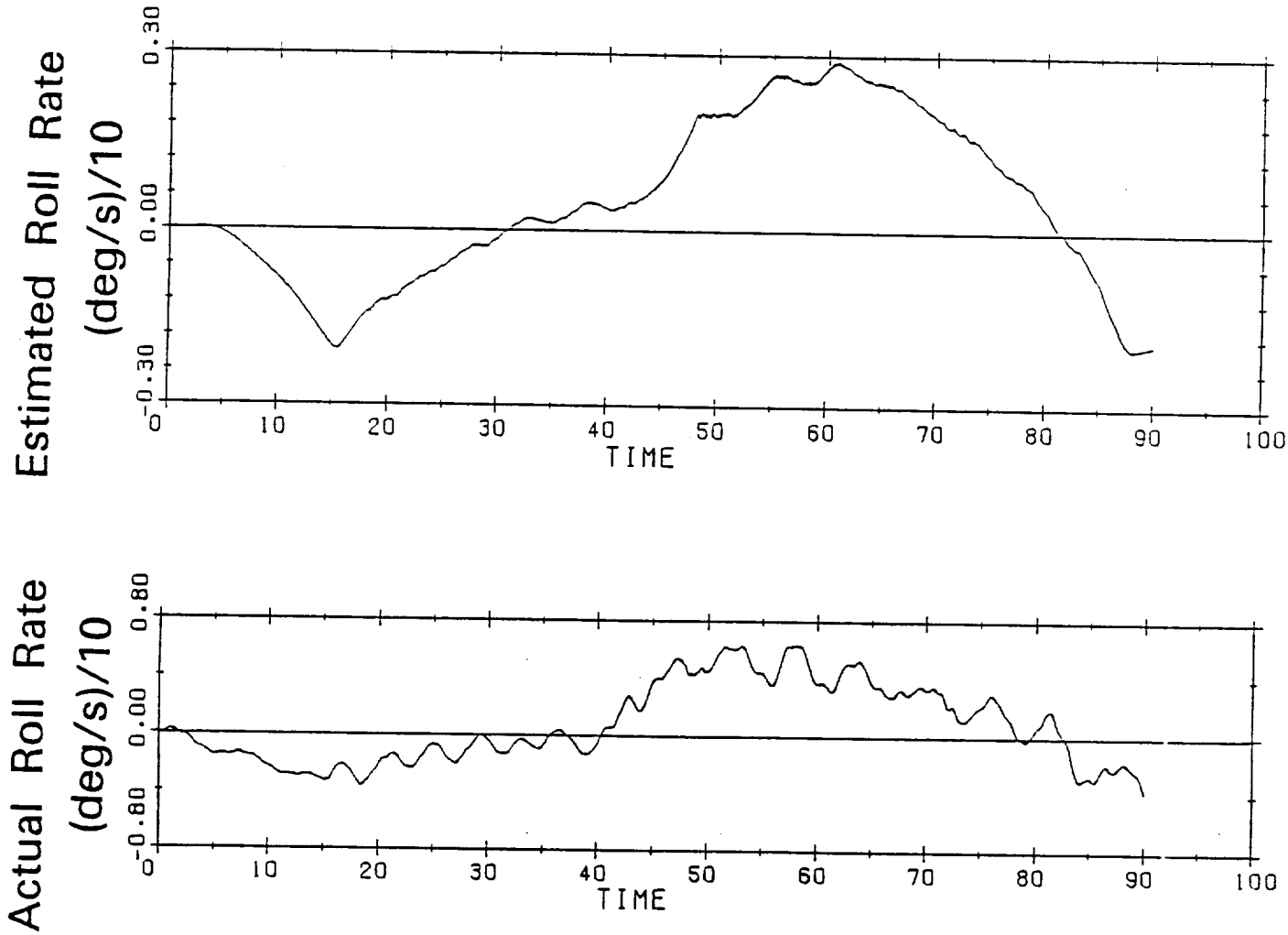

Figure 9-5. Run 13 - actual and estimated roll rates.

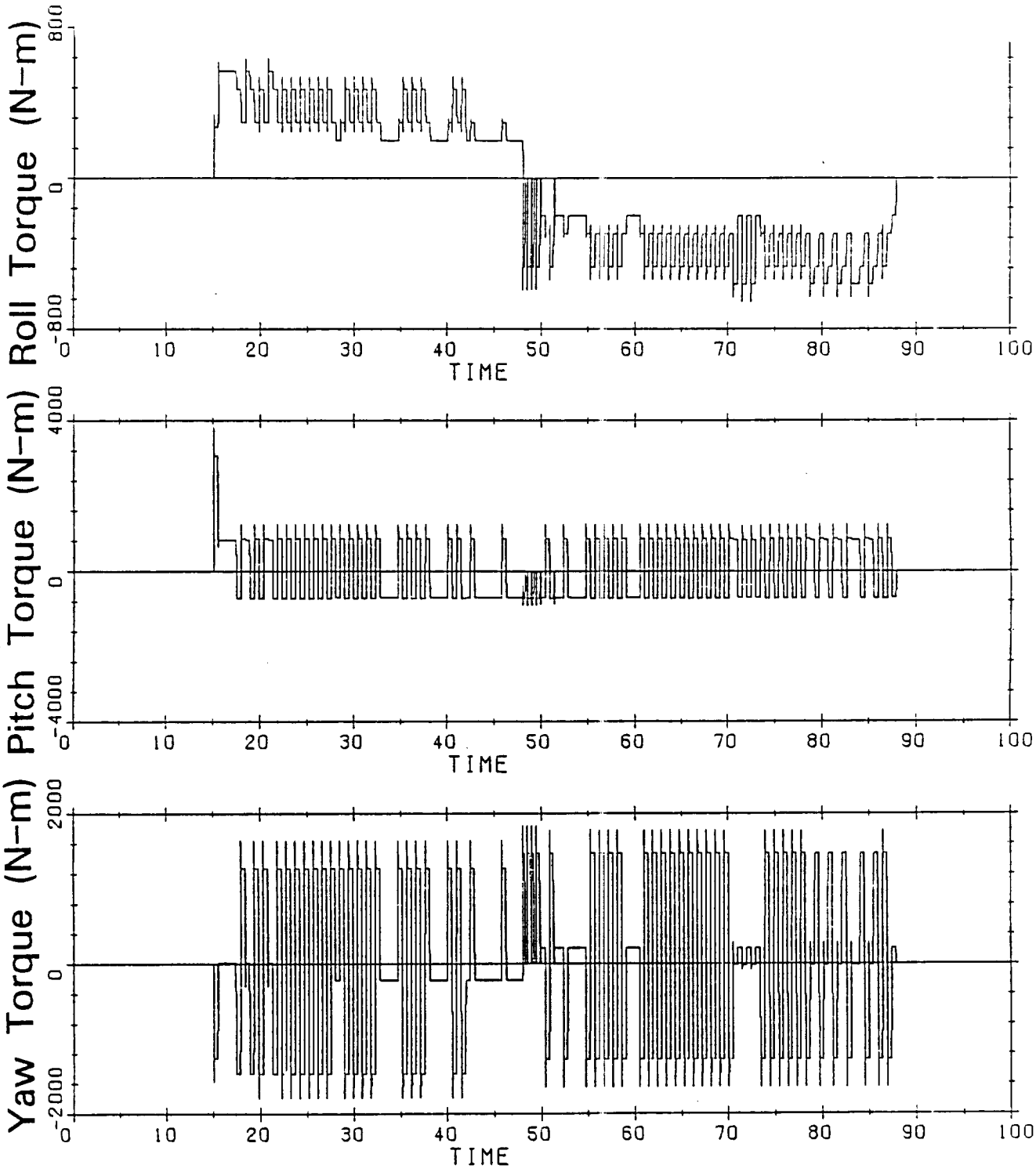

Figure 9-6. Run 13 - jet torques.

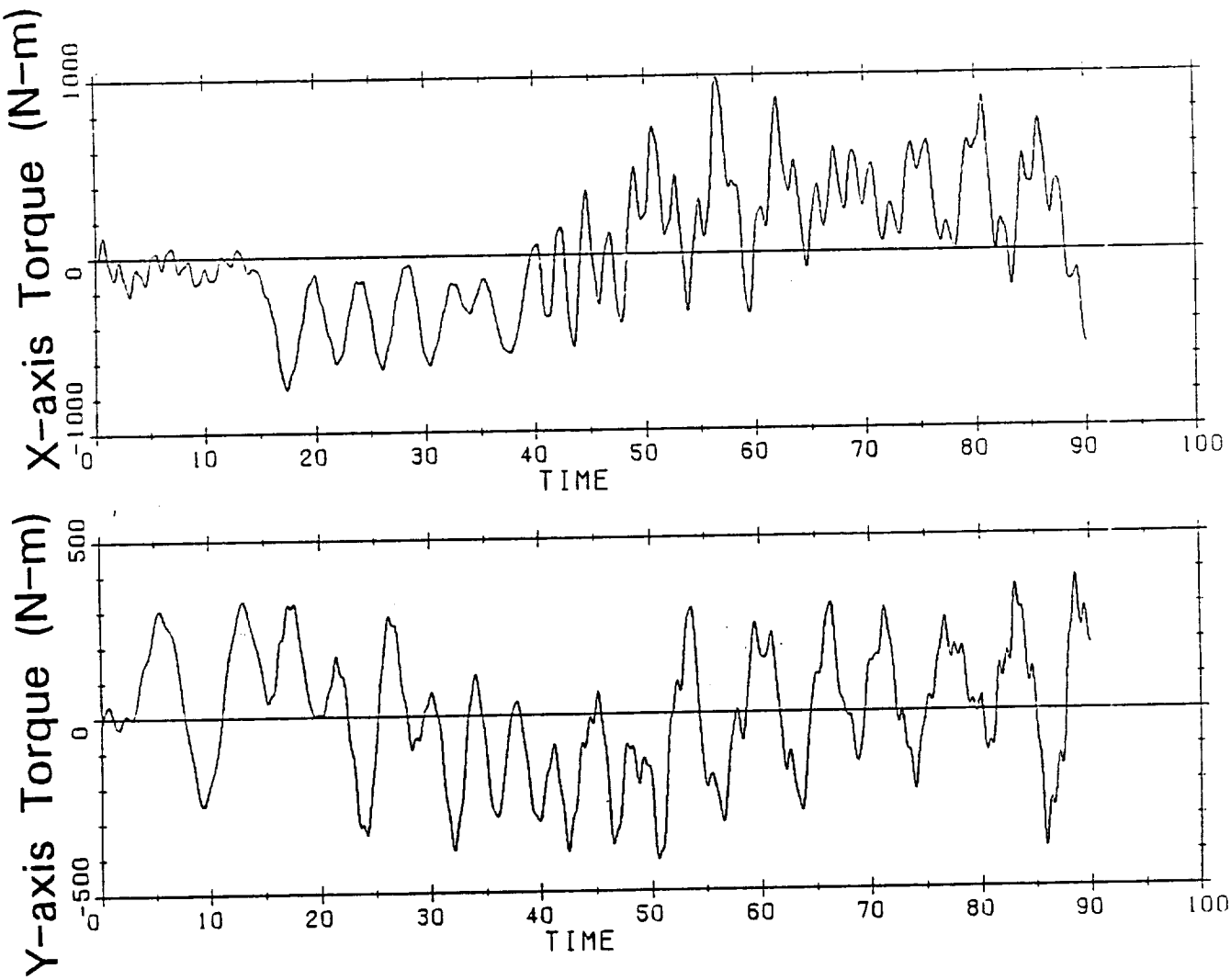

Figure 9-7. Run 13 - mast base loads.

Case 17 is similar to case 5 except for the mast damping. The mast base load is considerably smaller for case 17 than for case 5. This is not caused directly by the difference in damping. Basically, it is a "chaotic" effect. In both cases 5 and 17, the disturbance acceleration estimates (Figure 9-2) are close to zero at the time of the third major roll firing. But they were of opposite signs in the two cases. The sign difference caused a large change in the S11 switch line location and thus a large change in the duration of the firing. (Compare the phase planes of Figure 9-8 and 9-2.) In case 5, there was considerable reinforcement of the bending, which did not occur in case 17. These cases illustrate the observation that the resulting firing histories and loads can differ greatly for small differences in initial conditions or other inputs.

These runs did not investigate FCS instability directly. However, instability is unlikely. For instability to occur the flex oscillations must build up to a fairly large magnitude. Generally, many firings timed to reinforce the oscillations are needed. That is unlikely to occur given the chaotic firings observed in these runs. Although the active mast dampers had little effect on the runs performed, increased damping would reduce the probability of instability further.

Generally the effects seen in these runs were due to slew attitude disturbances and the resulting RCS jet firings and not due to flexibility. The VRCS jets did not cause much flexure and there was minimal flexure feedback to the FCS.

There were undesirable effects due to having an active FCS during the gimbal slewing. The FCS wastes fuel as it tries to correct for the unmodelled disturbance caused by the antenna motion. The RCS firings cause unnecessary stress on the systems, including the loads on the structure and on the gimbals and servo motors. The antenna slew angle is affected by the jet torques. Since the servo will probably be operated in an open loop saturated mode during a slew, the jet firings make it difficult to obtain a desired slew angle. Therefore, it is recommended that the FCS be in free drift mode during antenna slewing. At the end of a slew, the Orbiter will have changed attitude slightly. If desired, the attitude could be adjusted with RCS firings with the gimbals locked.

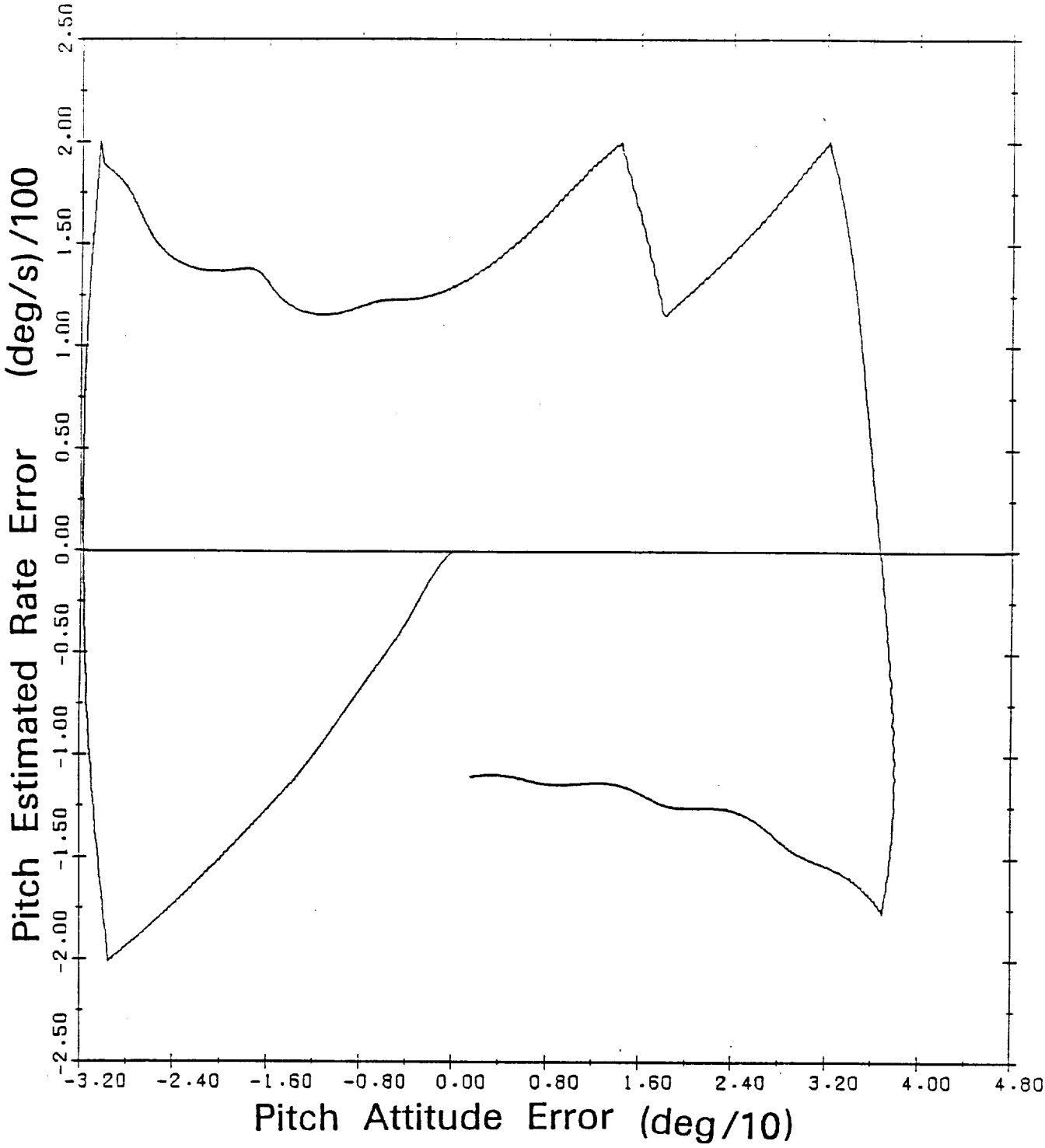

Figure 9-8. Run 17 - pitch phase plane.

SECTION 10
GIMBAL SERVO/STRUCTURAL DYNAMICS INTERACTION

One of the original goals of the COFS-II servo study was to determine the extent and impact of dynamic interaction between the structural dynamics and the servo and then the interaction between the servo and the orbiter flight control system. A second goal was to quantify the role played by the servos in damping structural vibrations.

It quickly became obvious, however, that the hardware parameters, specifically the ±33.9 Newton meters (±25 ft lbs) torque saturation and ±4 degree per second slew saturation of the Sperry Advanced Gimbal System (AGS), were not compatible with the high moment of inertia of the COFS-II antenna. Any attempt to achieve a servo closed loop bandwidth of the desired 10 rad/sec resulted in a system which saturated at the extremely small error signal of 0.0005 degrees. Thus, a conventional servo design would yield a highly oscillatory system. If the constraint to use the Sperry AGS is maintained, the proper design would entail the incorporation of a nonlinear, minimum transfer-time technique which involves dividing a desired angular repositioning distance in half, and accelerating (not slewing) at saturated torque for that half angle, then decelerating at negative saturated torque for the remaining half angle. Essentially, this is an open loop operation. Following this phase, the positional servo loop is automatically closed and any residual, small error signal can be stably eliminated since the load angular velocity should be close to zero.

Thus, investigating the dynamic interaction of this small angle, small angular velocity servo system with the COFS-II structural dynamics is a necessary precursor to quantifying the impact of the servos on structural vibrational damping.

An excellent method to describe the contribution to servo loop dynamics by the structural dynamics is to define a mechanical admittance function of gimbal servo motor angular velocity per unit motor torque, $\frac{\Omega_M}{T_M}(s)$, as portrayed in Fig. 10-1 (The solid lines are asymptotes of the function). With such a system, trying to close the servo loop with stability in the "high frequency" region of structural poles and zeros requires careful network compensation as portrayed in Fig. 10-2. Specifically, note the need for network compensation to achieve adequate phase margin, Φ_M, every time the amplitude spectrum has a downward zero db crossing.

For the COFS-II system, this mechanical admittance function was derived analytically from a multiple body idealization of the mechanical system and then verified by obtaining the mechanical admittance function amplitude and phase spectra via NASTRAN using a finite element model of the mechanical system truncated beyond 25 modes.

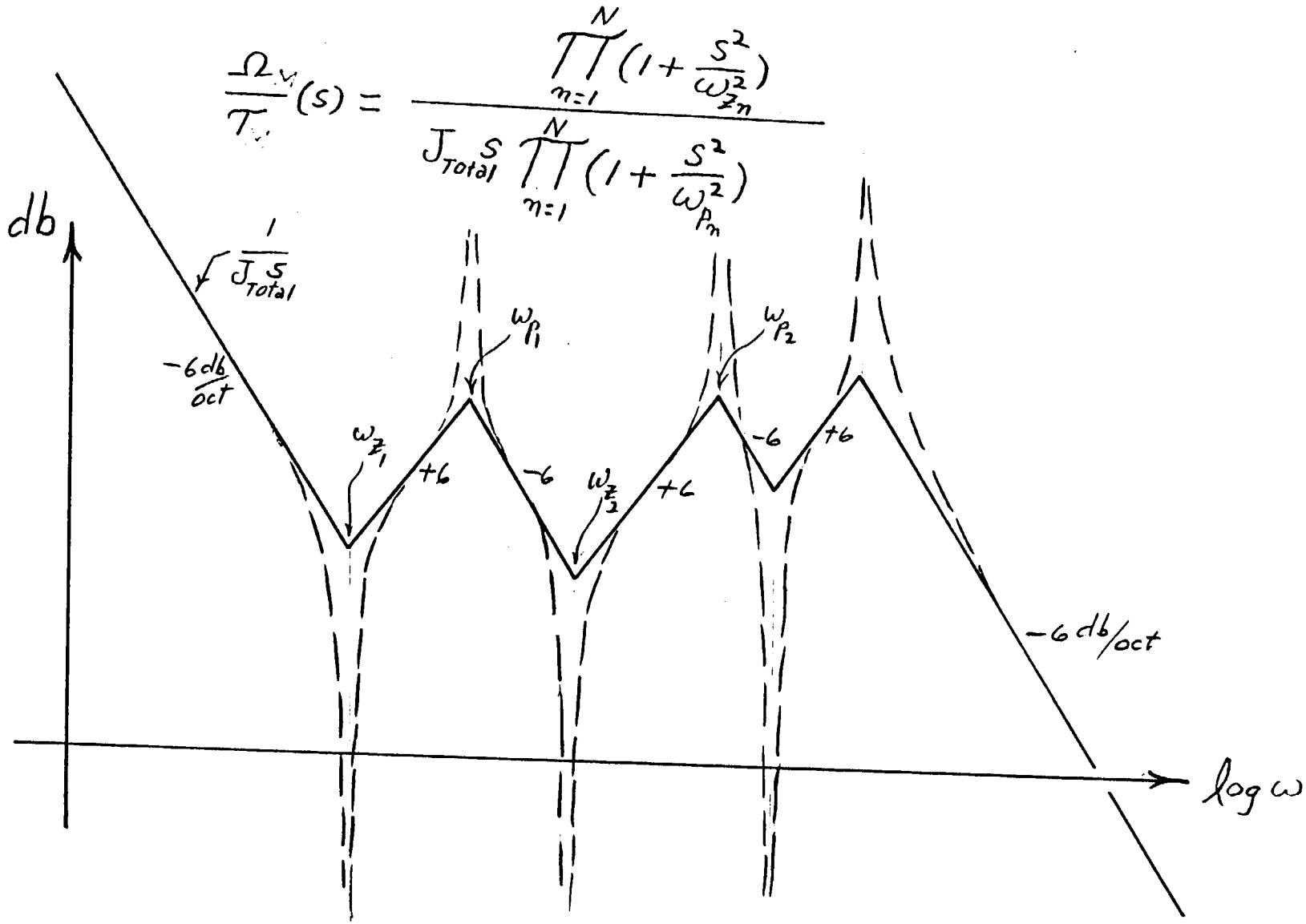

Figure 10-1. Mechanical admittance function at gimbal servo.

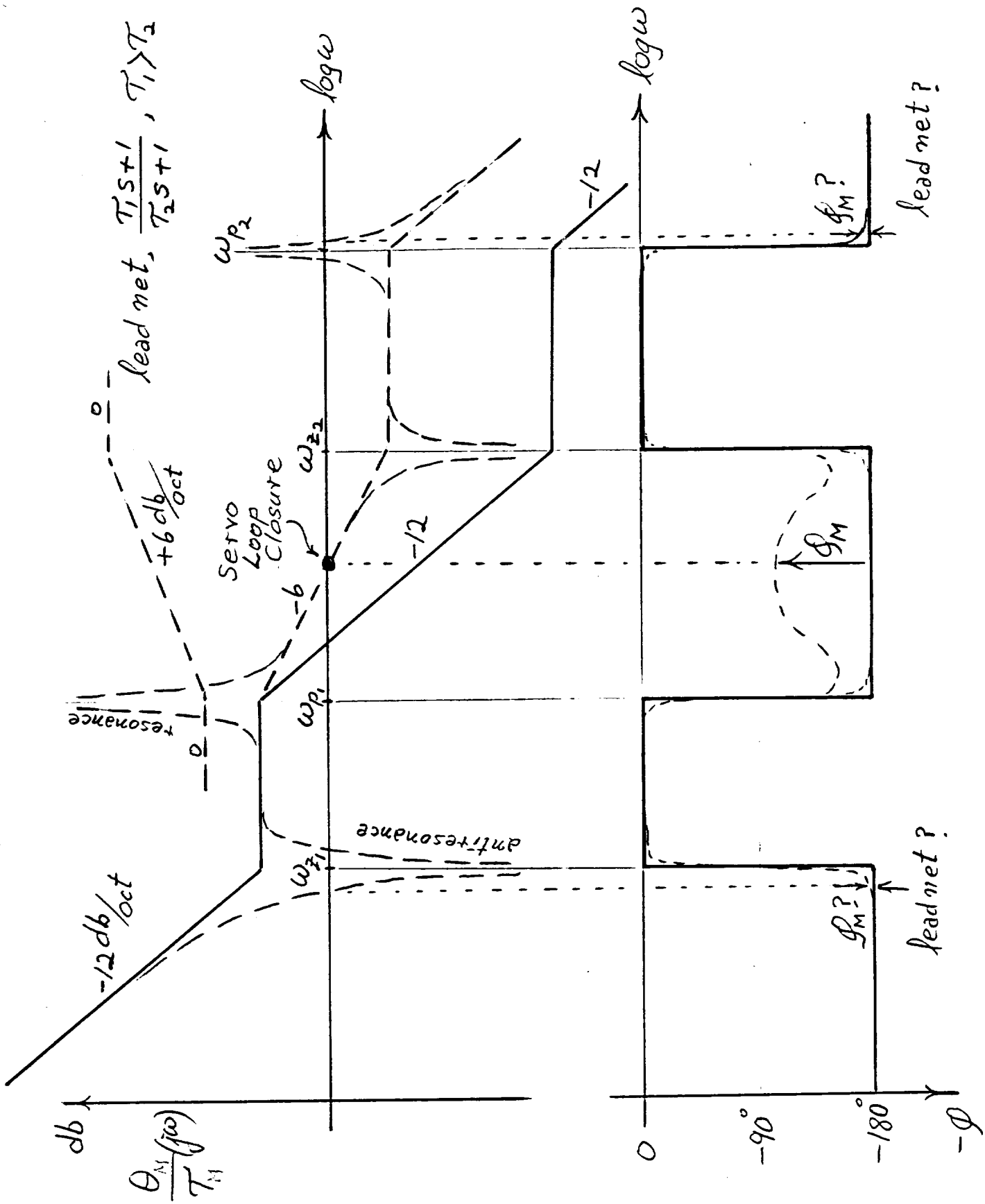

Figure 10-2. High frequency servo loop closure.

Analytically, the derived (see Appendix C) pitch gimbal angle per unit torque was:

$$\frac{\theta_M}{T_M}(s) = \frac{\Omega_M}{s\,T_M}(s) = \frac{1.617 \times 10^{-2}\,(s^2+\omega_{Z_1}^2)\,(s^2+\omega_{Z_2}^2)\,(s^2+\omega_{Z_3}^2)}{s^2\,(s^2+\omega_{P_1}^2)\,(s^2+\omega_{P_2}^2)\,(s^2+\omega_{P_3}^2)}$$

where $\omega_{Z_1} = 0.80$, $\omega_{Z_2} = 1.55$, $\omega_{Z_3} = 11$ rad/s

$\omega_{P_1} = 0.82$, $\omega_{P_2} = 10.6$, $\omega_{P_3} = 36$

Note the near cancellation of two pole-zero pairs, ω_{Z_1} with ω_{P_1} and ω_{P_2} with ω_{Z_3}

The asymptotes of the amplitude spectrum of this function may be depicted as follows:

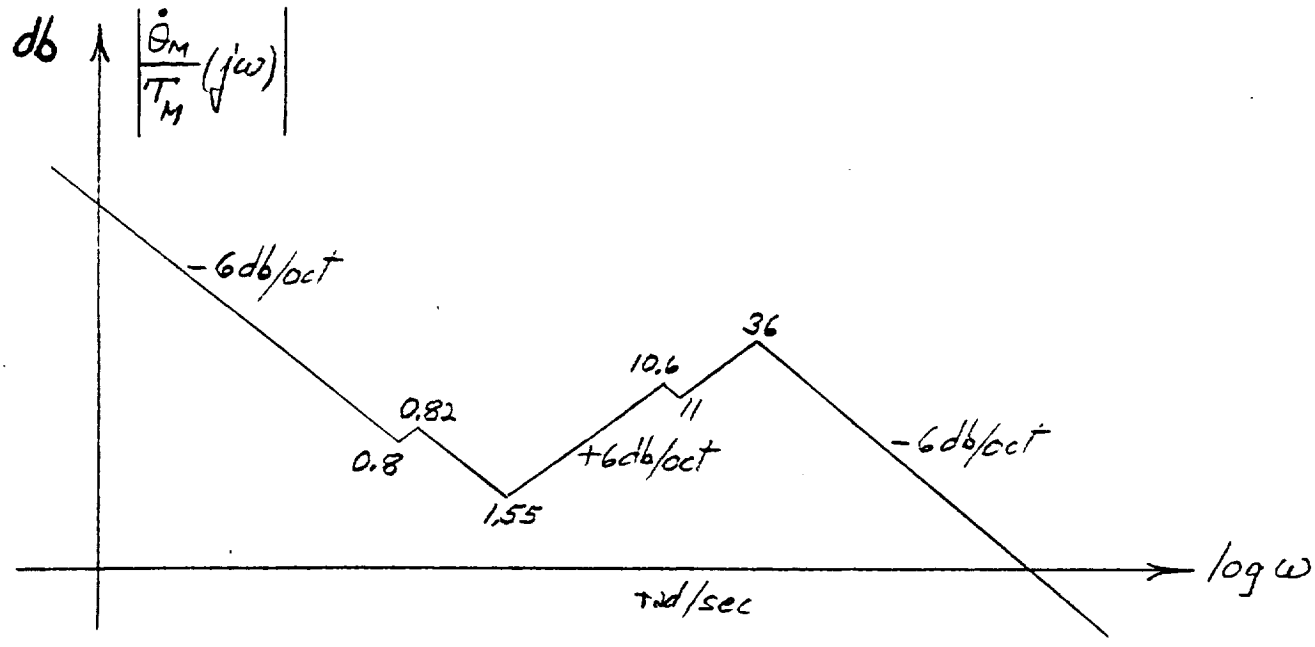

Any servo loop closure above the 1.55 rad/sec "zero," even with network compensation, would be futile with the existing hardware since the 25 ft lbs torque saturation coupled with the large moment of inertia of the COFS-II antenna produces a servo which saturates at minuscule fractions of a degree of command angle. A 10 rad/sec bandwidth servo would saturate and become bang-bang at any command over 0.0005 degrees. Thus, for the present purposes of examining servo contribution to structural damping, loop closure was achieved on the low frequency asymptote of the mechanical admittance function at 1 rad/sec.

Figure 10-3 assumes a basic quadratic portrayal for the two gimbal servo, where the units of the constants are:

K_1	Transducer constant, volts per radian
A	Amplifier gain, amps per volt
K_t	Torque motor constant, ft lbs per amp
T_M	Torque output of torque motor, ft lbs
T_L	Load torque of structure on torque motor
J_M	Motor moment of inertia, ft lb sec^2
J_1	Payload platform moment of inertia
k_t	Tachometer constant, radians per rad/sec
Θ_C	Command angle, radians
Θ_M	Motor angle, radians

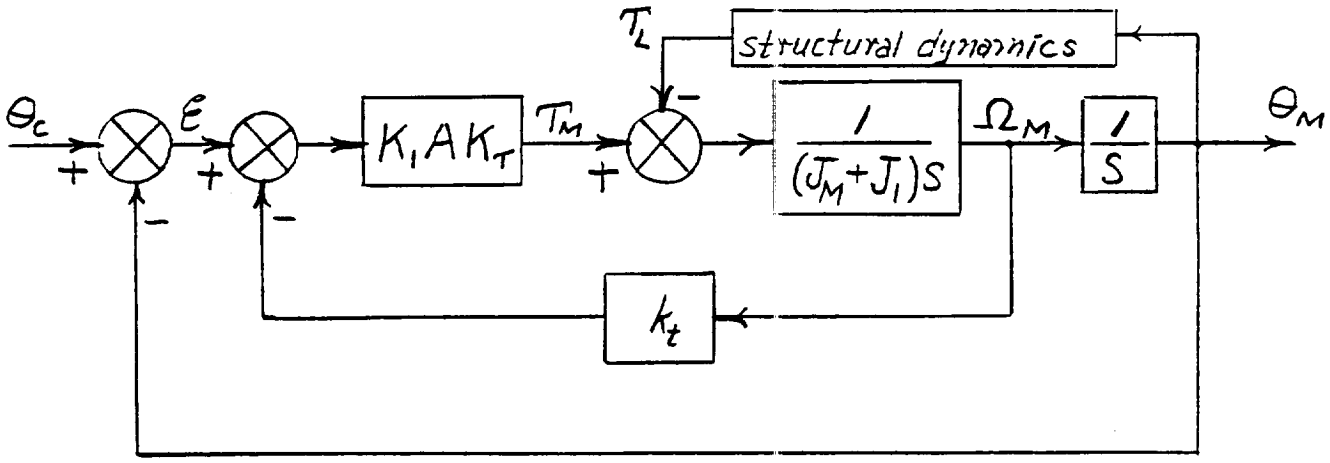

Figure 10-3. Basic quadratic gimbal servo.

Figure 10-4 is the same servo loop of Figure 10-3 expressed in the canonical form of the closed loop parameters ω_n (servo bandwidth), and ζ (dimensionless damping ratio). Note that J_L represents the entire rigidized-structure moment of inertia, whereas J_1 is only the payload platform moment of inertia.

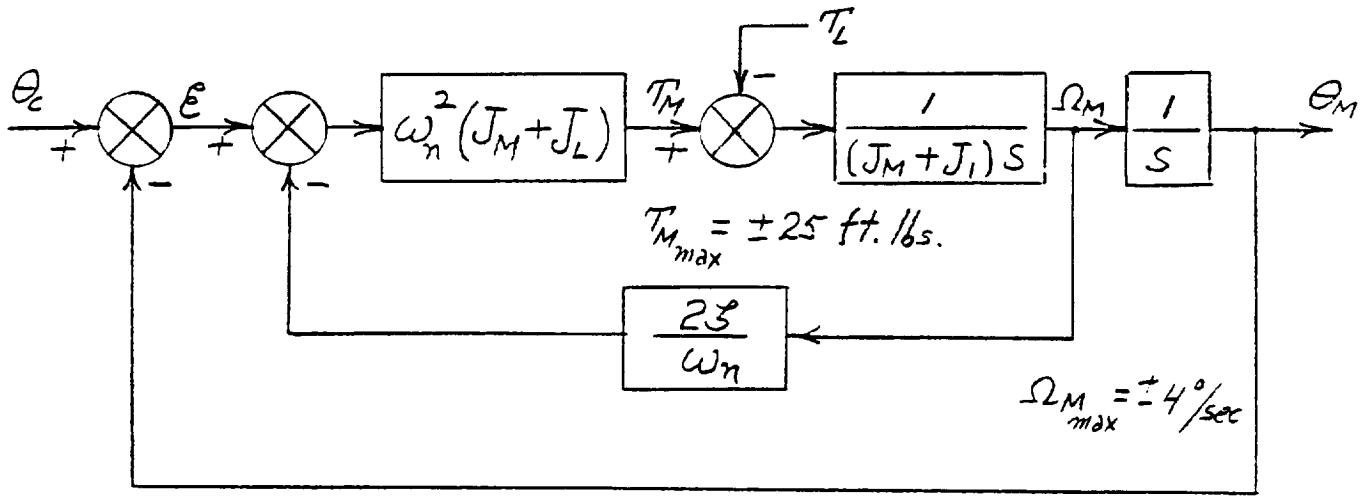

Figure 10-4. Quadratic gimbal servo in canonical form.

The format of Figure 10-4 assumes servo loop gains consistent with stability at loop closure low-band on the structural spectrum. Thus, from Figure 10-4:

$$T_M = \omega_n^2 (J_M + J_L) (\theta_c - \theta_M - \frac{2\zeta}{\omega_n} \dot{\theta}_M)$$

$$\text{where } T_{M_{max}} = \pm 25 \text{ ft lbs and } \dot{\theta}_{M_{max}} = \pm 4 \text{ deg/s}$$

Note that gimbal motor torque is impressed outward upon the antenna structure, and equal and oppositely downward upon the mast structure. (That is, the servo base is compliant, not rigid.)

A series of computer runs were submitted to investigate system stability and the ability of the servo to dampen structural vibrations. Of course, the 25 ft lbs torque saturation, when faced with the massiveness of the COFS-II antenna, did not allow much in the way of fast servo response. For a given error signal, torque saturation varies with the square of the servo bandwidth and proportional to the structural moment of inertia. Thus, for the given ±25 ft lb torque saturation, a 10 rad/sec servo coupled with the COFS-II antenna reaches saturation at

only 0.0005 degrees of error signal! A bandwidth of 1 rad/sec is 100 times more forgiving and saturates at 0.05 degrees. Notwithstanding these low saturation levels, the existing hardware still allows examination of the ability of the gimbal servo to dampen structural vibrations.

The following four computer simulation runs quantitatively demonstrate the effectiveness of the servo to improve structural damping.

Run 1

With the mast initially undeflected, the servo commanded angle (with respect to the top of the mast) was set to zero, the elevation gimbal of the antenna was given an initial deflection of 0.03 degrees and released at t=o+. The system constants were:

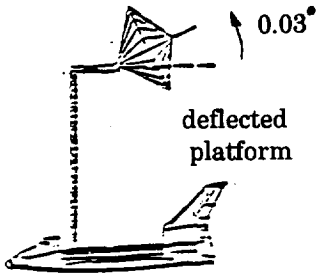

Servo B.W. = 1 rad/sec
Servo ζ = 0.5
Structural ζ = 0.005
Servo damping via tachometer

Results: The antenna platform vibration was attenuated consistent with a dimensionless damping ratio, ζ of 0.026

Run 2

To verify that the servo actually contributed to the antenna vibrational attenuation, the above run was repeated, but with the servo locked. The initial condition was deflection of the antenna base spring by 0.03 degrees and then release at t=o+.

Results: The measured effective ζ was 0.005, simply the structural intrinsic damping, thus demonstrating the damping effect of the servo when operating in Run 1.

Run 3

Next, to investigate the servo contribution to damping of mast vibration, the mast was now deflected and released. However, under these conditions the antenna elevation gimbal sees no initial deflection with respect to the top of the mast and hence there is no initial servo error signal as a result of the deflection. To remedy this situation, we must realize that we are concerned with stabilizing the antenna line of sight with respect to inertial space and not with respect to the top of the mast. Thus, we shall assume the employment of gyroscopic measurements to define the gimbal angles and commands with respect to inertial space. Consequently, the elevation gimbal command at t=o+ with respect to inertial space was set to

zero. Also, since the mast was deflected in its first mode shape with a tip deflection of 0.03 degrees, the elevation gimbal deflection (or more exactly, the elevation platform angle) with respect to inertial space at t=o+ was 0.03 degrees.

As seen in the accompanying configuration sketch, the top of the mast is initially deflected 0.03 degrees in elevation with the antenna gimbal elevation angle initially maintaining the antenna column orthogonal to the top of the mast. The deflected mast is then released at t=o+. The system constants were once again:

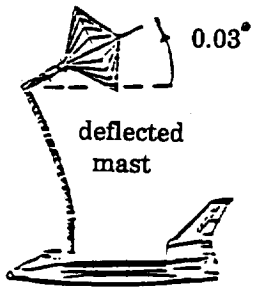

Servo B.W. = 1 rad/sec
Servo ζ = 0.5
Structural ζ = 0.005
Servo damping via tachometer

Results: Since we are interested in how well we are maintaining the antenna line of sight with respect to inertial space, we monitored the antenna platform angle with respect to inertial space and measured the vibrational atennuation. The effective ζ was only 0.008. Similarly, observations of the vibration of the tip of the mast showed attenuation consistent with a ζ of 0.008. Thus, the active servo was only somewhat damping the entire structural system which has intrinsic damping of ζ = 0.005. By making a proper change in servo design, much better results may be obtained as seen in the next run.

Run 4

This run is identical to Run 3 above except that the servo damping signal was obtained from a rate gyro instead of a tachometer. That is, servo viscosity was referenced to inertial space instead of the top of the mast. Thus:

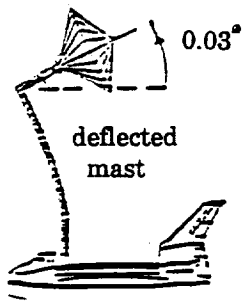

$\theta_c^{(i)}(o+) = 0$

$\theta_M^{(i)}(o+) = 0.03^\circ$ via deflection of the mast tip by 0.03°

$\dot{\theta}_M$ is with respect to inertial space

Servo BW = 1 rad/sec

Servo ζ = 0.5

Structural ζ = 0.005

Servo damping via rate gyro

Results: Monitoring the vibrating antenna platform angle with respect to inertial space exhibited an attenuation of vibration consistent with an effective ζ of 0.012!

Of significance here is the greatly increased structural damping achieved by the servo when its own damping signal was obtained from a rate gyro rather than a tachometer. This is understandable when one realizes that the tachometer signal can be zero if the servo gimbal angle remains fixed with respect to the top of the mast even with the mast vibrating.

SECTION 11
CONCLUSIONS

The COFS-II system has been assessed from the standpoint of dynamic interaction with the Shuttle Orbiter flight control system. Issues of FCS stability in the presence of the flexible mast/antenna system as well as internal loads and general FCS performance have been investigated with analysis and simulation. Two simulations were used. One assumes a fixed configuration (locked gimbals) of the COFS-II system; the other allows gimbal motion. Because of the small torque capability, the linear range of the servo is quite small. A study was made of the servo characteristics over this linear range.

A review was made of Shuttle requirements that would influence the amount of time the Orbiter could be in a free drift mode. Experimenters desire periods of free drift to minimize disturbances on the COFS-II system. NASA STS documentation, flight experience, other payload simulation experience, and simple analysis indicate that with no payload constraints given, the Orbiter may be in free drift for at least six hours under nominal conditions. Thermal, communications, and IMU alignment requirements were considered. During free drift, the attitude will vary depending on the effects of gravity gradient and aerodynamic torques and other disturbances.

Three fixed configurations were assessed for FCS stability, FCS performance, loads due to RCS firings and flexure, and the effect of adding the active mast damping system. It was found that FCS instability is possible. Several structural modes are potentially unstable. Typically, instability requires a large periodic disturbance for initiation, unless tight deadbands and rate limits are used. Experiment dampers somewhat reduce that probability of instability. FCS performance is affected by payload flexibility. However, for stable conditions, the effect is not large. Maneuvers should be simulated in advance of flight to minimize poor performance and reduce the probability of initiating an instability. Maneuver rates should be kept as small as practicable. Mast base loads appear to be acceptable for typical attitude maneuvers and attitude holds. Simulations also output mast tip loads and antenna base loads. Since load limits for those locations were not available they were not evaluated. Unstable oscillations can lead to large loads.

Simulations of antenna slew with the FCS active were performed. Because of the limited torque capability of the gimbal servo, the servo will probably be saturated during a slew. For most slew angles, the peak slew rate of 4 deg/s cannot be reached. Therefore, for slew simulations, the servo behavior was approximated by an open loop torque command at the gimbal location. It is recommended that slewing occur with the FCS inactive. An attitude hold during a slew wastes fuel, and the jet torques overcome the servo motor. Thus an open loop commanded slew can result in various slew angles, depending on the jet firing influence. The mast base loads were acceptable with active FCS for all the slew simulations performed. The simulations were limited to single axis, open loop, servo torque-saturated slews.

The servo interaction study was limited because of the small linear operating region of the servo. A closed loop bandwidth of 10 rad/s results in a system which saturates at only 0.0005 deg. Consequently, a conventional servo design is highly oscillatory. The impact of the servos on structural damping was investigated and it was found that reasonable damping could be obtained if the servos themselves were stabilized by rate gyros and if the servo was operating in its linear range.

Our study indicates possible undesirable interaction between the Orbiter FCS and the flexible, articulated COFS-II mast/antenna system, even when restricted to VRCS jets. Undesirable conditions can probably be avoided with careful planning, pre-flight analysis and simulations, and flight operational constraints.

Appendix A

Selection of Spring Constants for the Three Rigid Body Model of the COFS-II Hoop Column Antenna

DI-87-09

TO: Stan Fay

FROM: Steve Gates

DATE: 20 July 1987

SUBJECT: Selection of Spring Constants for the Three Rigid Body Model of the COFS-II Hoop-Column Antenna

This memorandum presents the analysis performed to determine the torsional spring constants for the articulated three rigid body model of the COFS-II Hoop-Column Antenna[1].

The mechanical idealization of the COFS-II Hoop-Column Antenna, described in Reference 1, is shown in Figure 1. The model consists of three distinct axisymmetric rigid bodies, labeled the column, feed, and hoop. These bodies are interconnected at pivot points by discrete massless torsional springs.

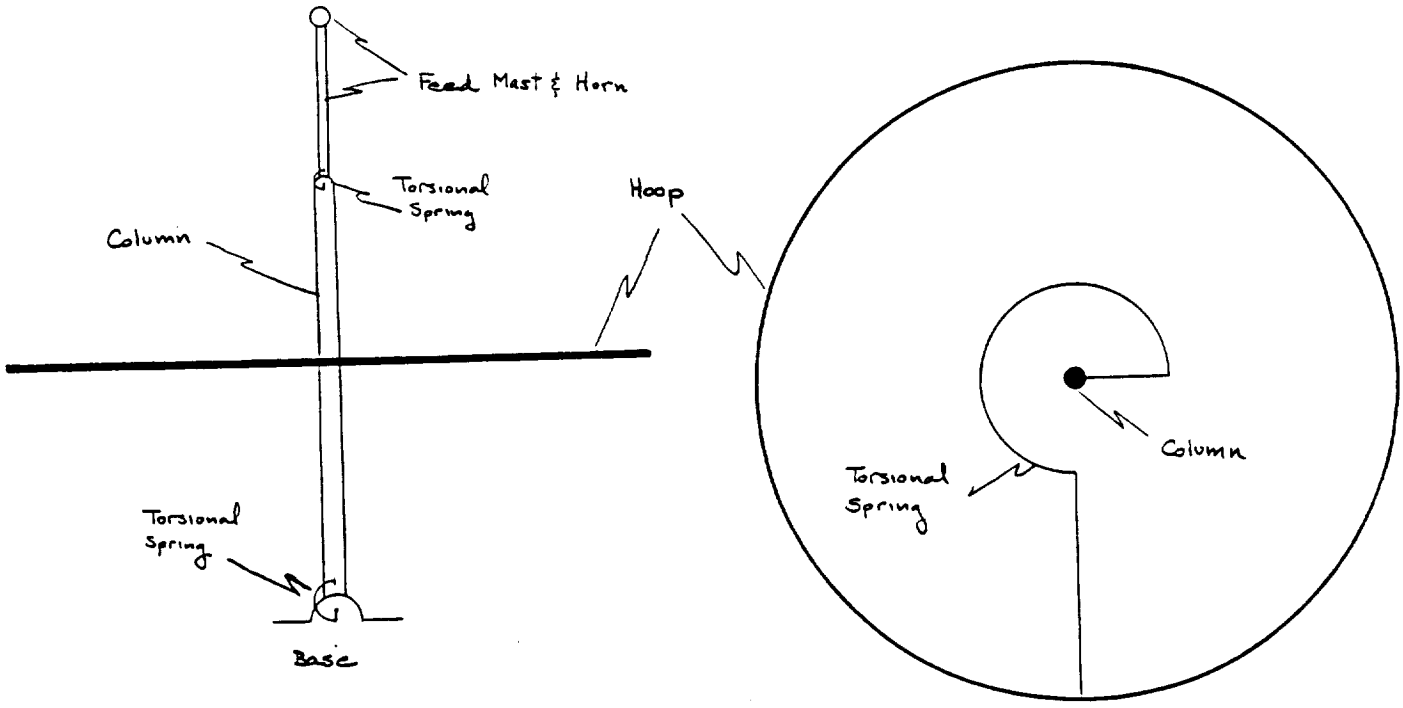

Figure 1. Idealized Hoop-Column Antenna

Refering to Figure 1, the column is connected to the base through a frictionless pivot which permits rotation about two mutually orthogonal axes oriented perpendicular to the column's nominal longitudinal axis. These two rotational degrees of freedom are resisted by identical torsional springs. The hoop is constrained to move in such a way that it has a single degree of freedom relative to the column. Specifically, the hoop lies in a plane perpendicular to the column's longitudinal axis at a fixed distance above the base. When the column deflects it is assumed that the hoop follows along such that there is no relative displacement between the two bodies except for a simple rotation of the hoop in its plane about the column axis. This angular displacement is resisted by a torsional spring acting between the hoop and column. The rigid feed is appended to the column top through another frictionless pivot. This joint allows rotations of the feed relative to the column about two mutually orthogonal axes perpendicular to the column's longitudinal axis. These two relative angular deflections are counteracted by identical torsional stiffnesses.

Equations of Motion for Small Vibrations

Nomenclature

We establish an inertial reference frame, with axes X Y Z and unit vectors $\vec{I}$ $\vec{J}$ $\vec{K}$, fixed to the base. For each of the bodies, we define a body fixed reference frame with origin at the respective mass center. The subscripts "c", "f", and "h" will be used to distinguish the coordinate frame axes, (x, y, z), and unit vectors, ($\vec{i}$, $\vec{j}$, $\vec{k}$), associated with the column, feed, and hoop respectively. Figure 2 illustrates the respective frames of reference. Note that for each body the respective x-axis corresponds to the axis of inertial symmetry.

Figure 3 displays the essential geometric parameters:

a - distance from column base to column tip
b - distance from feed base to feed centroid
c - distance from column base to column centroid
h - distance from column base to hoop plane

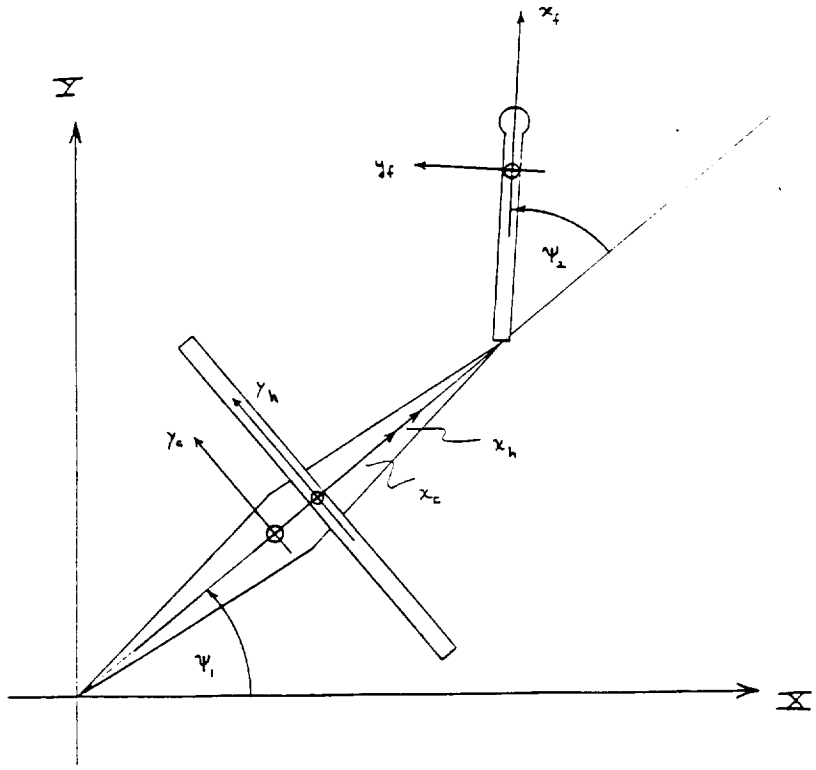

Figure 2. System Reference Frames

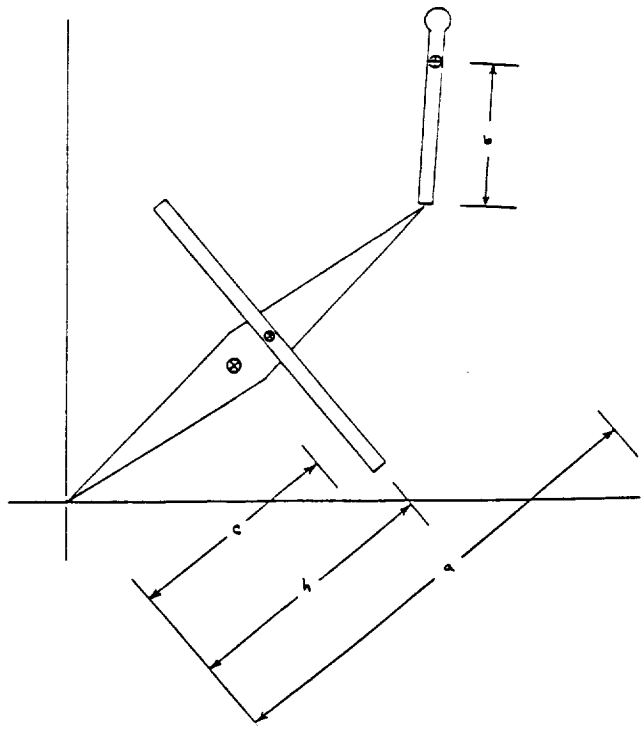

Figure 3. Geometric Parameters

The respective inertial parameters for the system are:

m_c, m_f, m_h - mass of column, feed, and hoop

$$[I^c] = \begin{bmatrix} I_s^c & 0 & 0 \\ 0 & I_t^c & 0 \\ 0 & 0 & I_t^c \end{bmatrix}$$

- centroidal inertia matrix of the column w.r.t. the column frame

$$[I^f] = \begin{bmatrix} I_s^f & & \\ & I_t^f & \\ & & I_t^f \end{bmatrix}$$

- centroidal inertia matrix of the feed w.r.t. the feed frame

$$[I^h] = \begin{bmatrix} I_s^h & & \\ & I_t^h & \\ & & I_t^h \end{bmatrix}$$

- centroidal inertia matrix of the hoop w.r.t. the hoop frame

We define also the torsional spring constants:

k_1 - stiffness of column/base spring

k_2 - stiffness of feed/column spring

k_3 - stiffness of hoop/column spring

Degrees of Freedom

Let the angular deflection of the column frame relative to the inertial frame be measured by the angles ϕ_1, and ψ_1, which correspond to a "2-3" Euler rotation sequence shown below:

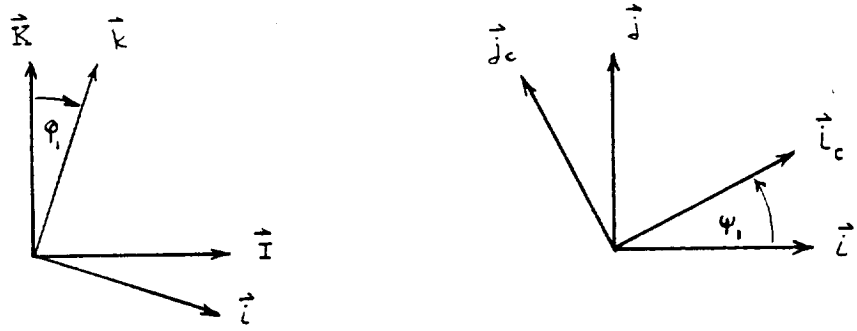

Since we are ultimately interested in the small oscillations of the system about the nominal equilibrium configuration, we shall restrict our attention to situations for which ϕ_1, and ψ_1, are "small" angles. Under these conditions, the relations between the column frame and inertial frame can be expressed as

$$\begin{Bmatrix} \vec{i}_c \\ \vec{j}_c \\ \vec{k}_c \end{Bmatrix} = \begin{bmatrix} 1 & \psi_1 & -\phi_1 \\ -\psi_1 & 1 & 0 \\ \phi_1 & 0 & 1 \end{bmatrix} \begin{Bmatrix} \vec{I} \\ \vec{J} \\ \vec{K} \end{Bmatrix}$$

In a completely analogous fashion we define the orientation of the feed relative to the column by the angles ϕ_2, ψ_2, and consider these angles to be small. The relations between the feed frame and column frame vector bases is then given by

$$\begin{Bmatrix} \vec{i}_f \\ \vec{j}_f \\ \vec{k}_f \end{Bmatrix} = \begin{bmatrix} 1 & \psi_2 & -\phi_2 \\ -\psi_2 & 1 & 0 \\ \phi_2 & 0 & 1 \end{bmatrix} \begin{Bmatrix} \vec{i}_c \\ \vec{j}_c \\ \vec{k}_c \end{Bmatrix}$$

The planar rotation of the hoop relative to the column will be measured by the angle γ, which will be treated as a small quantity. The hoop and column frames are related by

$$\begin{Bmatrix} \vec{i}_h \\ \vec{j}_h \\ \vec{k}_h \end{Bmatrix} = \begin{bmatrix} 1 & 0 & 0 \\ 0 & 1 & \gamma \\ 0 & -\gamma & 1 \end{bmatrix} \begin{Bmatrix} \vec{i}_c \\ \vec{j}_c \\ \vec{k}_c \end{Bmatrix}$$

The five degrees of freedom of the antenna model described above are capable of portraying "bending" deflections of the column and feed in two orthogonal planes, as well as simple torsional rotation of the hoop relative to the column.

Lagrange's Equations

We will obtain the free vibration motion equations for the system from Lagrange's equations. To this end we record the centroidal velocities and angular velocities of the respective components:

$\bar{v}_i$ - inertial velocity of the centroid of body i.

$\bar{\omega}_i$ - angular velocity of body i relative to the inertial frame.

$$\bar{\omega}_c = \dot{\phi}_1 \vec{j}_c + \dot{\psi}_1 \vec{k}_c$$

$$\bar{v}_c = c\dot{\psi}_1 \vec{j}_c - c\dot{\phi}_1 \vec{k}_c$$

$$\bar{\omega}_f = (\dot{\phi}_1 + \dot{\phi}_2)\vec{j}_f + (\dot{\psi}_1 + \dot{\psi}_2)\vec{k}_f$$

$$\bar{v}_f = [(a+b)\dot{\psi}_1 + b\dot{\psi}_2]\vec{j}_f - [(a+b)\dot{\phi}_1 + b\dot{\phi}_2]\vec{k}_f$$

$$\bar{\omega}_h = \dot{\gamma}\,\vec{i}_h + \dot{\phi}_1\,\vec{j}_h + \dot{\psi}_1\,\vec{k}_h$$

$$\bar{v}_h = h\,\dot{\psi}_1\,\vec{j}_h - h\,\dot{\phi}_1\,\vec{k}_h$$

Note that the expressions for the angular velocities reflect the added approximation of ignoring terms involving products of: (angular deflections) x (angular rates). This approximation, which together with the small angle assumption is in keeping with the usual "small motions" analysis, will yield the desired linear motion equations.

The respective component kinetic energy expressions,

$$T_c = \frac{1}{2}\left(m_c c^2 + I_t^c\right)\left(\dot{\phi}_1^2 + \dot{\psi}_1^2\right)$$

$$T_f = \frac{1}{2}\left[m_f(a+b)^2 + I_t^f\right]\left(\dot{\phi}_1^2 + \dot{\psi}_1^2\right) + \frac{1}{2}\left(m_f\, b^2 + I_t^f\right)\left(\dot{\phi}_2^2 + \dot{\psi}_2^2\right) + \left[m_f(a+b)\, b + I_t^f\right]\left(\dot{\phi}_1\dot{\phi}_2 + \dot{\psi}_1\dot{\psi}_2\right)$$

$$T_h = \frac{1}{2}\left(m_h\, h^2 + I_t^h\right)\left(\dot{\phi}_1^2 + \dot{\psi}_1^2\right) + \frac{1}{2}\, I_s^h\, \dot{\gamma}^2$$

together, give the system kinetic energy

$$T = \frac{1}{2}\,\{\dot{q}\}^T\,[M]\,\{\dot{q}\}$$

where $\{q\}^T = \{\gamma,\ \phi_1,\ \phi_2,\ \psi_1,\ \psi_2\}$

$[M] = [M]^T$

$M_{11} = I_s^h$

$M_{12} = M_{13} = M_{14} = M_{15} = 0$

$M_{22} = M_{44} = \left[m_c c^2 + m_f(a+b)^2 + m_h h^2 + I_t^c + I_t^f + I_t^h\right]$

$$M_{23} = M_{45} = \left[m_f(a+b)b + I_t^f\right]$$

$$M_{24} = M_{25} = 0$$

$$M_{33} = M_{55} = \left(m_f\, b^2 + I_t^f\right)$$

$$M_{34} = M_{35} = 0$$

The potential energy for the system is given by

$$V = \frac{1}{2}\left\{ k_1\left(\phi_1^2 + \psi_1^2\right) + k_2\left(\phi_2^2 + \psi_2^2\right) + k_3\gamma^2 \right\}$$

or

$$V = \frac{1}{2}\{q\}^T [K]\{q\}$$

where

$$[K] = \text{diagonal}\left(k_3,\ k_1,\ k_2,\ k_1,\ k_2\right)$$

Using the expressions for the total system kinetic and potential energies given above, Lagranges equations in the independent generalized coordinates, γ, ϕ_1, ϕ_2, ψ_1, ψ_2, for the unforced system, provide the system motion equations for small vibrations about the equilibrium configuration

$$[M]\{\ddot{q}\} + [K]\{q\} = \{0\}$$

It is evident from the structure of the mass and stiffness matricies that the "bending" deflections in the XZ and XY planes, (measured by (ϕ_1, ϕ_2) and (ψ_1, ψ_2), respectively) are uncoupled from each other as well as from the torsional motion of the hoop. Also, since the mass and stiffness coefficients corresponding to each plane of bending are identical, it is necessary to consider only one of the planes for the analysis of the free vibration characteristics.

Hoop Torsion

Considering the hoop torsion equation, (the first in the above set), it follows immediately that the natural frequency, ω_τ, associated with this degree of freedom is given by

$$\omega_\tau^2 = \frac{k_3}{I_s^h}$$

The spring constant required to produce a given natural frequency is simply

$$k_3 = \omega_\tau^2 I_s^h \tag{1}$$

Bending Vibration

Considering the equations corresponding to the bending vibrations in the XZ plane;

$$\begin{bmatrix} M_{22} & M_{23} \\ M_{23} & M_{33} \end{bmatrix} \begin{Bmatrix} \ddot{\phi}_1 \\ \ddot{\phi}_2 \end{Bmatrix} + \begin{bmatrix} k_1 & 0 \\ 0 & k_2 \end{bmatrix} \begin{Bmatrix} \phi_1 \\ \phi_2 \end{Bmatrix} = \begin{Bmatrix} 0 \\ 0 \end{Bmatrix}$$

it follows that the characteristic equation for the natural frequencies, ω_i, (i=1, 2), is given by

$$\omega_i^4 \left(M_{22} M_{33} - M_{23}^2\right) - \left(k_1 M_{33} + k_2 M_{22}\right) \omega_i^2 + k_1 k_2 = 0$$

We wish to determine spring constants k_1 and k_2 which produce given natural frequencies ω_1, and ω_2. The natural frequencies satisfy

$$\omega_1^4 \left(M_{22} M_{33} - M_{23}^2\right) - \left(k_1 M_{33} + k_2 M_{22}\right) \omega_1^2 + k_1 k_2 = 0 \tag{2a}$$

$$\omega_2^2 \left(M_{22} M_{33} - M_{23}^2\right) - \left(k_1 M_{33} + k_2 M_{22}\right) \omega_2^2 + k_1 k_2 = 0 \tag{2b}$$

Subtracting (2b) from (2a) we obtain

$$k_2 = (\omega_1^2 + \omega_2^2)\left(M_{33} - \frac{M_{23}^2}{M_{22}}\right) - k_1 \frac{M_{33}}{M_{22}} \qquad (3)$$

Adding (2a) and (2b), and eliminating k_2 from the result, leads to a quadratic equation in k_1, which has roots

$$k_1 = \frac{-B \pm \sqrt{B^2 - 4AC}}{2A} \qquad (4)$$

where

$$A = M_{33}$$

$$B = -(\omega_1^2 + \omega_2^2)(M_{22} M_{33} - M_{23}^2)$$

$$C = \omega_1^2 \omega_2^2 M_{22} (M_{22} M_{33} - M_{23}^2)$$

The possibility thus exists for there to be two real positive values of k_1, (and a corresponding pair of k_2's) which yield the desired natural frequencies for a given system. This was indeed found to be the case for the parameters of the system treated below. The question of which pair of spring constants to use was resolved by considering the mode shapes associated with each pair.

Let, $\{\Phi_i\}$, denote the eigenvector associated with the eigenvalue ω_i^2, (i=1, 2). Then

$$\begin{bmatrix} k_1 - \omega_i^2 M_{22} & -\omega_i^2 M_{23} \\ -\omega_i^2 M_{23} & k_2 - \omega_i^2 M_{33} \end{bmatrix} \begin{Bmatrix} \Phi_{1i} \\ \Phi_{2i} \end{Bmatrix} = \begin{Bmatrix} 0 \\ 0 \end{Bmatrix}$$

from which we can determine the eigenvector to within a constant factor, α, as

$$\{\Phi_i\} = \alpha \begin{Bmatrix} 1 \\ \left[\dfrac{k_1 - \omega_i^2 M_{22}}{\omega_i^2 M_{23}}\right] \end{Bmatrix} \qquad (5)$$

Numerical Results

Given below are mass properties and geometric parameters for the three body antenna model which were derived from a high fidelity NASTRAN finite element model of the cantilevered Hoop-Column Antenna, provided by NASA LaRC.

$$m_c = 126.951 \text{ kg} \quad ; \quad [I^c] = \begin{bmatrix} 11.264 & & \\ & 1743.736 & \\ & & 1743.736 \end{bmatrix} \text{kg-m}^2$$

$$m_f = 117.234 \text{ kg} \quad ; \quad [I^f] = \begin{bmatrix} 0.853 & & \\ & 34.861 & \\ & & 34.861 \end{bmatrix} \text{kg-m}^2$$

$$m_h = 118.337 \text{ kg} \quad ; \quad [I^h] = \begin{bmatrix} 6631.537 & & \\ & 3315.772 & \\ & & 3315.772 \end{bmatrix} \text{kg-m}^2$$

$$a = 9.4715 \text{ m}$$
$$b = 3.388 \text{ m}$$
$$c = 4.1755 \text{ m}$$
$$h = 5.2982 \text{ m}$$

The first five natural frequencies and corresponding mode shapes of the finite element model are given in Table 1, and Figure 4 respectively.

Mode 1
Hoop Torsion

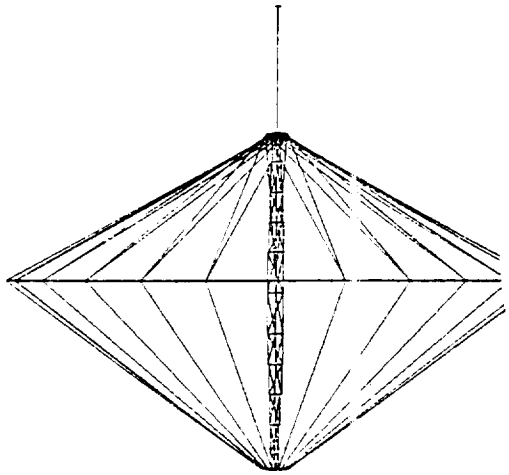

Modes 2 & 3
1st Planar Bending

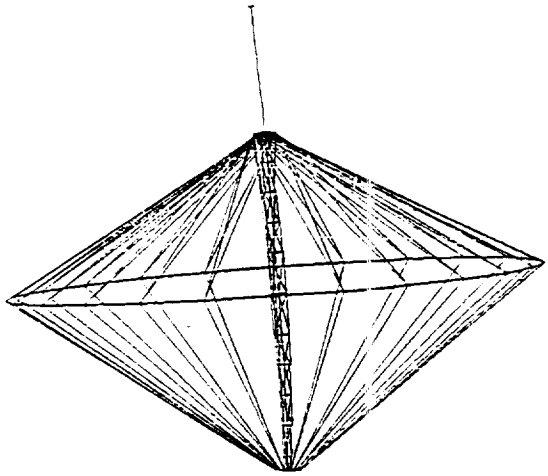

Modes 4 & 5
2nd Planar Bending

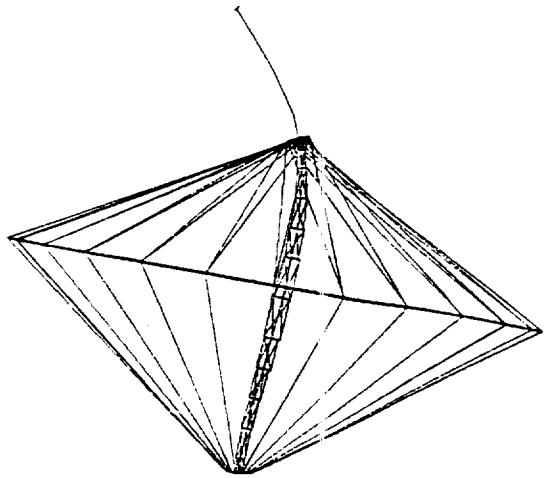

Figure 4. Finite Element Model Mode Shapes

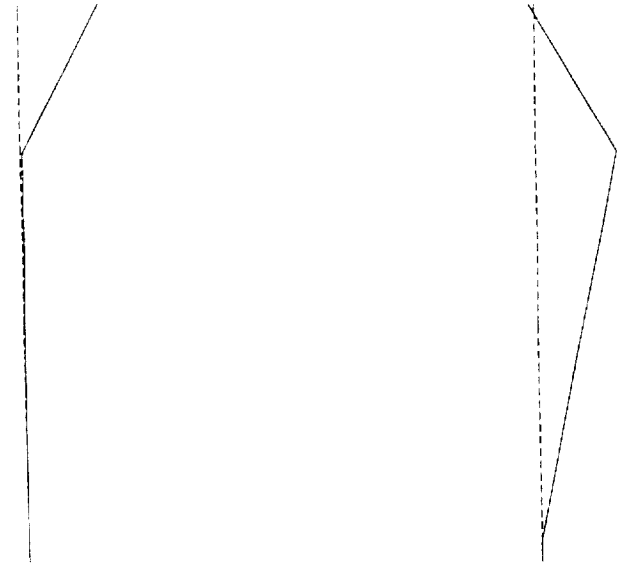

1st 2nd

Planar Bending Modes
Set I Spring Constants

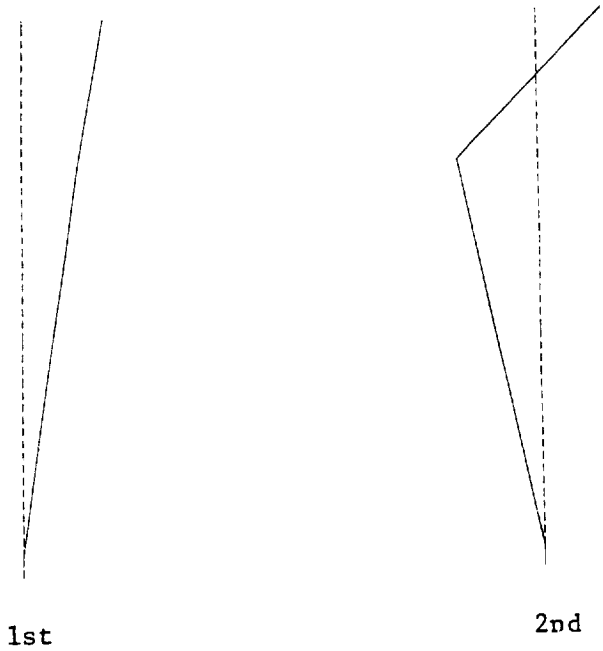

1st 2nd

Planar Bending Modes
Set II Spring Constants

Figure 5.

Natural Frequency (H_Z)	Mode Shape
$\omega_1 = 0.08$	Torsion of Hoop w.r.t. Column
$\omega_2 = \omega_3 = 0.24$	First Bending Mode (in 2 planes)
$\omega_4 = \omega_5 = 1.74$	Second Bending Mode (in 2 planes)

Table 1.

Using the system parameters and natural frequencies given above, Eqs. (1), (4) and (3) yield the spring constants

$$k_3 = 1698.141 \quad \text{N-m}$$

I) $k_1 = 1257562.126$ N-m
$k_2 = 3285.846$ N-m

II) $k_1 = 71442.17$ N-m
$k_2 = 57839.166$ N-m

Figure 5 illustrates the mode shapes, Eq. (5), corresponding to each pair of "bending" spring constants. It is clear from those results that the second pair yields mode shapes which are more in accord with those provided by the finite element model. Thus our choice of the second pair of constants for the three body model's bending spring stiffnesses.

Reference

1. Gates, S. and J. Storch, "Mechanical Idealization of the Orbiter/COFS II Structural System," CSDL Intralab Memorandum No. DI-87-02, Feb. 5, 1987.

Appendix B

Analysis of Free Vibration Characteristics of the COFS-II Mast Structure

INTRALAB MEMORANDUM

MEMO NO: DI-87-03

TO: S. Fay

FROM: J. Storch and S. Gates

DATE: April 7, 1987

SUBJECT: Analysis of Free Vibration Characteristics of the COFS-II Mast Structure

This memo presents analyses of the torsional and transverse free vibration characteristics of a hybrid continuum/discrete model of the COFS mast structure. These results are central to our treatment of this major structural component in the formulation of the complete COFS-II system motion equations.

The idealization of the COFS mast structure treated here is somewhat more general than that described originally in Reference 1. Specifically, it is assumed to be a uniform long slender inextensible continuous beam carrying a set of compact rigid bodies fixed along its span. Torsion and transverse bending are permitted independently. The discrete bodies may possess both mass and rotary inertia, however, their spatial dimensions are assumed negligible. The free vibration characteristics obtained from this model, provide the means for achieving a high fidelity representation of the mast at a minimum cost in the number of degrees of freedom.

The analyses which follow, respectively treat the torsional and transverse bending vibration problems. For each case, two independent analyses determining the natural frequencies and eigenfunctions are presented. One of the analyses is analytically exact, the other, analytically approximate. The former employs singularity functions, while the latter implements the assumed modes method. The exact results are intended for use in the ultimate system level dynamics model, where they will contribute to a simpler, more accurate and efficient set of final equations. The results of the approximate analyses serve to validate those

of the exact analyses. Each of the methods for each of the vibration problems have been implemented numerically in FORTRAN programs. Selected results from those programs are provided.

Torsional Vibrations of a Bar with Concentrated Inertias

Consider a uniform circular bar carrying a system of disks along its span as shown in Fig. 1. We wish to investigate the free torsional vibrations of the bar taking into account the moments of inertia of the disks about the bar's torsional axis.

We take the x axis as the bar's neutral axis and assume that the disks are of negligible thickness, with centroids located at the points $x=a_i$ $i=1, 2, \ldots, N$. The bar has length ℓ, torsional stiffness GJ, and mass polar moment of inertia per unit length I. The disks have moments of inertia I_i about the x axis. Let the sequence $a_1, a_2, \ldots, a_N$ be strictly increasing. For the purpose of the derivation we assume that $0<a_i<\ell$; however the results remain valid for a disk at the bar tip ($a_N=\ell$) by a simple continuity argument. The bar is clamped at x=0 and free at $x=\ell$.

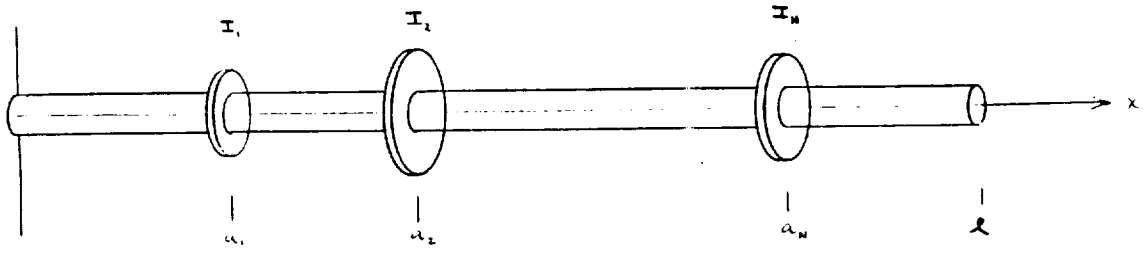

Figure 1. Uniform Circular Shaft Carrying Discrete Rigid Bodies

The partial differential equation governing the free torsional vibration of the bar can be written as:

$$GJ \frac{\partial^2 \theta}{\partial x^2} = \left[I + \sum_{i=1}^{N} I_i \delta(x-a_i) \right] \frac{\partial^2 \theta}{\partial t^2} \tag{1}$$

where $\theta(x,t)$ represents the angle of twist of a cross section at the point x and at time t. Note the use of the Dirac delta function to represent the concentrated mass polar moment of inertia of the disks. The boundary conditions take the form

$$\theta(0,\ t) = 0, \quad \frac{\partial \theta}{\partial x}(\ell,\ t) = 0 \tag{2}$$

Seeking solutions to Eq. (1) of the form $\theta = \Theta(x)\, e^{i\omega t}$ we obtain

$$\frac{d^2\Theta}{dx^2} + \frac{\beta^2}{\ell^2} \left[1 + \sum_{i=1}^{N} I_i^* \ell\, \delta(x-a_i) \right] \Theta(x) = 0 \tag{3}$$

where we have introduced the dimensionless parameters

$$\beta^2 = \frac{\ell^2 I}{GJ} \omega^2 \qquad \text{and} \qquad I_i^* = I_i / \ell I$$

The eigenfunctions $\Theta(x)$ are the nontrivial solutions to the differential equation, Eq. (3) satisfying the boundary conditions

$$\Theta(0) = 0, \qquad \frac{d\Theta}{dx}(\ell) = 0$$

Taking the Laplace transform of Eq. (3) and observing the first boundary condition we have

$$\mathcal{L}\{\Theta(x);\ s\} = \frac{\frac{d\Theta}{dx}(0)}{s^2+\beta^2/\ell^2} - \frac{\beta^2}{\ell} \sum_{i=1}^{N} \frac{I_i^*\, \Theta(a_i)\, e^{-a_i s}}{s^2+\beta^2/\ell^2}$$

Inverting, we obtain

$$\Theta(x) = C_1 \sin\frac{\beta x}{\ell} - \sum_{i=1}^{N} D_i \sin(\beta(x-a_i)/\ell)\, u(x-a_i) \tag{4}$$

where $C_1 = \frac{\ell}{\beta} \left.\frac{d\Theta}{dx}\right|_{x=0}$ and $D_i = \beta\, I_i^* \Theta(a_i) \quad i=1,\ 2,\ldots,\ N$

$u(\ )$ represents the unit step function.

The free end condition at $x=\ell$ requires that

$$\cos\beta \cdot C_1 - \sum_{i=1}^{N} \cos(\beta(1-\alpha_i)) \cdot D_i = 0 \quad ; \quad (\alpha_i = a_i/\ell) \tag{5}$$

In addition we have the N consistency relations

$$\lim_{x \to a_j} \theta(x) = \theta(a_j) \qquad j=1,\ 2,\ \ldots,\ N$$

which can be written in the form

$$\left.\begin{aligned} \sin\beta\alpha_1 \cdot C_1 - \frac{1}{\beta I_1^*} D_1 &= 0 \\ \sin\beta\alpha_j \cdot C_1 - \sum_{i=1}^{j-1} \sin(\beta(\alpha_j-\alpha_i))\ D_i - \frac{1}{\beta I_j^*} D_j &= 0 \end{aligned}\right\} \tag{6}$$

$$\text{for } j = 2,\ 3,\ \ldots,\ N$$

The system of equations (5)-(6) are homogeneous linear equations in the unknowns: $C_1,\ D_1,\ D_2, \ldots,\ D_N$. In order to have a nontrivial solution the determinant of the coefficient matrix must vanish. This condition yields the eigenvalues $\beta_1,\ \beta_2, \ldots,$ from which the natural frequencies can be obtained.

$$\omega_i = \sqrt{\frac{GJ}{\ell^2 I}}\ \beta_i$$

For the special case of a single disk located at the tip of the bar (N=1, $\alpha_1=1$) we have the condition

$$\begin{vmatrix} \cos\beta & -1 \\ \sin\beta & \dfrac{-1}{\beta I_1^*} \end{vmatrix} = 0 \quad \text{or} \quad \tan\beta = \frac{1}{I_1^*\ \beta}$$

which agrees with Meirovitch's result [2].

If for each eigenvalue β_i we assume that the coefficient matrix has rank N then we can set $C_1=1$ (assuming that the twisting moment at x=0 is nonzero) and solve for the remaining coefficients $D_1, D_2, \ldots, D_N$. Equation (4) then gives the non-normalized eigenfunction.

Orthogonality Condition

Let $\theta_m(x)$ and $\theta_n(x)$ be eigenfunctions corresponding to the distinct eigenvalues β_m and β_n respectively. With the aid of Eq. (3) we can write

$$\int_0^\ell \theta_m \theta_n'' dx + \frac{\beta_n^2}{\ell^2} \int_0^\ell \left[1 + \sum_{i=1}^N I_i^* \ell\, \delta(x-a_i)\right] \theta_n \theta_m \, dx = 0$$

Integrating the first term by parts, and invoking the boundary conditions we can write the above as

$$-\int_0^\ell \theta_n' \theta_m' dx + \frac{\beta_n^2}{\ell^2} \int_0^\ell \theta_n \theta_m \, dx + \frac{\beta_n^2}{\ell} \sum_{i=1}^N I_i^* \, \theta_n(a_i) \cdot \theta_m(a_i) = 0$$

Writing a similar equation with m and n interchanged and subtracting, we obtain

$$\frac{1}{\ell} \int_0^\ell \theta_m \theta_n \, dx + \sum_{i=1}^N I_i^* \, \theta_m(a_i) \, \theta_n(a_i) = 0 \qquad (m \neq n)$$

From Eq. (4) we see that the eigenfunction can be regarded as a function of the dimensionless variable $\xi = x/\ell$.

$$\theta_n(\xi) = \sin\beta_n\xi - \sum_{i=1}^N D_{in} \sin\beta_n(\xi-\alpha_i) \cdot u(\xi-\alpha_i)$$

With this understanding the orthogonality condition is

$$\int_0^1 \theta_m(\xi) \, \theta_n(\xi) \, d\xi + \sum_{i=1}^N I_i^* \theta_m(\alpha_i) \theta_n(\alpha_i) = 0 \quad (m \neq n) \qquad (7)$$

Transverse Vibrations of a Beam With Concentrated Masses and Rotary Inertias

We wish to investigate the transverse vibration of a uniform beam carrying a system of heavy bodies along its span. The beam is clamped at $x=0$ and free at $x=\ell$, where the x-axis coincides with the beams neutral axis in the undeformed state. The bodies are idealized as point masses with rotary inertia situated at the points $x=a_i$ in the undeformed state. As before, we assume that the sequence $a_1, a_2, \ldots, a_N$ is strictly increasing and for the purposes of the derivation that $0<a_i<\ell$. Again, the results remain valid for the case of a tip body ($a_N=\ell$).

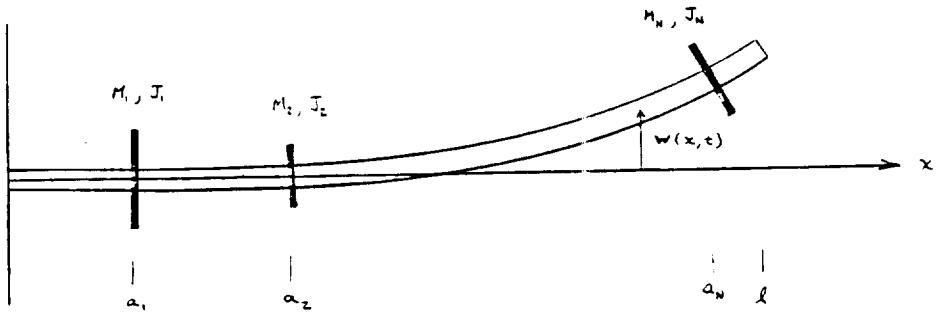

Figure 2. Uniform Beam Carrying Discrete Rigid Bodies

For a beam with bending stiffness EI (constant) and linear density $\rho(x)$ the partial differential equation governing free vibration is (neglecting shear deformation and rotary inertia) the well known Euler-Bernoulli equation

$$EI \frac{\partial^4 w}{\partial x^4} + \rho(x)\frac{\partial^2 w}{\partial t^2} = 0$$

where $w(x,t)$ denotes the transverse deflection. This equation is not directly applicable to our problem since its derivation assumes differentiability of the bending moment and shear force. The presence of the concentrated masses and inertias gives rise to discontinuities in the

shear force and bending moment. The conventional solution to this problem is to apply the above equation in each subdomain of $0<x<\ell$ separated by the points $a_1, a_2, \ldots a_N$. This gives rise to a fourth order equation in each subdomain; thus a large number of integration constants appear in the solution. The evaluation of these constants is arrived at by applying the boundary conditions at the ends of the beam, writing translational and rotational equations for each body, and demanding continuity of the beam deflection and slope at the points $x=a_i$. It is seen that the order of the determinant in the frequency equation is extremely large, even for moderate values of N. A much more compact solution can be realized by employing delta functions to represent the concentrated masses and inertias. This idea was first suggested by Pan [3,4].

If we follow the same derivation as in the Euler-Bernoulli equation but include rotary inertia we arrive at the so called Rayleigh beam equation

$$EI\frac{\partial^4 w}{\partial x^4} - \frac{\partial}{\partial x}\left[J(x)\frac{\partial^3 w}{\partial x\,\partial t^2}\right] + \rho(x)\frac{\partial^2 w}{\partial t^2} = 0$$

where $J(x)$ is rotary inertia per unit length. Using delta functions it is an easy matter to include the mass M_i and rotary inertia J_i of the ith body in the $\rho(x)$ and $J(x)$ distributions

$$\rho(x) \longrightarrow \rho + \sum_{i=1}^{N} M_i\,\delta(x-a_i)$$

$$J(x) \longrightarrow \sum_{i=1}^{N} J_i\,\delta(x-a_i)$$

Here ρ represents the uniform mass density of the beam alone. The rotary inertia of the beam (alone) is neglected. Inserting these expressions for $\rho(x)$ and $J(x)$ and seeking solutions of the form $e^{i\omega t}\,y(x)$ we arrive at the equation

$$EI\,\frac{d^4 y}{dx^4} + \omega^2\,\frac{d}{dx}\left[y'(x)\sum_{i=1}^{N} J_i\,\delta(x-a_i)\right] - \omega^2\left[\rho + \sum_{i=1}^{N} M_i\,\delta(x-a_i)\right] y(x) = 0 \qquad (8)$$

with boundary conditions

$$y(0)=y'(0)=0 \quad , \quad y''(\ell)=y'''(\ell)=0$$

Taking the Laplace transform of Eq. (8), and observing the boundary conditions at x=0 we obtain

$$\mathcal{L}\{y(x);s\} = \frac{s}{s^4 - k^4} y''(0) + \frac{1}{s^4 - k^4} y'''(0) - \frac{k^4}{\rho} \sum_{i=1}^{N} J_i y'(a_i) \frac{s\, e^{-a_i s}}{s^4 - k^4}$$

$$+ \frac{k^4}{\rho} \sum_{i=1}^{N} M_i y(a_i) \frac{e^{-a_i s}}{s^4 - k^4} \qquad \text{where } k^4 = \frac{\rho\omega^2}{EI}$$

Inverting, we obtain

$$\frac{1}{\ell} y(x) = C_1 \beta^{-2}[\cosh(\beta x/\ell) - \cos(\beta x/\ell)] + C_2 \beta^{-3}[\sinh(\beta x/\ell) - \sin(\beta x/\ell)]$$

$$-\beta^2 \sum_{i=1}^{N} D_i [\cosh \beta(x/\ell - \alpha_i) - \cos \beta(x/\ell - \alpha_i)] \cdot u(x/\ell - \alpha_i)$$

$$+\beta \sum_{i=1}^{N} E_i [\sinh \beta(x/\ell - \alpha_i) - \sin \beta(x/\ell - \alpha_i)] \cdot u(x/\ell - \alpha_i) \qquad (9)$$

where $\beta = k\ell$, $M_i^* = M_i/\rho\ell$, $J_i^* = J_i/\rho\ell^3$, $\alpha_i = a_i/\ell$,

$C_1 = \frac{\ell}{2} y''(0)$, $C_2 = \frac{\ell^2}{2} y'''(0)$,

$D_i = \frac{1}{2} J_i^* y'(a_i)$, $E_i = \frac{1}{2\ell} M_i^* y(a_i)$ $\quad i = 1, 2, 3, \ldots, N.$

At the free end of the beam we have $y''(\ell) = y'''(\ell) = 0$. With the aid of Eq. (9) these conditions can be written as

$$(\cosh \beta + \cos \beta) \cdot C_1 + \frac{1}{\beta} (\sinh \beta + \sin \beta) \cdot C_2$$

$$-\beta^4 \sum_{i=1}^{N} [\cosh(1 - \alpha_i)\beta + \cos(1 - \alpha_i)\beta] D_i \qquad (10)$$

$$+\beta^3 \sum_{i=1}^{N} [\sinh(1 - \alpha_i)\beta + \sin(1 - \alpha_i)\beta] E_i = 0$$

$$\beta(\sinh\beta - \sin\beta)\,C_1 + (\cosh\beta + \cos\beta)\,C_2$$

$$-\beta^5 \sum_{i=1}^{N} [\sinh(1-\alpha_i)\beta - \sin(1-\alpha_i)\beta]\,D_i \qquad (11)$$

$$+\beta^4 \sum_{i=1}^{N} [\cosh(1-\alpha_i)\beta + \cos(1-\alpha_i)\beta]\,E_i = 0$$

We also have the 2N consistency relations

$$\lim_{x\to a_j} y(x) = y(a_j)\,, \qquad \lim_{x\to a_j} y'(x) = y'(a_j)$$

which can be written in the form

$$\left.\begin{aligned} &\frac{1}{\beta^2}(\cosh\alpha_1\beta - \cos\alpha_1\beta)\cdot C_1 + \frac{1}{\beta^3}(\sinh\alpha_1\beta - \sin\alpha_1\beta)\cdot C_2 - \frac{2}{M_1^*}E_1 = 0 \\ &\frac{1}{\beta}(\sinh\alpha_1\beta + \sin\alpha_1\beta)\cdot C_1 + \frac{1}{\beta^2}(\cosh\alpha_1\beta - \cos\alpha_1\beta)\cdot C_2 - \frac{2}{J_1^*}D_1 = 0 \end{aligned}\right\} \qquad (12)$$

<u>for j=2, 3, 4,..., N</u>

$$\frac{1}{\beta^2}(\cosh\alpha_j\beta - \cos\alpha_j\beta)\cdot C_1 + \frac{1}{\beta^3}(\sinh\alpha_j\beta - \sin\alpha_j\beta)\cdot C_2$$

$$-\beta^2 \sum_{i=1}^{j-1} [\cosh(\alpha_j-\alpha_i)\beta - \cos(\alpha_j-\alpha_i)\beta\,]D_i \qquad (13)$$

$$+\beta \sum_{i=1}^{j-1} [\sinh(\alpha_j-\alpha_i)\beta - \sin(\alpha_j-\alpha_i)\beta]\,E_i - \frac{2}{M_j^*}E_j = 0$$

$$\frac{1}{\beta}(\sinh\alpha_j\beta + \sin\alpha_j\beta)\cdot C_1 + \frac{1}{\beta^2}(\cosh\alpha_j\beta - \cos\alpha_j\beta)\cdot C_2$$

$$-\beta^3 \sum_{i=1}^{j-1} [\sinh(\alpha_j-\alpha_i)\beta + \sin(\alpha_j-\alpha_i)\beta]\cdot D_i - \frac{2}{J_j^*}\cdot D_j \qquad (14)$$

$$+\beta^2 \sum_{i=1}^{j-1} [\cosh(\alpha_j-\alpha_i)\beta - \cos(\alpha_j-\alpha_i)\beta]\cdot E_i = 0$$

The system of equations (10 - 14) are homogeneous linear equations in the unknowns: C_1, C_2, D_1, D_2,..., D_N, E_1, E_2,..., E_N. Setting the determinant of the coefficient matrix to zero yields the eigenvalues, β_1, β_2,..., from which the natural frequencies of transverse vibration can be obtained.

For the special case of a single tip body (N=1, α_1=1) we have the condition

$$\begin{vmatrix} (\cosh\beta + \cos\beta) & \beta^{-1}(\sinh\beta + \sin\beta) & -2\beta^4 & 0 \\ \beta(\sinh\beta - \sin\beta) & (\cosh\beta + \cos\beta) & 0 & 2\beta^4 \\ \beta^{-2}(\cosh\beta - \cos\beta) & \beta^{-3}(\sinh\beta - \sin\beta) & 0 & -2/M_1^* \\ \beta^{-1}(\sinh\beta + \sin\beta) & \beta^{-2}(\cosh\beta - \cos\beta) & -2/J_1^* & 0 \end{vmatrix} = 0$$

Expanding this determinant we have the frequency equation

$$M_1^* J_1^* \beta^4 (1 - \cos\beta \cosh\beta) + M_1^* \beta (\cos\beta \sinh\beta - \sin\beta \cosh\beta)$$

$$-J_1^* \beta^3 (\sin\beta \cosh\beta + \sinh\beta \cos\beta) + 1 + \cos\beta \cosh\beta = 0$$

which agrees with Eq. (2-19) in [5] (with $C^* = 0$).

In a manner completely analogous to that discussed for torsional vibration we set C_1=1 (assuming the root bending moment is nonzero) and solve for the remaining coefficients. The eigenfunction then follows from Eq. (9).

Orthogonality Condition

Following a procedure similar to that described for the torsional vibration we can show with the aid of Eq. (8) that

$$\int_0^\ell \rho\, y_m(x)\, y_n(x)\, dx + \sum_{i=1}^{N} M_i\, y_m(a_i)\, y_n(a_i) + \sum_{i=1}^{N} J_i\, y_m'(a_i)\, y_n'(a_i) = 0$$

where $y_m(x)$ and $y_n(x)$ are eigenfunctions corresponding to distinct eigenvalues. In terms of the nondimensional eigenfunction $S_n(\xi)$ we have $y_n(x)=\ell\, S_n(\xi)$ where $\xi = x/\ell$. The orthogonality condition takes on the form

$$\int_0^1 S_m(\xi)\, S_n(\xi)\, d\xi + \sum_{i=1}^{N} M_i^* S_m(\alpha_i)\, S_n(\alpha_i) + \sum_{i=1}^{N} J_i^* S_m'(\alpha_i)\, S_n'(\alpha_i) = 0 \qquad (15)$$

where (') now indicates differentiation with respect to ξ.

Natural Frequencies and Eigenfunctions
Assumed - Modes Method

In this section we obtain approximate expressions for the natural frequencies and eigenfunctions of a uniform cantilevered beam carrying a set of compact rigid bodies along its span. Both the torsional and transverse vibrations are considered, respectively. The formulations are implementations of the assumed modes method [2]. The results of this section serve to validate the previous exact analyses.

Torsional Vibration

Here we consider the pure torsional vibration of a uniform circular bar carrying a set of N rigid bodies along its length. While the bodies possess inertia about the torsion axis, their spatial dimensions are assumed negligible. The centroids of the bodies are restricted to lie along the neutral axis of the bar.

Let the x-axis correspond to the neutral axis of the bar. The bar has length ℓ, torsional stiffness GJ, and polar mass moment of inertia per unit length I. The i^{th} rigid body is located at $x=a_i$, and has polar mass moment of inertia I_i. Designating the angle of twist of the cross

section by, $\theta(x,t)$, the kinetic and strain energies for the system are, respectively

$$T = \frac{1}{2}\int_0^{\ell} I \left(\frac{\partial\theta}{\partial t}\right)^2 dx + \frac{1}{2}\sum_{i=1}^{N} I_i \left[\frac{\partial\theta}{\partial t}(a_i,t)\right]^2 \tag{16}$$

$$V = \frac{1}{2} GJ \int_0^{\ell} \left(\frac{\partial\theta}{\partial x}\right)^2 dx \tag{17}$$

We choose to express the twist angle, $\theta(x,t)$, as a series involving the eigenfunctions of a simple uniform clamped-free circular shaft. Those eigenfunctions, in terms of the nondimensional variable $\eta = x/\ell$, are given by

$$\Phi_k(\eta) = \sqrt{2} \sin \sigma_k \eta$$

where $$\sigma_k = (2k-1)\frac{\pi}{2} \qquad (k = 1,2,\ldots)$$

The eigenfunctions, $\Phi_K(\eta)$, satisfy the eigenvalue problem

$$\frac{d^2\Phi_k}{d\eta^2} + \sigma_k^2 \Phi_k(\eta) = 0$$

$$\Phi_k(0) = \frac{d\Phi_k}{d\eta}(1) = 0$$

and orthonormality condition

$$\int_0^1 \Phi_i(\eta)\, \Phi_j(\eta)\, d\eta = \delta_{ij}$$

where, δ_{ij} is the Kronecker delta.

Introducing the expansion

$$\theta(x,t) = \sum_{k=1}^{m} \Phi_k(\eta)\, p_k(t)$$

into the energy expressions Eqs. (16) and (17), and making the appropriate

coordinate transformation, one obtains

$$T = \frac{1}{2} I \ell \sum_{j=1}^{m} \dot{p}_j^2 + \frac{1}{2} \sum_{i=1}^{N} \sum_{j=1}^{m} \sum_{k=1}^{m} I_i \Phi_j(\alpha_i) \Phi_k(\alpha_i) \dot{p}_j \dot{p}_k$$

$$V = \frac{1}{2} \frac{GJ}{\ell} \sum_{j=1}^{m} \sigma_j^2 p_j^2$$

where

$$\alpha_i = \frac{a_i}{\ell}$$

Application of Lagrange's equations yields the free vibration motion equations

$$[\mathcal{I}] \{\ddot{p}\} + \frac{GJ}{I\ell^2} [\sigma^2] \{p\} = \{0\} \tag{18}$$

where

$$[\mathcal{I}] = [1] + [P] [I^*] [P]^T$$

$[1]$ = (m x m) identity matrix

$[I^*]$ = diagonal $(I_1^*, I_2^*, \ldots, I_N^*)$

$$I_i^* = \frac{I_i}{I\ell}$$

$[P]$ - (m x N), with (i,j) element: $P_{ij} = \Phi_i(\alpha_j)$

$[\sigma^2]$ = diagonal $(\sigma_1^2, \sigma_2^2, \ldots, \sigma_m^2)$

Seeking harmonic solutions; $\{p\} = \{U\} e^{i\Omega t}$ to Eqs. (18), leads to the algebraic eigenvalue problem

$$([\sigma^2] - \lambda[\mathcal{I}]) \{U\} = \{0\}$$

The eigenvalues, λ_r, which are roots of the characteristic equation

$$\det ([\sigma^2] - \lambda[\mathcal{I}]) = 0 \tag{19}$$

are related to the natural frequencies of the bar with rigid bodies, Ω_r, by

$$\Omega_r = \sqrt{\frac{GJ}{I\ell^2}} \sqrt{\lambda_r}$$

These estimates of the torsional vibration frequencies will be upper bounds to the true values.

Approximate expressions for the eigenfunctions corresponding to the torsional vibrations of the bar with rigid bodies, can be expressed in terms of the nondimensional variable, η, as

$$\Gamma_r(\eta) = \sum_{k=1}^{m} \Phi_k(\eta)\, U_k^{(r)}$$

where $U_k^{(r)}$ is the k^{th} element of the eigenvector, $\{U^{(r)}\}$ corresponding to eigenvalue λ_r.

In order to directly compare (numerically) the approximate eigenfunctions of this section with those of the exact analysis, we enforce the normalization

$$\int_0^1 \theta_r^2(\eta)\, d\eta + \sum_{i=1}^{N} I_i^* \left[\theta_r(\alpha_i)\right]^2 = 1$$

The approximate eigenfunctions that satisfy the above normality condition are given by

$$\Theta_r(\eta) = \frac{1}{\sqrt{t_r}} \sum_{k=1}^{m} \Phi_k(\eta)\, U_k^{(r)}$$

where

$$t_r = \sum_{k=1}^{m} \left[U_k^{(r)}\right]^2 + \sum_{i=1}^{N} I_i^* \left(\sum_{k=1}^{m} \Phi_k(\alpha_i)\, U_k^{(r)} \right)^2$$

Transverse Vibration

Here we present an approximate analysis of the planar transverse bending vibrations of a uniform cantilevered Euler-Bernoulli beam carrying a set of N compact rigid bodies. The motion plane is taken to be a plane of inertial symmetry for the bodies. The bodies possess mass and inertia, however, their spatial dimensions are assumed negligible.

The beam is taken to have length ℓ, bending stiffness EI, and mass per unit length ρ. The rigid bodies are fixed to the beam with their centroids on the neutral axis. In the undeformed state, the beam's longitudinal axis

coincides with the coordinate x-axis, and the rigid body has position $x = a_i$. Body i has mass M_i, and centroidal mass moment of inertia about an axis normal to the motion plane, J_i. Letting, $w(x,t)$, be the transverse displacement of the beam's neutral axis, the kinetic and strain energies for the system are

$$T = \frac{1}{2}\rho \int_0^{\ell} \left(\frac{\partial w}{\partial t}\right)^2 dx + \frac{1}{2} \sum_{i=1}^{N} M_i \left[\frac{\partial w}{\partial t}(a_i,t)\right]^2 + \frac{1}{2} \sum_{i=1}^{N} J_i \left[\frac{\partial^2 w}{\partial t\,\partial x}(a_i,t)\right]^2 \tag{20}$$

$$V = \frac{1}{2} EI \int_0^{\ell} \left(\frac{\partial^2 w}{\partial x^2}\right)^2 dx \tag{21}$$

We will express the elastic displacement, $w(x,t)$, in terms of a set of eigenfunctions corresponding to a simple uniform cantilevered-free beam. We record that eigenvalue problem, in terms of the dimensionless parameter, $\eta = \frac{x}{\ell}$, as

$$\frac{d^4 S}{d\eta^4} - \beta^4 S(\eta) = 0$$

$$S(0) = \frac{dS}{d\eta}(0) = \frac{d^2 S}{d\eta^2}(1) = \frac{d^3 S}{d\eta^3}(1) = 0$$

The eigenfunction solutions can be expressed as

$$S_k(\eta) = \cosh\beta_k\eta - \cos\beta_k\eta + \frac{\sin\beta_k - \sinh\beta_k}{\cos\beta_k + \cosh\beta_k}\left(\sinh\beta_k\eta - \sin\beta_k\eta\right)$$

where β_k corresponds to the k^{th} root of the associated characteristic equation

$$\cosh\beta\cos\beta + 1 = 0$$

These eigenfunctions satisfy the orthonormality condition

$$\int_0^1 S_i(\eta)\, S_j(\eta)\, d\eta = \delta_{ij}$$

Introducing the expansion

$$w(x,t) = \ell \sum_{k=1}^{n} S_k(\eta)\, q_k(t)$$

into the energy expressions, Eqs. (20) and (21), and making the appropriate coordinate transformation, one obtains

$$T = \frac{1}{2}\rho\ell^3 \sum_{j=1}^{n} \dot{q}_j^2$$

$$+ \frac{1}{2} \sum_{i=1}^{N} \sum_{j=1}^{n} \sum_{k=1}^{n} \left[\ell^2 M_i S_j(\alpha_i) S_k(\alpha_i) + J_i S_j'(\alpha_i) S_k'(\alpha_i) \right] \dot{q}_j \dot{q}_k$$

where $\alpha_i = \frac{a_i}{\ell}$, and

$$V = \frac{EI}{2\ell} \sum_{j=1}^{n} \beta_j^4 q_j^2$$

Application of Lagrange's equations yields the free vibration motion equations

$$[\mathcal{M}] \{\ddot{q}\} + \frac{EI}{\rho\ell^4} [\beta^4] \{q\} = \{0\} \tag{22}$$

where

$$[\mathcal{M}] = [I] + [S][M^*][S]^T + [S'][J^*][S']^T$$

$[I]$ - (n x n) identify matrix

$[M^*]$ = diagonal $(M_1^*, M_2^*, \ldots, M_N^*$

$[J^*]$ = diagonal $(J_1^*, J_2^*, \ldots, J_N^*$

$$M_i^* = \frac{M_i}{\rho\ell} \quad ; \quad J_i^* = \frac{J_i}{\rho\ell^3}$$

[S] - (n x N), with (i,j) element: $S_{ij} = S_i(\alpha_j)$

[S'] - (n x N), with (i,j) element: $S'_{ij} = \frac{dS_i}{d\eta}(\alpha_j)$

$[\beta^4]$ = diagonal$(\beta_1^4, \beta_2^4, \ldots, \beta_n^4)$

Seeking harmonic solutions; $\{q\} = \{V\} e^{i\Omega t}$ to the Eqs. (22), leads to the algebraic eigenvalue problem

$$([\beta^4] - \lambda[\mathcal{M}])\{V\} = \{0\} \tag{23}$$

The eigenvalues, λ_r, are related to the natural frequencies of the cantilevered beam with rigid bodies, Ω_r, by

$$\Omega_r = \sqrt{\frac{EI}{\rho \ell^4}}\ \sqrt{\lambda_r}$$

These approximate natural frequencies will be upper bounds to the true values.

Approximate expressions for the eigenfunctions of the cantilevered beam with rigid bodies can be written in terms of the nondimensional variable η, as

$$W_r(\eta) = \sum_{k=1}^{n} S_k(\eta)\, V_k^{(r)} \qquad (r = 1, 2, \ldots n)$$

where $V_k^{(r)}$ is the $k^{\underline{th}}$ element of the eigenvector, $\{V^{(r)}\}$, associated with eigenvalue λ_r. Clearly, these eigenfunctions have been scaled to the interval $0 \leq \eta \leq 1$.

In order to directly compare (numerically) the approximate eigenfunctions of this section with those of the exact analysis, we enforce the normalization:

$$\int_0^1 [W_r(\eta)]^2\, d\eta + \sum_{i=1}^{N} M_i^* [W_r(\alpha_i)]^2 + \sum_{i=1}^{N} J_i^* [W_r'(\alpha_i)]^2 = 1$$

The approximate eigenfunctions normalized to satisfy the above condition are given by

$$W_r(\eta) = \frac{1}{\sqrt{c_r}} \sum_{k=1}^{n} S_k(\eta)\, V_k^{(r)}$$

where

$$c_r = \sum_{k=1}^{n} [V_k^{(r)}]^2 + \sum_{i=1}^{N} M_i^* \left[\sum_{k=1}^{n} S_k(\alpha_i) V_k^{(r)} \right]^2$$

$$+ \sum_{i=1}^{N} J_i^* \left[\sum_{k=1}^{n} S_k'(\alpha_i) V_k^{(r)} \right]^2$$

Selected Numerical Results

Validation of Natural Frequencies

Tables 1 and 2 provide the natural frequencies for the torsion and transverse bending vibrations, respectively, of a beam carrying six small rigid bodies. The data for the body distributions and their mass and inertia ratios are consistent with the parameters for the COFS-I mast[6]. The exact results of Table 1 (for torsion), and Table 2 (for bending) are the solutions from the characteristic equations associated with the homogenous systems given by Eqs. (5) & (6), and Eqs. (10) - (14), respectively. The exact results are clearly corroborated by the solutions obtained from the assumed modes method, which were yield from Eq. (19) in the case of torsion, and Eqs. (23) in the case of bending.

Comparison of Eigenfunctions

Figures 3 and 4 show plots which compare the corresponding eigenfunctions of a simple uniform clamped-free beam with those of a clamped-free beam carrying six small rigid bodies. The data for the rigid bodies, for both the torsion and bending cases, are the same as that given in Tables 1 and 2. Figure 3 presents the first four eigenfunctions for torsion, while Figure 4 gives the first four eigenfunctions for transverse bending. All the eigenfunctions have been normalized to have a maximum amplitude of unity. These figures are intended to simply illustrate the change in the eigenfunctions associated with the addition of several small rigid bodies.

NATURAL FREQUENCIES FOR TORSION COFS-I SYSTEM					
Mode Number r	Exact Solution γ_r	Assumed Modes Solution for γ_r Using n Clamped-Free Eigenfunctions			
		n=5	n=10	n=20	n=40
1	1.07	1.07	1.07	1.07	1.07
2	3.53	3.62	3.58	3.55	3.54
3	6.26	6.50	6.38	6.32	6.29
4	9.06	9.46	9.24	9.15	9.10

NATURAL FREQUENCIES FOR TORSION Uniform Clamped-Free Bar	
Mode No. r	Exact γ_r
1	1.57
2	4.71
3	7.85
4	11.00

Natural Frequency : $\omega_r = \sqrt{\frac{GJ}{I\ell^2}}\,\gamma_r$

COFS-I Data from NASA CP-2447 pp 265 - 279

$\alpha_1 = .22$; $I_1^* = .024$

$\alpha_2 = .44$; $I_2^* = .0087$

$\alpha_3 = .56$; $I_3^* = .024$

$\alpha_4 = .70$; $I_4^* = .0087$

$\alpha_5 = .81$; $I_5^* = .024$

$\alpha_6 = 1.00$; $I_6^* = .48$ ← Represents Tip Mass + PMD @ Maximum Inertia

TABLE * 1

NATURAL FREQUENCIES FOR TRANSVERSE BENDING
COFS-I SYSTEM

Mode Number r	Exact Solution γ_r	Assumed Modes Solution for γ_r using n Uniform Clamped-Free Eigenfunctions			
		n=5	n=10	n=20	n=40
1	1.54	1.54	1.54	1.54	1.54
2	12.66	12.68	12.66	12.66	12.66
3	39.29	39.46	39.32	39.30	39.30
4	72.64	73.16	72.75	72.65	72.64

NATURAL FREQUENCIES for TRANSVERSE BENDING
Uniform Clamped-Free Beam

Mode No. r	Exact γ_r
1	3.52
2	22.03
3	61.70
4	120.90

Natural Frequency: $\omega_r = \sqrt{\frac{EI}{\rho \lambda^4}}\,\gamma_r$

COFS-I Data from NASA CP-2447 pp 265-279

$\alpha_1 = .22$; $M_1^* = .18$; $J_1^* = 2 \cdot 10^{-6}$
$\alpha_2 = .44$; $M_2^* = .05$; $J_2^* = 1 \cdot 10^{-6}$
$\alpha_3 = .56$; $M_3^* = .18$; $J_3^* = 2 \cdot 10^{-6}$
$\alpha_4 = .70$; $M_4^* = .05$; $J_4^* = 1 \cdot 10^{-6}$
$\alpha_5 = .81$; $M_5^* = .18$; $J_5^* = 2 \cdot 10^{-6}$
$\alpha_6 = 1.00$; $M_6^* = .88$; $J_6^* = 2.08 \cdot 10^{-5}$

Rotary inertias assumed to be the same as I_E, except: $J_6 = 21.6$ kg-m²

EIGENFUNCTIONS FOR TORSION

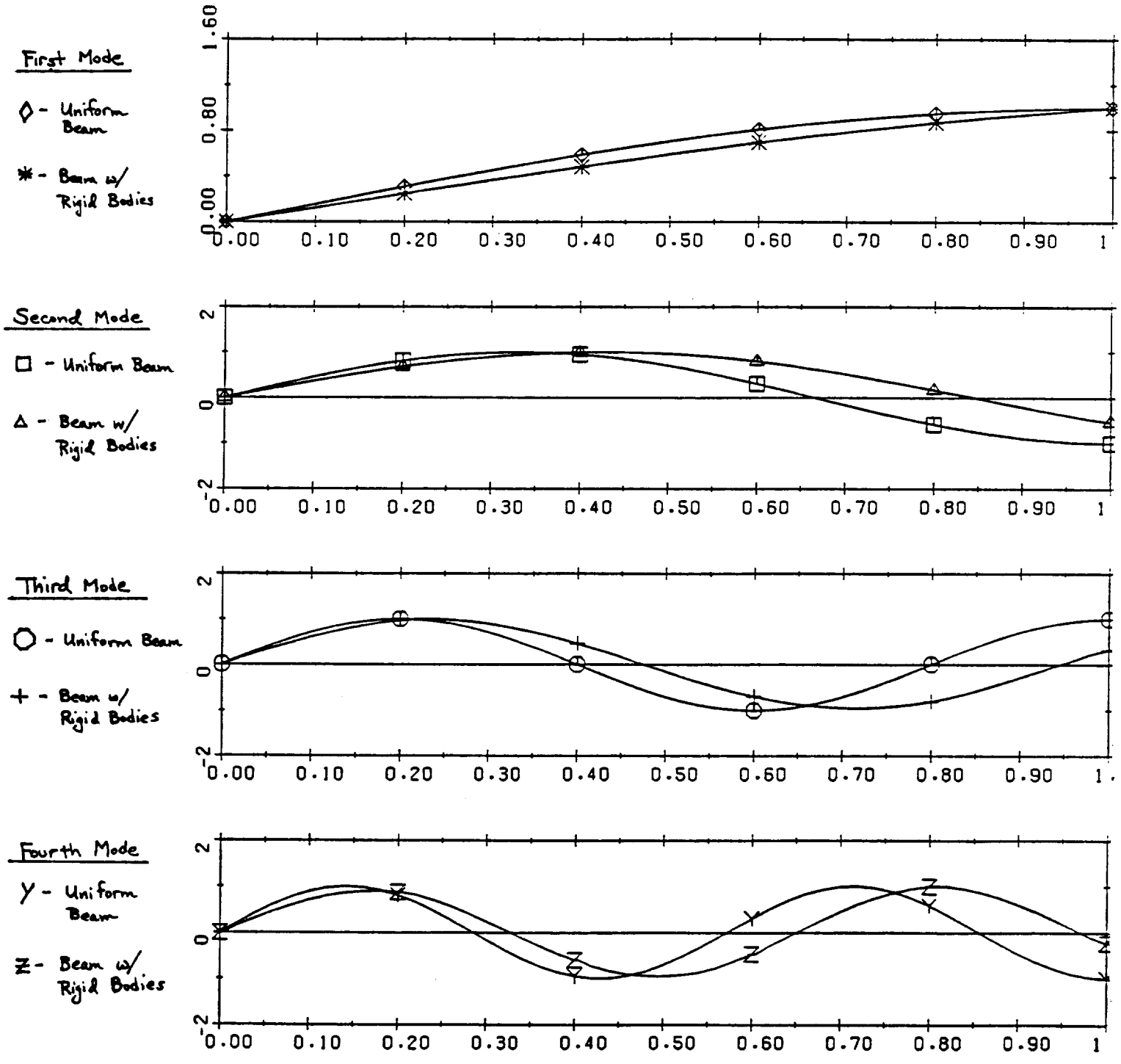

Figure 3

EIGENFUNCTIONS FOR BENDING

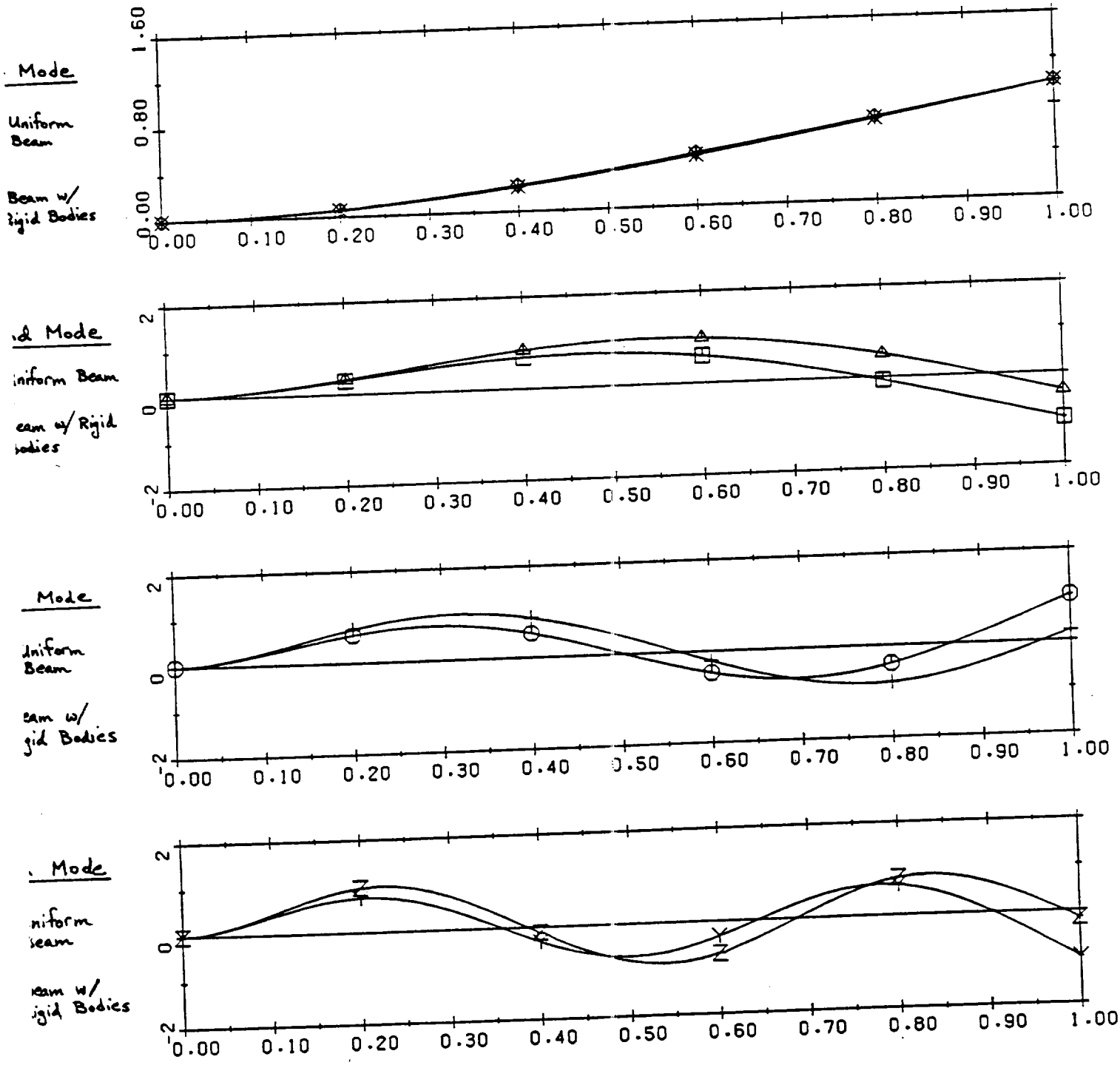

Figure 4

References

1. S. Gates & J. Storch "Mechanical Idealization of the Orbiter/COFS II Structural System," CSDL Intralab Memo No. DI-87-02, February 5, 1987.

2. L. Meirovitch, "Analytical Methods in Vibrations," Macmillan, 1971. pp. 156-60; pp. 233-235

3. H.H. Pan, "Some Applications of Symbolic Functions on Beam Problems," Journal of the Franklin Institute, Vol. 303, 1963 pp. 303-313

4. H. H. Pan, "Transverse Vibration of an Euler Beam Carrying a System of Heavy Bodies," Journal of Applied Mechanics, June 1965, pp. 434-437.

5. J. Storch & S. Gates "Planar Dynamics of Uniform Beam with Rigid Bodies Affixed to the Ends," Report CSDL-R-1629, May, 1983.

6. Lenzi, D.C. & Shipley, J.W. "Mast Flight System Beam Structure and Beam Structure Performance," NASA CP-2447, pp. 265-279, Presented at the First NASA/DOD CSI Technology Conference, Nov. 18-21, 1986, Norfolk, Virginia.

Appendix C

Orbiter/COFS-II Pitch Plane Dynamics

The Charles Stark Draper Laboratory, Inc.
555 Technology Square, Cambridge, Massachusetts 02139 Telephone (617) 258-

DI-87-14

TO: Stan Fay
FROM: Joel Storch
DATE: 5 October 1987
SUBJECT: Orbiter/COFS II Pitch Plane Dynamics

In a previous memorandum (Draper memo # DI-87-02, Feb. 5, 1987) the mechanical idealization of the orbiter/COFS II structural system was described. Presently, we restrict our attention to the vehicle pitch plane and obtain linearized equations of motion, with the ultimate aim of obtaining the transfer function between the pitch servo torque and corresponding gimbal angle. For a representative set of vehicle parameters the zeros and poles of the transfer function are obtained numerically.

Figure 1 depicts the situation in a general state of motion and deformation. All displacements (rigid and elastic) are treated as "small" and are restricted to a single plane. The term "small" will be understood to mean that the displacements are restricted in magnitude so as to result in a set of differential equations of motion with constant coefficients.

Vehicle Coordinate Frames

Fi - Inertial frame. Rotation by angle θ about z axis brings us to the orbiter body frame.

F_1 - Orbiter body frame with origin at orbiter mass centre. x_1 axis along orbiter roll axis, positive towards aft. z_1 axis along orbiter pitch axis, positive toward port. The y_1 axis completes the right handed system. Note that this results in the mast's underformed axis to be along y_1.

F_2 - Frame rigidly attached to mast tip (P_2). Misalignment relative to F_1 due to transverse bending of mast in x,y, plane.

F_3 - Frame with origin rigidly attached to mass centre of gimbal platform. Misalignment relative to F_2 due to rotation by gimbal angle α about Z_2 axis.

F_4 - Frame with origin rigidly attached to mass centre of antenna column. Misalignment relative to F_3 due to rotation by restoration angle ψ_1 about Z_3 axis. Note that the x_4 axis is along the symmetry axis of the column.

F_5 - Frame with origin rigidly attached to mass centre of feed mast/horn. Misalignment relative to F_4 due to rotation by restoration angle ψ_2 (at P_5) about Z_4 axis. Note that the x_5 axis is along the symmetry axis of the feed mast/horn.

Vehicle Geometry and Mass Properties

$\underline{c}^1$ - Vector from orbiter mass centre to mast attachment point P_1. (Resolved in F_1).

L - Length of undeformed mast.

$\underline{c}^2$ - Vector from mast tip P_2 to mass centre of offset structure (resolved in F_2).

$\underline{r}^2$ - Vector from mast tip P_2 to gimbal pivot P_3 (resolved in F_2).

$\underline{c}^3$ - Vector from gimbal pivot P_3 to mass centre of payload platform (resolved in F_3).

$\underline{r}^3$ - Vector from gimbal pivot P_3 to base P_4 of antenna column (resolved in F_3).

c - Distance from base P_4 of antenna column to its mass centre (measured along X_4).

h - Distance from base P_4 of antenna column to hoop's mid plane (measured along X_4).

a - Length of antenna column $\overline{P_4P_5}$.

b - Distance from antenna column tip P_5 to mass centre of feed mast & horn.

m_1 - Mass of orbiter.

$I_{zz}^{(1)}$ - Moment of inertia of orbiter about z_1 axis.

ρ - Uniform mass per unit length of mast.

m_2 - Mass of offset structure.

$I_{zz}^{(2)}$ - Moment of inertia of offset structure about its mass center, axis parallel to z_2.

m_3 - Mass of gimbal platform.

$I_{zz}^{(3)}$ - Moment of inertia of gimbal platform about z_3 axis.

m_4 - Mass of antenna column.

$I_{zz}^{(4)}$ - Moment of inertia of antenna column about z_4 axis.

m_5 - Mass of feed mast & horn.

$I_{zz}^{(5)}$ - Moment of inertia of feed mast & horn about z_5 axis.

m_6 - Mass of antenna hoop.

$I_{zz}^{(6)}$ - Moment of inertia of hoop about diametrical axis.

Elastic Moduli

EI - Bending stiffness of mast in x-y plane (lb. ft^2).

K_1 - Torsional spring modules at antenna column base P_4 (ft. lb./rad).

K_2 - Torsional spring modules at antenna column tip P_5 (ft. lb./rad).

System Strain Energy

The Strain energy V is stored in the two discrete torsional springs at P_4, P_5, and in the mast.

$$V(t) = \tfrac{1}{2} k_1 \psi_1^2 + \tfrac{1}{2} k_2 \psi_2^2 + \tfrac{1}{2} EI \int_0^L \left(\frac{\partial^2 u}{\partial y^2}\right)^2 dy$$

where u(y,t) denotes the transverse deflection of the mast in the xy plane. Introduce the one term modal expansion.

$$u(y,t) = L \; p(t) \; S_1(\xi)$$

with $\xi = y/l$, p(t) is an undetermined generalized coordinate, and $s_1(\xi)$ is the first eigenfunction corresponding to transverse vibration of a uniform cantilevered-free beam.

$$\frac{d^4 S_1}{d\xi^4} - \beta_1^4 S_1 = 0$$

$$S_1(0) = S_1'(0) = S_1''(1) = S_1'''(1)$$

The eigenvalues are the roots of the transcendental equation $1+\cos\beta \cosh\beta = 0$, with $\beta_1 \doteq 1.8751$. The eigenfunctions satisfy the orthonormality condition

$$\int_0^1 S_i(\xi) S_j(\xi) \, d\xi = \delta_{ij}$$

Inserting the modal expansion into the strain energy integral, integrating by parts twice, and observing the properties of $S_1(\xi)$ we obtain

$$V(t) = \frac{1}{2} k_1 \psi_1^2(t) + \frac{1}{2} k_2 \psi_2^2(t) + \frac{EI}{2L} \beta_1^4 p^2(t) \qquad (1)$$

Orbiter Kinetic Energy

Let $[X(t), Y(t)]^t$ be the position vector of the mass centre of the orbiter relative to the inertial origin. The kinetic energy T_1 of the orbiter is then given by

$$T_1 = \frac{1}{2} m_1 (\dot{X}^2 + \dot{Y}^2) + \frac{1}{2} I_{zz}^{(1)} \dot{\theta}^2 \qquad (2)$$

Kinetic Energy of Mast

Under small angle assumptions, the transformation matrix from F_i to F_1 can be written as

$$[R^{1I}] = \begin{bmatrix} 1 & \theta \\ -\theta & 1 \end{bmatrix}$$

The inertial velocity of point P_1 expressed in F_1 is given by

$$\underline{v}^{(P_1)} = [R^{1I}] \begin{pmatrix} \dot{X} \\ \dot{Y} \end{pmatrix} + \dot{\theta} \vec{k}_1 \times \vec{C}^{(1)}$$

$$\underline{v}^{(P_1)} \cong \begin{bmatrix} \dot{X} - C_y^{(1)} \dot{\theta} \\ \dot{Y} + C_x^{(1)} \dot{\theta} \end{bmatrix}$$

where we have dropped the nonlinear terms $\theta\dot{X}$ and $\theta\dot{Y}$

The masts transverse deflection $u(y,t)$ is measured in F_1

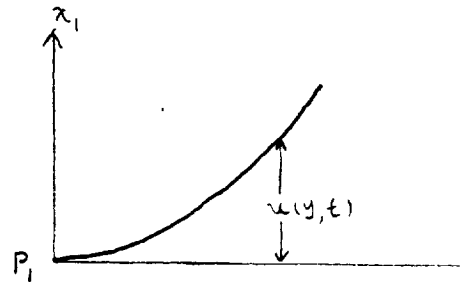

The inertial velocity of a point along the mast's neutral axis is given by

$$\underline{v}^{(P_1)} + \frac{\partial u}{\partial t}\vec{i}_1 + \dot{\theta}\vec{k}_1 \times y\vec{j}_1$$

where we have neglected terms of the order structural deflection x angular rate. Using the above expression for $\underline{v}^{(P1)}$ this expression assumes the form

$$\begin{bmatrix} \dot{X} - C_y^{(1)}\dot{\theta} + \frac{\partial u}{\partial t} - \dot{\theta} y \\ \dot{Y} + C_x^{(1)}\dot{\theta} \end{bmatrix} \quad \text{in } \mathcal{F}_1$$

The kinetic energy of the mast due to transverse bending and base motion is given by

$$T_2 = \tfrac{1}{2}\rho L\left[(\dot{Y} + C'_x\dot{\theta})^2 + (\dot{X} - C'_y\dot{\theta})^2\right] +$$
$$\tfrac{1}{2}\rho\int_0^L \left(\frac{\partial u}{\partial t} - \dot{\theta} y\right)^2 dy + \rho(\dot{X} - C'_y\dot{\theta})\int_0^L \left(\frac{\partial u}{\partial t} - \dot{\theta} y\right) dy$$

Introducing the modal expansion and defining the modal parameters

$$u_{41} \equiv \int_0^1 \xi S_1(\xi)\, d\xi \doteq .56883$$
$$u_{31} \equiv \int_0^1 S_1(\xi)\, d\xi \doteq .78299 \qquad (3)$$

we can write the kinetic energy in the form

$$T_2 = \tfrac{1}{2}\rho L\left[(\dot{Y} + C'_x\dot{\theta})^2 + (\dot{X} - C'_y\dot{\theta})^2\right] +$$

$$\frac{1}{2}\rho L^3\left(\dot{p}^2+\frac{1}{3}\dot{\theta}^2-2u_{41}\dot{\theta}\dot{p}\right)+$$

$$\rho L^2\left(\dot{x}-c'_y\dot{\theta}\right)\left(u_{31}\dot{p}-\frac{1}{2}\dot{\theta}\right) \qquad (4)$$

Kinetic Energy of Offset Structure

Defining the two additional modal parameters

$$u_{21}\equiv S_1(1)\doteq 2.000$$

$$u_{11}\equiv S_1'(1)\doteq 2.753 \qquad (5)$$

we can write the inertial velocity of point P_2 as

$$\underline{v}^{(P_2)}=\begin{bmatrix}\dot{x}-(c'_y+L)\dot{\theta}+Lu_{21}\dot{p}\\ \dot{Y}+c'_x\dot{\theta}\end{bmatrix}\quad \text{in } F_1$$

and the angular velocity of F_2 in the form

$$(\dot{\theta}-u_{11}\dot{p})\,\vec{k}$$

The inertial velocity of the mass centre of the offset structure resolved in F_2 can be written as

$$\begin{pmatrix}\dot{x}-g_1\dot{\theta}+b_1\dot{p}\\ \dot{Y}+g_2\dot{\theta}-u_{11}c_x^{(2)}\dot{p}\end{pmatrix}$$

Where we have neglected non linear terms and define

$$g_1 = L + c_y^{(1)} + c_y^{(2)}$$
$$g_2 = c_x^{(1)} + c_x^{(2)} \qquad (6)$$
$$b_1 = L u_{21} + c_y^{(2)} u_{11}$$

The kinetic energy T_3 of the off-set structure is then given by

$$T_3 = \tfrac{1}{2} m_2 \left[(\dot{x} - g_1 \dot{\theta} + b_1 \dot{p})^2 + (\dot{y} + g_2 \dot{\theta} - u_{11} c_x^2 \dot{p})^2 \right] + \tfrac{1}{2} I_{zz}^{(2)} (\dot{\theta} - u_{11} \dot{p})^2 \qquad (7)$$

Kinetic Energy of Gimbal Platform

The inertial velocity of point P_3 follows directly from that of the mass centre of the offset structure if we replace $\underline{c}^2$ with $\underline{r}^2$.

$$\underline{v}^{(P_3)} = \begin{pmatrix} \dot{x} - g_3 \dot{\theta} + b_2 \dot{p} \\ \dot{y} + g_4 \dot{\theta} - u_{11} r_x^2 \dot{p} \end{pmatrix} \quad \text{in } \mathcal{F}_2$$

with

$$g_3 = L + c_y^{(1)} + r_y^{(2)}$$
$$g_4 = c_x^{(1)} + r_x^{(2)} \qquad (8)$$
$$b_2 = L u_{21} + r_y^{(2)} u_{11}$$

Angular velocity of $\mathcal{F}_3 = (\dot{\theta} - u_{11}\dot{p} + \dot{\alpha})\,\vec{k}$

The inertial velocity of the mass centre of the gimbal platform resolved in F_3 is given by

$$[R^{32}]\,\underline{v}^{(P_3)} + (\dot{\theta} - u_{11}\dot{p} + \dot{\alpha})\,\vec{k} \times \underline{c}^{(3)}$$

which can be written as

$$\begin{pmatrix} \dot{x} - g_5\,\dot{\theta} + b_3\,\dot{p} - c_y^{(3)}\,\dot{\alpha} \\ \dot{y} + g_6\,\dot{\theta} - b_4\,\dot{p} + c_x^{(3)}\,\dot{\alpha} \end{pmatrix} \quad \text{in } \mathcal{F}_3$$

again dropping nonlinear terms.

Here

$$\begin{aligned} g_5 &= g_3 + c_y^{(3)} \quad , \quad b_3 = b_2 + c_y^{(3)}\,u_{11} \\ g_6 &= g_4 + c_x^{(3)} \quad , \quad b_4 = u_{11}\,(r_x^{(3)} + c_x^{(3)}) \end{aligned} \tag{9}$$

The kinetic energy T_4 of the gimbal platform can now be written as

$$\begin{aligned} T_4 = \tfrac{1}{2} m_3 \big[&(\dot{x} - g_5\,\dot{\theta} + b_3\,\dot{p} - c_y^{(3)}\,\dot{\alpha})^2 + \\ &(\dot{y} + g_6\,\dot{\theta} - b_4\,\dot{p} + c_x^{(3)}\,\dot{\alpha})^2 \big] + \\ &\tfrac{1}{2} I_{zz}^{(3)}\,(\dot{\theta} - u_{11}\,\dot{p} + \dot{\alpha})^2 \end{aligned} \tag{10}$$

Kinetic Energy of Antenna Column & Hoop

The inertial velocity of point P_4 resolved in F_3 is given by

$$\underline{v}^{(P_4)} = \begin{pmatrix} \dot{x} - g_7\,\dot{\theta} + b_5\,\dot{p} - r_y^3\,\dot{\alpha} \\ \dot{y} + g_8\,\dot{\theta} - b_6\,\dot{p} + r_x^3\,\dot{\alpha} \end{pmatrix}$$

C-3

where

$$g_7 = g_3 + r_y^{(3)} \quad , \quad b_5 = b_2 + r_y^{(3)} u_{11}$$

$$g_8 = g_4 + r_x^{(3)} \quad , \quad b_6 = u_{11}(r_x^{(4)} + r_x^{(3)}) \tag{11}$$

Angular velocity of $\mathcal{F}_4 = (\dot{\theta} - u_{11}\dot{p} + \dot{\alpha} + \dot{\psi}_1)\,\vec{k}$

Let $\bar{c}$ be the distance (measured along the x_4 axis) from P_4 to the combined mass centre, and $\bar{I}$ the moment of inertia of the combined bodies about an axis parallel to the z direction passing through the composite centre of mass.

$$\bar{c} = (m_4 c + m_6 h)/(m_4 + m_6)$$

$$\bar{I} = I_{zz}^{(4)} + m_4(c-\bar{c})^2 + I_{zz}^{(6)} + m_6(c-h)^2 \tag{12}$$

The inertial velocity of the mass centre of the combined system (antenna column & hoop) resolved in F_4 is given by

$$\begin{pmatrix} \dot{x} - g_7\dot{\theta} + b_5\dot{p} - r_y^{(3)}\dot{\alpha} \\ \dot{Y} + g_9\dot{\theta} - b_7\dot{p} + g_{10}\dot{\alpha} + \bar{c}\,\dot{\psi}_1 \end{pmatrix}$$

where

$$g_7 = g_8 + \bar{c}, \quad g_{10} = r_x^{(3)} + \bar{c}, \quad b_7 = b_6 + u_{11}\bar{c} \tag{13}$$

The kinetic energy T_5 of the antenna column+hoop . is then given by

$$T_5 = \tfrac{1}{2}(m_4+m_6)\left[(\dot{x} - g_7\dot{\theta} + b_5\dot{p} - r_y^{(3)}\dot{\alpha})^2 + (\dot{Y} + g_9\dot{\theta} - b_7\dot{p} + g_{10}\dot{\alpha} + \bar{c}\,\dot{\psi}_1)^2\right]$$

$$+ \tfrac{1}{2}\bar{I}\,(\dot{\theta} - u_{11}\dot{p} + \dot{\alpha} + \dot{\psi}_1)^2 \tag{14}$$

Kinetic Energy of Feed Mast & Horn

The inertial velocity of point P_5 resolved in F_4 is given by

$$\underline{v}^{P_5} = \begin{pmatrix} \dot{x} - g_7\dot{\theta} + b_5\dot{p} - r^{(3)}_y\dot{\alpha} \\ \dot{y} + (g_8+a)\dot{\theta} - (b_6+a u_{11})\dot{p} + (r^3_x+a)\dot{\alpha} + a\dot{\psi}_1 \end{pmatrix}$$

Angular velocity of $\mathcal{F}_5 = (\dot{\theta} - u_{11}\dot{p} + \dot{\alpha} + \dot{\psi}_1 + \dot{\psi}_2)\,\hat{k}$

The inertial velocity of the feed mast & horn mass centre resolved in F_5 is given by

$$\begin{pmatrix} \dot{x} - g_7\dot{\theta} + b_5\dot{p} - r^3_y\dot{\alpha} \\ \dot{y} + g_{11}\dot{\theta} - b_8\dot{p} + g_{12}\dot{\alpha} + g_{13}\dot{\psi}_1 + b\dot{\psi}_2 \end{pmatrix}$$

where

$$g_{11} = g_8 + a + b \quad , \quad g_{12} = r^3_x + a + b \qquad (15)$$
$$g_{13} = a + b \quad , \quad b_8 = b_6 + u_{11}(a+b)$$

The kinetic energy T_6 of the feed mast & horn is given by

$$T_6 = \tfrac{1}{2} m_5 \left[(\dot{x} - g_7\dot{\theta} + b_5\dot{p} - r^3_y\dot{\alpha})^2 + (\dot{y} + g_{11}\dot{\theta} - b_8\dot{p} + g_{12}\dot{\alpha} + g_{13}\dot{\psi}_1 + b\dot{\psi}_2)^2 \right] + \tfrac{1}{2} I^{(3)}_{zz} (\dot{\theta} - u_{11}\dot{p} + \dot{\alpha} + \dot{\psi}_1 + \dot{\psi}_2)^2 \qquad (16)$$

System Stiffness and Mass Matrices

The 7x1 vector of generalized coordinates $\underline{q}$ consists of

(1) Orbiter x translation
(2) Orbiter y translation
(3) Orbiter pitch
(4) Mast modal coordinate

(5) Pitch gimbal angle
(6) Torsional angle at antenna column base
(7) Torsional angle at antenna column tip

$$\underline{q} = [\, x, y, \theta, \phi, \alpha, \psi_1, \psi_2 \,]^T$$

From eq.(1) the strain energy V(t) can be written as the quadratie form

$$V(t) = \tfrac{1}{2}\, \underline{q}^T\, [K]\, \underline{q}$$

where the stiffness matrix [K] is given by

$$[K] = \mathrm{diag}\left(0, 0, 0, \frac{EI}{L}\beta_1^4, 0, k_1, k_2\right) \qquad (17)$$

The total system kinetic energy T, can be obtained by summing equations (2), (4), (7), (10), (14) and (16).

Writing $T = \tfrac{1}{2}\, \dot{\underline{q}}^T\, [M]\, \dot{\underline{q}}$

the elements of the mass matrix [M] follow.

$$m_{11} = \sum_{i=1}^{6} m_i + \rho L$$

$$m_{12} = 0$$

$$m_{13} = -\rho \frac{L}{2}(L + 2c'_y) - g_7(m_4 + m_5 + m_6) - g_5 m_3 - g_1 m_2$$

$$m_{14} = \rho L^2 u_{31} + b_5(m_4 + m_5 + m_6) + b_3 m_3 + b_1 m_2$$

$$m_{15} = -m_3 c^3_y - r^3_y (m_4 + m_5 + m_6)$$

$$m_{16} = 0$$

$$m_{17} = 0$$

$$m_{22} = m_{11}$$

$$m_{23} = \rho L\, c_x^{(1)} + (m_4 + m_6)\, g_9 + m_5 g_{11} + m_3 g_6 + m_2 g_2$$

$$m_{24} = -m_2 u_{11} c_x^{(2)} - (m_4 + m_6) b_7 - m_5 b_8 - m_3 b_4$$

$$m_{25} = m_3 c_x^{(3)} + (m_4 + m_6) g_{10} + m_5 g_{12}$$

$$m_{26} = (m_4 + m_6)\, \bar{c} + m_5 g_{13}$$

$$m_{27} = b\, m_5$$

$$m_{33} = I_{zz}^{(1)} + I_{zz}^{(2)} + I_{zz}^{(3)} + I_{zz}^{(5)} + \bar{I} + m_2 (g_1^2 + g_2^2) + m_3 (g_5^2 + g_6^2)$$
$$m_4 (g_7^2 + g_4^2) + m_5 (g_{10}^2 + g_7^2) + m_6 (g_7^2 + g_4^2) +$$
$$\rho L \left[(c_x')^2 + (c_y')^2 \right] + \rho L^2 c_y^{(1)} + \tfrac{1}{3} \rho L^3$$

$$m_{34} = -\rho L^3 u_{41} - \rho L^2 c_y^{(1)} u_{31} - u_{11} (m_2 g_2 c_x^2 + \bar{I} + I_{zz}^{(5)} + I_{zz}^{(3)} + I_{zz}^{(2)}$$
$$-(m_4 + m_6)(b_7 g_9 + b_5 g_7) - m_5 (b_5 g_7 + b_8 g_{11}) - m_3 (b_4 g_6 + b_3 g_5)$$
$$- m_2 b_1 g_1$$

$$m_{35} = g_7 r_y^{(3)} (m_4 + m_5 + m_6) + (m_4 + m_6) g_9 g_{10} + m_5 g_{11} g_{12} +$$
$$m_3 (c_x^3 g_6 + c_y^3 g_5) + \bar{I} + I_{zz}^{(5)} + I_{zz}^{(3)}$$

$$m_{36} = I_{zz}^{(5)} + \bar{I} + m_5 g_{11} g_{13} + \bar{c}\, g_9 (m_4 + m_6)$$

$$m_{37} = I_{zz}^{(5)} + m_5 b\, g_{11}$$

$$m_{44} = u_{11}^2 \left[m_2 (c_x^2)^2 + \bar{I} + I_{zz}^{(5)} + I_{zz}^{(3)} + I_{zz}^{(2)} \right] + \rho L^3 +$$
$$(m_4 + m_6)(b_5^2 + b_7^2) + m_5 (b_5^2 + b_8^2) + m_3 (b_3^2 + b_4^2) + m_2 b_1^2$$

$$m_{45} = -u_{11} (I_{zz}^{(3)} + I_{zz}^{(5)} + \bar{I}) - (m_4 + m_5 + m_6) b_5 r_y^3 - (m_4 + m_6) g_{10} b_7$$
$$- m_5 g_{12} b_8 - m_3 (b_3 c_y^3 + b_4 c_x^3)$$

$$m_{46} = -u_{11}\left(I^{(5)}_{zz} + \bar{I}\right) - (m_4 + m_6)\, b_7\, \bar{c} - m_5\, g_{13}\, b_8$$

$$m_{47} = -u_{11}\, I^{(5)}_{zz} - m_5\, b\, b_8$$

$$m_{55} = \sum_{i=4}^{6} m_i\, (r^3_y)^2 + (m_4 + m_6)\, g_{10}^2 + m_5\, g_{12}^2 + m_3\left[(c^3_x)^2 + (c^3_y)^2\right] + \bar{I} + I^{(5)}_{zz} + I^{(3)}_{zz}$$

$$m_{56} = I^{(5)}_{zz} + \bar{I} + (m_4 + m_6)\, \bar{c}\, g_{10} + m_5\, g_{12}\, g_{13}$$

$$m_{57} = I^{(5)}_{zz} + m_5\, b\, g_{12}$$

$$m_{66} = I^{(5)}_{zz} + \bar{I} + (m_4 + m_6)\, \bar{c}^2 + m_5\, g_{13}^2$$

$$m_{67} = I^{(5)}_{zz} + m_5\, b\, g_{13}$$

$$m_{77} = I^{(5)}_{zz} + m_5\, b^2$$

Note that [M] is symmetric

Generalized Forces

At the gimbal pivot (P_3) a servo torque $\tau(t)$ is present which when positive, tends to increase the gimbal angle $\alpha(t)$. No other noncoservative forces are acting upon the vehicle. During an arbitrary virtual displacement of the system the virtual work δw done by the servo is

$$\delta w = \tau(t)\,\delta\alpha$$

Equations of Motion & Transfer Function

It follows from Lagranges' equations that

$$[M]\ddot{\underline{q}} + [K]\underline{q} = \underline{Q}$$

All elements of the generalized force vector $\underline{Q}$ are are zero except for $Q_5 = \tau(t)$. Taking the Laplace transform of the equations of motion and assuming that $\underline{q}(0) = \dot{\underline{q}}(0) = \underline{0}$, we have

$$\left(s^2[M] + [K]\right)\bar{\underline{q}}(s) = \bar{\underline{Q}}(s)$$

$$\therefore \quad \frac{\bar{\alpha}(s)}{\bar{\tau}(s)} = \frac{\Delta_1(s)}{\Delta(s)}$$

where $\Delta(s) = \det(S^2[M] + [K])$ and $\Delta_1(s)$ is the determinat of a matrix obtained by replacing the fifth column of $(S^2[M] + [K])$ with $(0,0,0,0,1,0,0)^t$. The transfer function will be of the form

$$\frac{\bar{\alpha}(s)}{\bar{\tau}(s)} = \frac{A}{s^2}\,\frac{(s^2+\Omega_1^2)(s^2+\Omega_2^2)(s^2+\Omega_3^2)}{(s^2+\omega_1^2)(s^2+\omega_2^2)(s^2+\omega_3^2)}$$

ω_1, ω_2, and ω_3 are the non zero natural frequencies of the unforced vehicle. Note that in addition to these values use have four rigid body modes: orbiter translation (x and y), orbiter

pitch, and rotation about the gimbal pivot.

Numerical Results

Data (MKS)

$m_1 = 84831.4$, $I_{zz}^{(1)} = 8913427.0$, $\underline{c}^{(1)} = (-5.386, -.204)$,

$L = 60.693$, $\rho = 10.0156$, $EI = 2.863 \times 10^7$,

$\underline{c}^{(2)} = (2.7442, 0)$, $\underline{r}^{(2)} = (3.3274, 0)$

$m_2 = 102.409$, $I_{zz}^{(2)} = 40.6$

$\underline{c}^{(3)} = (.358, 0)$, $\underline{r}^{3} = (.508, 0)$, $m_3 = 172.176$, $I_{zz}^{(3)} = 9.52$,

$m_4 = 126.951$, $I_{zz}^{(4)} = 1743.736$, $c = 4.175$, $a = 9.4715$,

$h = 5.298$, $b = 3.388$, $m_5 = 117.234$, $I_{zz}^{(5)} = 34.861$

$m_6 = 118.337$, $I_{zz}^{(6)} = 3315.772$

$k_1 = 71442.17$, $k_2 = 57839.17$

$$\frac{\tilde{\alpha}(s)}{\tilde{\tau}(s)} = \frac{.01617}{s^2} \frac{(s^2+.64122)(s^2+2.4227)(s^2+120.124)}{(s^2+.67441)(s^2+112.64)(s^2+1248.4)}$$

COFS-II Mechanical Admittance Function

$$\frac{\theta_M}{T_M}(s) = \frac{\Omega_M}{s\,T_M}(s) = \frac{1.617 \times 10^{-2}}{s^2} \frac{(s^2 + \omega_{z_1}^2)(s^2 + 0.641)}{(s^2 + \omega_{p_1}^2)(s^2 + 0.674)} \frac{(s^2 + \omega_{z_2}^2)(s^2 + 2.42)}{(s^2 + \omega_{p_2}^2)(s^2 + 112)} \frac{(s^2 + \omega_{z_3}^2)(s^2 + 120)}{(s^2 + \omega_{p_3}^2)(s^2 + 1298)}$$

or

$\omega_{z_1} = 0.80$	$\omega_{z_2} = 1.55$	$\omega_{z_3} = 11$
$\omega_{p_1} = 0.82$	$\omega_{p_2} = 10.6$	$\omega_{p_3} = 36$

rad/sec

Note the near cancellation of two pole-zero pairs, ω_{z_1} with ω_{p_1} and ω_{p_2} with ω_{z_3}.

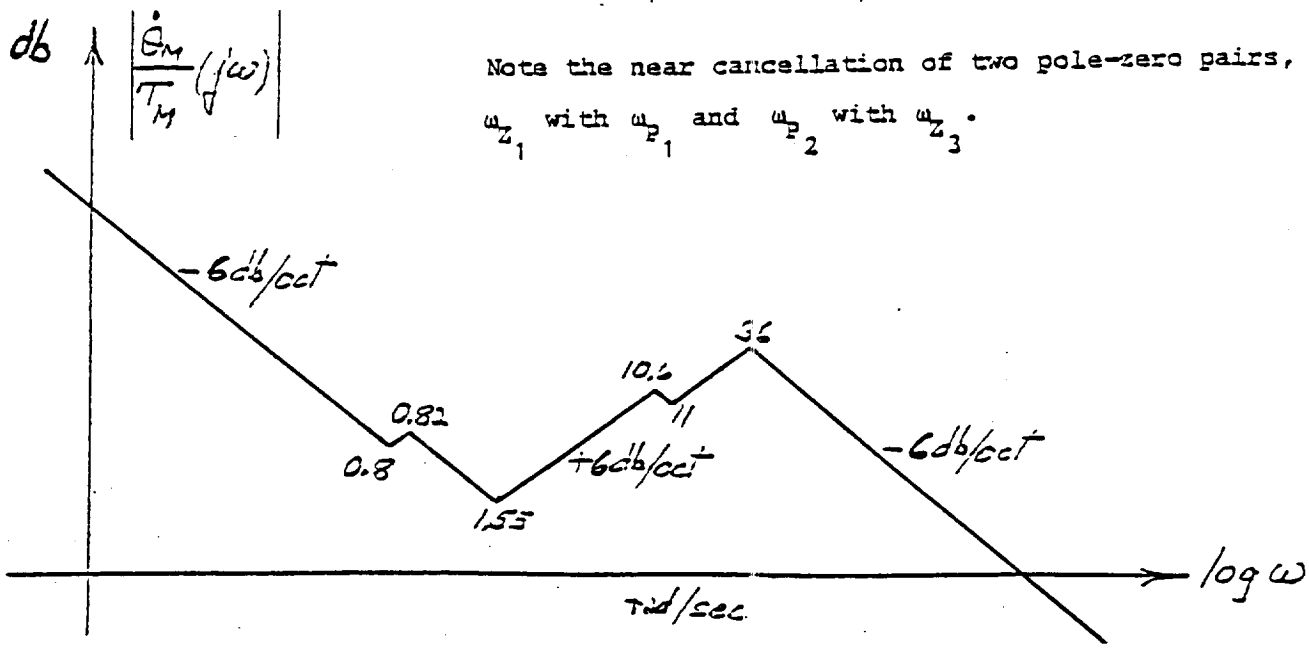

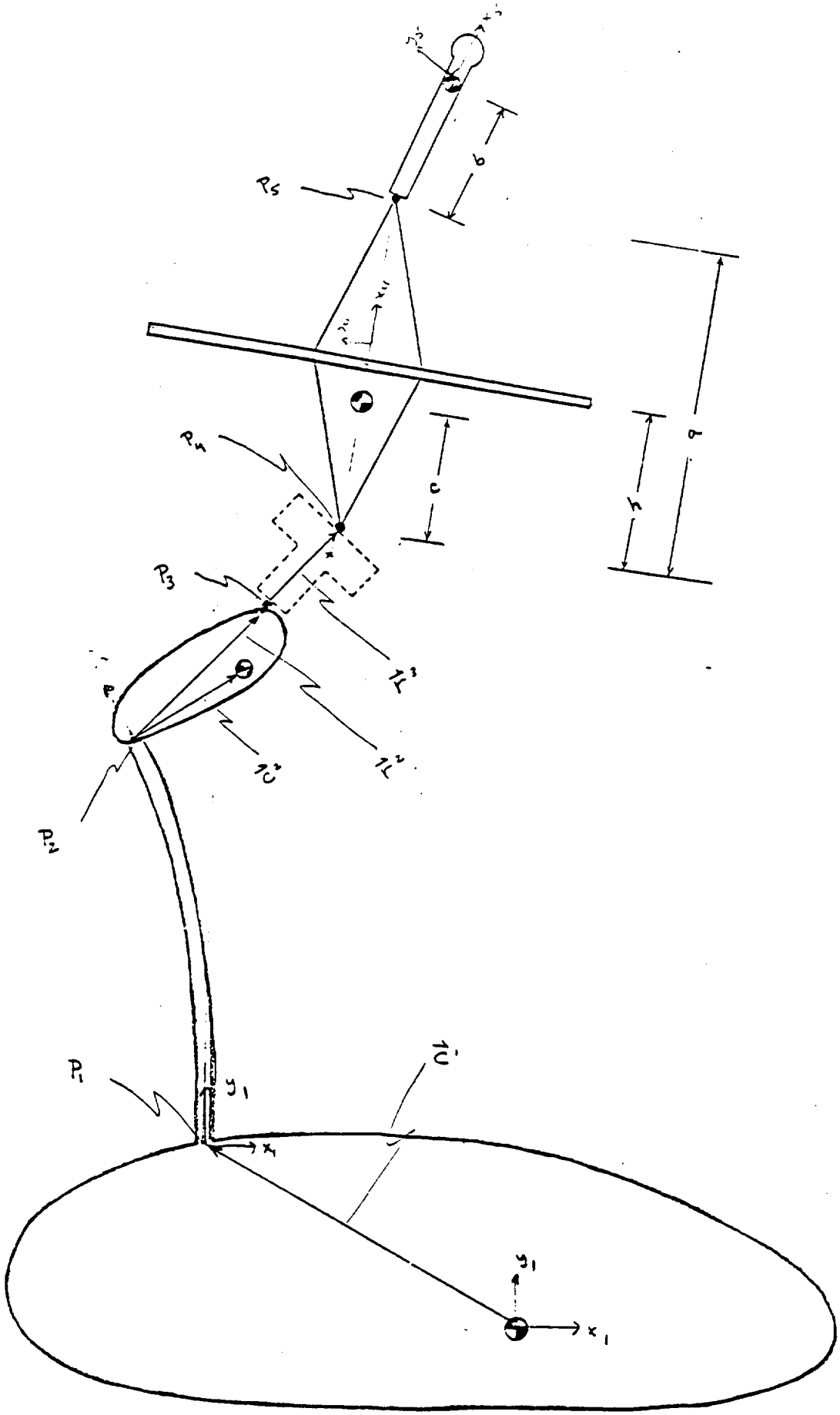

Fig. 1

TECHNICAL REPORT STANDARD TITLE PAGE

1. Report No.	2. Government Accession No.	3. Recipient's Catalog No.

4. Title and Subtitle	5. Report Date
Control of Flexible Structures-II (COFS-II) Flight Control, Structure, and Gimbal System Interaction Study	September 1988
	6. Performing Organization Code
7. Author(s) S. Fay, S. Gates, T. Henderson, L. Sackett, C. Kirchwey, I. Stoddard, J. Storch	8. Performing Organization Report No. R-2088
9. Performing Organization Name and Address Charles Stark Draper Laboratory, Inc. 555 Technology Square Cambridge, MA 02139	10. Work Unit No.
	11. Contract or Grant No. NAS9-17560
	13. Type of Report and Period Covered
12. Sponsoring Agency Name and Address Langley Research Center National Aeronautics and Space Administration Hampton, VA 23665	Final Report
	14. Sponsoring Agency Code

15. Supplementary Notes

16. Abstract

The second Control of Flexible Structures Flight Experiment (COFS-II) includes a long mast as in the first flight experiment, but with the Langley 15-m hoop-column antenna attached via a gimbal system to the top of the mast. The mast would be mounted in the Space Shuttle cargo bay. The servo-driven gimbal system could be used to point the antenna relative to the mast. The dynamic interaction of the Shuttle Orbiter/COFS-II system with the Orbiter on-orbit Flight Control System (FCS) and the gimbal pointing control system has been studied using analysis and simulation. The Orbiter pointing requirements have been assessed for their impact on allowable free drift time for COFS experiments. Three fixed antenna configurations were investigated. Also simulated was Orbiter attitude control behavior with active vernier jets during antenna slewing. The effect of experiment mast dampers was included. Control system stability and performance and loads on various portions of the COFS-II structure were investigated. The study indicates possible undesirable interaction between the Orbiter FCS and the flexible, articulated COFS-II mast/antenna system, even when restricted to vernier reaction jets. Undesirable conditions can probably be avoided with careful planning, pre-flight analysis and simulations, and flight operational constraints. The FCS should be inactive during antenna slews. The gimbal control system was analyzed for small gimbal angle excursions with no active Orbiter attitude control. The torque authority of the gimbal motor is so small that control is quickly saturated.

17. Key Words Suggested by Author	18. Distribution Statement
Orbiter Flight Control System Stability Dynamic Interaction, Large Space Structures	Unlimited Distribution

19. Security Classif. (of this report)	20. Security Classif. (of this page)	21. No. of Pages	22. Price
Unclassified	Unclassified		